MICROSTRUCTURE DESIGN AND MULTIFUNCTIONALITY OF BARIUM ZIRCONATE TITANATE-BARIUM CALCIUM TITANATE THIN FILMS PREPARED BY CHEMICAL SOLUTION DEPOSITION

Sabi William Konsago

Doctoral Dissertation
Jožef Stefan International Postgraduate School
Ljubljana, Slovenia

Supervisor: Prof. Dr. Barbara Malič, Jožef Stefan Institute, Ljubljana, Slovenia
Co-Supervisor: Prof. Dr. Hana Uršič Nemevšek, Jožef Stefan Institute, Ljubljana, Slovenia

Evaluation Board:
Prof. Dr. Vid Bobnar, Chair, Jožef Stefan Institute, Ljubljana, Slovenia
Dr. Katarina Vojisavljević, Member, Institute for Multidisciplinary Research, University of Belgrade, Serbia.
Prof. Miguel Algueró Giménez, Member, Instituto de Ciencia de Materiales de Madrid, Madrid, Spain

MEDNARODNA PODIPLOMSKA ŠOLA JOŽEFA STEFANA
JOŽEF STEFAN INTERNATIONAL POSTGRADUATE SCHOOL

Sabi William Konsago

MICROSTRUCTURE DESIGN AND MULTIFUNCTIONALITY OF BARIUM ZIRCONATE TITANATE-BARIUM CALCIUM TITANATE THIN FILMS PREPARED BY CHEMICAL SOLUTION DEPOSITION

Doctoral Dissertation

NAČRTOVANJE MIKROSTRUKTURE IN MULTIFUNKCIONALNOST TANKIH PLASTI BARIJEVEGA CIRKONATA TITANATA-BARIJEVEGA KALCIJEVEGA TITANATA, PRIPRAVLJENIH S SINTEZO V RAZTOPINI

Doktorska disertacija

Supervisor: Prof. Dr. Barbara Malič

Co-Supervisor: Prof. Dr. Hana Uršič Nemevšek

Ljubljana, Slovenia, December 2024

Acknowledgments

This PhD thesis at the Electronic Ceramics Department – K5 at the Jožef Stefan Institute was a life-changing experience, and I would like to take time to acknowledge people who made this experience possible, who have been a source of inspiration, helped, and guided me during this five-years journey.

First of all, I would like to thank my supervisor Prof. Dr. Barbara Malič, and express my sincere gratitude for giving me the opportunity to work at the Electronic Ceramics Department, Jožef Stefan Institute, for the multitude of opportunities to visit foreign laboratories, attend trainings, schools, international conferences. She exceeded the duties of a PhD mentor and showed great support and patience in guiding a synthetic organic chemistry student into the world of micro- and nanoelectronic ceramics. I am truly grateful to her for her numerous advices, motivation, continuous guidance, and scientific discussions.

I would like to thank Prof. Dr. Hana Uršič, my co-mentor, for numerous advices and discussions related to atomic force microscopy (AFM), piezoelectric force microscopy (PFM), and energy storage properties.

Prof. Dr. Andreja Benčan and Katarina Žiberna are gratefully acknowledged for their help with scanning electron microscopy (SEM), energy-dispersive X-ray spectroscopy (EDS), scanning transmission microscopy (STEM), and fruitful discussions.

Special thanks to Dr. Aleksander Matavž and Prof. Dr. Vid Bobnar (Condensed Matter Physics Department, Jožef Stefan Institute) for dielectric measurements as a function of temperature across a broad frequency range, macroscopic piezoelectric measurements by double beam laser interferometry (DBLI); Dr. Jerney Ekar and Prof. Dr. Janez Kovač (Department of Surface Engineering, Jožef Stefan Institute) for time-of-flight secondary Ion mass spectrometry (ToF-SIMS) and X-ray photoelectron spectroscopy (XPS) analyses.

My special thanks are extended to Brigita Kmet for her help with SEM and assistance with cleanroom and electrical measurements equipment, Silvo Drnovšek for his help with electrode depositions, Jena Cilenšek for her help with thermal analysis and thermal expansion coefficient measurements, Andrej Debevec for his help with bulk ceramics processing and their properties measurements, Dr. Matej Šadl and Ivana Goričan for their help with energy storage measurements, Val Fišinger for his help with conductive AFM and PFM measurements, Maja Koblar for her assistance with the Aixacct system, Dean Birmančević for his help with thin film depositions. Dr. Mirela Dragomir is acknowledged for her help with XRD data analysis and training using X-ray Diffractometer (Rigaku MiniFlex 600), and Edi Krajnc (National Institute of Chemistry)

for the XRD measurements. I thank all my colleagues at the Electronic Ceramic Department, especially Tina Ručigaj for a supportive and helpful atmosphere.

I want to acknowledge our international collaborators: Dr. Sebastjan Glinšek, Barnik Mandal, and Dr. Yves Fleming from Luxembourg Institute of Science and Technology (LIST) for their help with Grazing Incidence X-ray diffraction (GIXRD), pole-figure XRD, and tilted angle XRD measurements, and the fruitful discussions; Prof. Geoff L. Brennecka from Colorado School of Mines for his advice and fruitful discussions.

I would like to acknowledge Dr. Marco Deluca for hosting me at the Materials Center in Leoben, Austria. My acknowledgments are extended to Dr. Harvey AMORÍN for hosting me at the Instituto de Ciencia de Materiales de Madrid, CSI, Spain.

I am also would like to express my gratitude to the Slovenian Research and Innovation Agency (core funding P2-0105, S.W.K - young researcher programme), JECS Trust fund, Erasmus+ programme, WTZ Slowenien S&T Slovenia 2020_21 for the funding, NANOCENTER for access to FIB.

Finally, I would like to thank my family and friends for their support and encouragement.

Najlepša hvala!

Abstract

Barium zirconate titanate-barium calcium titanate $0.5Ba(Zr_{0.2}Ti_{0.8})O_3$-$0.5(Ba_{0.7}Ca_{0.3})TiO_3$ (BZT-BCT) ceramic exhibits a high piezoelectric response in the vicinity of room temperature. It is an environment-friendly alternative to $Pb(Zr_{1-x}Ti_x)O_3$ (PZT), the most used ceramic material in piezoelectric applications. Thin films meet the requirements related to the miniaturization of electronic components such as in energy harvesting or storage applications. Chemical solution deposition (CSD) of thin films steps out among versatile physical or chemical vapour deposition routes due to the easy adaptation of the chemical composition via the solution chemistry.

However, challenges related to CSD of BZT-BCT thin films prepared from the conventional carboxylic-acid-based synthetic route include the instability of the coating solution, fine-grained and porous microstructure, cracks and consequently non-optimal functional properties. To resolve the challenges and establish the microstructure-properties relation in BZT-BCT thin films, we developed an alternative synthetic approach. The new procedure uses ethylene glycol (EG) and ethanol (EtOH) as solvents for alkaline-earth acetates and transition-metal alkoxides, respectively. Barium titanate ($BaTiO_3$, BT), the prototype ferroelectric, was selected as a reference material. EG-EtOH-based BT coating solution was stable for more than one year. Crack-free BT thin films with columnar microstructure and thickness of about 130 nm on platinized silicon substrates (Pt/Si) exhibit dielectric permittivity of 600, measured at room temperature (R.T.) and 1 kHz, maximum polarization (P_{max}) of 26 $\mu C \cdot cm^{-2}$ and survive electric fields of 2.4 $MV \cdot cm^{-1}$.

The EG-EtOH synthesis was transferred to the BZT-BCT system. Achieving chemically homogeneous BZT-BCT thin films with columnar microstructure and without interaction with Pt/Si substrates required diluting the coating solution to 0.1 M and increasing the annealing temperature to 850 °C.

Manganese doping (1 mole %) effectively reduced the leakage and enabled measurements of macroscopic functional properties. About 120 nm thick BZT-BCT films doped with manganese on Pt/Si substrates exhibit dielectric permittivity of 670 measured at RT and 1 kHz, P_{max} of 32 $\mu C \cdot cm^{-2}$ at 1.15 $MV \cdot cm^{-1}$, piezoelectric d_{33} coefficient of 20 $pm \cdot V^{-1}$ and strain (S) of 0.18 % measured using a double-beam laser interferometer. The recoverable energy (U_{rec}) and energy storage efficiency (η) of 10 $J \cdot cm^{-3}$ and 69 %, respectively, are obtained. The film thickness exceeding ≈120 nm on Pt/Si resulted in the evolution of intergranular cracks due to the thermal expansion mismatch between the film and silicon substrate. Using platinized sapphire (Pt/Sapp) substrates reduced the thermal stress in the films due to the smaller difference in thermal expansion coefficients between BZT-BCT and sapphire. Up to 680 nm thick crack-free BZT-BCT films doped with manganese on Pt/Sapp substrates with columnar microstructure were obtained upon multistep annealing at 850 °C. The 340 nm thick films are characterized by dielectric permittivity of 930 at 1 kHz, d_{33} of ~40 $pm \cdot V^{-1}$, S of ~ 0.77 %, and P_{max} ~ 47 $\mu C \cdot cm^{-2}$ at a maximum electric field of about 3.5 $MV \cdot cm^{-1}$. The energy storage efficiency of 89 % and U_{rec} ~ 46 $J \cdot cm^{-3}$ make BZT-BCT films a promising option for energy storage applications.

Povzetek

Keramika na osnovi barijevega cirkonata titanata-barijevega kalcijevega titanata $0{,}5Ba(Zr_{0,2}Ti_{0,8})O_3$-$0{,}5(Ba_{0,7}Ca_{0,3})TiO_3$ (BZT-BCT) predstavlja okolju prijazno nadomestilo komercialno najbolj razširjeni svinčevi piezoelektrični keramiki $Pb(Zr_{1-x}Ti_x)O_3$ (PZT). Tanke plasti omogočajo miniaturizacijo elektronskih komponent, na primer v napravah za zbiranje ali shranjevanje energije.

Priprava tankih plasti BZT-BCT s sintezo iz raztopine predstavlja izziv, saj je za plasti značilna porozna mikrostruktura z enakoosnimi zrni in razpoke po mejah med zrni, kar posledično omejuje doseganje dobrih funkcijskih lastnosti. Poleg tega lahko v raztopinah za pripravo tankih plasti, ki kot topilo vsebujejo karboksilno kislino, poteče delna hidroliza alkoksidnih reagentov, kar vodi do izgube kemijske homogenosti.

Da bi raziskali povezavo med mikrostrukturo in funkcijskimi lastnostmi tankih plasti BZT-BCT, smo razvili alternativno sintezo raztopin za nanašanje plasti. Nova sinteza vključuje etilenglikol (EG) in etanol (EtOH) kot topili za zemljoalkalijska acetata in alkoksida kovin prehoda. Najprej smo z novo kombinacijo topil pripravili tanke plasti osnovne spojine barijevega titanata ($BaTiO_3$, BT). Raztopina za nanašanje plasti je bila obstojna več kot leto. Raztopino s koncentracijo 0,2 M smo nanesli na podlage platiniziranega silicija (Pt/Si) z metodo vrtenja in po vsakem nanosu plast žgali pri 800 °C. Plasti BT z debelino ≈130 nm in stebričasto mikrostrukturo izkazujejo dielektričnost ≈600 pri 1 kHz in sobni temperaturi ter največjo polarizacijo 26 $\mu C \cdot cm^{-2}$ pri polju 2,4 $MV \cdot cm^{-1}$.

Nadalje smo s sintezo s topiloma EG in EtOH pripravili tanke plasti BZT-BCT. Izkazalo se je, da je bilo za plasti s kolumnarno mikrostrukturo potrebno znižati koncentracijo raztopine za nanašanje plasti na 0,1 M in povišati temperaturo žganja na 850 °C. Tanke plasti s stebričasto mikrostrukturo so kemijsko homogene po preseku, brez sekundarnih faz ali interakcij s podlago Pt/Si.

Tok puščanja v tankih plasteh BZT-BCT smo učinkovito zmanjšali z dopiranjem z manganom (1 molski %). Približno 120 nm debele plasti na podlagah Pt/Si izkazujejo dielektričnost ≈670 pri 1 kHz in sobni temperaturi, največjo polarizacijo 32 $\mu C \cdot cm^{-2}$ pri polju 1,15 $MV \cdot cm^{-1}$, piezoelektrični koeficient d_{33} 20 $pm \cdot V^{-1}$ in deformacijo 0.18 %, izmerjeno z dvožarkovnim laserskim interferometrom. Plasti so primerne za shranjevanje energije, pri čemer sta obnovljiva energija (U_{rec}) 10 $J \cdot cm^{-3}$ in izkoristek (η) 69 %.

Ko je debelina plasti na podlagah Pt/Si presegla ≈120 nm, so se začele pojavljati razpoke po mejah med zrni kot posledica napetosti, ki se pojavijo zaradi velike razlike v temperaturnih razteznostnih koeficientih (TEK) plasti in silicijeve podlage. Z uporabo podlage platiniziranega safirja z nekajkrat večjim TEK v primerjavi s silicijem smo močno zmanjšali napetosti v plasteh. Uspeli smo pripraviti do 680 nm debele plasti BZT-BCT, dopirane z manganom in s stebričasto mikrostrukturo. Tanke plasti z debelino 340 nm izkazujejo dielektričnost 930 pri 1 kHz in sobni temperaturi, največjo polarizacijo ~47 $\mu C \cdot cm^{-2}$ pri polju 3,5 $MV \cdot cm^{-1}$, piezoelektrični koeficient d_{33} 40 $pm \cdot V^{-1}$ in deformacijo 0,77 %. Z izmerjeno obnovljivo energijo ~46 $J \cdot cm^{-3}$ in izkoristkom 89 % predstavljajo tanke plasti BZT-BCT obetavno možnost za shranjevanje energije.

Contents

List of Figures

List of Tables

Abbreviations

AC	...	alternating current
AcOH	...	acetic acid
AFM	...	atomic force microscopy
a.u.	...	arbitrary units
BT	...	$BaTiO_3$
BCT	...	$(Ba_{0.7}Ca_{0.3})TiO_3$
BCT_x	...	$Ba_xCa_{1-x}TiO_3$
BZT	...	$Ba(Zr_{0.2}Ti_{0.8})O_3$
BZT_x	...	$BaZ_xTi_{1-x}O_3$
BZT-BCT	...	$0.5Ba(Zr_{0.2}Ti_{0.8})O_3$-$0.5(Ba_{0.7}Ca_{0.3})TiO_3$
cAFM	...	conductive atomic force microscopy
CMOS	...	complementary metal oxide semiconductor
CSD	...	chemical solution deposition
DBLI	...	double-beam laser interferometer
DC	...	direct current
DRAM	...	dynamic random-access memory
DTA	...	differential thermal analysis
EDXS	...	energy-dispersive X-ray spectrometer
EG	...	ethylene glycol
EGA		evolved gas analysis
EtOH	...	ethanol
FeRAM	...	ferroelectric random-access memory
FE-SEM	...	field-emission scanning electron microscope
FIB	...	focused ion beam
FTIR	...	fourier transform infrared spectroscopy
GIXRD	...	grazing incidence X-ray diffraction
LNO	...	$LaNiO_3$
MOE	...	2-methoxyethanol
PCT	...	$Pb_{0.8}Ca_{0.2}TiO_3$
PFM	...	piezo-response force microscopy
PLCT	...	$Pb_{0.8}La_{0.1}Ca_{0.1}TiO_3$
PLD	...	pulsed laser Deposition
PZT	...	$Pb(Zr,Ti)O_3$
rms	...	root-mean-square roughnesses
RT	...	room temperature
RTA	...	rapid thermal annealing
SAED	...	selected-area electron diffraction
SEM	...	scanning electron microscopy
STEM	...	scanning transmission electron microscopy
TEC	...	thermal expansion coefficient
TEM	...	transmission electron microscopy

TG	...	thermogravimetry
ToF-SIMS	...	time-of-flight secondary ion mass spectrometry
XPS	...	X-ray photoelectron spectroscopy
XRD	...	X-ray diffraction

Symbols

P ... polarization
ε_o ... dielectric permittivity of vacuum
ε_r' ... relative dielectric permittivity
χ_e ... dielectric susceptibility
E ... electric field
ε' ... real part of permittivity
ε'' ... imaginary part of permittivity
$\tan\delta$ ... dielectric losses
C ... capacitance
j ... current density
D ... dielectric displacement
d_{33} ... direct effective longitudinal piezoelectric coefficient
σ ... stress
S ... strain
2θ ... X-ray diffraction angle
Ψ ... tilt-angle
D_{hkl} ... interplanar spacing
T_c ... Curie temperature
E_c ... coercive field
P_r ... remanent polarization
P_{max} ... maximum polarization
E_{max} ... maximum field
U_{st} ... energy storage density
U_{rec} ... recovered energy storage density
U_{loss} ... energy loss
η ... energy storage efficiency

Chapter 1

Introduction

In the first part of this chapter, we describe barium titanate ($BaTiO_3$, BT) as the prototype ferroelectric material and its basic properties. We then describe BT-based materials, namely (1-x)$Ba(Zr_{0.2}Ti_{0.8})O_3$-x$(Ba_{0.7}Ca_{0.3})TiO_3$ (BZT–xBCT), as alternatives to lead-based materials for piezoelectric applications. Selected physical properties of polar oxides related to this thesis are summarized in Appendix B. The second part of the chapter describes the chemical solution deposition (CSD) of functional-oxide thin films, including the chemistry of precursors, the deposition techniques, and the heat treatment that leads to crystallization from the amorphous phase. The last part of the chapter is dedicated to a short review of the microstructure evolution in BT-based thin films, the relationship between the microstructure and functional properties of BT, $Ba(Zr_xTi_{1-x})O_3$(BZT_x), $(Ba_{1-x}Ca_x)TiO_3$ (BCT_x) and BZT-xBCT thin films. The main functional properties of interest are dielectric, ferroelectric, and piezoelectric properties of respective thin films, particularly those prepared by CSD.

1.1. Polar Oxide Materials and Their Basic Properties

1.1.1. Barium titanate: prototype ferroelectric material

Barium titanate ($BaTiO_3$, BT) is a prototype ferroelectric oxide. It crystallizes in the perovskite (ABO_3) structure. Above the phase transition temperature or Curie temperature at 130 °C, the structure of BT is centrosymmetric cubic. Upon cooling, the tetragonal distortion of the unit cell occurs as a consequence of the non-centrosymmetric position of the B cation, as shown in Figure 1, which results in the generation of spontaneous polarization (P_S, electric dipole per unit volume) [1], [2].

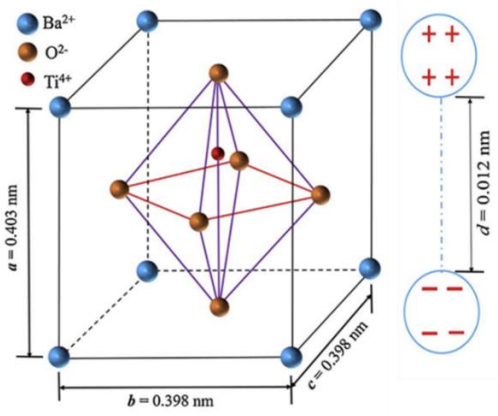

Figure 1: Unit cell of BT showing the displacement of Ti^{+4} in the TiO_6 octahedron (from [2]).

BT undergoes phase transitions from tetragonal to orthorhombic and rhombohedral phase upon further cooling. The ferroelectric phase transitions are accompanied by changes in the dimensions of the unit cell and anomalies in spontaneous polarization, dielectric, and other physical properties of the material [1], [3]. The sharp transitions observed in Figure 2 are characteristic of BT single crystals. However, in polycrystalline bulk materials, the phase transitions are diffuse, and the broadening of the dielectric permittivity peak depends on the grain size [4], [5]. In polycrystalline thin films, especially with fine grain size, it is often challenging to identify phase transitions [6], [7].

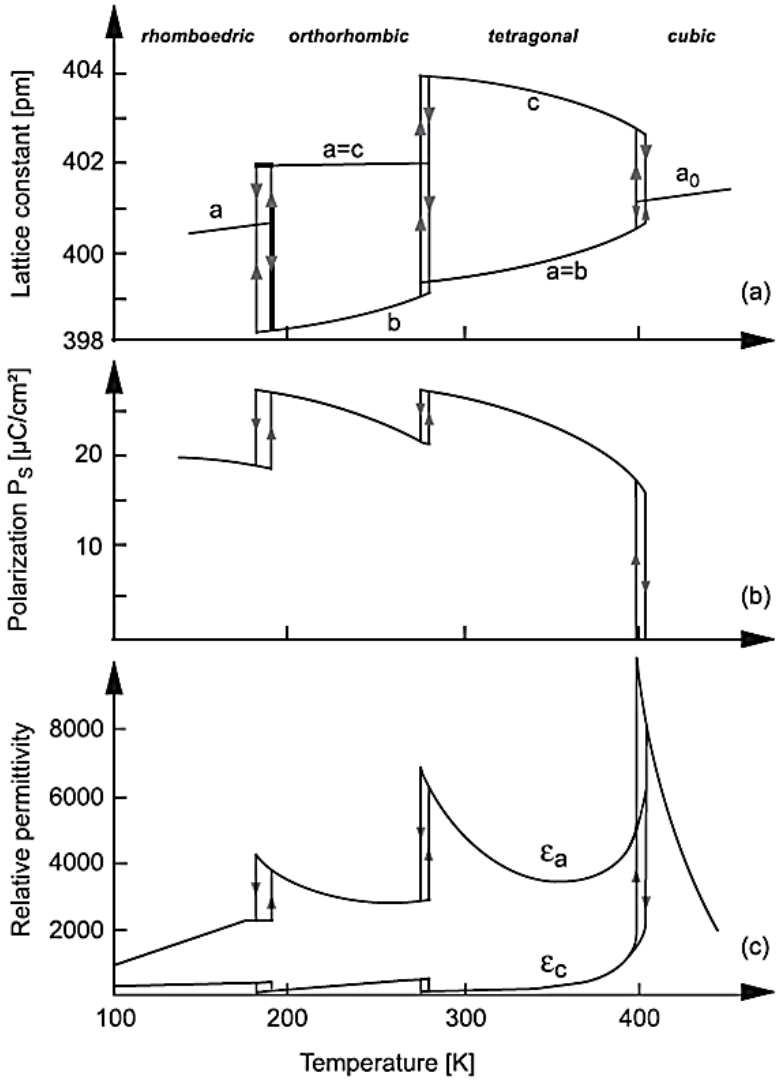

Figure 2: Phases and selected properties in BT single crystal as a function of temperature, showing (a) lattice constants, (b) spontaneous polarization P_s, and (c) relative permittivity (from [8]).

1.1.2. Barium titanate based materials as alternative to $Pb(Zr,Ti)O_3$ for piezoelectric applications

Lead zirconate titanate ($Pb(Zr,Ti)O_3$ or PZT) is the most used ferroelectric ceramic material for piezoelectric applications because of its high piezoelectric effect and high Curie temperature of about 350 °C [9], [10], [11]. The piezoelectric charge coefficient d_{33} of PZT ranges from 200 to

500 pC/N, depending on the type of heterovalent doping. Usually, donor cations such as La^{3+} or Nb^{5+} are doped on A or B sites, respectively, of the perovskite unit cell to soften the properties or acceptor dopants such as Fe^{+3} on the B sites to harden PZT. Hard PZT bulk ceramics are characterized by low permittivity, low losses, and high mechanical quality factor, and they are difficult to pole and depole. Soft PZT bulk ceramics, on the other hand, are easier to pole and have a lower coercive field, high d_{33}, lower mechanical quality factor, high permittivity and losses [12]. With such versatility in functional response, PZT has been and still is the most used material in piezoelectric applications. However, the toxicity of lead is an environmental concern. In 2002, the European Union introduced directives regulating using Pb and other toxic elements in commercial products [13]. Since then, interest in lead-free piezoelectrics that could replace lead-based materials has been growing. The piezoelectric d_{33} coefficient of BT bulk ceramics ranges from about 100 pC/N to a few 100 pC/N and depends on grain size [14]. Research on lead-free piezoelectric BT-based materials was triggered in 2009 by the paper of Liu and Ren [15] on excellent piezoelectric properties in (1-x)$Ba(Zr_{0.2}Ti_{0.8})O_3$-x$(Ba_{0.7}Ca_{0.3})TiO_3$ (BZT–xBCT)[1] bulk ceramic (d_{33} of 620 pC/N for x = 0.5) with a high longitudinal electromechanical coupling coefficient (k_{33}) of 0.65 which is similar to that of hard PZT showing a potential for actuator applications. Furthermore, BZT–xBCT is now investigated for energy storage, and as a potential biocompatible material for medical applications [16], [17], [18].

The idea behind the design of BZT-xBCT was to create a morphotropic phase boundary (MPB) composition, such as in PZT. The phase diagram of the $PbZrO_3$-$PbTiO_3$ solid solution is included in Figure 3. In the vicinity of the molar ratio of $PbZrO_3$ and $PbTiO_3$ of 48/52, there is a coexistence of a rhombohedral $PbZrO_3$-rich and tetragonal $PbTiO_3$-rich phase [19]. The MPB compositions exhibit a peak in piezoelectric properties [20], [21].

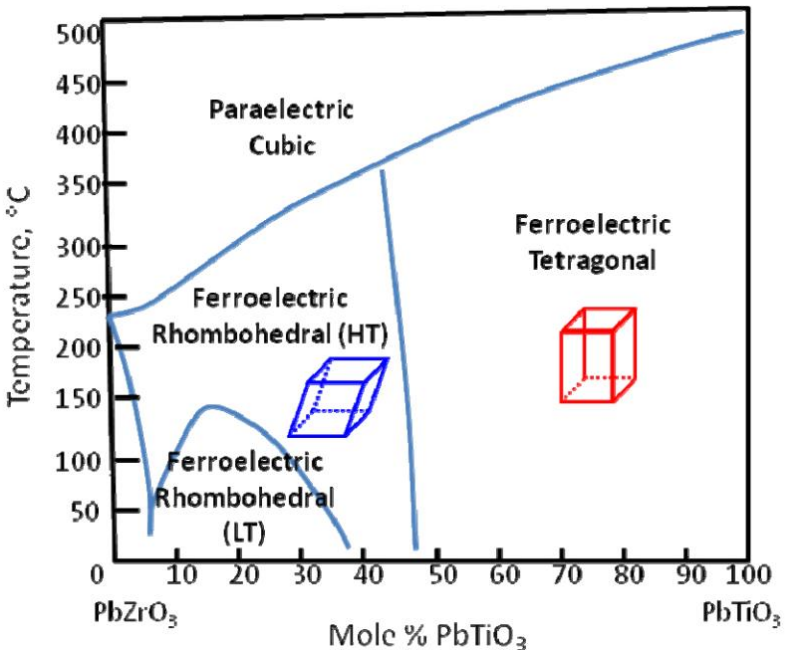

Figure 3: Phase diagram of PZT bulk ceramics (from [21]).

Similar to PZT, the BZT-xBCT solid solution was designed to have the coexistence of rhombohedral $Ba(Zr_{0.2}Ti_{0.8})O_3$ (BZT)[1] and tetragonal $(Ba_{0.7}Ca_{0.3})TiO_3$ (BCT)[1] phases as shown in Figure 4. The MPB observed at the composition close to 50 mole % of BZT and 50 mole % of

[1] $Ba(Zr_{02}Ti_{O.8})O_3$, $(Ba_{0.7}Ca_{0.3})TiO_3$ and $0.5Ba(Z_{r0.2}Ti_{0.8})O_3$ – $0.5(Ba_{0.7}Ca_{0.3})TiO_3$ are designated as BZT, BCT and BZT-BCT respectively. Solid solutions with different molar ratios of A- or B-site cations are written with chemical formulas or abbreviations explained in the text.

BCT was reported to be the reason for the high piezoelectric response in this material [15]. It is noted that the Curie temperature of BZT-xBCT formulations close to MPB is below 100 °C. In 2014, the coexistence of another, third phase in the BZT-xBCT phase diagram, close to 50% of BZT and 50 % of BCT, was reported [22], [23]. The updated phase diagram is shown in Figure 5. The piezoelectric properties peak close to this orthorhombic-tetragonal phase coexistence region. The BZT-xBCT ceramic is considered one of the alternatives to PZT-based materials for piezoelectric applications, especially for use in ambient environments. In BZT-BCT bulk ceramics, the grain size strongly influences the piezoelectric properties and the phase transitions. High piezoelectric responses were measured in BZT-BCT bulk ceramics with grain sizes above 10 μm [24]. In microelectronics including nano-electro-mechanical systems (NEMS), micro-electro-mechanical systems (MEMS), and micro-energy harvesters, the piezoelectric materials are used in the form of thin films to meet the size constraints [25].

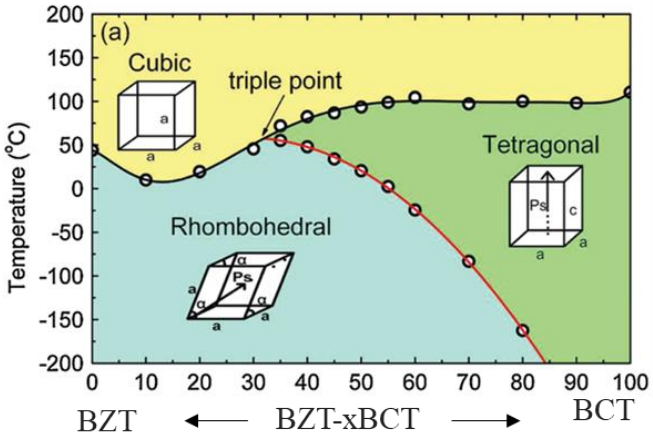

Figure 4. Phase diagram of BZT-BCT ceramics (from [15]).

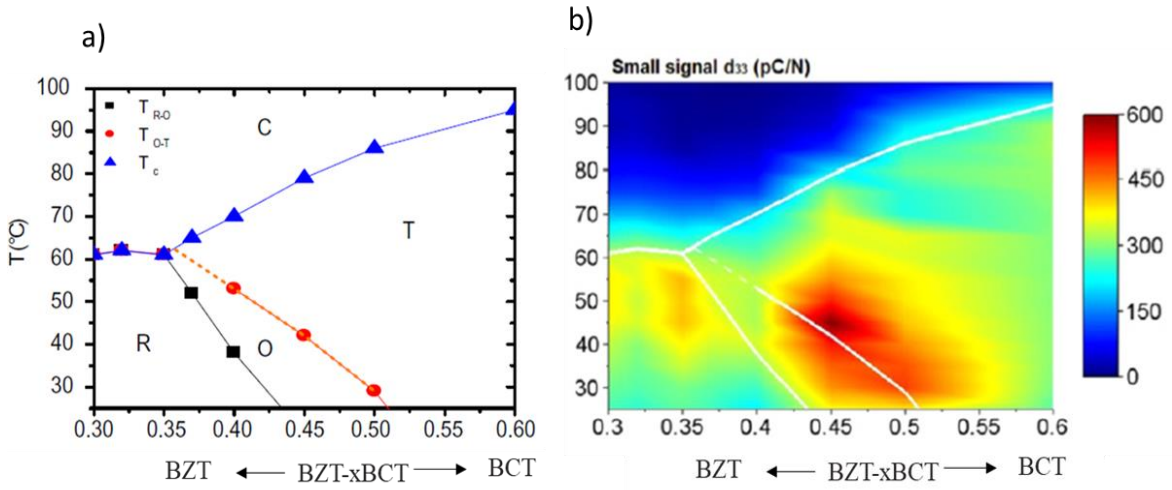

Figure 5: Corrected phase diagram and piezoelectric response of BZT-xBCT bulk ceramics (from [22]).

1.2. Chemical Solution Deposition of Ferroelectric Perovskite Oxide Thin Films

Ferroelectric oxide thin films are prepared either by physical vapour deposition methods such as sputtering, pulsed laser deposition, and evaporation or by chemical deposition methods, including

liquid phase methods. Chemical solution deposition (CSD) offers several advantages over physical deposition methods in terms of economic effectiveness, control of the stoichiometry in coating solutions, simple and fast processing, and the possibility of upscaling [26], [27], [28].

CSD starts with synthesizing a chemically homogeneous coating solution containing the desired ions (metal cations) as constituents of the metal-oxide film. Chemical reagents should be well soluble in the solvents selected for the coating solution. The reagents should be able to thermally oxidise into oxides or oxide compounds as the final products of the reaction without harmful (toxic) residues. The commonly used metal reagents are metal carboxylates, metal alkoxides, or metallo-organic compounds that are commercially available or can be synthesized. Carboxylic acids and alcohols are commonly used solvents for carboxylates and alkoxides (theory of like dissolves like) [29], [30]. The coating solution is deposited onto a substrate using one of several deposition techniques, including spin coating. The selection of the substrate is based on the compatibility of the film with the substrate, the processing temperature, thermal expansion (mis)match between the film-material and the substrate, and it also depends on the application the material is meant for [31]. Different substrates, such as metal-oxide single crystals, metal foils, glass, etc., are used for thin film deposition. Polymer foils are also used for flexible devices. After the deposition, the deposited film is exposed to a heat treatment to remove the remaining solvents, decompose organic residues, and crystallize. A schematic description of the different steps of CSD for metal-oxide thin films is presented in Figure 6.

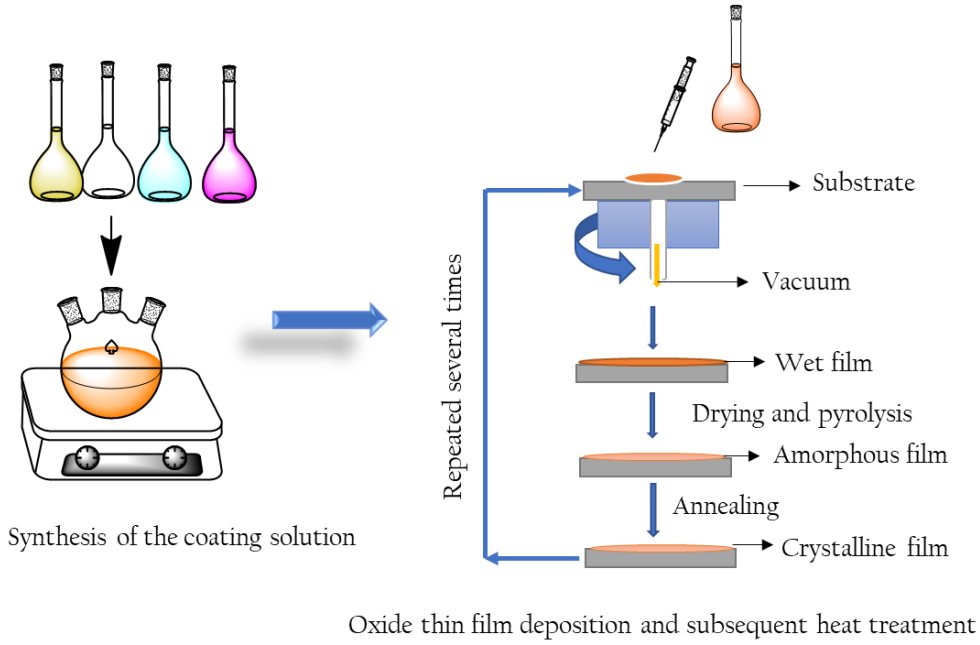

Figure 6: The schematic description of CSD of metal-oxide thin films.

1.2.1. Chemistry of $BaTiO_3$-based precursors

The common procedure for the preparation of alkaline-earth perovskite, including BT-based thin films relies on the use of alkaline earth (Ba, Ca, Sr...) carboxylates and transition metal (Ti, Zr...) alkoxides as the starting reagents and carboxylic acids and alcohols (frequently 2-methoxyethanol) as solvents for carboxylates and alkoxides respectively [26], [28], [30]. The general formulas of alkaline earth carboxylates and transition metal alkoxides are $M(COOR)_2$ and $M'(OR)_4$, respectively, where M and M' are the alkaline earth and transition metal and R- is the organic (alkyl) group. A schematic description of the preparation of the BT coating solution

is included in Figure 7. Barium carboxylate is dissolved in a carboxylic acid at 60 °C, and titanium alkoxide is diluted in an alcohol. Both solutions are mixed at room temperature (R.T.) after the complete dissolution of the carboxylate. The storage and manipulation of the reagents take place in a dry, inert atmosphere. Namely, the humidity in the ambient air could initiate the hydrolysis of transition metal alkoxides.

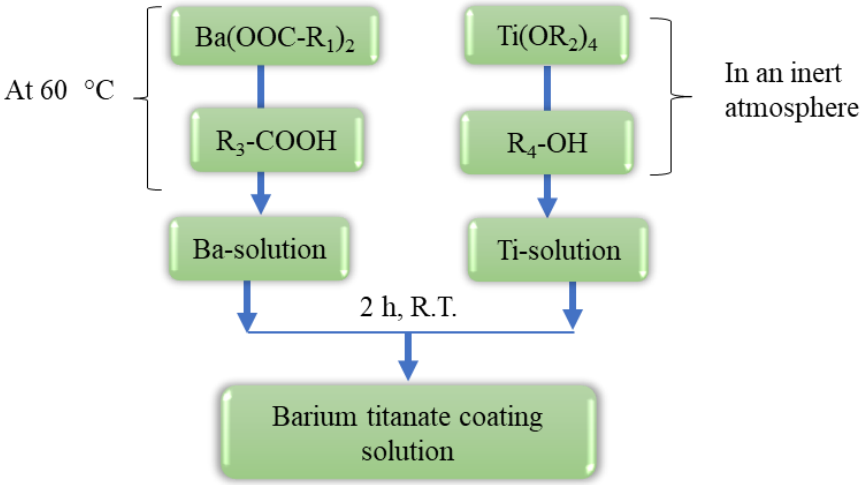

Figure 7: Procedure of the BT coating solution preparation.

In the BT coating solution synthesis, the reagents and the solvents are $Ba(OOCR_1)_2$ and $T(OR_2)_4$, as well as R_3-COOH and R_4-OH. The principal reactions are alcohol exchange, esterification, hydrolysis, and condensation. The reaction of $Ti(OR_2)_4$ with the solvent R_4-OH depends on the nature of the organic group, but eventually, it leads to partial or complete alcohol exchange [32], [33] as shown in Equation 1.

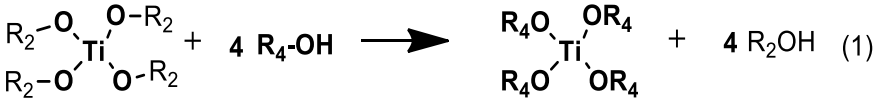

After mixing the Ba- and Ti-solutions, the solvents carboxylic acid and alcohol slowly undergo the reaction of esterification, yielding water as the side-product, as illustrated in Equation 2 [32], [34].

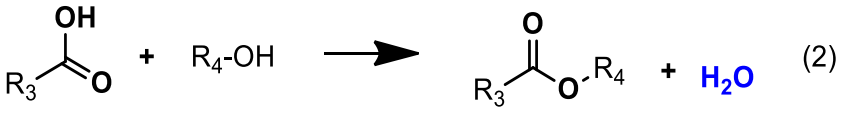

Then, depending on the reaction conditions (molar ratios of the reagents and solvents, temperature), the in-situ formed water may initiate the reaction of hydrolysis of titanium alkoxide followed by condensation. The respective reactions are collected below in Equations 3 and 4 [32], [33], [34], [35].

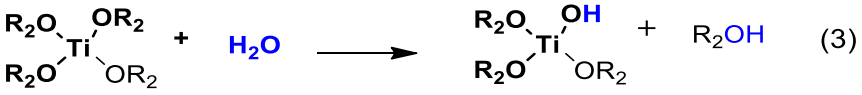

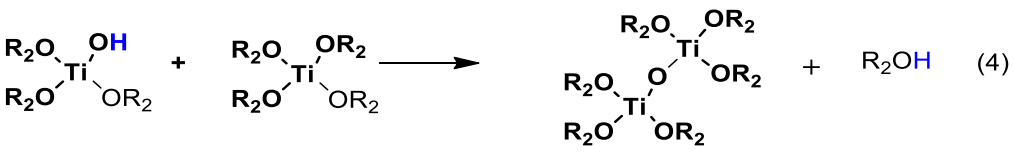

The progressive reaction of esterification eventually increases the water content in the solution which may promote precipitation in the coating solution[2]. Note that zirconium alkoxide is more reactive than titanium alkoxide due to the lower electronegativity and larger coordination number of the zirconium ion [33], [36].

Additives, such as acetylacetone and diethanolamine, are often used as chelating agents to reduce the reactivity of transition metal alkoxides [37], [38], [39], [40]. However, an increased fraction of organics leads to increased film porosity [41]. Some solvents could act as complexing agents, thus avoiding additional carbon source additives. Diol-based chemistry has been used to prepare stable solutions for deposition of lead-based perovskite oxide thin films by CSD [42], [43], [44]. It was shown that 1,3-propanediol ($HO\text{-}CH_2\text{-}CH_2\text{-}CH_2\text{-}OH$) coordinatively bonds to metal ions [45]. In the case of BT-based thin films, diols were used mainly as additives to enhance the stability of the coating solution and improve the film's morphology [46], [47].

1.2.2. Deposition, thermal decomposition, and crystallization of $BaTiO_3$-based thin films

Spin coating is the most frequently used thin film deposition technique as it is fast and enables upscaling [48], [49]. The substrate surface should be clean and smooth to enable a homogenous distribution of the solution and low roughness of the films, especially in films with low thickness.

After a small volume of the coating solution is dispensed on a substrate, the spin coater is accelerated to a few thousand rotations per minute (rpm) for about 30-60 seconds. The high rotation speed facilitates the complete coverage of the substrate and promotes evaporation of the volatile compounds [48]. For optimum substrate coverage by the coating solution, the solution should completely wet the surface, and the substrate should be thoroughly cleaned [50], [51], [52]. The as-deposited film contains organic groups bonded to the inorganic network and remaining solvents. Evaporation of solvents, decomposition of organic residues and crystallization occur during the drying, pyrolysis and rapid thermal annealing steps of the heat treatment process. The drying step takes place in a temperature range from 100 °C to 250 °C depending on the choice of the solvents, while the pyrolysis temperatures are from 250 °C to 400 °C [34]. In the carboxylate-based CSD, organic components are mainly decomposed during the pyrolysis step approximatively between 200 °C and 350 °C, as evidenced by thermogravimetry (TG), differential thermal analysis (DTA), and evolved gas analysis (EGA) [53], [54]. The carbonate and oxycarbonate species form during the pyrolysis as evidenced by Fourier transform infrared (FTIR) spectroscopy and X-ray diffraction (XRD). An intermediate $Ba_2Ti_2O_5CO_3$ was reported to form at temperatures between 450 -600 °C before decomposing into BT perovskite at temperatures of 600-750 °C [28], [55], [56]. Hasenkox et al studied the influence of the length of the organic chain of barium carboxylates (i.e., acetate, propionate, etc.) on the decomposition of the intermediate oxo-carbonate phase by FTIR as shown in Figure 8 a) and b). The precursors were barium carboxylates and titanium alkoxide as reagents and carboxylic acid and alcohol as solvents. The decomposition temperature of the oxo-carbonate phase increased as the length of the organic chain decreased. The perovskite phase was formed at a 100 °C higher temperature in the precursor prepared from Ba-propionate ($[C_3H_5O_4]_2Ba$ or $C_6H_{10}BaO_4$) than Ba-2-ethylhexanoate ($[CH_3(CH_2)_3CH(C_2H_5)CO_2]_2Ba$ or $C_{16}H_{30}BaO_4$), see Figure 8 c) and d) [28].

[2] In the case of BZT-BCT, the stability of the coating solution containing alkaline earth carboxylates and transition metal alkoxides is about one week.

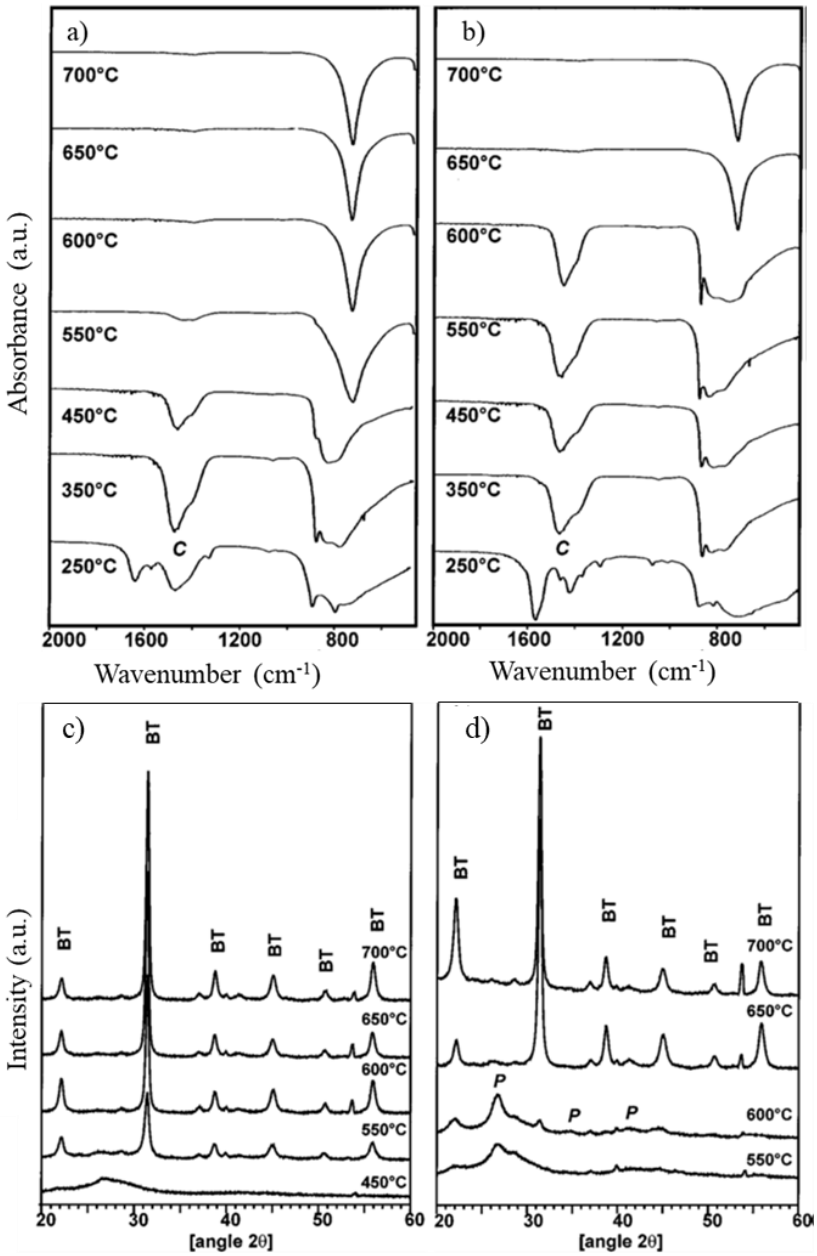

Figure 8: FTIR spectra of BT films prepared from a) Ba-2-ethylhexanoate and b) Ba-propionate precursors and their respective XRD patterns in c) and d) (from [28]).

The amount of organics in the precursor and their decomposition behavior are crucial for the crystallization path of the perovskite phase. Chelating agents are frequently used to reduce the reactivity of transition metal alkoxides and avoid uncontrolled hydrolysis [37]. Aygün et al prepared a BT coating solution from barium acetate, titanium isopropoxide as reagents, glacial acetic acid and acetylacetone as solvents and diethanolamine as chelating agent for titanium alkoxide. The XRD patterns of thin films deposited from this solution and annealed at different temperatures are shown in Figure 9. The presence of carbonate species at 750 °C upshifts the perovskite crystallization temperature to about 800 °C [57].

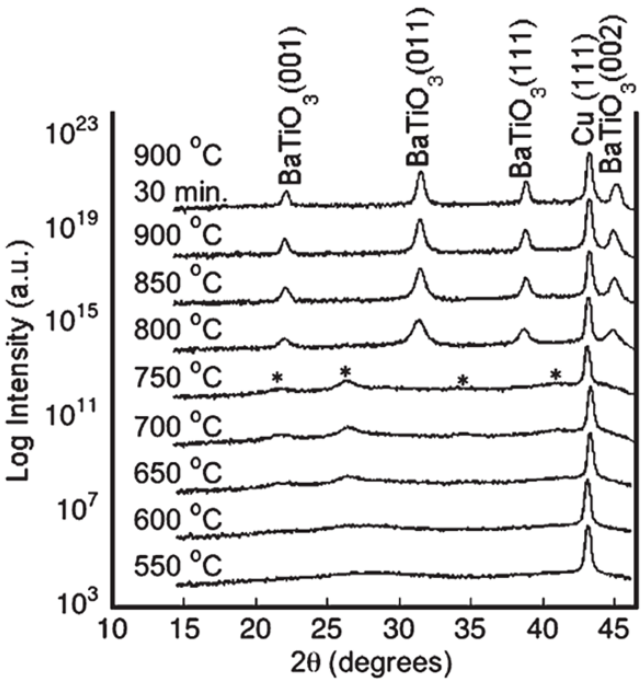

Figure 9: (a) X-ray diffraction patterns (* corresponds to $Ba_2Ti_2O_5CO_3$) of BT thin films prepared at different temperatures (from [57]).

Crystallization consists of the nucleation and growth of the crystalline phase, as explained by thermodynamic principles. There are two types of nucleation: homogeneous and heterogeneous nucleation. The principles of crystallization of thin films from solutions were described in detail by Schwartz et al. [34], [58], [59], [60]. The thin-film microstructure consisting of fine equiaxed grains results from preferentially homogeneous nucleation from the amorphous phase. The nuclei of the crystalline phase form within the bulk of the amorphous film and grow until they impinge on neighbouring grains, resulting in equiaxed grains. Such a type of microstructure is also referred to as granular. The columnar microstructure develops via preferentially heterogeneous nucleation. Here, the nuclei preferentially form on the substrate, which serves as the nucleation layer and they grow towards the top of the film [59], [60], [61], [62]. The study of the crystallization of $Pb(Zr,Ti)O_3$ (PZT) and BT films revealed that PZT preferentially crystallizes via heterogeneous nucleation, while the crystallization of BT proceeds via homogeneous nucleation [34]. The evolution of granular and columnar microstructure is schematically illustrated in Figure 10.

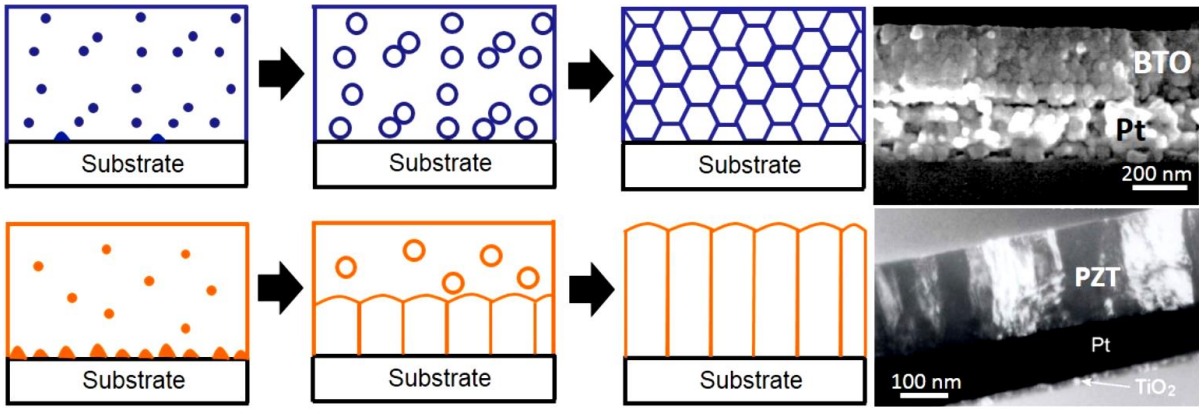

Figure 10: Mechanism of homogeneous (top) and heterogeneous (bottom) nucleation and growth of solution-derived thin films. The cross-section micrographs of BT (top) and PZT (bottom) films on platinized silicon substrates reveal the granular and columnar microstructure (from [61]).

BT thin films prepared by chemical solution deposition (CSD) crystallized through homogeneous nucleation which results in equiaxed grain growth. However, films with a columnar microstructure can be achieved by optimizing the processing which includes diluting the concentration of coating solution and multistep annealing [28], [63], [64] as shown in Figure 11. The mechanism behind this processing consists of crystallizing each deposited layer in one grain in thickness, and the following layer follows the previous one thus promoting the columnar growths of grains.

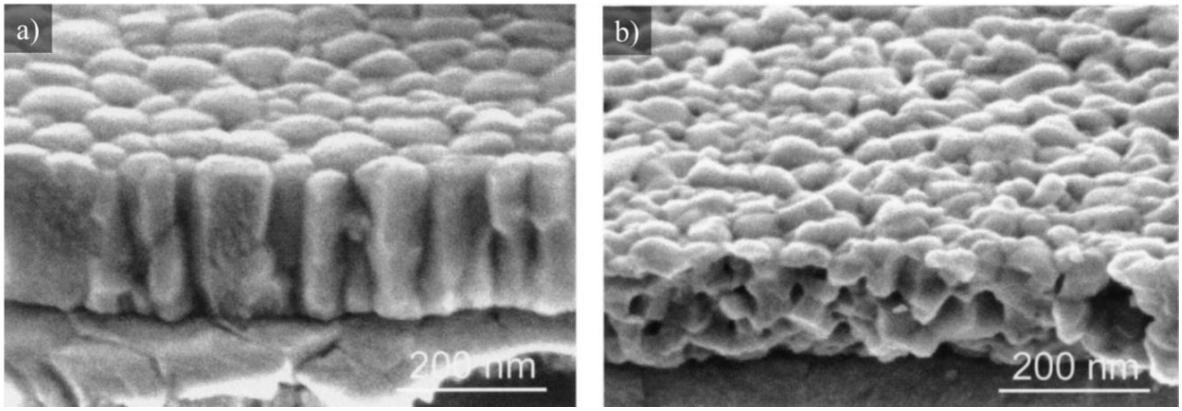

Figure 11: SEM micrographs of the cross-section and surface of two $BaTiO_3$ thin films prepared with a) from 22 layers, 0.1 M solution, and b) six layers, 0.3 M solution (from [63]).

Another solution for promoting the columnar microstructure is optimizing the solution chemistry that reduces the organic residue decomposition temperature, thus promoting the crystallization at a relatively low temperature or by increasing the annealing temperature, eventually leading to coarsening of grains. The latter alternative is limited by delamination of the substrates, especially in the case of platinized silicon substrates, which are the most commonly used in academia; the former seems to be beneficial since it reduces the processing thermal budget.

1.3. Microstructure and Functional Properties of $BaTiO_3$-Based Thin Films

1.3.1. Microstructure and dielectric permittivity of $BaTiO_3$ thin films

Barium titanate ($BaTiO_3$, BT) is one of the most studied dielectric materials. Discovered during the Second World War, BT ceramic was developed for military use as a capacitor for radar system development due to its high dielectric permittivity [65]. Nowadays, BT and BT-based thin films are used in many applications, including advanced complementary metal oxide semiconductor (CMOS) circuits [66]. They are extensively investigated and used for photonic devices, dynamic random-access memory (DRAM), and non-volatile ferroelectric random-access memory (FeRAM) devices [67], [68], [69]. In transistor technology, dielectrics such as BT are used as dielectric gates of metal-oxide-semiconductor field-effect transistors (MOSFET) [70], [71].

The dielectric properties of BT depend on grain size in its bulk form or/and the shape of grains in thin film form. The respective dependence is referred to as the grain size effect. For example, in bulk BT ceramics with grains in the micron range, the relative permittivity increases as the grain size decreases to about 1 μm, as shown in Figure 12 a). This effect was related to

the increase of domain walls or internal stresses in each grain clamped by neighbouring grains [8]. In BT thin films with granular and columnar microstructure, the relative permittivity increases more than two times, from less than 400 to above 800, respectively, as shown in Figure 12 b). The dielectric permittivity of fine-grained and/or grainy BT thin films shows almost no dependence on the temperature, while the columnar BT films have a relatively broad permittivity peak. In BT bulk ceramics, the series of permittivity peaks indicates different phase transitions with the evolution of the temperature [8].

The Curie temperature (Tc) of BT materials is about 130 °C [72], [73]. However, in fine-grained microstructure, the T_c of BT is diffuse [74]. The diffuse permittivity peak is explained by the local tetragonality due to the grain size distribution which leads to a distribution of T_c thus resulting in broad T_c in BT-thin films with fine equiaxed grains [5].

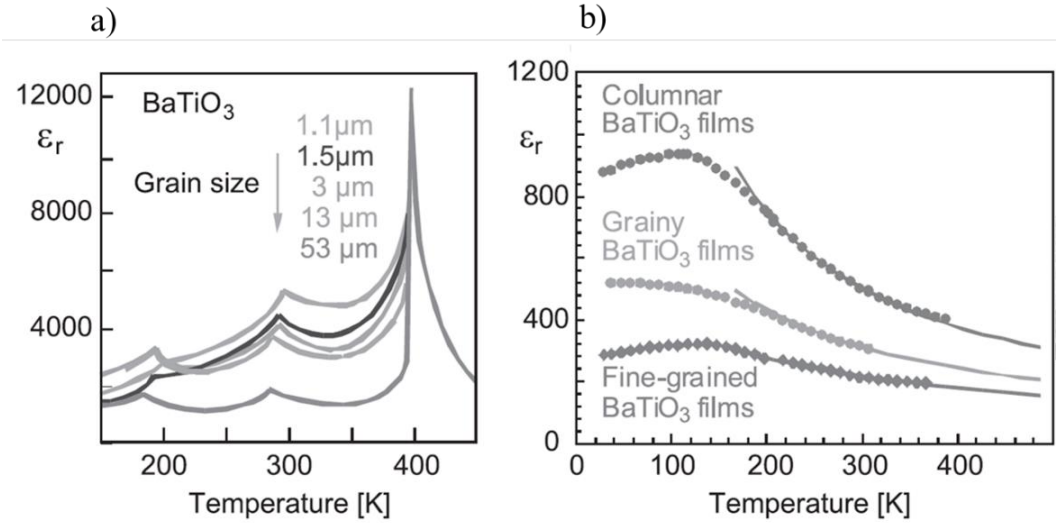

Figure 12: Temperature dependence of the permittivity in barium titanate for a) bulk ceramics with different grain sizes and b) thin films with different grain sizes (from [8]).

Similar to dielectric properties, ferroelectric and piezoelectric properties are also influenced by the grain size (GS) effect in BT bulk ceramics as shown in Figure 13 but also in BT thin films forms. The maximum polarization (P_{max}) and remanent polarization (P_r) in BT bulk ceramics increase with increasing grain size (GS) up to about 2-3 µm while the coercive field (E_c) decreases with the increase of GS. The highest d_{33} is reported in BT ceramics with GS of about 1 µm and gradually decreases with the increase of GS [75].

The GS dependence of polarization in thin films follows the same trend as in GS-permittivity as shown by modeling. The polarization increases with the increase of GS as it is illustrated in Figure 14 [77].

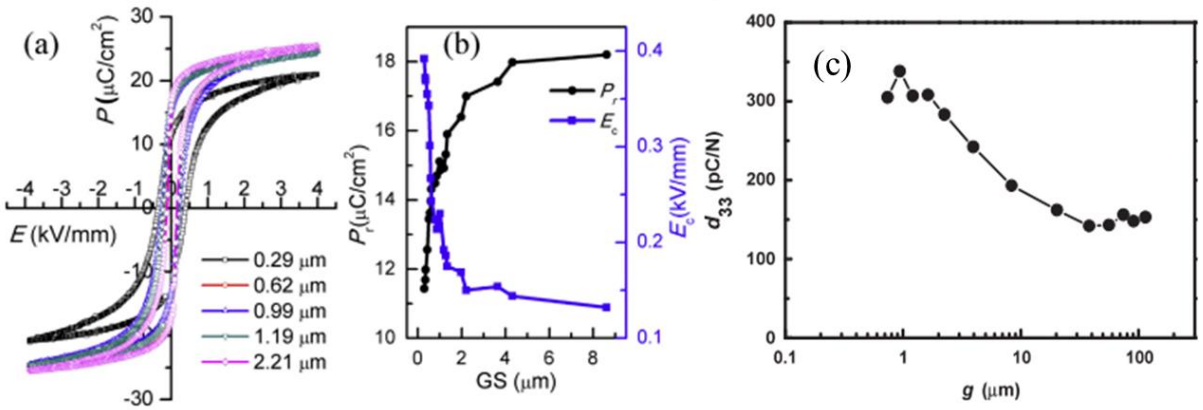

Figure 13: *P-E* hysteresis loops of the BT ceramics with different GS (a) and evolutions of remanent P_r and E_c as functions of GS (b), from [76] and piezoelectric coefficient as a function of GS (c) (from [75]).

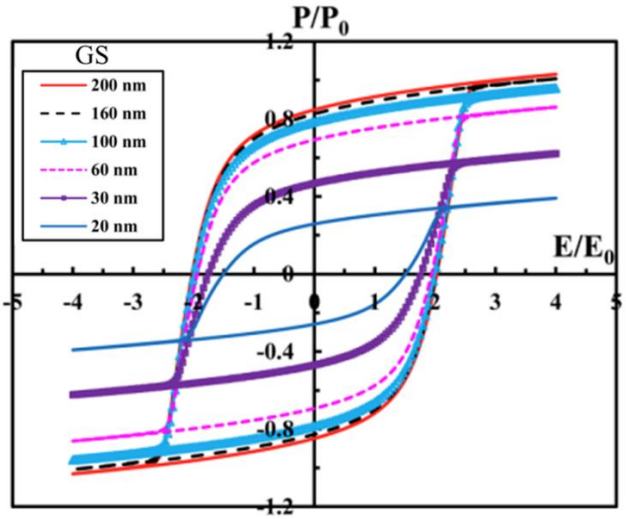

Figure 14: The modelled GS dependence of polarization as function of electric field BT thin films with columnar grains. The film thickness is 160 nm (from [77]).

1.3.2. Microstructure, dielectric and ferroelectric properties of Zr-modified $BaTiO_3$ thin films

Modifying chemical composition by introducing Zr in the lattice of BT changes the material's properties. The microstructure, dielectric permittivity, and phase transition temperature of $Ba(Zr_xTi_{1-x}O)_3$ (BZT_x) films as a function of Zr amount are shown in Figure 15. All measured quantities decrease with increasing amount of Zr [78], [79], [80]. As pointed out by Ihlefeld et al., the decrease in permittivity of BZT films could be due to the decrease in grain size caused by Zr-addition or Zr incorporation in the BT lattice [79]. Bulk BZT_x ceramics with the Zr content above 20% exhibit relaxor ferroelectric behaviour [81], [82], [83]. The ferroelectric-relaxor crossover was observed in BZT thin films [79], and even at lower Zr fractions at 15%, evidenced by the frequency dispersion of relative dielectric permittivity versus temperature [84].

The microstructure of BZT thin films prepared by CSD is usually characterized by fine and equiaxed grains [78], [85]. To increase the lateral grain size, a high annealing temperature of up to 1100 °C was needed [86], [87].

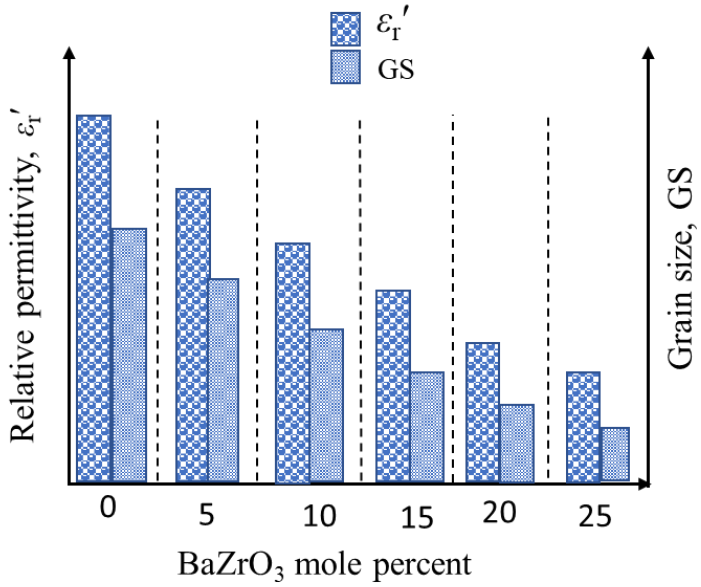

Figure 15: Influence of Zr content on grain size and dielectric permittivity of BZT thin films analyzed data (from [79]).

1.3.3. Microstructure, dielectric and ferroelectric properties of Ca-modified $BaTiO_3$ thin films

Just like in BZT films, a similar trend in grain size effect on dielectric permittivity was observed in calcium-modified barium titanate ($(Ba_{1-x}Ca_x)TiO_3$, BCT_x) prepared by CSD. The permittivity decreases with the increase of calcium amount in the solid solution as shown in Figure 16 [88]. However, there is no available data on the microstructure of BCT thin films prepared by CSD and its influence on dielectric properties.

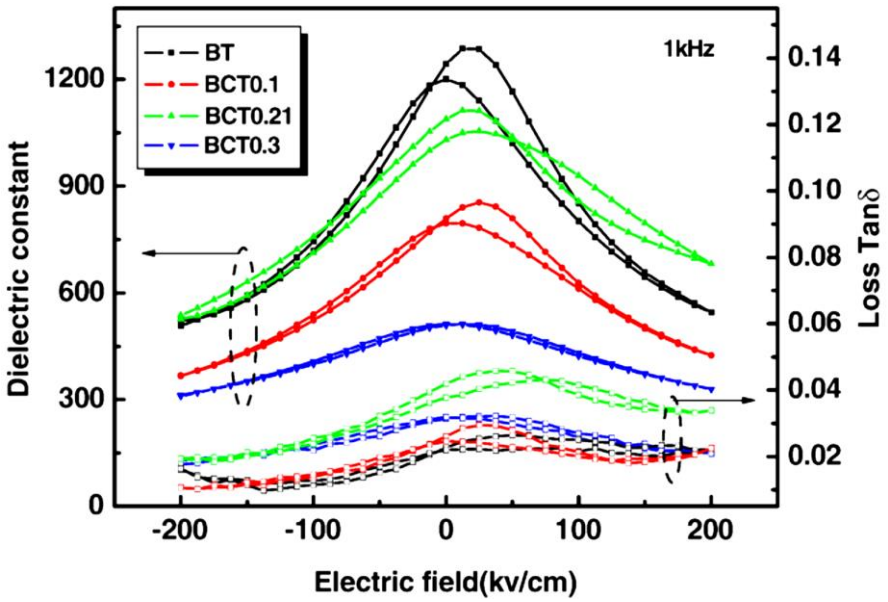

Figure 16: Electric field dependent dielectric permittivity and losses of BCT thin with different amounts of Ca (from [88]).

Due to the low ferroelectric properties and leaky behavior of BCT materials as shown in Figure 17 [89], there is not much study on BCT thin films that would give insight into the relationship between the microstructure and ferroelectric or piezoelectric properties.

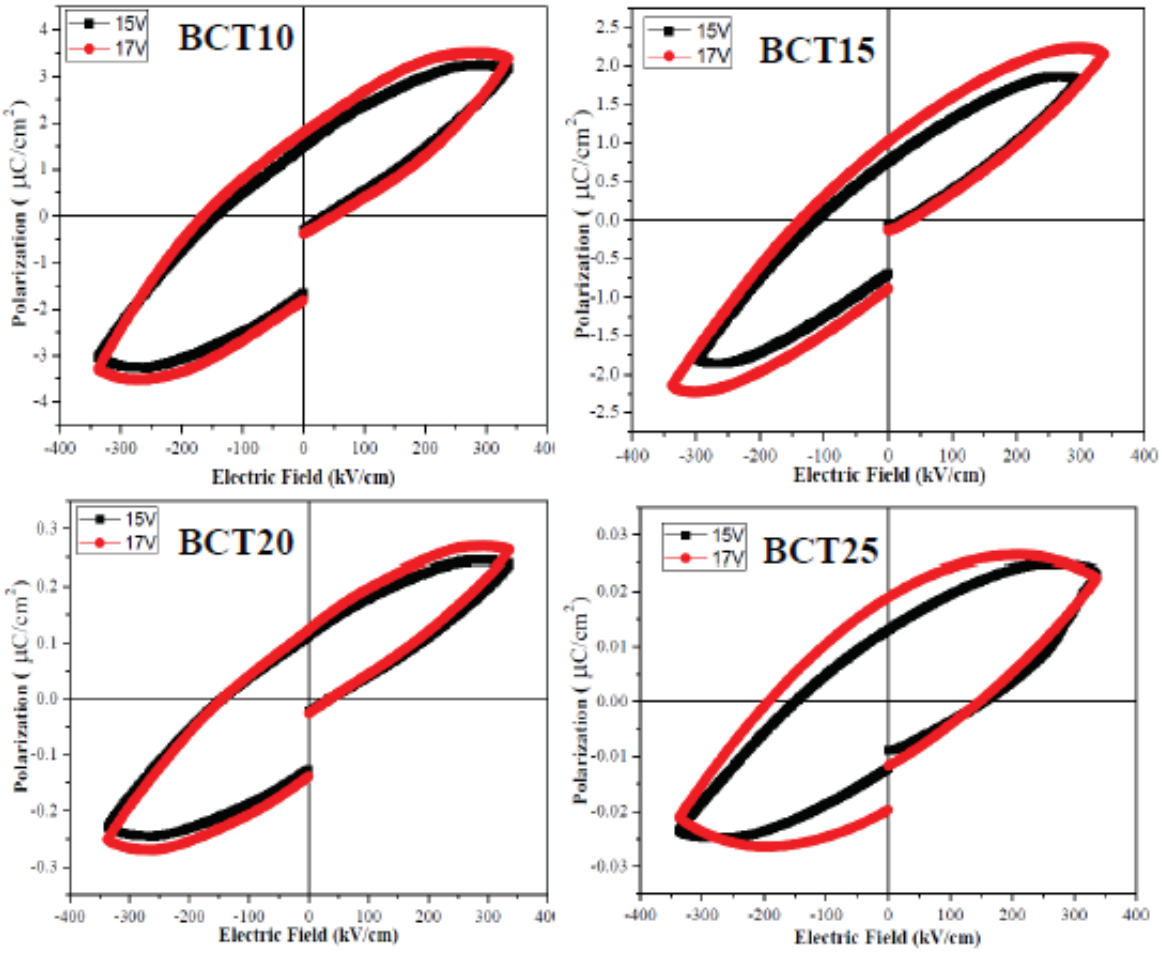

Figure 17: *P-E* loops of $(Ba_{1-x}Ca_x)TiO_3$, x = 0.1 (BCT10), X = 0.15 (BCT15), x = 0.20 (BCT20) and x = 0.25 (BCT25), thin films annealed at 750 °C (from [89]).

1.3.4. (1-x)Ba(Ti$_{0.8}$Zr$_{0.2}$)O$_3$-x(Ba$_{0.7}$Ca$_{0.3}$)TiO$_3$ (BZT-xBCT) thin films

1.3.4.1. Microstructure of BZT-xBCT thin films by CSD

Solution-derived (1-x)Ba($Zr_{0.2}Ti_{0.8}$)O_3 – x($Ba_{0.7}Ca_{0.3}$)TiO_3 (BZT-xBCT) thin films follow similar processing steps as other BT-based thin films. The BZT-xBCT coating solutions are usually prepared using alkaline earth carboxylates such as barium and calcium acetates as sources of A-site cations and metal transition alkoxides including titanium, zirconium butoxides or propoxides as sources of B-site cations [90], [91]. Additives are sometimes introduced to increase the stability of the coating solution, but usually, they contribute to granular and porous microstructure, which is presumably related to higher temperatures needed for their thermal decomposition. Some modifications in solution chemistry were reported; for example, calcium carbonate was also used instead of acetate by Reddy et al. The films annealed at 700 °C and 800 °C resulted in granular and porous microstructure [92]. Some examples of BZT-BCT films with fine granular microstructure are collected in Figure 18.

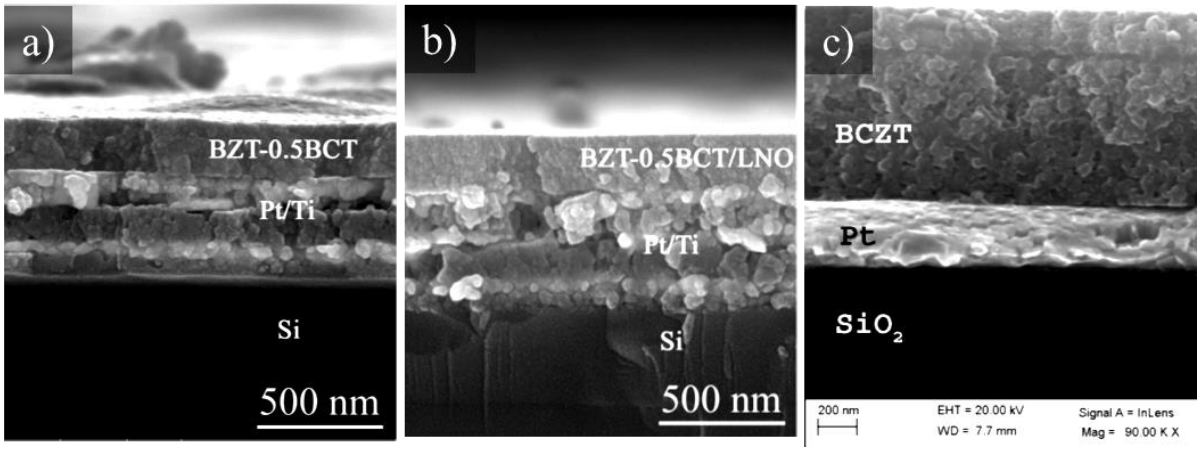

Figure 18: Cross-section micrographs of CSD-derived BZT-BCT thin films a) deposited on platinized silicon, b) deposited on platinized silicon with $LaNiO_3$ as a seed layer both annealed at 750 °C [91], and c) BZT-BCT prepared using calcium carbonate as a source of Ca ion and annealed at 800 °C (from [92]).

Kang and al. reported the formation of a pyrochlore phase that could not be eliminated even by increasing the annealing temperature using BZT-BCT coating solutions prepared from barium and calcium nitrates and transitions metal alkoxides as reagents. Furthermore, using metal barium and calcium nitrate annealing up to 1000 °C resulted in films with granular microstructure and cracks [93].

1.3.4.2. Functional properties of BZT-xBCT thin films by CSD

The BZT-xBCT films were deposited on seed layers such as $LaNiO_3$ (LNO), $Pb_{0.8}La_{0.1}Ca_{0.1}TiO_3$ (PLCT), and $(Pb_{0.8}Ca_{0.2})TiO_3$ (PCT) on platinized silicon substrate in an attempt to increase the texture in the films and to improve dielectric properties [91], [94], [95], [96]. Thicker films were also prepared with the purpose of increasing the functional properties [92], [97], [98]. The literature data on dielectric properties of BZT-xBCT thin films are summarized in Table 1. While the composition of the films at x = 0.5 does not have the highest relative permittivity, it exhibits the lowest losses compared to other composition prepared at the same conditions. By introducing a seed layer, the relative permittivity can be slightly increased and losses decreased. The relative permittivity of the films prepared from a solution with a lower concentration (0.1 M) is higher than of the films prepared with higher concentrations (0.2 M, 0.35 M or 0.67 M) even when the annealing temperatures of the latter films are higher than of the former films. The thicker films prepared from the 0.1 M coating solution and annealed at 700 °C exhibit a similar value of the relative permittivity as the thinner films prepared from the same solution but annealed at higher temperature of 850 °C. However, the comparison of relative permittivity of the films with the same thickness (490 nm) and prepared from the same solution (0.1 M) but annealed at different temperatures (700 °C and 800 °C), shows that a higher annealing temperature contributes to higher relative permittivity due to the increase of crystallinity in the films [98]. The same trend is observed in the films prepared from the 0.67 M coating solution [92]. The thickness effect in

the films was explained in BST and PZT thin films by the existence of nonswitching or dead layers which are located at the dielectric material-electrode interface, thus affecting the material polarizability [99], [100], [101]. It was pointed out that, in thicker films, dielectric properties are almost independent of the dead layer effect.

Table 1: Literature data of dielectric properties of BZT-xBCT thin films prepared by CSD and deposited by spin coating. Molar concentration: C_M, annealing temperature: T_{anneal}, relative permittivity at 1 kHz: ε_r', losses: tan δ, LNO: $LaNiO_3$, PLCT: $Pb_{0.8}La_{0.1}Ca_{0.1}TiO_3$, and PCT: $(Pb_{0.8}Ca_{0.2})TiO_3$, and Pt(111)/TiO_2/SiO_2/(100)/Si: Pt/Si.

Films	substrate	C_M, mol/l	T_{anneal}, °C	Thickness, nm	ε'	tan δ	Ref.
BZT-0.40BCT	LNO/Pt/Si	0.35	750	~200	~365	~0.06	[91]
BZT-0.45BCT	LNO/Pt/Si	0.35	750	~200	~380	~0.08	
BZT-0.50BCT	LNO/Pt/Si	0.35	750	~200	~280	~0.04	
BZT-0.55BCT	LNO/Pt/Si	0.35	750	~200	~370	~0.09	
BZT-0.60BCT	LNO/Pt/Si	0.35	750	~200	~280	~0.1	
BZT-0.50BCT	Pt/Si	0.35	700	~300	220	0.63	[94]
BZT-0.50BCT	PLCT/Pt/Si	0.35	700	~300	457	0.031	
BZT-0.50BCT	PLCT/Pt/Si	0.35	500	~300	130	0.026	
BZT-0.50BCT	Pt/Si	0.2	950	380	420	NA	[102]
BZT-0.50BCT	Pt/Si	0.67	700	~750	539	0.032	[92]
BZT-0.50BCT	Pt/Si	0.67	800	~750	602	0.026	
BZT-0.40BCT	Pt/Si	0.2	700	~400	341	0.033	[97]
BZT-0.45BCT	Pt/Si	0.2	700	~400	444	0.027	
BZT-0.50BCT	Pt/Si	0.2	700	~400	377	0.022	
BZT-0.55BCT	Pt/Si	0.2	700	~400	462	0.028	
BZT-0.50BCT	Pt/Si	0.35	700	~450	157	0.037	[96]
BZT-0.50BCT	PCT/Pt/Si	0.35	700	~450	259	0.024	
BZT-0.50BCT	Pt/Si	0.1	700	~490	~600	~0.05	[98]
BZT-0.50BCT	Pt/Si	0.1	800	~490	~800	~0.05	
BZT-0.50BCT	Pt/Si	0.1	850	~290	~600	~0.03	
BZT-0.50BCT	Pt/Si	0.1	900	~290	~700	~0.06	

One of the characteristics of BZT-xBCT materials for considering applications is its Curie Temperature (T_c). In the bulk form, the Tc of $Ba(Zr_{0.2}Ti_{0.8})O_3$–$(Ba_{0.7}Ca_{0.3})TiO_3$ (BZT-BCT) was reported to be about 85 °C - 93 °C depending on the grain size [15], [24], [103]. However, the phase transition temperature in the films is difficult to determine especially if the microstructure is fine-grained. Nevertheless, the T_c of BZT-xBCT films for x between 0.4 and 0.6 prepared by CSD was estimated by permittivity measurements as a function of temperature [91]. The temperature of the broad permittivity peak increases as the molar ratio of BCT end member in the solid solution increases as shown in Figure 19.

The electric field-dependent properties mainly ferroelectric, energy storage, and piezoelectric properties in BZT-xBCT films were reported. Although electric field-dependent properties are strongly tied to the microstructure and phase composition of the films, some works reported high maximum polarization in BZT-xBCT thin films even in fine-grained films [46], [91], [104]. However, there is no consensus about remanent polarization. This polarization could include the contribution of leakage current which is often not investigated. For example, Li et al. reported the ferroelectric properties of BZT-BCT films deposited on LNO seed layers prepared by CSD, withstanding an electric of 1 MV/cm however, the P-E loops show no saturation see Figure 20 [91]. Similar results were reported by Wang et al. in the films also prepared by CSD [104].

Nevertheless, the films with high polarization and withstanding large electric field show a good potential for energy storage applications.

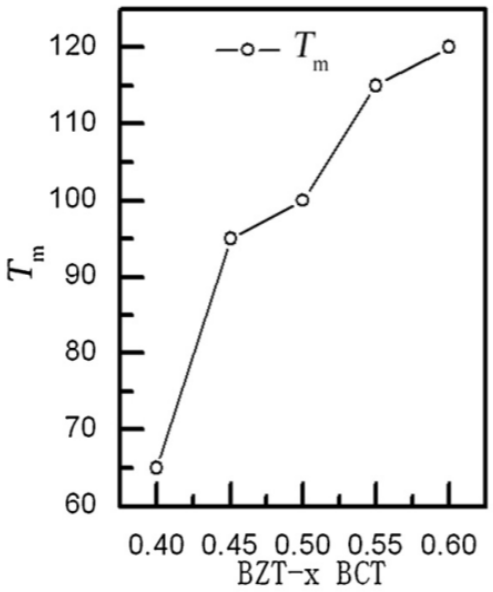

Figure 19: The peak dielectric permittivity temperature T_m values in BZT-xBCT thin films measured at 1 kHz (from [91]).

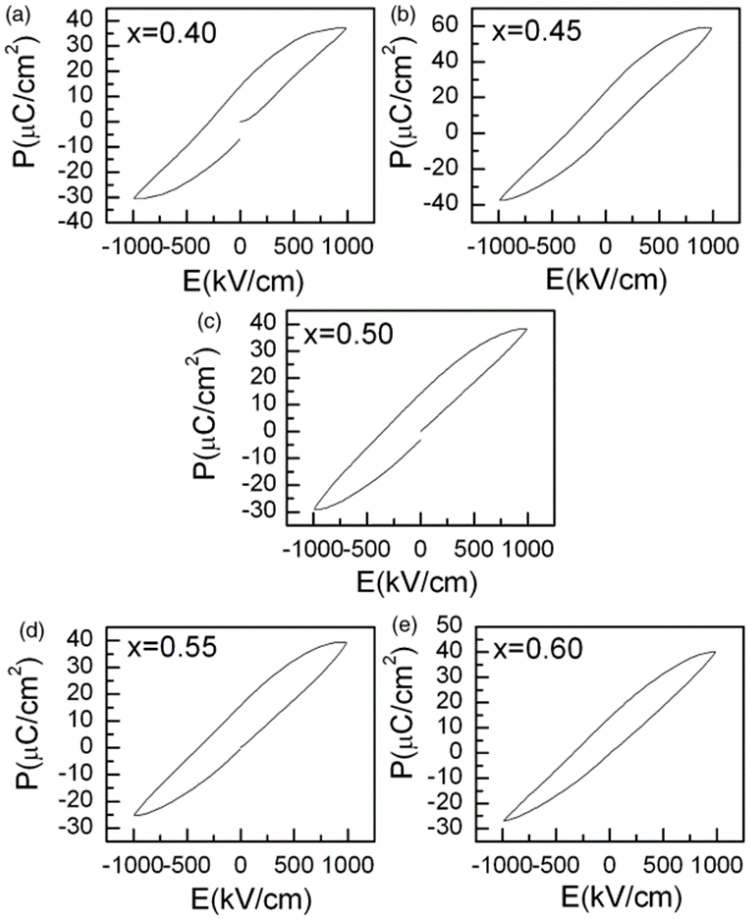

Figure 20: *P–E* loops of BZT–xBCT/LNO thin films. (a) x = 0.40, (b) x = 0.45, (c) x = 0.50, (d) x = 0.55, and (e) x = 0.60 (from [91]).

Microstructural or compositional defects such as intra- or intergranular cracks, and secondary phases may contribute to increasing the leakage current in the film [46], [105], [106] thus decreasing the energy storage efficiency. In BZT-xBCT films prepared by CSD, designing columnar and crack-free microstructure will be the preconditions for achieving high energy storage properties.

For piezoelectric applications such as actuators, sensors, or energy harvesting, the key functional properties to consider are the piezoelectric coefficients, strain, dielectric permittivity, and dielectric losses [107], [108]. These properties as also mentioned above are influenced by the microstructural features of the films. To our knowledge, the piezoelectric properties of BZT-BCT thin films have been measured only locally by piezo-response force microscopy (PFM) [46], [91], [94], [109], [110], [111]. For use in devices, the macroscopic piezoelectric properties in BZT-BCT films should be known. The films with a columnar microstructure are expected to exhibit better piezoelectric properties than those with fine-grained microstructure.

Chapter 2

Aims and Hypotheses

Chemical solution deposition (CSD) of thin films presents some advantages over vapour deposition methods, including moderate investment in the equipment. It enables the control of thin film characteristics such as grain size, phase purity, and chemical homogeneity, which influence the functional properties of the films. The complex chemical composition of $0.5Ba(Zr_{0.2}Ti_{0.8})O_3$-$0.5(Ba_{0.7}Ca_{0.3})TiO_3$ (BZT-BCT) makes the preparation of a stable homogeneous coating solution challenging. In literature, BZT-BCT thin films prepared by the conventional acetic acid-based CSD are often characterized by porous, fine-grained microstructure, cracks, and poor functional properties.
In this dissertation, we aim for the following goals:

1. Synthesis of a stable coating solution for $BaTiO_3$ (BT) thin films as reference and transfer of the procedure to BZT-BCT so that the respective coating solutions would exhibit good temporal stability (weeks or months).
2. Optimization of the thermal decomposition and crystallization processes of the deposited BZT-BCT films to yield single-phase, dense and chemically homogenous thin films.
3. Design of the microstructure of BZT-BCT films consisting of predominantly columnar grains of a few 10 nm across.
4. Enhancing the functional response of BZT-BCT films using chemical modification and changing the stress state of the films. This includes enhancing piezoelectric properties and the electric breakdown field and reducing hysteretic losses needed to improve energy harvesting and storage properties.

The following hypotheses are formulated for this dissertation based on the knowledge of the solution chemistry of alkaline-earth and transition metal compounds and on the literature of BT and $(Ba,Sr)TiO_3$ thin films prepared by CSD.

1. The slowly progressing esterification reaction between a carboxylic acid and an alcohol used as solvents in the conventional carboxylic-acid-based synthesis of the BZT-BCT coating solution leads to progressive evolution of water resulting in precipitation of hydroxide products. Using the combination of solvents that would not release water would increase the stability of the BZT-BCT coating solution
2. Adjusting the drying and pyrolysis temperatures and times of the as-deposited BZT-BCT films so that the thermal decomposition of residual functional groups is completed at as low temperature as possible will contribute to the crystallization of the pure perovskite phase.
3. The dense and columnar microstructure of BZT-BCT films can be achieved by the multistep annealing process.
4. The columnar microstructure contributes to enhanced functional properties of BZT-BCT films.
5. Chemical modification of BZT-BCT, such as manganese doping, contributes to reduced leakage of the BZT-BCT films

6. The thermal expansion mismatch between the BZT-BCT film and silicon substrate contributes to intergranular crack evolution in films with thicknesses above 120 nm. Thicker crack-free BZT-BCT films can be prepared using substrates with a thermal expansion coefficient closer to that of BZT-BCT.

Chapter 3

Results and Discussion

3.1. Chemical Solution Deposition of Barium Titanate Thin Films with Ethylene Glycol as Solvent for Barium Acetate

Porous and fine microstructure, intergranular cracks, and, notably, the instability of coating solutions have often been reported as challenges in studying $0.5Ba(Zr_{0.2}Ti_{0.8})O_3$-$0.5(Ba_{0.7}Ca_{0.3})TiO_3$ (BZT-BCT) thin films prepared by chemical solution deposition (CSD). Consequently, the functional properties of CSD-derived BZT-BCT thin films could not be studied and/or optimized from the viewpoint of the processing-microstructure-properties relationship.

In general, CSD of $BaTiO_3$ (BT) or BT-based thin films such as BZT-BCT, alkaline-earth carboxylates, and transition-metal alkoxide are dissolved and diluted respectively in carboxylic-acid and alcohol solvents. Depending on the reaction conditions, the esterification reaction of the solvents leads to the evolution of water and, eventually, progressive hydrolysis of transition metal alkoxide and precipitation. To resolve these problems, we developed a new synthesis route in which ethylene glycol (EG) is used as the solvent for alkaline-earth carboxylate.

BT was selected as the reference material for BZT-BCT or, more generally, for complex BT-based formulations with substitutions on A and/or B sites of the perovskite lattice. EG was the solvent for barium acetate, and 2-methoxyethanol (MOE), EG, and ethanol (EtOH) were chosen as the solvents for titanium butoxide. As a reference, BT coating solution was prepared following the conventional procedure using acetic acid (AcOH) as the solvent for barium acetate and MOE to dilute titanium butoxide.

The three EG-based BT coating solutions were stable for about one year, while the reference AcOH-MOE BT solution was stable only for a few weeks. The thermal decomposition of the dried precursors (xerogels) from EG-MOE and EG-EG solutions is concluded at a few 100 °C higher temperatures than of the xerogels obtained from AcOH-MOE and EG-EtOH solutions (about 700 °C). The ≈100 nm thick films are prepared by multistep annealing at 800 °C from the latter solutions and crystallize in a perovskite phase with columnar microstructure. The EG-EtOH-derived BT films are characterized by polarization-electric field hysteresis loops at electric fields of up to 2.4 MV/cm, while the AcOH-MOE-derived films are leaky.

This article addresses the first aim of the Thesis.

Published in: S. W. Konsago, K. Žiberna, B. Kmet, A. Benčan, H. Uršič, and B. Malič, "Chemical solution deposition of barium titanate thin films with ethylene glycol as solvent for barium acetate" J. Molecules, 27(12), 3753, 2022. (IF = 4.6, 2022)

My contribution: I synthesized the BT coating solutions, dried them to obtain xerogels and prepared thin films by spin-coating and multistep annealing. I analysed the data obtained by simultaneous thermal analysis coupled with mass spectrometry. I performed the Fourier transform infrared spectroscopy, X-ray diffraction, atomic force microscopy (AFM), piezo-response force microscopy, and conductive AFM of the films. I measured the dielectric and ferroelectric properties of the films in metal-insulator-metal geometry. I prepared the paper concept jointly with my supervisor and wrote the manuscript with all co-authors.

molecules

MDPI

Article

Chemical Solution Deposition of Barium Titanate Thin Films with Ethylene Glycol as Solvent for Barium Acetate

Sabi William Konsago [1,2,*], Katarina Žiberna [1,2], Brigita Kmet [1,2], Andreja Benčan [1,2], Hana Uršič [1,2] and Barbara Malič [1,2,*]

[1] Electronic Ceramics Department, Jožef Stefan Institute, Jamova Cesta 39, 1000 Ljubljana, Slovenia; katarina.ziberna@ijs.si (K.Ž.); brigita.kmet@ijs.si (B.K.); andreja.bencan@ijs.si (A.B.); hana.ursic@ijs.si (H.U.)
[2] Jožef Stefan International Postgraduate School, Jamova Cesta 39, 1000 Ljubljana, Slovenia
* Correspondence: sabi.william.konsago@ijs.si (S.W.K.); barbara.malic@ijs.si (B.M.)

Abstract: Chemical solution deposition (CSD) of $BaTiO_3$ (BT) or BT-based thin films relies on using a carboxylic acid and alcohol as the solvents for alkaline-earth carboxylate and transition-metal alkoxide, respectively; however, the esterification reaction of the solvents may lead to in-situ water formation and precipitation. To avoid such an uncontrolled reaction, we developed a route in which ethylene glycol (EG) is used as the solvent for Ba-acetate. The EG-based BT coating solutions are stable for at least a few months. The thermal decomposition of the BT xerogel obtained by drying the EG-based solutions depends on the choice of the solvent for the Ti-alkoxide as well: in the case of EG and 2-methoxyethanol solvents carbon residues are removed at only about 1100 °C, while in the case of ethanol it is concluded at about 700 °C. About 100 nm thick BT films derived from the EG-ethanol solution deposited on platinized silicon reveal dense, crack-free columnar microstructure. They exhibit local ferro- and piezoelectric properties. The macroscopic polarization-electric field loops were obtained up to a quite high electric field of about 2.4 MV/cm. The EG-ethanol based CSD route is a viable alternative to the established acetic acid–alcohol route for BT and BT-based films.

Keywords: $BaTiO_3$ thin films; solvent influence; chemical solution deposition; crystallinity; ferroelectric; piezoelectric

Citation: Konsago, S.W.; Žiberna, K.; Kmet, B.; Benčan, A.; Uršič, H.; Malič, B. Chemical Solution Deposition of Barium Titanate Thin Films with Ethylene Glycol as Solvent for Barium Acetate. *Molecules* **2022**, *27*, 3753. https://doi.org/10.3390/molecules27123753

Academic Editors: Giuseppe Cirillo and Igor Djerdj

Received: 28 April 2022
Accepted: 8 June 2022
Published: 10 June 2022

Publisher's Note: MDPI stays neutral with regard to jurisdictional claims in published maps and institutional affiliations.

1. Introduction

Among lead-free piezoelectric materials, barium titanate-based materials, especially $Ba(Zr_{0.2}Ti_{0.8})O_3$-$(Ba_{0.7}Ca_{0.3})TiO_3$ solid solution or BZT-BCT, show outstanding piezoelectric properties with a d_{33} coefficient exceeding the value of $Pb(Zr,Ti)O_3$ (PZT) based materials [1–3]. Materials in the form of thin film are considered for the miniaturization of devices. In the BZT-BCT formulation, barium titanate (BT) is the main component, so we can consider it as the reference material for studies on the BZT-BCT. On the other hand, BT is the end-member of $(Ba, Sr)TiO_3$ solid solution that has been proven to be a good candidate for tunable microwave devices as well [4–6].

One of the most commonly used methods to fabricate BT-based thin films is chemical solution deposition (CSD). This method offers several advantages, such as low capital cost, control of the stoichiometry of the coating solutions, simple and fast preparation procedures, the possibility of large-scale deposition, and control of the thickness of the coatings [6–9]. We note that in the majority of CSD routes organic solvents have been used. Recently, environmentally-friendlier water-based synthetic approaches have been reported, which mainly focused on deposition on single-crystal perovskite substrates [10,11].

In CSD of BT as well as BT-based thin films, alkaline earth carboxylates and transition metal alkoxides are commonly used as starting materials to prepare the coating solutions [12–15]. Normally, alkaline-earth metal carboxylates are dissolved in carboxylic acids, and alkoxides are diluted with an alcohol [6,8,16]. As a side reaction, the slow

Molecules **2022**, *27*, 3753

interaction between alcohol and carboxylic acid, i.e., the esterification reaction leads to the progressive in-situ formation of water (Scheme 1).

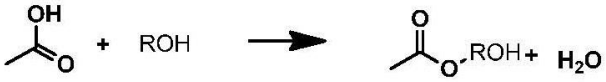

Scheme 1. The esterification reaction leads to the progressive in-situ formation of water.

Transition metal alkoxides are very sensitive to water, leading to hydrolysis (Scheme 2) and, hence, the precipitation of hydroxides.

Scheme 2. The hydrolysis reaction leads to the precipitation of hydroxides.

In the case of BZT-BCT, a higher reactivity of zirconium alkoxides towards water compared to titanium may increase the possibility of precipitation [17,18]. Indeed, our preliminary experiments on CSD of BZT-BCT revealed that the temporal stability of conventionally synthesized solutions was only a few weeks. A possible solution would be to reduce the reactivity of zirconium alkoxide by adding chelating agents such as acetylacetone, 3-hydroxy-2-butanone or certain amine compounds [16,19]. However, the esterification reaction and thus the possibility of hydrolysis would not be impeded.

Another possibility would be to replace acetic acid with another solvent for the alkaline earth reagent to avoid the esterification reaction that could lead to the formation of water in the coating solutions. Ethylene glycol (EG) was used to dissolve lead acetate in CSD of PZT films [20]. We found that EG can dissolve Ba-acetate as well, which has not been reported earlier. Otherwise, EG also serves as a solvent and chelating agent for Ti alkoxide [21,22].

In this work, we established a systematic study on CSD of BT films using EG as the solvent for barium acetate instead of acetic acid. We note that in this case, the solvent for the transition metal alkoxide was 2-methoxyethanol as reported in [6]. BT served as the reference material for a more complicated BZT-BCT solid solution. Furthermore, we also introduced different solvents for the transition-metal alkoxide. In addition to 2-methoxyethanol, we used EG as the common solvent for both metal compounds and ethanol. Furthermore, we optimized the heat treatment conditions.

We find that the BT solutions containing EG, the alkaline-earth acetate solvent, are stable for months. The thermal decomposition of the dried solution that contains ethanol is concluded at a lower temperature than the solutions containing EG or 2-methoxyethanol as the solvent for the alkoxide. The films deposited from the EG-ethanol based solution yield perovskite films with columnar microstructure and good dielectric and ferroelectric properties.

2. Results and Discussion

2.1. Thermal Decomposition of BT Xerogels

The BT coating solutions prepared with different solvents were dried at 200 °C for 12 h to yield xerogels. The gels and thin films obtained from respective solutions, namely acetic acid-2-methoxyethanol, ethylene glycol, ethylene glycol-ethanol and ethylene glycol-2-methoxyethanol are denoted as AcOH-MOE, EG, EG-EtOH and EG-MOE.

The FTIR spectra of the gels collected in Figure 1 reveal the absorption bands at 1565 cm^{-1} and 1419 cm^{-1} corresponding to acetate groups in agreement with [7,23]. The FTIR spectra of the EG, EG-EtOH and EG-MOE gels contain weak bands at about 3500 and 2900 cm^{-1}, which we attribute to the presence of trace EG residues. The boiling point of EG is 197 °C and it is possible that the solvent or its residues were not fully evaporated at 200 °C from the gel network which is not the case for the AcOH-MOE specimen.

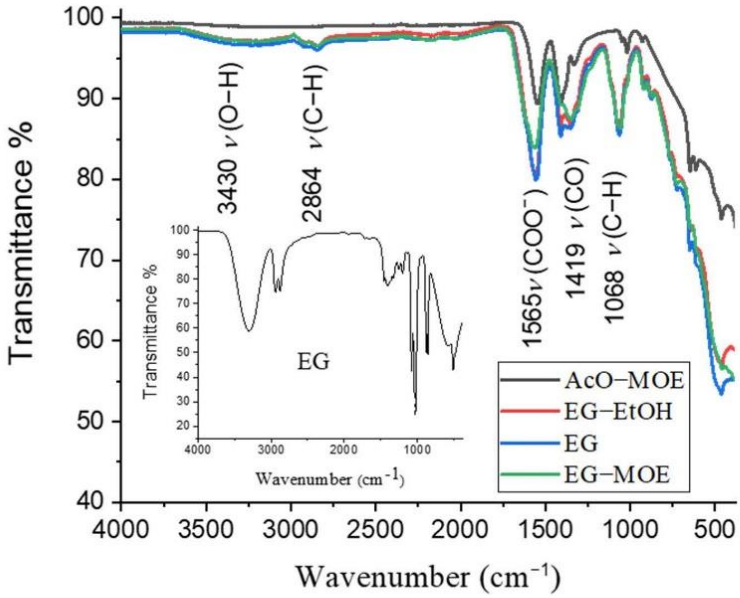

Figure 1. FTIR spectra of BT xerogels were obtained by drying the AcOH-MOE, EG, EG-EtOH and EG-MOE coating solutions at 200 °C for 12 h. The FTIR spectrum of ethylene glycol is included as an inset.

The thermal decomposition of the xerogels was analyzed by thermogravimetry and differential thermal analysis (TG and DTA) coupled with evolved gas analysis (EGA). TG, DTA and EGA curves of the AcOH-MOE, EG-EtOH, EG and EG-MOE gels are shown in Figures 2 and 3. In all samples, a small mass loss upon heating to about 100 °C accompanied by a slight endotherm and the evolution of water evident in the EGA curves is attributed to evaporation of adsorbed humidity. Likewise, in EGA, trace amounts of acetone (CH_3COCH_3) were recorded in all samples upon heating around 400 °C, see Figures S1 and S2 in Supplementary Materials. Acetone is a side product in the decomposition pathway of the acetate groups as documented in the literature [24–26].

The thermal decomposition of the AcOH-MOE sample takes place upon heating to 730 °C and is characterized by a two-step weight loss of 32.68%. The first weight loss of 19.01% from 280 °C to 402 °C is accompanied by an exothermic peak and simultaneous evolution of H_2O and CO_2 which indicates the thermal oxidation of organic groups [26]. In the interval from 620 °C to 734 °C, the weight loss of 13.67% is accompanied by a series of weak exothermic peaks and the evolution of CO_2 corresponding to carbonate decomposition. The decomposition pathway of the AcOH-MOE sample agrees with earlier reports [23].

The thermal decomposition of the EG-EtOH gel is concluded upon heating to 719 °C. The weight loss of 18.49% from 280 °C to 422 °C is marked by a series of exothermic peaks, with the strongest one at 402 °C and the simultaneous evolution of H_2O and CO_2. We observe a slight weight loss upon heating to about 580 °C where the evolution of both H_2O and CO_2 indicates the decomposition of traces of organic residues. Between 585 and 719 °C, an exothermic weight loss of 13.02% is due to carbonate groups decomposition. Clearly, the decomposition pathways of the AcOH-MOE and EG-EtOH samples show similarities, the organic groups are decomposed in the first step. The second step of mass loss in these two samples is accompanied by a relatively small exothermic peak in DTA and by the evolution of CO_2 due to the decomposition of carbonate that is concluded at about 700 °C.

In contrast, the thermal decomposition processes of the EG and EG-MOE samples collected in Figure 3 are concluded at much higher temperatures, 1076 °C, and 1127 °C, respectively. Upon heating from room temperature, we observe progressive weight loss

with a series of exothermic peaks and evolution of H_2O and CO_2 peaks up to about 600 °C. Between 600 and 800 °C, only CO_2 is evolved indicating carbonate groups decomposition.

Upon further heating to the final temperature of 1200 °C, there is another weight loss, upon which CO_2 is evolved.

It is worth mentioning that the important difference between these two samples and the AcOH-MOE and EG-EtOH is that in the former group the final mass loss is concluded only at about 1100 °C. We expect that the oxide material prepared from AcOH-MOE or EG-EtOH could be consolidated at lower temperatures than that prepared from EG or EG-MOE solvents as carbonaceous residues are decomposed at about 400 °C lower temperature.

To support the thermal analysis data, the xerogels were calcined at 900 °C for 15 min. The FTIR analysis revealed the presence of metal-oxygen bonds in the AcOH-MOE and EG-EtOH samples. The obvious band at wavenumber 1415 cm^{-1} in the spectra of EG-MOE and EG samples is attributed to the presence of carbonate groups [7], see Figure 4a. Quite similarly, Ashiri detected weak carbonate bands in IR spectra of BT gels heated up to the final temperature of 800 °C [23]. For the EG-MOE and EG samples, a higher calcination temperature was required to yield the oxide phase only, as evident from Figure 4b.

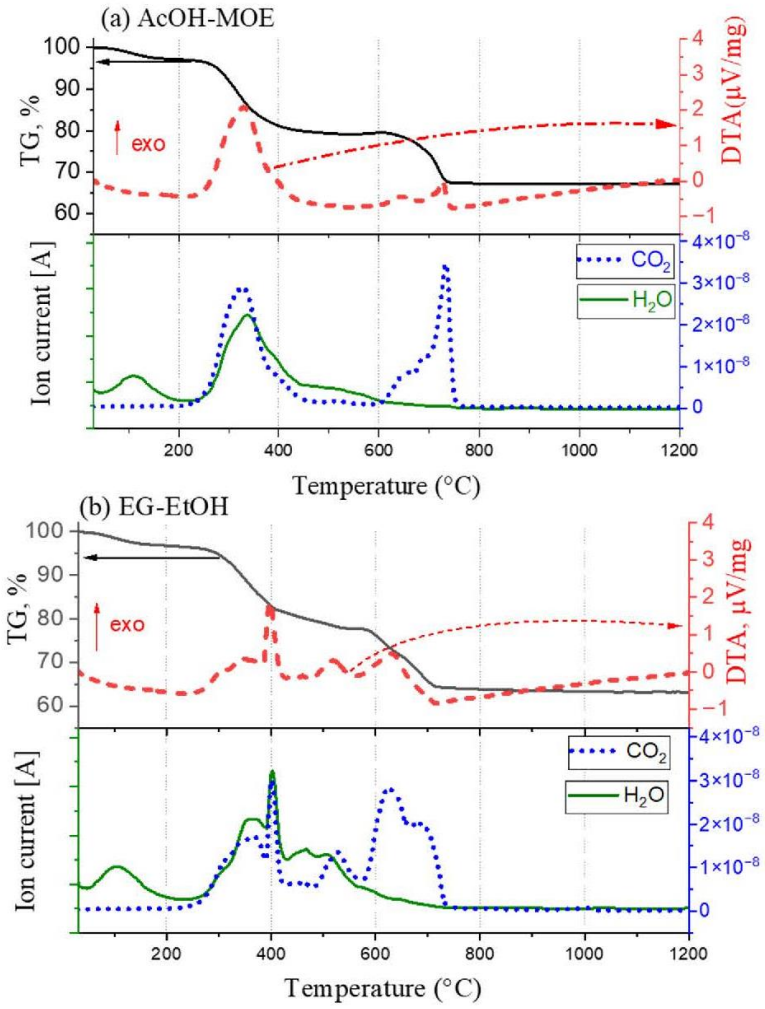

Figure 2. Thermal decomposition (TG, DTA) and EGA (H_2O and CO_2) of: (**a**) ACOH-MOE, (**b**) EG-EtOH xerogels.

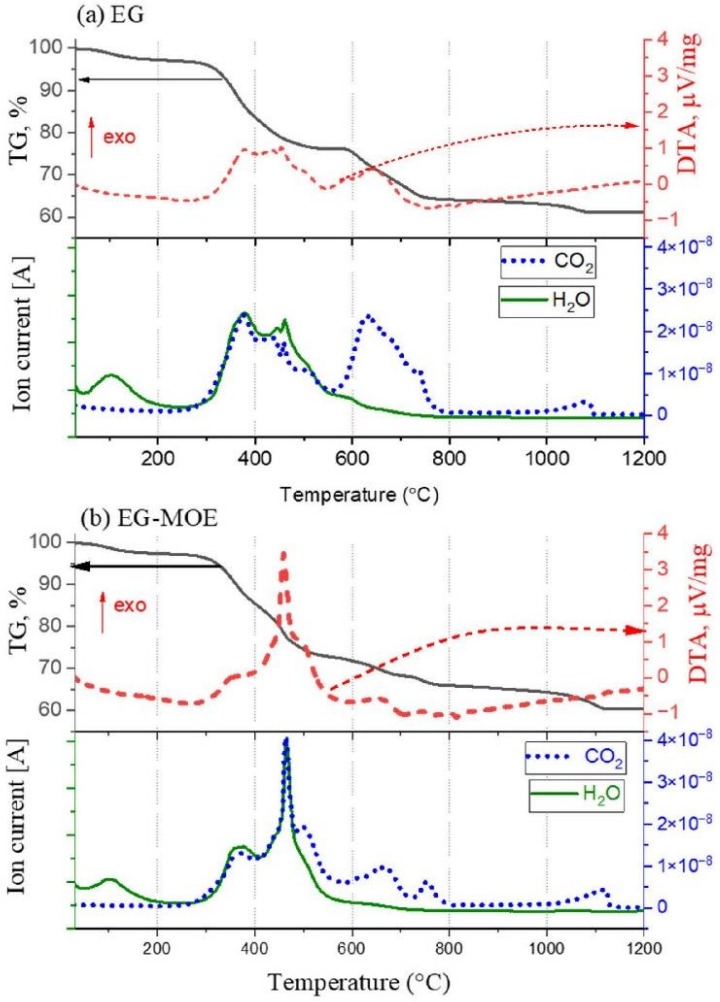

Figure 3. Thermal decomposition (TG, DTA) and EGA (H_2O and CO_2) of: (**a**) EG and (**b**) EG-MOE xerogels.

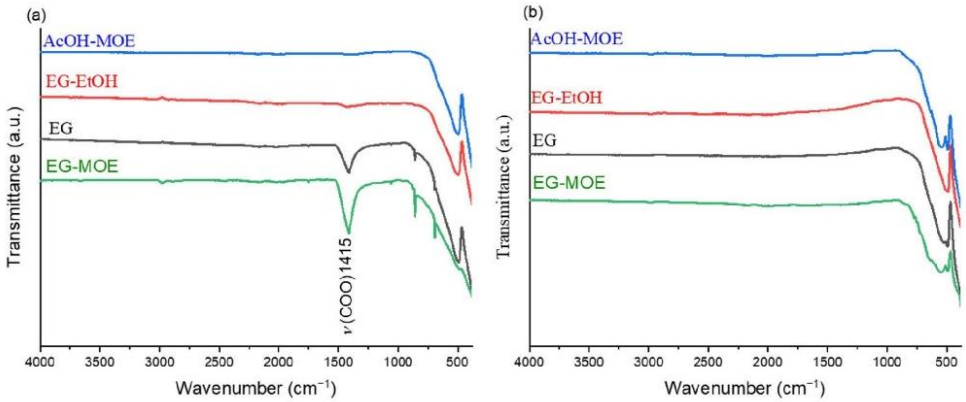

Figure 4. FTIR spectra of BT samples calcined at: (**a**) 900 °C for 15 min and (**b**) BT powder after thermal analysis up to 1200 °C.

3.1. Chemical Solution Deposition of Barium Titanate Thin Films with Ethylene Glycol as Solvent for Barium Acetate

2.2. Phase Composition, Microstructure and Properties of BT Thin Films

We spin-coated four BT solutions on platinized silicon substrates, dried and pyrolyzed them at 250 °C for 2 min, and at 350 °C for 2 min, and annealed them at 800 °C. The coating-heat treatment procedure was repeated four times. Multiple annealing steps were introduced to enable crystallization of individually deposited layers with the thickness of a few 10 nm via heterogeneous nucleation and, consequently, the formation of predominantly columnar microstructure in agreement with earlier studies [27,28].

Figure 5 shows the XRD patterns of BT thin films. All films crystallize in the perovskite phase (JCPDS 96-154-2141). We note that the peak of the (111) crystallographic plane coincides with the (111) Pt peak of the substrate. In all films, the (110) peak is the most intense, especially in the AcOH-MOE and EG-MOE; however, it should be noted that the Pt (111) peak coincides with the BT (111) peak. A comparison of crystallite sizes calculated from the (110) peak broadening using the Scherrer equation (see Supplementary Material, Table S2) reveals almost two times larger values compared to the crystallite sizes of the EG-EtOH and EG films, about 90 nm versus 55–60 nm.

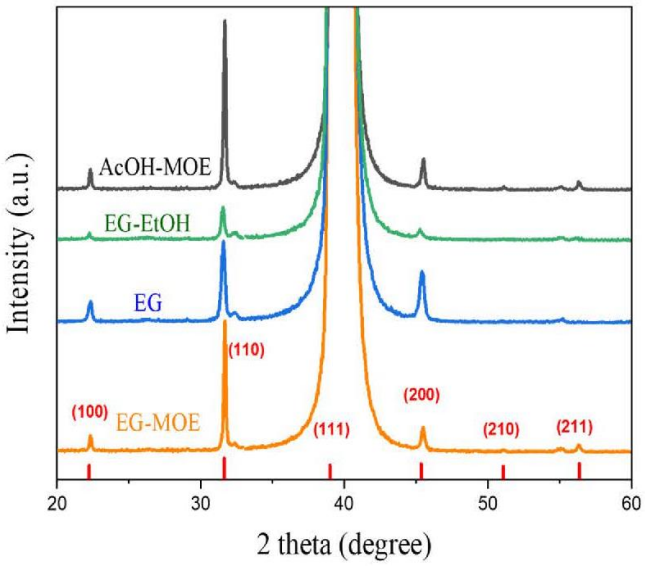

Figure 5. XRD diffraction patterns of BT thin films. The BT peaks are indexed according to the JCPDS 96-154-2141.

In Figure 6a–d, the plan-view and inset the cross-section micrographs of AcOH-MOE, EG, EG-MOE, and EG-EtOH BT films are collected. The average thickness of all films is about 100 nm, and the cross-section images reveal predominantly columnar microstructures. The plan-view images reveal dense microstructures with grains in the range of 50–100 nm across. However, in the AcOH-MOE and EG-MOE films, obvious intergranular cracks are visible on the surface, which is not the case for the EG and EG-EtOH films. It is worth mentioning that these four films were prepared under the same conditions, so the cracks are presumably not associated with the material formulation, film thickness or annealing, or phase-transition temperature-related thermal stresses. We speculate that the cracks are due to the larger grain and crystallite sizes of the AcOH-MOE and EG-MOE films (see Table S2 in Supplementary Material). In (Ba,Sr)TiO_3 thin films, the appearance of intergranular cracks was related to the combined effects of increased grain size and films thickness [6]. Local electrical measurements show that all these films are locally ferroelectric/piezoelectric active (see PFM images and local hysteresis loops in Supplementary Material, Figures S3 and S4). The dielectric permittivity and losses of the EG-EtOH film measured at 1 kHz and room temperature were 495 and 0.2, respectively, while the

measurements of other films could not be reliably performed which we mainly attribute to the presence of intergranular cracks.

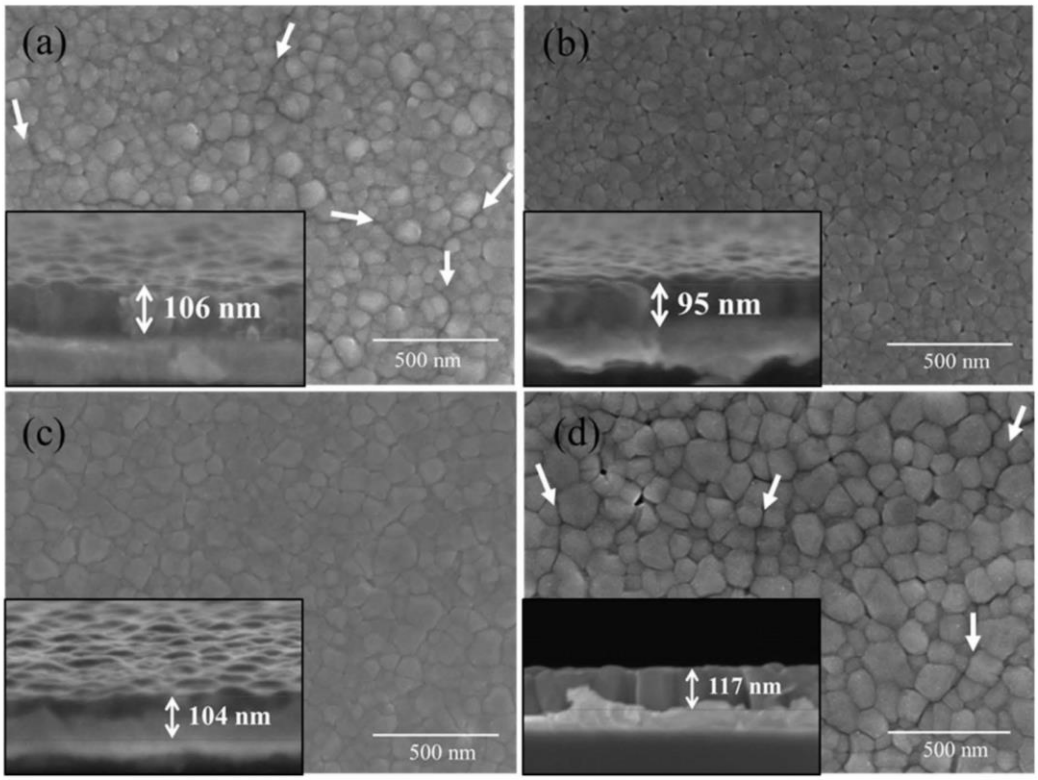

Figure 6. FE-SEM plan view and inset cross-section micrographs of: (**a**) AcOH-MOE, (**b**) EG-EtOH, (**c**) EG and (**d**) EG-MOE BT films deposited from corresponding coating solutions and annealed at 800 °C. The arrows on plan-view micrographs indicate intergranular cracks.

In the process of selecting the optimum EG-based coating solution formulation we considered two arguments:

- The final temperature of the thermal decomposition of the xerogels was in the case of EG and EG-MOE gels at about 1100 °C to ensure complete removal of carbonaceous residues, while for the EG-EtOH gel the thermal decomposition was concluded at a much lower temperature, about 700 °C, cf. Figures 2 and 3.
- Intergranular cracks developed in the EG-MOE film while the EG and EG-EtOH films were crack-free.

In further work, we thus focused on the EG-EtOH films and compared them with the AcOH-MOE films which served as reference.

Additionally, we increased the time of drying and pyrolysis steps of the EG-EtOH and AcOH-MOE films from 2 min to 15 min so that we would ensure the complete removal of residual organics. Namely, we observed that we needed quite long drying times of coating solutions (12 h) to obtain reproducible thermal decompositions of xerogels, cf. Figures 2 and 3. Furthermore, earlier reports on CSD of BT films indicated quite long times for pyrolysis, for example, 7.5 min at 250 °C [29]. We prepared the films consisting of one deposited layer only, and recorded FTIR patterns after the drying at 250 °C for 15 min, pyrolysis at 350 °C for 15 min, and rapid-thermal annealing steps at 400 °C, 500 °C, 600 °C and 700 °C. The acetate groups evidenced by the absorption bands at about 1430 cm^{-1} and 1580 cm^{-1} for (COO-) symmetric and (COO-) asymmetric stretching vibrations could be

identified in the dried and pyrolyzed films, see Figure 7, in agreement with [23]. In the AcOH-MOE film, the band of the carbonate group was present upon heating to 600 °C, and only at 700 °C did it disappear. The FTIR patterns of propionate-derived BT thin films contained carbonate bands upon annealing to 650 °C while at 700 °C only metal-oxygen bands were observed [7]. In the EG-EtOH film, the carbonates were decomposed between 500 and 600 °C, about 100 °C lower than in the AcOH-MOE films.

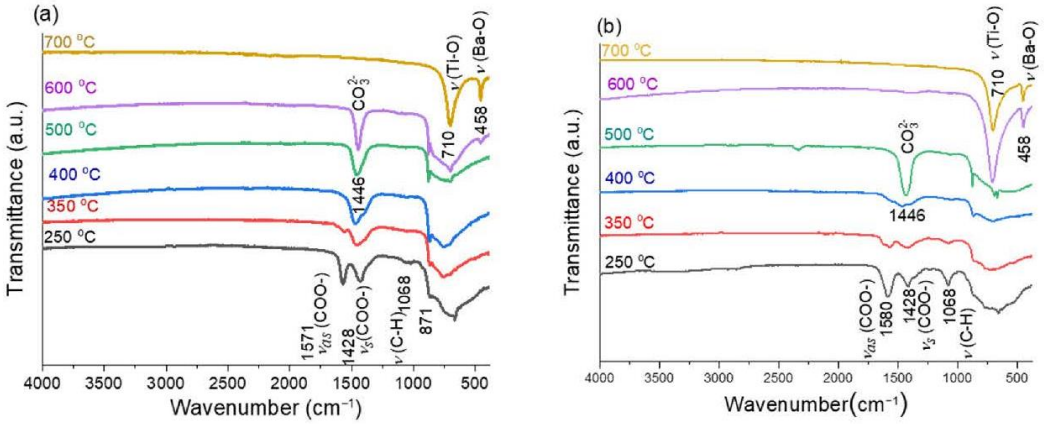

Figure 7. FTIR of BT films at different temperatures prepared from: (**a**) AcOH-MOE and (**b**) EG-EtOH solutions.

In Figure 8, XRD patterns of AcOH-MOE and EG-EtOH films prepared with 15 min drying pyrolysis times and annealed at 800 °C, consisting of four deposited layers are collected. The films crystallize in the perovskite phase (JCPDS 96-154-2141). We note that the AcOH-MOE film is strongly (110) oriented. The crystallite size of the AcOH-MOE film is 91 nm, indicating only a slight increase compared to the film with shorter drying/pyrolysis times (87 nm). A significant increase in the crystallite size is observed in the EG-EtOH film if the drying/pyrolysis time increases from 2 to 15 min, namely from 59 nm to 76 nm (see Table S1 in Supplementary Material).

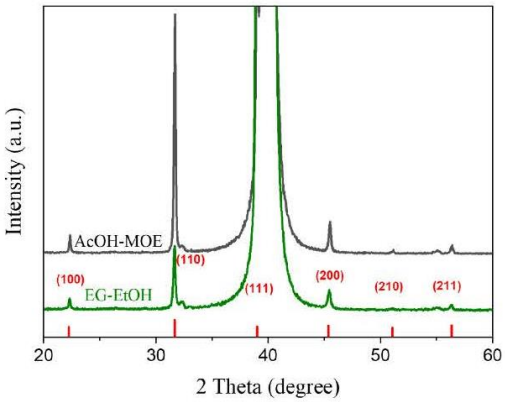

Figure 8. XRD patterns of AcOH-MOE and EG-EtOH BT films prepared with 15 min of drying and pyrolysis times and annealed at 800 °C. The perovskite peaks are indexed according to JCPDS 96-154-2141.

The plan-view and cross-section microstructures of the AcOH-MOE and EG-EtOH films are collected in Figure 9. In the surface microstructure of the AcOH-MOE film, some intergranular cracks are observed, while the EG-EtOH film is crack-free. The grain size is

50–100 nm in both cases. The cross-sections of about 100 nm thick films consist of predominantly columnar grains. In comparison with the films prepared with the short, 2 min drying and pyrolysis steps, these films seem to have more pronounced columnar microstructures.

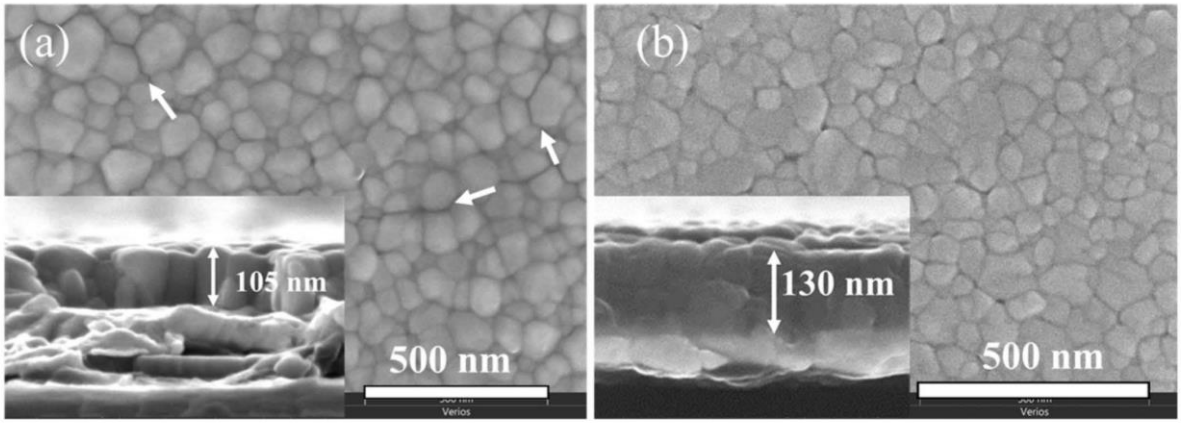

Figure 9. SEM plan-view micrographs of: (**a**) ACOH-MOE and (**b**) EG-EtOH films dried and pyrolyzed for 15 min and annealed at 800 °C. Inset: cross-section microstructures. The arrows on the plan-view micrograph in panel (**a**) indicate intergranular cracks.

A more detailed investigation of the AcOH-MOE and EG-EtOH films microstructure was performed by transmission electron microscopy (TEM). In Figure 10a,b, the cross-section microstructures of AcOH-MOE and EG-EtOH films, respectively, reveal predominantly columnar grains of about 50–100 nm across, in agreement with the SEM analysis. Such microstructure formed as a result of sequential crystallization of individually deposited layers on top of pre-crystallized layers in the process of multistep annealing [27]. In some parts, we also observe smaller equiaxed grains. In Figure 10c,d, the selected area diffraction (SAED) patterns are shown together with the TEM images of the analyzed regions. According to the diffraction data, grains in both films are preferentially [110] and [111] oriented.

Local piezoelectric/ferroelectric properties of AcOH-MOE and EG-EtOH films were investigated by PFM analysis. Figure 11a,b show the topography, PFM amplitude and PFM phase images of 3 × 3 μm^2 area scans of AcOH-MOE and EG-EtOH thin films. We note that the topography (deflection mode) of both films agrees with the SEM micrographs (Figure 9). From AFM height images it can be seen that AcOH-MOE and EG-EtOH films are flat, with surface roughness values (Rq) of 2.1 nm and 2.0 nm, respectively. The peak-to-valley values determined from the AFM height images shown in Figure 11 are 15.5 nm and 17.9 nm. The PFM amplitude and phase images of both films show different contrast under the applied voltage indicating the local piezoelectric/ferroelectric response. Local PFM amplitude and phase hysteresis loops of AcOH-MOE and EG-EtOH samples show the typical ferroelectric/piezoelectric behavior (see Figure 12a,b) indicating that both films are locally ferroelectric.

The dielectric permittivity of the AcOH-MOE film at 1 kHz and room temperature is 536 while the value for the EG-EtOH film is 604, in both cases a slight decrease with increasing frequency is observed. Both values agree with literature data for BT films with similar grain sizes [29–32]. The dielectric losses are about 3.5% and 3% at 1 kHz in Figure 13.

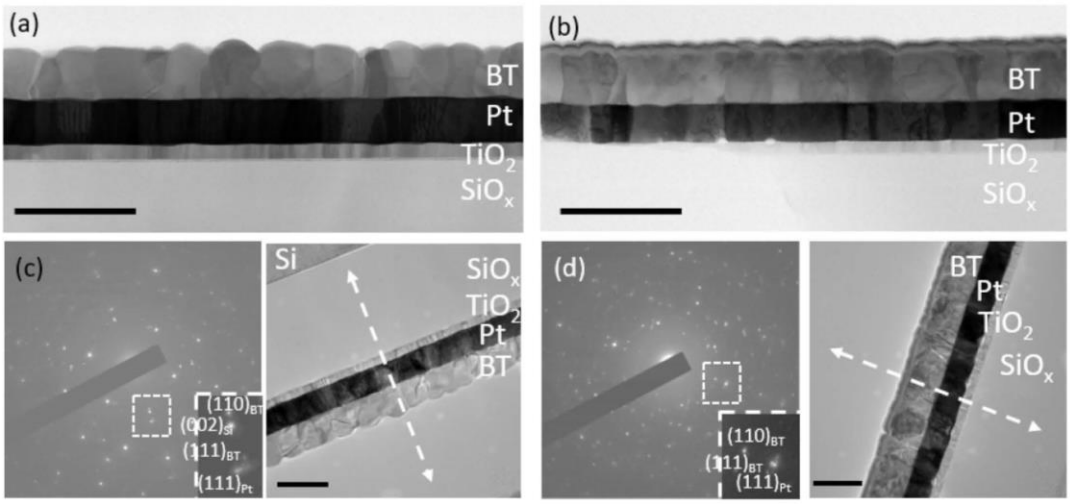

Figure 10. Bright-field scanning TEM image of a cross-section of: (**a**) AcOH-MOE, (**b**) EG-EtOH BT thin film and SAED pattern of selected region (**c**) and (**d**), respectively, of film substrate prepared under optimized heating conditions (15 min for drying and pyrolysis processes and then annealed at 800 °C). Perpendicular to the film substrate the $(110)_{BT}$ and $(111)_{BT}$ planes in both films are parallel to $(111)_{Pt}$ planes. Direction perpendicular to the film substrate is indicated by a double arrow. Bars mark 200 nm.

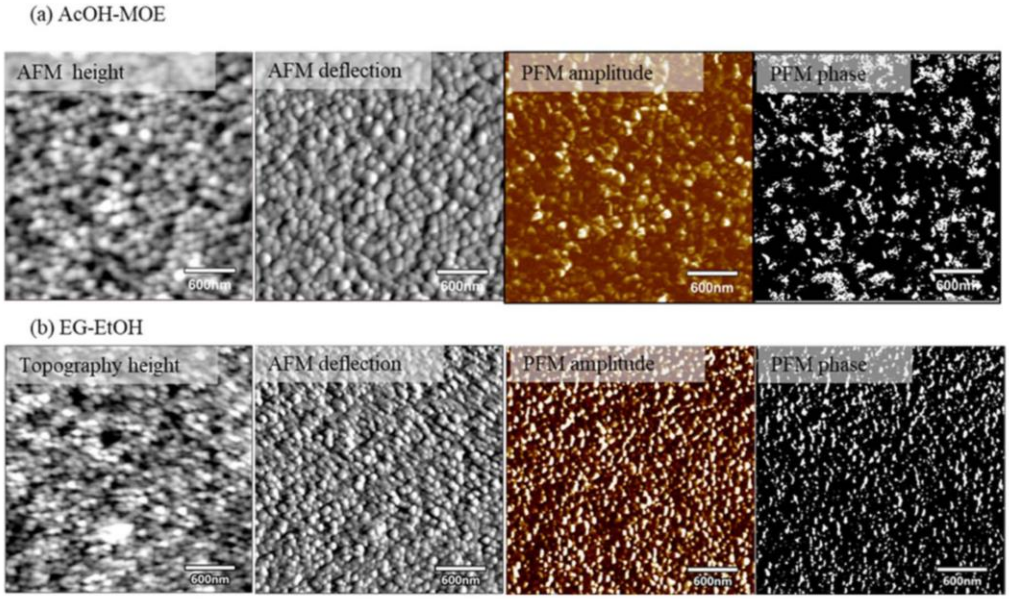

Figure 11. PFM analysis of BT films: topography—AFM height and deflection images, PFM amplitude and phase images of: (**a**) AcOH-MOE, (**b**) EG-EtOH BT films prepared by drying at 250 °C for 15 min, pyrolysis at 350 °C for 15 min and annealing at 800 °C.

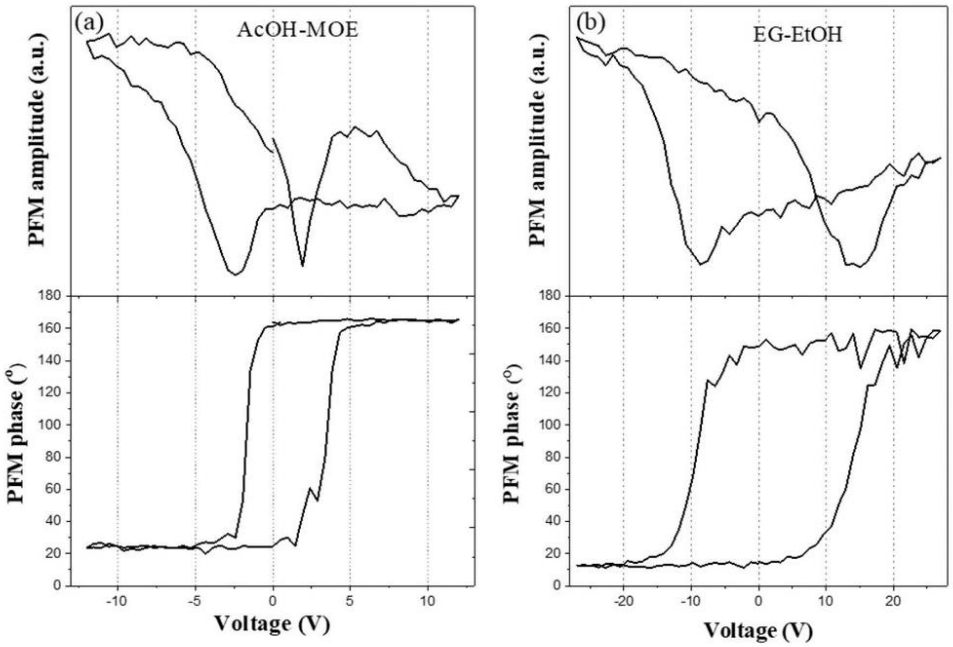

Figure 12. PFM amplitude and phase hysteresis loops of: (**a**) AcOH-MOE, (**b**) EG-EtOH optimized BT films prepared by drying at 250 °C for 15 min, pyrolysis at 350 °C for 15 min and annealing at 800 °C.

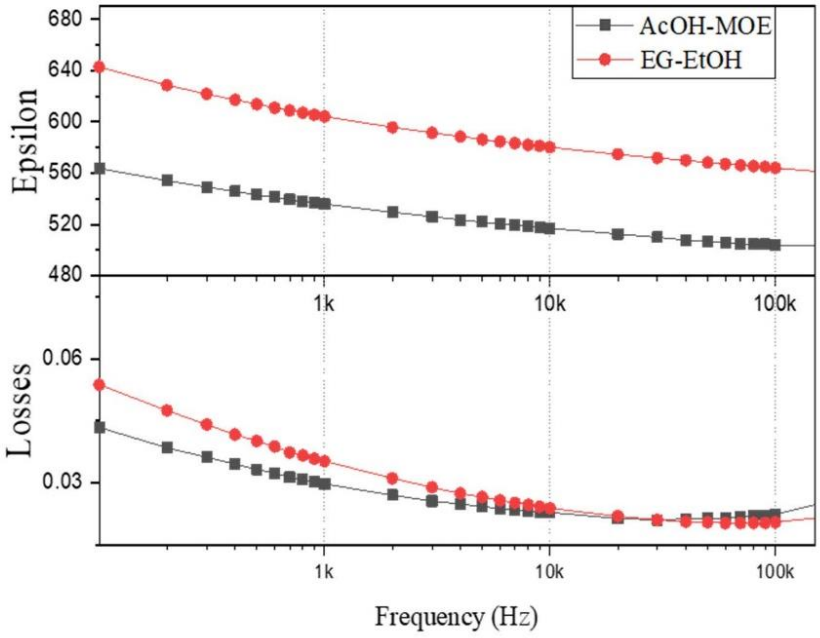

Figure 13. The frequency dependence of dielectric permittivity and losses at room temperature of AcOH-MOE and EG-EtOH BT thin films prepared by drying at 250 °C for 15 min, pyrolysis at 350 °C for 15 min and annealing at 800 °C.

The hysteresis loop of the AcOH-MOE film in Figure 14 a indicates leakage, which could probably be explained by the presence of intergranular cracks observed in this film (Figure 9). It is noted, nevertheless, that this film exhibited local ferro- and piezoelectric responses (Figure 12) and also local current measurements performed with CAFM confirmed the absence of leakage currents higher than 1 pA (see Supplementary Material, Figure S5).

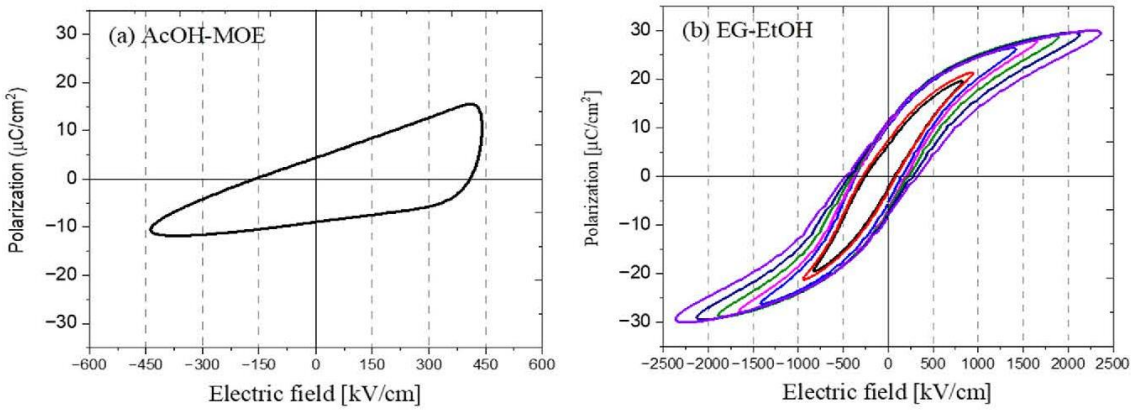

Figure 14. Polarization as a function of electric field of (**a**) AcOH-MOE and (**b**) EG-EtOH BT thin films prepared by drying at 250 °C for 15 min, pyrolysis at 350 °C for 15 min and annealing at 800 °C. Note different x-axis scales.

In contrast, the EG-EtOH film exhibits a well-developed polarization-electric field hysteresis loop shown in Figure 14 b confirming the macroscopic ferroelectric behavior of the film. We note that the film survived a quite high electric field of about 2.4 MV/cm. At the field amplitude of 1.4 MV/cm, the values of remnant and saturation polarizations are 8 $\mu C/cm^2$ and 26 $\mu C/cm^2$, respectively, and a coercive field of about 275 kV/cm. The values cannot be compared with earlier works where the maximum electric fields were about an order of magnitude lower, e.g., [31,33].

3. Materials and Methods

Barium titanate ($BaTiO_3$, BT) thin films were prepared by chemical solution deposition (CSD). Barium acetate ($Ba(CH_3COO)_2$, $Ba(OAc)_2$) with purity 99.999%, and titanium butoxide ($Ti(OC_4H_9)_4$, $Ti(OnBu)_4$) with purity 99.61% were used as reagents, both purchased from Alfa Aesar, Karlsruhe, Germany. Four coating solutions were prepared by dissolving these reagents in different combinations of solvents: acetic acid (CH_3COOH, AcOH, 100%, Alfa Aesar, Karlsruhe, Germany), 2-methoxyethanol ($CH_3OCH_2CH_2OH$, MOE, 99.3+%, Sigma-Aldrich, St. Louis, USA), ethylene glycol ($OHCH_2CH_2OH$, EG 99.5%, Riedel-de Haën, Seelze, Germany) and absolute ethanol (CH_3CH_2OH, EtOH 99.9%, Carlo Erba, Valde-Reuil, France). The manipulation of chemicals and chemical reactions took place in a dry nitrogen atmosphere.

The coating solutions and samples prepared from these solutions are named according to the solvents used for their preparation. The procedures are described below and schematically summarized in Figure 15. In a typical experiment, 25 mL of the 0.2 M Ba-Ti coating solution was prepared.

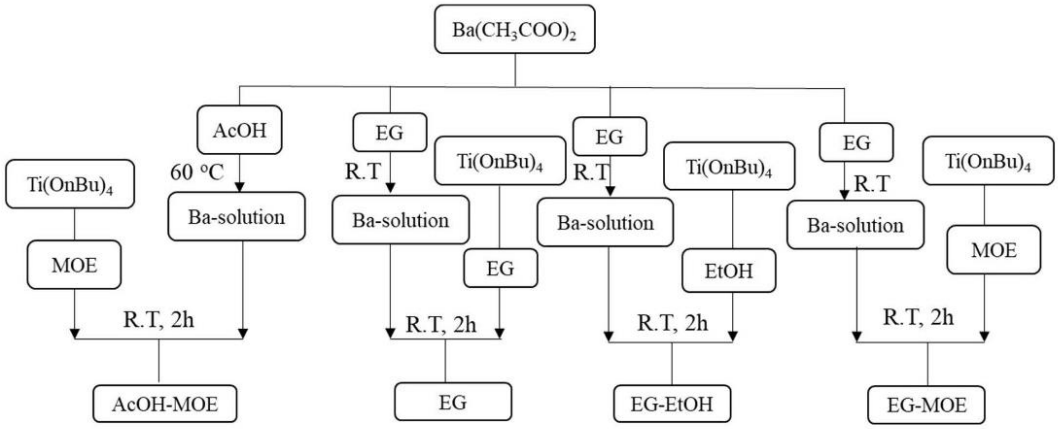

Figure 15. The procedure of preparation of BT coating solutions.

The AcOH-MOE solution was prepared using AcOH and MOE as solvents following the procedure described in earlier papers [6,28]. $Ba(OAc)_2$ was dissolved in AcOH at 60 °C and cooled to room temperature. $Ti(OnBu)_4$ was diluted with MOE and mixed for ≥15 min. Then the two solutions were mixed in the equimolar ratio for 2 h at room temperature and the concentration was adjusted to 0.2 M. The AcOH/MOE volume ratio was 3/2.

The solution denoted EG was prepared using EG as the only solvent. $Ba(OAc)_2$ was dissolved in EG at room temperature. The $Ti(OnBu)_4$ solution in EG was added to the $Ba(OAc)_2$ solution in the equimolar ratio. After mixing at room temperature for 2 h the concentration of the Ba-Ti solution was adjusted to 0.2 M. In the solution denoted EG-EtOH, $Ti(OnBu)_4$ was diluted with absolute EtOH at room temperature, mixed with the solution of $Ba(OAc)_2$ in EG in equimolar ratio for 2 h to yield the 0.2 M Ba-Ti solution. In the EG-MOE solution, $Ti(OnBu)_4$ was diluted with MOE instead of EtOH. In EG/EtOH or EG/MOE the volume ratio of respective solvents was 3/2.

$BaTiO_3$ films were deposited from the four solutions on $Pt(111)/TiO_2/SiO_2/(100)/Si$ substrates (Pt/Si, purchased from SINTEF, Oslo, Norway) by spin coating at 3000 rpm for 30 s (WS -400B-6NPP/LITE, North Wales, PA, Laurell). The as-deposited wet films were dried at 250 °C for 2 min and pyrolyzed at 350 °C for 2 min on hot plates. For selected AcOH-MOE and EG-EtOH films, the times of drying and pyrolysis steps were prolonged to 15 min. The films were annealed at 800 °C with heating and cooling rates of 13,33 °C/s and 2,6 °C/s, respectively, in a rapid thermal annealing furnace (Mila 5000, Ulvac-Riko, Yokohama, Japan) after each deposition-drying pyrolysis step. The annealing times for the first and the last deposited layers were 15 min, and 5 min for intermediate layers. This procedure was repeated four times to achieve a film thickness of about 100 nm. Please note that the films have been named after the coating solutions they were deposited from.

The thermal decomposition of the xerogels obtained by drying the respective coating solutions at 200 °C for 12 h was followed using a simultaneous thermal analyzer coupled with a mass spectrometer (STA 409, Netzsch, Selb, Germany + ThermoStar, Balzers Instruments, Oerlikon, Switzerland). The samples with a mass of about 33 mg were heated in Pt/Rh crucibles with a heating rate of 10 K/min. Thermogravimetric curves (TG), differential thermal analysis (DTA) and evolved gas analysis (EGA) were recorded up to 1200 °C, in a flowing synthetic air atmosphere.

The BT gels, calcined at 900 °C for 15 min and the powder samples obtained after the thermal analysis were collected for Fourier transform infrared spectroscopy (Perkin Elmer FTIR Spectrum 100, Waltham, Massachusetts USA, 4000–380 cm^{-1}). FTIR was also used to follow the chemical composition of the AcOH-MOE and EG-EtOH films. The films consisting of one spin-coated layer were dried at 250 °C for 15 min, pyrolyzed at 350 °C for

15 min and then rapid-thermally annealed at 400 °C, 500 °C, 600 °C and 700 °C for 6 s. The FTIR spectrum was recorded after each drying/pyrolysis/heating step.

XRD analysis of the prepared films was performed using a high-resolution diffractometer (X'Pert PRO, PANalytical, Cu Kα radiation, Almelo, The Netherlands) with 2 theta = 10–39, 40–65 deg, step = 0.016, time per step = 100 s, soller slit = 0.02, mask10. Note that the 2-theta range was selected so that the Pt (111) peak was not recorded. The XRD data were analyzed by X'Pert High Score Plus software for the phase analysis.

Scanning electron microscopy analysis was performed using field emission scanning electron microscopes (FE-SEM) JSM-7600F (JEOL, Tokyo, Japan) with 10 kV accelerating voltage and Verios 4G HP (Thermo Fischer, Waltham, Massachusetts, USA). To avoid charging problems during analysis, the samples were pre-coated with 5 nm of carbon using a Precise Etching and Coating System 628A (Gatan, Pleasanton, California, USA).

A detailed investigation of the thin film microstructure was performed using a scanning-transmission electron microscope JEOL ARM 200 CF (JEOL Ltd., Tokyo, Japan) operated at 200 kV. The cross-section specimens were prepared by a classical sandwich technique—the films were cut with a diamond saw, glued face-to-face and mounted in brass rings with epoxy. The samples were then ground, polished and dimpled. Electron transparency was archived by Ar+ milling using a PIPS 691 ion milling system (Gatan, Peasanton, California, USA).

Piezo-response force microscopy (PFM) and conductive atomic force microscopy (C-AFM) were performed using Jupiter XR and MFP-3D atomic force microscopes (Asylum Research, Santa Barbara, California, USA) equipped with a PFM and C-AFM modules. For PFM and C-AFM scanning, a conductive tip with a diameter of about 15 nm made of Ti/Ir layer coated on Si (Asyelec-01, Atomic Force F&E GmbH, Abingdon, UK) was used. During PFM scanning in dual ac resonance tracking mode, an electric voltage of 3 V and a frequency of ~350 kHz were applied between a conductive AFM tip and the bottom electrode of the samples. The PFM amplitude and phase hysteresis loops were measured in the off-electric-field switching spectroscopy mode with the pulsed dc step signal and the superimposed ac drive signal, as described in [34]. The waveform parameters were: the sequence of increasing dc step signal was driven at 20 Hz; the frequency of the triangular envelope was 0.2 Hz; a superimposed sinusoidal ac signal with an amplitude of 3 V and a frequency of ~350 kHz was used. Three cycles were measured, the second cycle is shown in Figure 12. CAFM measurements were performed with ORCA mode using dc signal of up to 25 V.

Dielectric permittivity and losses as functions of frequency were measured using an impedance analyzer at room temperature (HP 4284A) with a frequency range of 100 Hz to 100 kHz. Ferroelectric hysteresis loops were measured using an Aixacct TF analyzer 2000 (Systems GmbH, Aachen, Germany) with a sinusoidal signal, a frequency of 1 kHz. Gold electrodes with a diameter of 0.4 mm and 0.2 mm were deposited on the films by magnetron sputtering (5 Pascal). The platinum bottom contact was reached by etching the films with a mixture of HF, HCl and H_2O in the ratio (2:5:20).

4. Conclusions

Since early papers on CSD of BT and BT-based films, the synthesis of the coating solution has involved a carboxylic acid as the solvent for alkaline-earth salt and an alcohol as the solvent for the transition metal alkoxide. Such choice of the solvents unavoidably results in slow but progressive in-situ evolution of water, which contributes to uncontrolled hydrolysis of the alkoxide and reduces the stability of the solution.

By replacing acetic acid (AcOH) with ethylene glycol (EG) as the solvent for Ba-acetate the stability of coating solutions was increased from weeks to months. We found that the choice of the alcohol solvent for Ti-alkoxide influenced the course of the thermal decomposition of the xerogels obtained by drying the respective coating solutions. In the case of EG and 2-methoxyethanol (MOE), which can both act as chelating agents the thermal decomposition of the xerogels was concluded only at about 1100 °C. The xerogel

obtained from the EG-ethanol based solution was thermally decomposed into an oxide at about 700 °C, which is comparable to the data for the acetic-acid derived xerogel.

BT thin films were deposited on platinized silicon substrates, dried, pyrolyzed and rapid thermally annealed at 800 °C. The about 100 nm thick films crystallized in the perovskite phase with predominantly columnar microstructures. Intergranular cracks were observed in the BT films deposited from the AcOH-MOE and EG-MOE solutions, which could be tentatively related to larger grain and crystallite sizes (about 90 nm) of respective films compared to EG-ethanol derived films (about 60 nm).

The films prepared using the latter solvent formulation were considered for further study and after optimizing the drying-pyrolysis conditions compared to the acetic-acid derived films. PFM analysis revealed that the films show the local piezoelectric/ferroelectric behavior. The room temperature dielectric permittivity values at 1 kHz of the EG-ethanol and AcOH-MOE films are about 600 and 540, in agreement with the literature data. The EG-EtOH film exhibits polarization-electric field loops up to the field amplitude of 2.4 MV/cm, while the AcOH-MOE film revealed only leaky behavior presumably due to the presence of cracks.

The present results are a good starting point for design of coating solutions containing EG as the alkaline-earth reagent solvent in CSD of more complex BT-based formulations such as lead-free piezoelectric $Ba(Zr_xTi_{1-x})O_3$-$(Ba_{1-x}Ca_x)TiO_3$ films. In these films the control of chemical homogeneity, phase composition and microstructure are the preconditions for the design of their functional properties.

Supplementary Materials: The following supporting information can be downloaded at: https://www.mdpi.com/article/10.3390/molecules27123753/s1, Figure S1. Thermal decomposition (TG, DTA) and EGA (H_2O, CH_3COCH_3, and CO_2) of: (**a**)-ACOH-MOE, (**b**)-EG-EtOH xerogels. Figure S2. Thermal decomposition (TG, DTA) and EGA (H_2O, CH_3COCH_3 and CO_2) of: (**a**)-EG and (**b**) EG-MOE xerogels. Table S1. Crystallite size (**d**) of BT films, Figure S3. PFM analysis of BT films: Topography deflection, PFM amplitude and phase images of: (**a**) AcOH-MOE, (**b**) EG-EtOH, (**c**) EG, (**d**) EG-MOE films. Figure S4. Local PFM amplitude and phase hysteresis loops of: (**a**) AcOH-MOE, (**b**) EG-EtOH, (**c**) EG, (**d**) EG-MOE films. [35] Figure S5. C-AFM analysis of: (**a**) AcOH-MOE, (**b**) EG-EtOH films.

Author Contributions: Conceptualization, S.W.K. and B.M.; methodology, B.M., H.U., A.B.; S.W.K.: chemical solution deposition of thin films, FTIR analysis, XRD analysis, S.W.K.; thermal analysis, S.W.K., B.M.; SEM, STEM: K.Ž., A.B., B.K.; AFM-PFM-C-AFM: S.W.K. and H.U.; electrical measurements: S.W.K., B.K.; resources, B.M.; writing—original draft preparation, S.W.K. and B.M.; writing—review and editing, all authors; supervision, B.M.; funding acquisition, B.M. All authors have read and agreed to the published version of the manuscript.

Funding: This work was funded by the Slovenian Research Agency in the frame of core funding P2-0105 and national postgraduate research funding (S.W.K. and K.Ž.).

Institutional Review Board Statement: Not applicable.

Informed Consent Statement: Not applicable.

Data Availability Statement: Not applicable.

Acknowledgments: We thank Jena Cilenšek for performing thermal analyses, Mirela Dragomir for advice in X-ray diffraction analysis and Val Fišinger for help with C-AFM.

Conflicts of Interest: The authors declare no conflict of interest.

Sample Availability: Samples of the xerogels and thin films are available from the authors.

References

1. Liu, W.; Ren, X. Large piezoelectric effect in Pb-free ceramics. *Phys. Rev. Lett.* **2009**, *103*, 257602. [CrossRef] [PubMed]
2. Gao, J.; Ke, X.; Acosta, M.; Glaum, J.; Ren, X. High piezoelectricity by multiphase coexisting point: Barium titanate derivatives. *MRS Bull.* **2018**, *43*, 595–599. [CrossRef]
3. Acosta, M.; Novak, N.; Rojas, V.; Patel, S.; Vaish, R.; Koruza, J.; Rödel, J.J.A.P. $BaTiO_3$-based piezoelectrics: Fundamentals, current status, and perspectives. *Appl. Phys. Rev.* **2017**, *4*, 041305. [CrossRef]

4. Krupanidhi, S.B.; Peng, C.J. Studies on structural and electrical properties of barium strontium titanate thin films developed by metallo-organic decomposition. *Thin Solid Films* **1997**, *305*, 144–156. [CrossRef]
5. Bao, P.; Jackson, T.J.; Wang, X.; Lancaster, M.J. Barium strontium titanate thin film varactors for room-temperature microwave device applications. *J. Phys. D Appl. Phys.* **2008**, *41*, 063001. [CrossRef]
6. Pečnik, T.; Glinšek, S.; Kmet, B.; Malič, B. Combined effects of thickness, grain size, and residual stress on the dielectric properties of $Ba_{0.5}Sr_{0.5}TiO_3$ thin films. *J. Alloys Compd.* **2015**, *646*, 766–772. [CrossRef]
7. Hasenkox, U.; Hoffmann, S.; Waser, R. Influence of precursor chemistry on the formation of $MTiO_3$ (M = Ba, Sr) ceramic thin films. *J. Sol-Gel Sci. Technol.* **1998**, *12*, 67–79. [CrossRef]
8. Schwartz, R.W.; Clem, P.G.; Voigt, J.A.; Byhoff, E.R.; Van Stry, M.; Headley, T.J.; Missert, N.A. Control of Microstructure and Orientation in Solution-Deposited $BaTiO_3$ and $SrTiO_3$ Thin Films. *J. Am. Cer. Soc.* **1999**, *82*, 2359–2367. [CrossRef]
9. Edmondson, B.I.; Kwon, S.; Lam, C.H.; Ortmann, J.E.; Demkov, A.A.; Kim, M.J.; Ekerdt, J.G. Epitaxial, electro-optically active barium titanate thin films on silicon by chemical solution deposition. *J. Am. Cer. Soc.* **2020**, *103*, 1209–1218. [CrossRef]
10. Raeder, T.M.; Bakken, K.; Glaum, J.; Einarsrud, M.A.; Grande, T. Enhanced in-plane ferroelectricity in BaTiO3 thin films fabricated by aqueous chemical solution deposition. *AIP Adv.* **2018**, *8*, 105228. [CrossRef]
11. Bakken, K.; Blichfeld, A.B.; Chernyshov, D.; Grande, T.; Glaum, J.; Einarsrud, M.A. Mechanisms for texture in BaTiO3 thin films from aqueous chemical solution deposition. *J. Sol-Gel Sci. Technol.* **2020**, *95*, 562–572. [CrossRef]
12. Schneller, T. Simple Alkoxide Based Precursor Systems. In *Chemical Solution Deposition of Functional Oxide Thin Films*; Schneller, T., Waser, R., Kosec, M., Payne, D., Eds.; Springer: Vienna, Austria, 2013; pp. 3–28.
13. Shneller, T.; Griesche, D. Carboxylate Based Precursor Systems. In *Chemical Solution Deposition of Functional Oxide Thin Films*; Schneller, T., Waser, R., Kosec, M., Payne, D., Eds.; Springer: Vienna, Austria, 2013; pp. 29–50.
14. Chi, Q.G.; Zhu, H.F.; Xu, J.C.; Wang, X.; Lin, J.Q.; Sun, Z.; Lei, Q.Q. Microstructures and electrical properties of $0.5(Ba_{0.7}Ca_{0.3})TiO_3-0.5Ba(Zr_{0.2}Ti_{0.8})O_3$ thin films prepared by a sol–gel route. *Cer. Int.* **2013**, *39*, 8195–8198. [CrossRef]
15. Huang, L.; Dai, Y.; Wu, Y.; Pei, X.; Chen, W. Enhanced ferroelectric and piezoelectric properties of $(1-x)BaZr_{0.2}Ti_{0.8}O_3-xBa_{0.7}Ca_{0.3}TiO_3$ thin films by sol–gel process. *Appl. Surf. Sci.* **2016**, *388*, 35–39. [CrossRef]
16. Ihlefeld, J.F.; Maria, J.P.; Borland, W. Dielectric and microstructural properties of barium titanate zirconate thin films on copper substrates. *J. Mater. Res.* **2005**, *20*, 2838–2844. [CrossRef]
17. Laaziz, I.; Larbot, A.; Julbe, A.; Guizard, C.; Cot, L. Hydrolysis of mixed titanium and zirconium alkoxides by an esterification reaction. *J. Solid State Chem.* **1992**, *98*, 393–403. [CrossRef]
18. Bradley, D.C.; Mehrotra, R.C.; Gaur, D.P. Physical Properties of Metal Alkoxides. In *Metal Alkoxides*; Academic Press: London, UK; New York, NY, USA; San Franscisco, CA, USA, 1978; pp. 159–164.
19. Imhoff, L.; Barolin, S.; Pellegri, N.; Stachiotti, M.G. Chelate route for the synthesis of $PbZr_xTi_{1-x}O_3$ thin films. *J. Sol-Gel Sci. Technol.* **2017**, *83*, 375–381. [CrossRef]
20. Livage, C.; Safari, A.; Klein, L.C. Glycol-based sol-gel process for the fabrication of ferroelectric PZT thin films. *J. Sol-Gel Sci. Technol.* **1994**, *2*, 605–609. [CrossRef]
21. Budd, K.D.; Payne, D.A. Preparation of strontium titanate ceramics and internal boundary layer capacitors by the Pechini method. In Proceedings of the Better Ceramics Trough Chemistry, Albuquerque, NM, USA, February 1984.
22. Bradley, D.C.; Mehrotra, R.C.; Gaur, D.P. Synthesis of Metal Alkoxides. In *Metal Alkoxides*; Academic Press: London,UK; New York, NY, USA; San Franscisco, CA, USA, 1978; p. 191.
23. Ashiri, R. Detailed FT-IR spectroscopy characterization and thermal analysis of synthesis of barium titanate nanoscale particles through a newly developed process. *Vib. Spectrosc.* **2013**, *66*, 24–29. [CrossRef]
24. Malič, B.; Kosec, M.; Smolej, K.; Stavber, S. Effect of precursor type on the microstructure of $PbTiO_3$ thin films. *J. Eur. Ceram. Soc.* **1999**, *19*, 1345–1348. [CrossRef]
25. Malič, B.; Calzada, M.L.; Cilensek, J.; Pardo, L.; Kosec, M. Thermal analysis study of diol based precursors for chemical solution deposition of $0{\cdot}7Pb(Mg_{1/3}Nb_{2/3})O_3$-$0{\cdot}3PbTiO_3$ thin films. *Adv. Appl. Cer.* **2010**, *109*, 147–151. [CrossRef]
26. Malič, B.; Kupec, A.; Kosec, M. Thermal Analysis. In *Chemical Solution Deposition of Functional Oxide Thin Films*; Schneller, T., Waser, R., Kosec, M., Payne, D., Eds.; Springer: Vienna, Austria, 2013; pp. 163–179.
27. Hoffmann, S.; Hasenkox, U.; Waser, R.; Jia, C.L.; Urban, K. Chemical Solution Deposited $BaTi0_3$ AND $SrTi0_3$ Thin Films with Columnar Microstructure. *MRS Online Proc. Libr.* **1997**, *474*, 9. [CrossRef]
28. Pečnik, T.; Benčan, A.; Glinšek, S.; Malič, B. Tailoring the microstructure and dielectric properties of $Ba_{0.5}Sr_{0.5}TiO_3$ thin films by solution-based processing in the frame of the Microstructural Zone Model. *J. All. Comp.* **2018**, *743*, 812–818. [CrossRef]
29. Ihlefeld, J.F.; Borland, W.J.; Maria, J.P. Enhanced dielectric and crystalline properties in ferroelectric barium titanate thin films. *Adv. Funct. Mater.* **2007**, *17*, 1199–1203. [CrossRef]
30. Ihlefeld, J.F.; Vodnick, A.M.; Baker, S.P.; Borland, W.J.; Maria, J.P. Extrinsic scaling effects on the dielectric response of ferroelectric thin films. *J. Appl. Phys.* **2008**, *103*, 074112. [CrossRef]
31. Kuwabara, M.; Takahashi, S.; Kuroda, T. Preparation of ferroelectric $BaTiO_3$ thin films on polycrystalline $BaPbO_3$ substrates by sol-gel processing and their electrical properties. *Appl. Phys. Lett.* **1993**, *62*, 3372–3374. [CrossRef]
32. Bajac, B.; Vukmirović, J.; Tripković, Đ.; Đurđić, E.; Stanojev, J.; Cvejić, Ž.; Srdić, V.V. Structural characterization and dielectric properties of $BaTiO_3$ thin films obtained by spin coating. *Proc. Appl. Cer.* **2014**, *8*, 219–224. [CrossRef]

33. Basantakumar Sharma, H.; Sarma, H.N.K.; Mansingh, A. Ferroelectric and dielectric properties of sol-gel processed barium titanate ceramics and thin films. *J. Mater. Sci.* **1999**, *34*, 1385–1390. [CrossRef]
34. Uršič, H.; Prah, U. Investigations of ferroelectric polycrystalline bulks and thick films using piezoresponse force microscopy. *Proc. R. Soc. A Math. Phys. Eng. Sci.* **2019**, *475*, 20180782. [CrossRef]
35. ORCA—Conductive AFM, Asylum Research. Available online: https://mundylab.umd.edu/wp-content/uploads/ORCASupportNote_rev1.pdf (accessed on 25 April 2022).

Supplementary Materials

Chemical Solution Deposition of Barium Titanate Thin Films with Ethylene Glycol as Solvent for Barium Acetate

Sabi William Konsago* [1,2], Katarina Žiberna [1,2], Brigita Kmet [1,2], Andreja Benčan [1,2], Hana Uršič [1,2], Barbara Malič[1,2]

[1] Electronic Ceramics Department, Jožef Stefan Institute, Jamova Cesta 39, 1000 Ljubljana, Slovenia;
[2] Jožef Stefan International Postgraduate School, Jamova Cesta 39, 1000 Ljubljana, Slovenia ;
* Correspondence: sabi.william.konsago@ijs.si, barbara.malic@ijs.si

Supplement S1. Thermal analysis of BT xerogels.

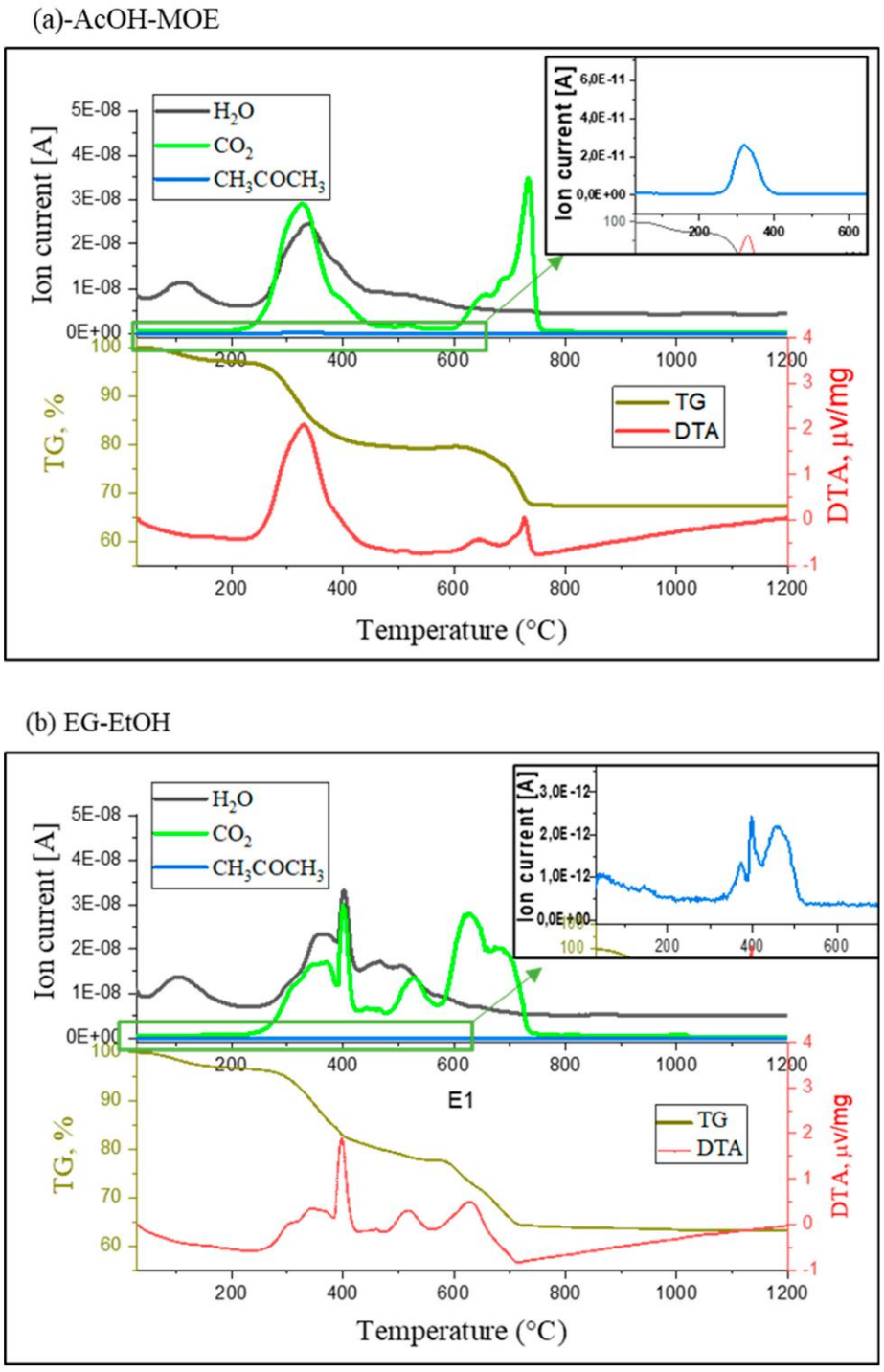

Figure S1. Thermal decomposition (TG, DTA) and EGA (H_2O, CH_3COCH_3, and CO_2) of (a)-ACOH-MOE, (b)-EG-EtOH xerogels.

3.1. Chemical Solution Deposition of Barium Titanate Thin Films with Ethylene Glycol as Solvent for Barium Acetate

(a) EG

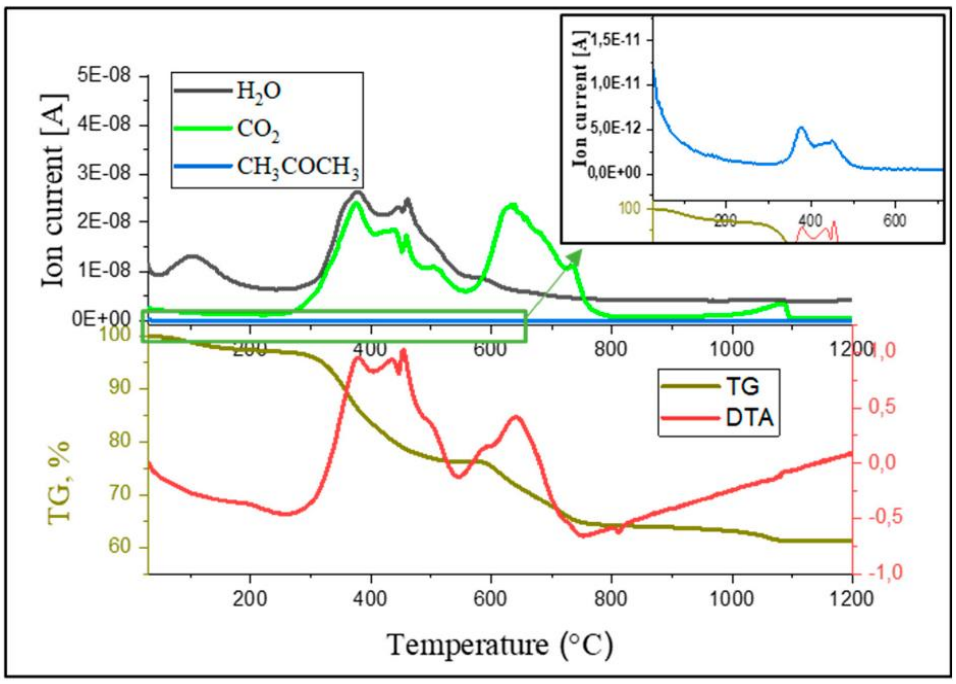

(b) EG-MOE

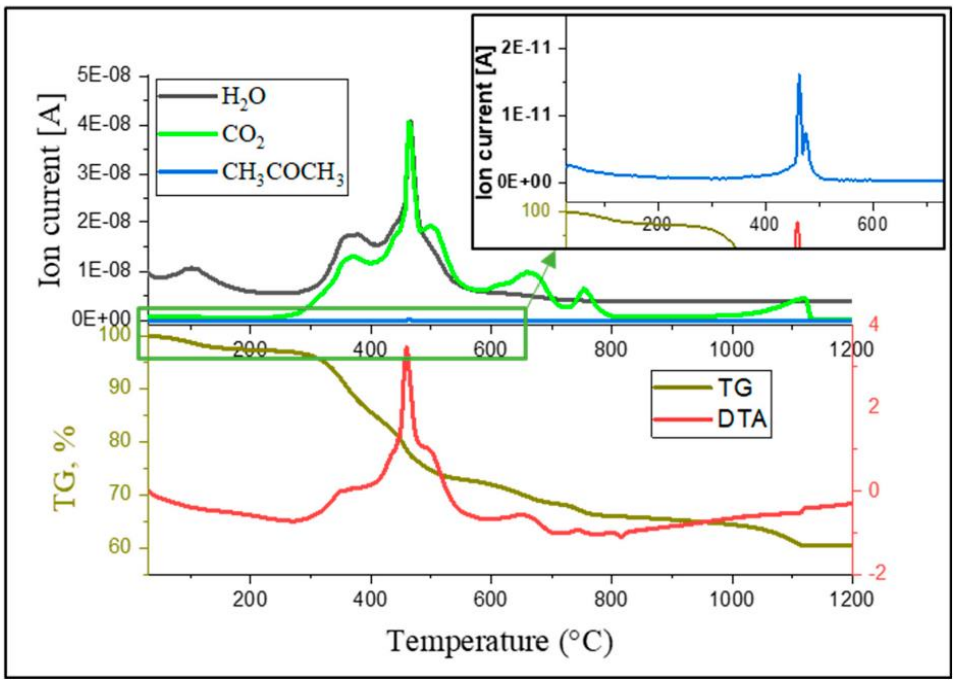

Figure S2. Thermal decomposition (TG, DTA) and EGA (H_2O, CH_3COCH_3, and CO_2) of (a)-EG and (b) EG-MOE xerogels.

Supplement S2. Crystallite size of $BaTiO_3$ (BT) thin films

In Table S1 crystallite sizes of BT thin films calculated using Scherrer equation (1) from the (110) reflection are collected. The films were prepared by drying at 250 °C, pyrolysis at 350 °C and rapid thermal annealing at at 800 °C.

Table S1. Crystallite size (d) of BT films

Film	FWHM, radian	d, nm
2 minutes of drying and 2 minutes of pyrolysis processes		
AcOH-MOE	0.00160	87
EG-EtOH	0.00234	59
EG	0.00264	53
EG-MOE	0.00147	94
15 minutes of drying and 15 minutes of pyrolysis processes		
AcOH-MOE	0.00152	91
EG-EtOH	0.00182	76

AcOH-MOE- BT film derived from the solution containing acetic acid and 2-methoxyethanol solvents,

EG-EtOH- BT film derived from the solution containing ethylene glycol and ethanol solvents,

EG- BT film derived from EG as the only solvent in BT coating solution,

EG-MOE- BT film derived from the solution containing ethylene glycol and 2-methoxyethanol solvents.

$$d = \frac{K.\lambda}{L.cos\theta} \quad (1)$$

where d is the crystallite size, K is the Scherrer constant (0.9), λ is the wavelength of X-ray (0.15406 nm), L is the full width at half maximum (FWHM, radian) and θ is the peaks position of peak (radian).

Supplement S3. PFM analysis of BT films

Figure S3 shows the results of PFM analysis of 3 × 3 μm² area scans of AcOH-MOE, EG-EtOH, EG, and EG-MOE BT films. In all cases, topography deflection images agree with SEM images regarding the grain size of the films. The PFM amplitude and phase images of all films show the local piezoelectric/ferroelectric responses.

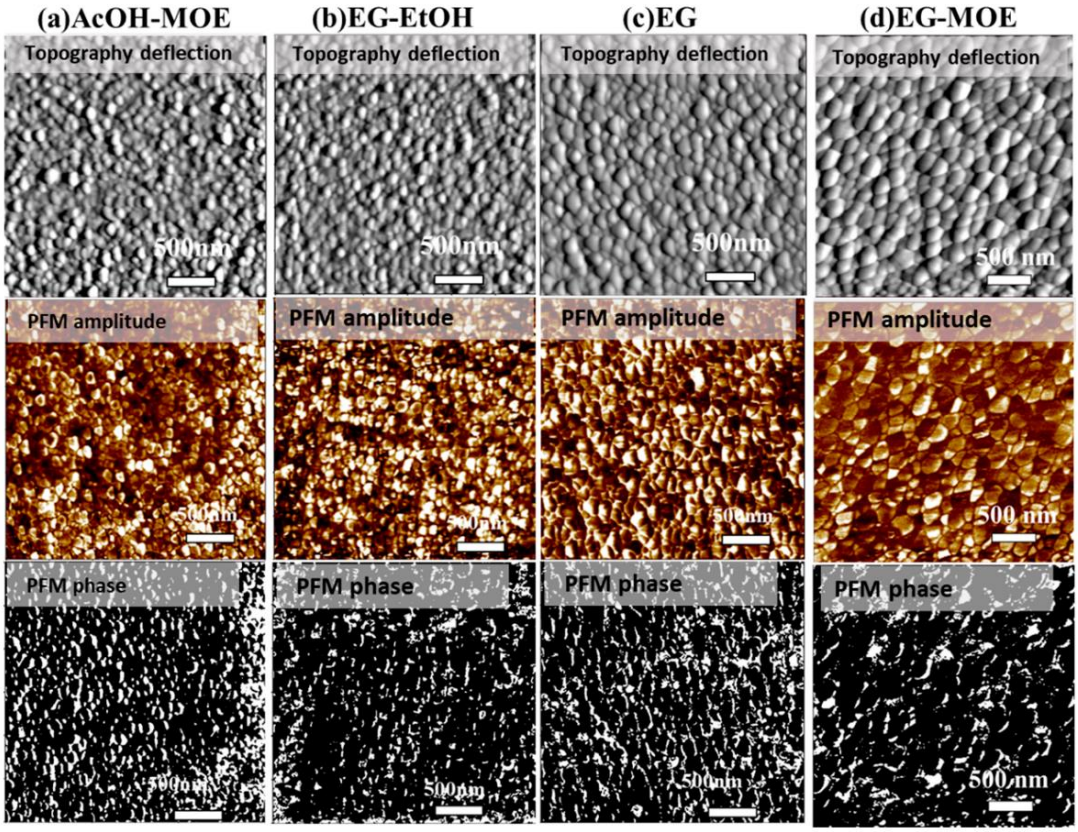

Figure S3. PFM analysis of BT films: Topography deflection, PFM amplitude, and phase images of (a) AcOH-MOE, (b) EG-EtOH, (c) EG, (d) EG-MOE films.

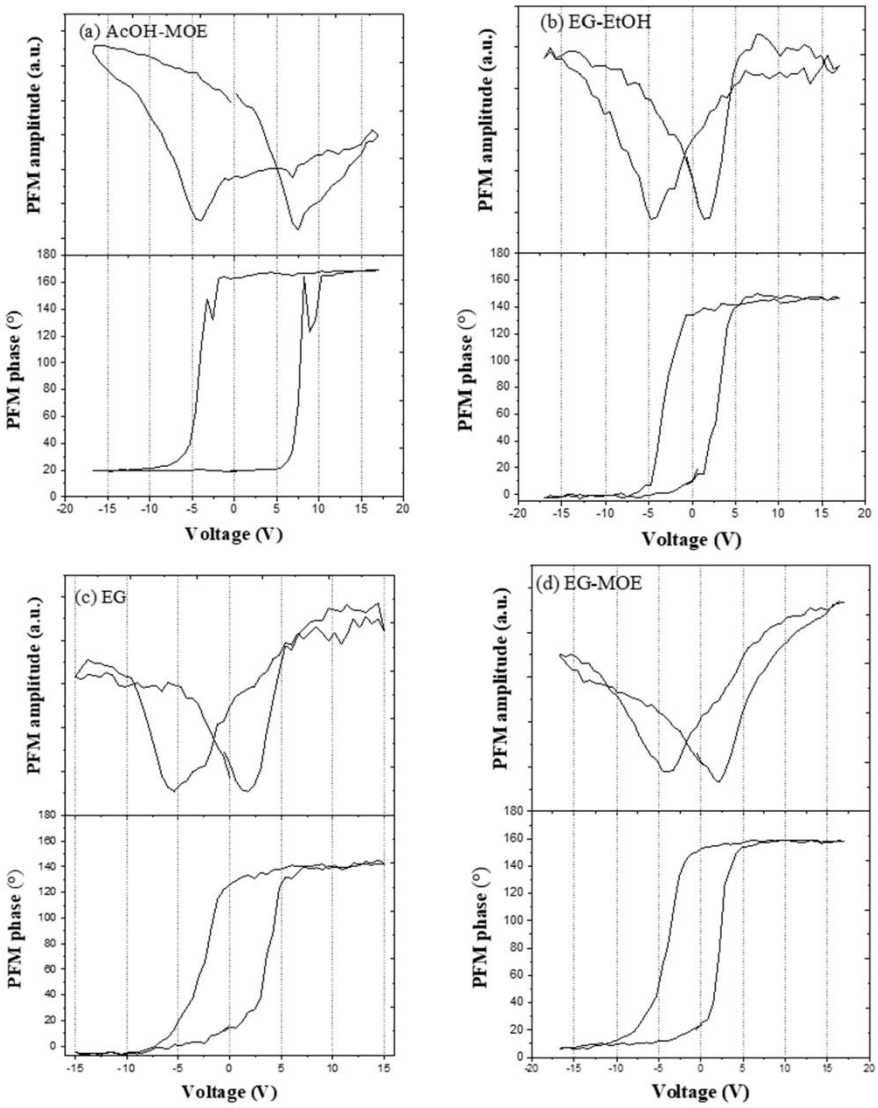

Figure S4. Local PFM amplitude and phase hysteresis loops of (a) AcOH-MOE, (b) EG-EtOH, (c) EG, (d) EG-MOE films.

Supplement S4. Conductive AFM (C-AFM)

Figure S5 shows the results of C-AFM analysis of 3 × 3 μm² area scans of AcOH-MOE and EG-EtOH films. As shown by the noise signal in Figure S5, no local electric current was detected in either sample. Therefore, the local current flowing through the samples was below ~1 pA, which is the detection limit of the C-AFM technique in ORCA mode [35].

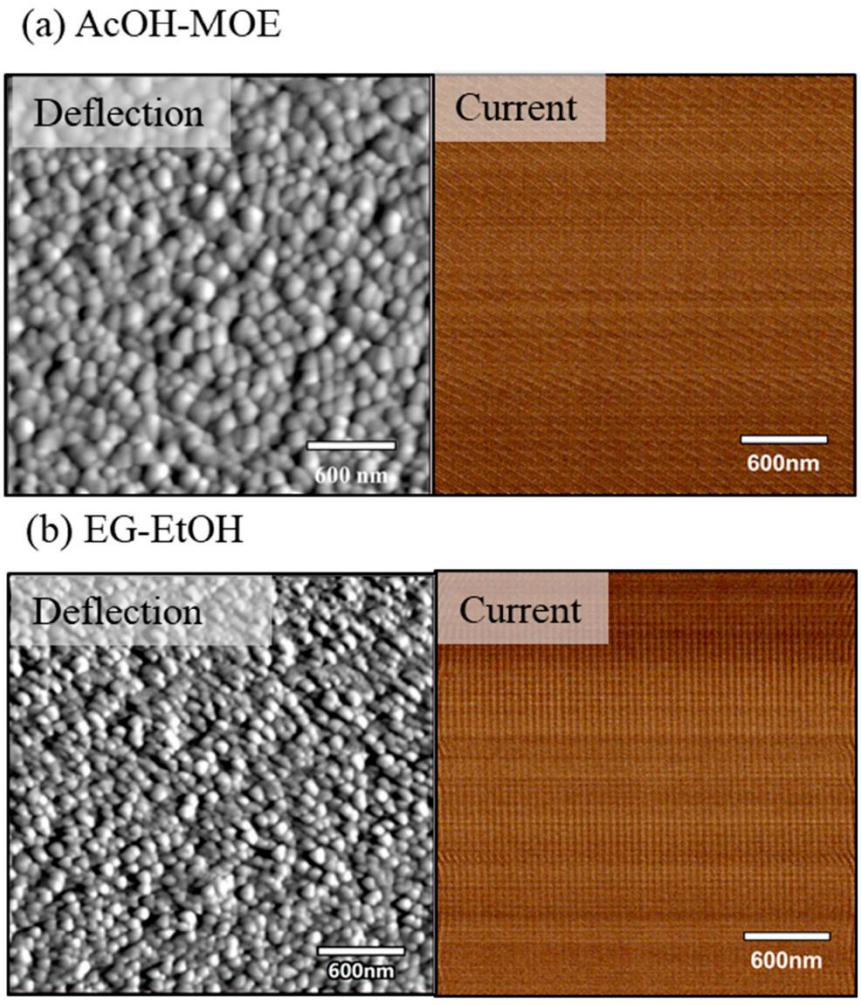

Figure S5. C-AFM analysis of (a) AcOH-MOE, (b) EG-EtOH films.

References

[35] ORCA - Conductive AFM, Asylum Research. Available at https://mundylab.umd.edu/wp-content/uploads/ORCASupportNote_rev1.pdf (accessed on 25 April 2022)

3.2. Designing the Thermal Processing of $Ba(Ti_{0.8}Zr_{0.2})O_3$ - $(Ba_{0.7}Ca_{0.3})TiO_3$ Thin Films from Ethylene Glycol-Derived Precursor

Lead-free $0.5Ba(Zr_{0.2}Ti_{0.8})O_3$-$0.5(Ba_{0.7}Ca_{0.3})TiO_3$ (BZT–BCT) bulk ceramic is one of the potential alternatives of $Pb(Zr,Ti)O_3$ (PZT) material for piezoelectric applications, especially at ambient-temperatures. Due to its good piezoelectric properties, BZT-BCT is intensively investigated for various applications, including micro- and nano-electromechanical systems, where the materials are used as thin films. However, the researchers have faced some challenges in the chemical solution deposition (CSD) of BZT-BCT thin films on platinized silicon substrates, including the porous and fine microstructure and the evolution of intergranular cracks. Consequently, these microstructural features hinder the functional properties of the films.

This article describes the design of the thermal processing, i.e., drying, pyrolysis and rapid thermal annealing, of BZT-BCT thin films on platinized silicon substrates using the ethylene glycol-based solution route introduced in our previous study (Chapter 3.1.). To gain insight into the chemical processes in the precursor upon heating, the xerogel was analyzed by simultaneous thermal analysis coupled with mass spectrometry. The carbon residues are decomposed at about 775 °C. Fourier Transform Infrared Spectroscopy (FTIR) and Time of Flight Secondary Ion Mass Spectrometry of the films reveal that prolonging the time of the drying step at 250 °C and pyrolysis at 350 °C from 2 minutes to 15 minutes and lowering the concentration of the coating solution from 0.2 M to 0.1 M contribute to more complete thermal oxidation of organic residues. Multistep annealed BZT-BCT films are deposited using the optimal processing conditions, i.e., 0.1 M coating solution and drying and pyrolysis times of 15 minutes, and have a columnar microstructure. Contrarily, the films deposited from a 0.2 M solution consist of fine equiaxed grains. Furthermore, depth profiling by X-ray photoelectron Spectroscopy confirms that the about 100 nm thick BZT-BCT film with columnar grains is chemically homogeneous over a large area of about 0.1 mm^2.

The results of this article reveal that by designing the thermal processing of BZT-BCT films and adequate dilution of the coating solution, chemically homogeneous BZT-BCT thin films with a dense columnar microstructure are prepared by CSD.

This paper addresses the first three aims and confirms the first three hypotheses of the Thesis.

Published in: S. W. Konsago, K. Žiberna, J. Ekar, J. Kovač, and B. Malič, "Designing the thermal processing of $Ba(Ti_{0.8}Zr_{0.2})O_3$ - $(Ba_{0.7}Ca_{0.3})TiO_3$ thin films from ethylene glycol-derived precursor" *Journal of Materials Chemistry C*, 12(36), 14658-14666, 2024. (IF = 5.7, 2023)

My contribution: I synthesized the BZT-BCT coating solutions and prepared the xerogels and thin films. I performed the XRD and FTIR analysis of BZT-BCT samples. I analysed the XRD and thermal analysis data. I prepared the paper concept jointly with my supervisor and wrote the manuscript with all co-authors.

3.2.Designing the Thermal Processing of $Ba(Ti_{0.8}Zr_{0.2})O_3$-$(Ba_{0.7}Ca_{0.3})TiO_3$ Thin Films from Ethylene Glycol-Derived Precursor

Journal of Materials Chemistry C

ROYAL SOCIETY OF CHEMISTRY

PAPER

View Article Online
View Journal | View Issue

Cite this: J. Mater. Chem. C, 2024, 12, 14658

Designing the thermal processing of $Ba(Ti_{0.8}Zr_{0.2})O_3$–$(Ba_{0.7}Ca_{0.3})TiO_3$ thin films from an ethylene glycol-derived precursor

Sabi William Konsago, *[ab] Katarina Žiberna,[ab] Jernej Ekar,[ab] Janez Kovač[ab] and Barbara Malič*[ab]

Received 14th June 2024,
Accepted 8th August 2024

DOI: 10.1039/d4tc02495h

rsc.li/materials-c

Lead-free ferroelectric $0.5Ba(Ti_{0.8}Zr_{0.2})O_3$–$0.5(Ba_{0.7}Ca_{0.3})TiO_3$ (BZT–BCT) thin films on platinized silicon substrates are prepared by a chemical solution deposition route. The solution chemistry involves the use of ethylene glycol and ethanol as solvents for alkaline earth acetates and transition metal alkoxides, respectively. The thermal decomposition of the BZT–BCT xerogel, the crystallization process of BZT–BCT thin films, and their homogeneity are investigated. In the xerogel, the decomposition of the organic residues occurs between 290 °C and 514 °C, followed by the formation of carbonate groups and their decomposition between 580 °C and 775 °C. In the thin films, the sequence of drying and pyrolysis steps, and the concentration of the coating solution influence the formation of carbonate groups and their decomposition upon annealing. Extending the drying and pyrolysis times from 2 minutes to 15 minutes and lowering the concentration of the coating solution from 0.2 M to 0.1 M contribute to an easier thermal decomposition of the carbon residues. Time-of-flight secondary ion mass spectrometry analysis reveals that upon rapid thermal annealing, the decomposition of the carbonate residues in a few tens of nanometres thick BZT–BCT film proceeds from the top downwards, resulting in a pure perovskite phase faster in the thinner films than in thicker ones. The about 100 nm thick BZT–BCT film annealed at 850 °C exhibits a columnar microstructure with a homogeneous distribution of elements across the thickness of the film.

Introduction

Barium zirconate titanate–barium calcium titanate ($Ba(Ti_{0.8}Zr_{0.2})O_3$–$(Ba_{0.7}Ca_{0.3})TiO_3$, BZT–BCT) with an approximately equimolar ratio of BZT to BCT has been recently intensively studied due to the discovery of its large piezoelectric response as a lead-free alternative to lead-based materials in applications.[1–4] The origin of the large piezoelectric response in this material has been essentially explained by its chemical composition and the multiphase coexistence.[1,5–8] A high polarization and a low coercive field, in addition to large piezoelectric coefficients, indicate the multifunctionality of BZT–BCT as an attractive material for potential piezoelectric and energy storage applications.[9] The design of actuators, sensors, transducers, *etc.* for nanoelectromechanical systems (NEMS) requires a small-scale size of the functional material where the materials are used in the thin film form.[10,11]

For the successful design of thin film microstructures and properties, especially using chemical solution deposition (CSD), which presents some advantages over physical vapor deposition methods, including low-cost investment, the control of stoichiometry, fast processing, and uniform surface coverage over large areas, it is critical to control the chemistry of the coating solution, and understand the thermal decomposition process of the deposited film and the film–substrate interaction upon heating. Such detailed studies of the decomposition process, crystallization, and distribution of elements in BZT–BCT thin films by CSD are still missing.

Barium titanate ($BaTiO_3$, BT) is the reference material for studying the processing and properties of BT-based compositions such as BZT–BCT. In CSD, following the conventional method using carboxylic acids, mainly acetic acid, and alcohols as solvents for barium carboxylates and titanium alkoxides, respectively,[12] the perovskite BT phase is formed through oxycarbonate intermediate phases, and temperatures above 650 °C are needed to decompose carbon residues.[12–14] The persistence of carbon residues in CSD-derived BT thin films, even at temperatures up to 1000 °C, has been reported.[15,16] Varying the solution chemistry and optimizing the processing conditions could contribute to lowering the decomposition temperatures of (oxy-)carbonate groups in BT-based films. We reported a new CSD route for BT thin films using

[a] Jožef Stefan Institute, Jamova cesta 39, 1000 Ljubljana, Slovenia. E-mail: sabi.william.konsago@ijs.si, barbara.malic@ijs.si
[b] Jožef Stefan International Postgraduate School, Jamova cesta 39, 1000 Ljubljana, Slovenia

ethylene glycol (EG) and ethanol (EtOH) as solvents, in which the carbonate decomposition is concluded at about 600 °C as evidenced by Fourier transform infrared (FTIR) spectroscopy.[17] Furthermore, the BT coating solution prepared using the combination of EG–EtOH solvents is stable for several months.

In the process of BZT–BCT film crystallization, in addition to barium oxycarbonate as an intermediate, we expect calcium oxycarbonate to form as well. Similar to barium carbonate, the decomposition of calcium carbonate requires high temperatures of 765–790 °C.[18,19] Zirconium alkoxides are more reactive than their titanium counterparts due to the lower electronegativity and larger coordination number of the former ion. The electronegativity values (Pauling scale) of titanium and zirconium are 1.54 and 1.33.[20,21] The coordination numbers of respective elements in *n*-alkoxides are 5 and 6, respectively,[22,23] and they could react with other constituents of the coating solution differently. Four cations in the solid solution make the control of the solution chemistry, crystallization, microstructure, and homogeneity of the BZT–BCT films very challenging.

The commonly reported microstructure of CSD-derived BZT–BCT thin films, prepared by the conventional carboxylic acid-based route with thicknesses of up to a few 100 nm consists of fine equiaxed grains with sizes of about 10 nm to a few 10 nm, intergranular pores and cracks.[24–26] In an attempt to control the microstructure of BZT–BCT films, barium metal, calcium nitrate, and transition metal alkoxides were introduced as reagents, but secondary phases in the films were reported.[27] It was speculated that the secondary calcium-zirconium-oxide phase is formed in a BZT–BCT film on a Si-substrate prepared by a conventional carboxylic acid-based CSD route and annealed at 800 °C due to the diffusion of Ca and Zr from the perovskite phase and their consequent reaction with oxygen.[28] Xu *et al.* observed a TiO_2 peak on the XRD pattern of the BZT–BCT film doped with 1 mol% Er^{3+}, with a fine granular microstructure and annealed at 800 °C.[29]

In our previous work, BZT–BCT films with a columnar microstructure with the preferred (111) perovskite orientation were achieved *via* CSD from a 0.1 M coating solution based on an EG–EtOH solvent combination and deposited on platinized silicon substrates using a multistep deposition/annealing process at 850 °C. Doping with manganese (1 mol%) significantly reduced the leakage current and enabled good ferroelectric and piezoelectric properties.[30]

In this work, the thermal processing of BZT–BCT thin films prepared using the above-mentioned solution chemistry is studied. The analysis of the thermal decomposition of the xerogel helped to determine the optimal temperatures of drying, pyrolysis, and annealing. The functional group decomposition and crystallization process in the films, the homogeneity, and distribution of elements across the thickness of selected BZT–BCT thin films are investigated.

Experimental

The $0.5Ba(Ti_{0.8}Zr_{0.2})O_3$–$0.5(Ba_{0.7}Ca_{0.3})TiO_3$ (BZT–BCT) precursor was prepared using barium acetate ($Ba(CH_3COO)_2$ with a purity of 99.97%, Sigma-Aldrich, St. Louis, Missouri, USA), calcium acetate ($Ca(CH_3COO)_2$, 99.999%, Alfa Aesar, Karlsruhe, Germany), titanium *n*-butoxide ($Ti(OC_4H_9)_4$, $Ti(OnBu)_4$), 99.61% and zirconium *n*-butoxide ($Zr(OC_4H_9)_4$ $Zr(OnBu)_4$), 80% both alkoxides purchased from Alfa Aesar, Karlsruhe, Germany are used as reagents. Ethylene glycol ($OHCH_2CH_2OH$, EG, 99.8%) and absolute ethanol (CH_3CH_2OH, EtOH 99.9%) both from Sigma-Aldrich, St. Louis, USA and stored in the dry box, were used to dissolve alkaline earth metal acetates and to dilute transition metal alkoxides, respectively. Both solutions were then mixed at room temperature for 2 hours, with the concentration adjusted to 0.2 M and 0.1 M. All manipulations of reagents were performed in a dry nitrogen atmosphere. The BZT–BCT solutions were stored at 4 °C. The coating solutions are stable for several months. For more details about the synthesis, please refer to our previous study.[30]

The BZT–BCT xerogel was prepared by drying the BZT–BCT solution at 200 °C for 12 h. A thermal analyzer coupled with a mass spectrometer (STA 409, Netzsch + ThermoStar, Balzers Instruments) was used to investigate the thermal decomposition of the gel. The thermogravimetric curve (TG), and the differential thermal analysis (DTA), and evolved gas analysis (EGA) were recorded from room temperature up to 1200 °C in 33.25 mg of BZT–BCT xerogel in a Pt/Rh crucible with a heating rate of 10 K min^{-1} in a flowing synthetic air atmosphere. The rest of the xerogel was calcined at 900 °C and X-ray diffraction (XRD) of the obtained powder was recorded using an X-ray diffractometer (Rigaku MiniFlex 600) with the following parameters: 2 theta = 20–60°, step = 0.034°, time per step = 100 s, soller slit = 0.02, mask10.

BZT–BCT films were deposited by spin coating 0.2 M and 0.1 M BZT–BCT solutions on $Pt(111)/TiO_2/SiO_2/Si(100)$ substrates (Pt/Si, purchased from SINTEF, Oslo, Norway) at 3000 rpm for 30 seconds. The as-deposited films were dried at 250 °C for 2 minutes or 15 minutes and pyrolyzed at 350 °C for 2 minutes or 15 minutes on hot plates. The pyrolysis step was followed by rapid thermal annealing (RTA) in the Mila 5000 furnace (Ulvac-Riko, Yokohama, Japan) at different temperatures with a heating rate of 13.3 °C s^{-1} between 500 °C and 800 °C with the hold-times of 6 seconds. The films consisting of one deposited layer were prepared to study the decomposition process of organics, the formation of carbonates, and their decomposition. For simplification, the following designation is used for these BZT–BCT films:

0.2M-2min: films deposited from the 0.2 M solution with 2 minutes of drying and pyrolysis;

0.2M-15min: films deposited from the 0.2 M solution with 15 minutes of drying and pyrolysis;

0.1M-15min: films deposited from the 0.1 M solution with 15 minutes of drying and pyrolysis.

Within the study of the microstructure and homogeneity, BZT–BCT films were prepared from the 0.2 M and 0.1 M coating solutions by repeating 4 and 10 times, respectively, the deposition/drying at 250 °C for 15 minutes/pyrolysis at 350 °C for 15 minutes/annealing at 600 °C, 700 °C, 800 °C and 850 °C with the same heating rate of 13.3 °C s^{-1}. The first and last layers

3.2.Designing the Thermal Processing of $Ba(Ti_{0.8}Zr_{0.2})O_3$-$(Ba_{0.7}Ca_{0.3})TiO_3$ Thin Films from Ethylene Glycol-Derived Precursor

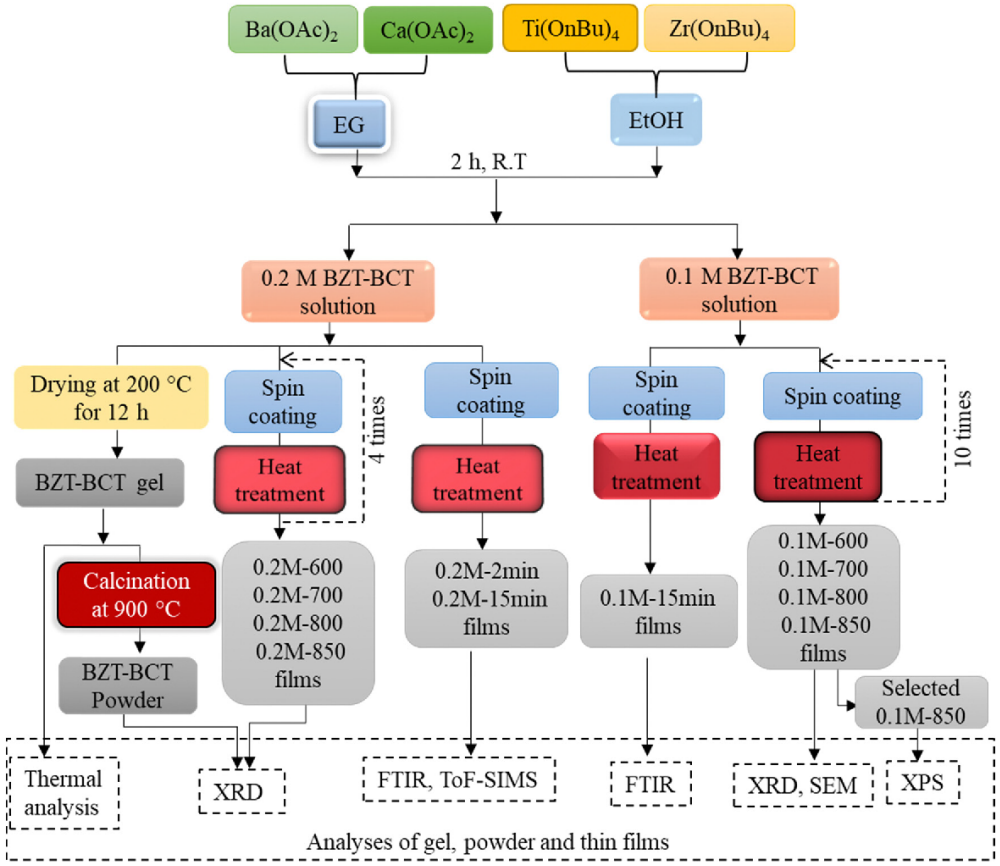

Fig. 1 Schematic description of BZT–BCT solution synthesis, the processing of the gel, powder, thin films and the analyses of the samples.

were annealed for 15 minutes, and the intermediate layers were annealed for 5 minutes at the corresponding temperatures. The films prepared from the 0.2 M and 0.1 M coating solutions are denoted as 0.2M-600, 0.2M-700, 0.2M-800, 0.2M-850, and 0.1M-600, 0.1M-700, 0.1M-800 and 0.1M-850.

One-layer films prepared at different temperatures were analyzed by attenuated total reflectance-Fourier transform infrared spectroscopy (PerkinElmer ATR-FTIR spectrum 100, 4000–380 cm^{-1}).

XRD of the BZT–BCT films were recorded on a high-resolution diffractometer (X'Pert PRO, PANalytical, Almelo, The Netherlands, Cu Kα radiation) using the following parameters: 2 theta = 10–39°, 40–65°, step = 0.034°, time per step = 100 s, soller slit = 0.02, mask10. The X'pert high score plus software for the phase analysis was used to analyze the XRD data.

The microstructure analyses of the films were performed on a field-emission scanning electron microscope (SEM) Verios 4G HP (Thermo Fischer, Waltham, Massachusetts, USA).

Time-of-flight secondary ion mass spectrometry (ToF-SIMS) dual-beam depth profiling was performed on the TOF-SIMS 5 instrument from IONTOF (Münster, Germany). Bi^+ ions were used for the analysis and Cs^+ ions for the depth profiling (crater etching). The energy of the Bi^+ ion beam was 30 keV and the current approximately 1.1 pA. The energy of the Cs^+ ions was 1 keV and the current between 64 and 66 nA. The information depth was around 2 nm and lateral resolution 5 μm. The secondary ions were detected over the *m/z* range from 0 to 800 in the negative polarity. The analytical scanning area was of the size of 100 μm × 100 μm in the center of the Cs-sputtering generated crater of the size of 400 μm × 400 μm. The pressure in the analytical chamber was in the range of 10^{-10} mbar.

The X-ray photoelectron spectroscopy (XPS) analyses were carried out on the PHI-TFA XPS spectrometer produced by Physical Electronics Inc. equipped with an Al-monochromatic source emitting photons at the energy of 1486.6 eV. The analyzed area was 0.4 mm in diameter. Quantification of surface composition was performed from XPS peak intensities taking into account relative sensitivity factors provided by the instrument manufacturer.[31] XPS depth profiling was performed *via* a 3 keV Ar^+ ion beam rastering over an area of 3 × 3 mm with an etching rate of 3.0 nm min^{-1} measured on a Ni/Cr multilayer of known thickness.

Fig. 1 summarizes the procedure for BZT–BCT solution synthesis, the processing of gel, powder, and thin films, and the analyses of individual samples.

Results and discussion

The thermal decomposition process of the BZT–BCT gel is analyzed by using TG-DTA coupled with EGA, and the results are shown in Fig. 2. A slight weight loss of about 1% from room temperature to about 200 °C observed in the TG curve is accompanied by a weak endothermic peak due to the evaporation of captured moisture by the gel. This evaporation is recorded in the EGA curve at about 100 °C. From 217 °C, we observe a progressive weight loss of 31% accompanied by a series of massive exothermic peaks at 290 °C, 316 °C, 410 °C and 514 °C. The weight loss of 12% is concluded upon heating from 514 °C to 775 °C, indicating the final decomposition of carbon residues. On the other hand, the evolution of gases in EGA curves shows two main characteristic steps in the decomposition: the first step consists of simultaneous detection of H_2O and CO_2, indicating the thermal oxidation of CH-groups from 217 °C to 514 °C, and the second step is the evolution of only CO_2 gas indicating the decomposition of carbonate groups in the interval 580 °C to 775 °C where the last CO_2 peak is recorded. For comparison, the thermal decompositions of 2-methoxyethanol-acetic acid- and 1-methoxy-2-propanol-acetic acid-based gels were concluded at about 150 °C and 246 °C higher temperatures, at 924 °C and 1021 °C, respectively.[32]

Fig. 3 shows the XRD pattern of the BZT–BCT xerogel calcined at 900 °C for 30 minutes demonstrating that the sample crystallizes in the perovskite phase. The result supports the thermal analysis data.

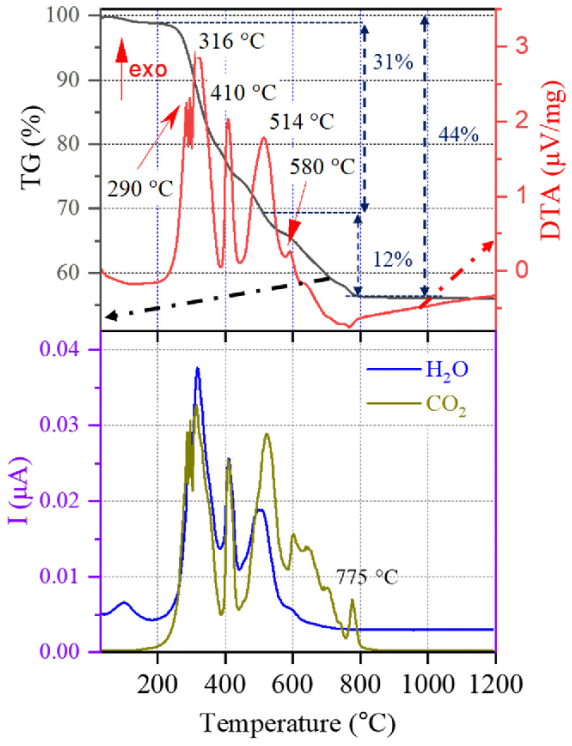

Fig. 2 Thermal decomposition of the BZT–BCT xerogel in synthetic air followed by TG, DTA and EGA (H_2O and CO_2). I: ion current.

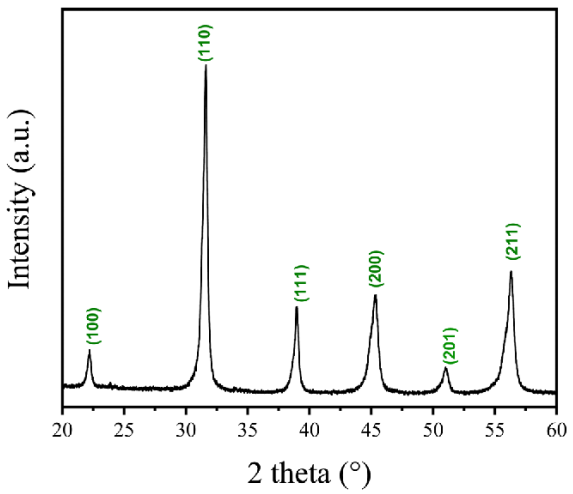

Fig. 3 XRD pattern of BZT–BCT xerogel calcined at 900 °C. The peaks are indexed according to PDF 01-074-4539 (BT cubic phase).

The FTIR spectra of 0.2M-2min and 0.2M-15min films were recorded after the pyrolysis and RTA steps at 500 °C, 600 °C, 700 °C, 750 °C and 800 °C and are shown in Fig. 4(a) and (b), respectively. The thickness of such one-layer films is estimated to be a few tens of nanometers. In 0.2M-2min and 0.2M-15min films heated at 350 °C and at 500 °C, the acetate groups are identified by the absorption bands at about 1428 cm ^{1} and 1571 cm ^{1} for (COO) symmetric and (COO) asymmetric stretching vibrations. The obvious band of the carbonate groups is recorded at 1446 cm ^{1} in both films upon heating to 600 °C which agrees with the EGA data (*cf.* Fig. 2). At 750 °C, the carbonate groups are almost fully decomposed in the 0.2M-15min film while their presence is evident in the 0.2M-2min film. In both films, the metal–oxygen (M–O) band is evident at/above 750 °C. This reveals that the drying and pyrolysis times influence the decomposition process of organic residues and could affect the microstructure.

Fig. 5 shows the time-of-flight secondary ion mass spectrometry (ToF-SIMS) analysis of 0.2M-2min and 0.2M-15min films annealed at 500 °C, 600 °C and 750 °C. The detection of carbonate ions during the sputtering reveals that up to 500 °C, there is almost no formation of carbonates in both 0.2M-2min and 0.2M-15min films, see Fig. 5(a) and (d). Note that the signals at the beginning of sputtering are due to the contamination of the sample surface. At 600 °C a significant amount of carbonate ions is identified. Although the analysis is not quantitative, the same secondary ions can be compared between each other since we have very similar composition of the samples. From the intensity ratios of carbonate CO_3 ions to the intensity of BaO_2 ions, it is obvious that the 0.2M-2min film contains more carbonaceous residues than the 0.2M-15min film at the same temperature; compare Fig. 5(b) and (e). This difference is attributed to insufficient drying and pyrolysis times

3.2.Designing the Thermal Processing of $Ba(Ti_{0.8}Zr_{0.2})O_3$-$(Ba_{0.7}Ca_{0.3})TiO_3$ Thin Films from Ethylene Glycol-Derived Precursor

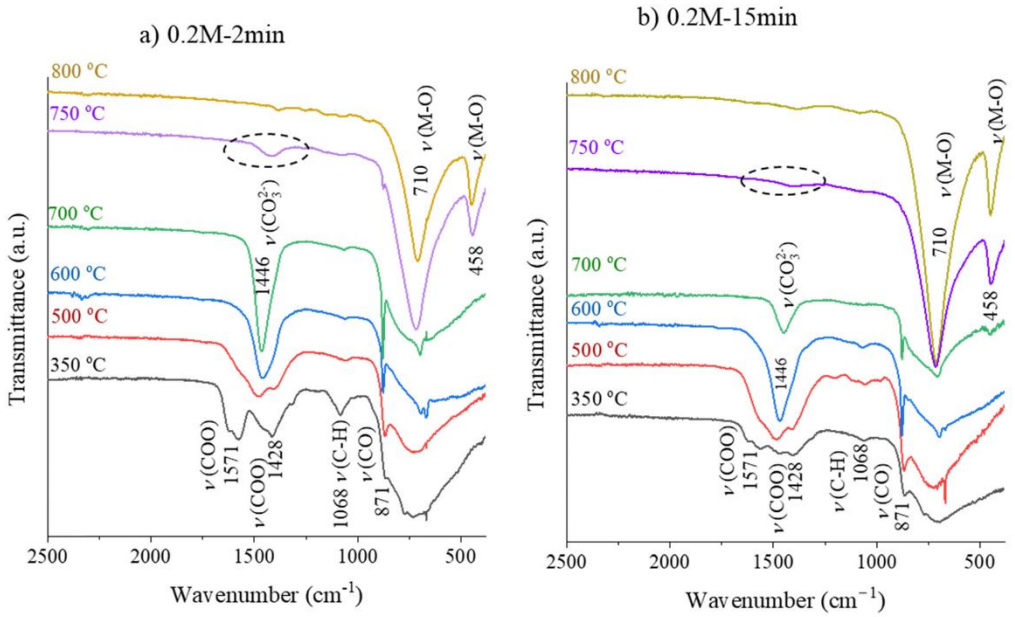

Fig. 4 FTIR spectra of the (a) 0.2M-2min and (b) 0.2M-15min films heated at different temperatures for 6 seconds.

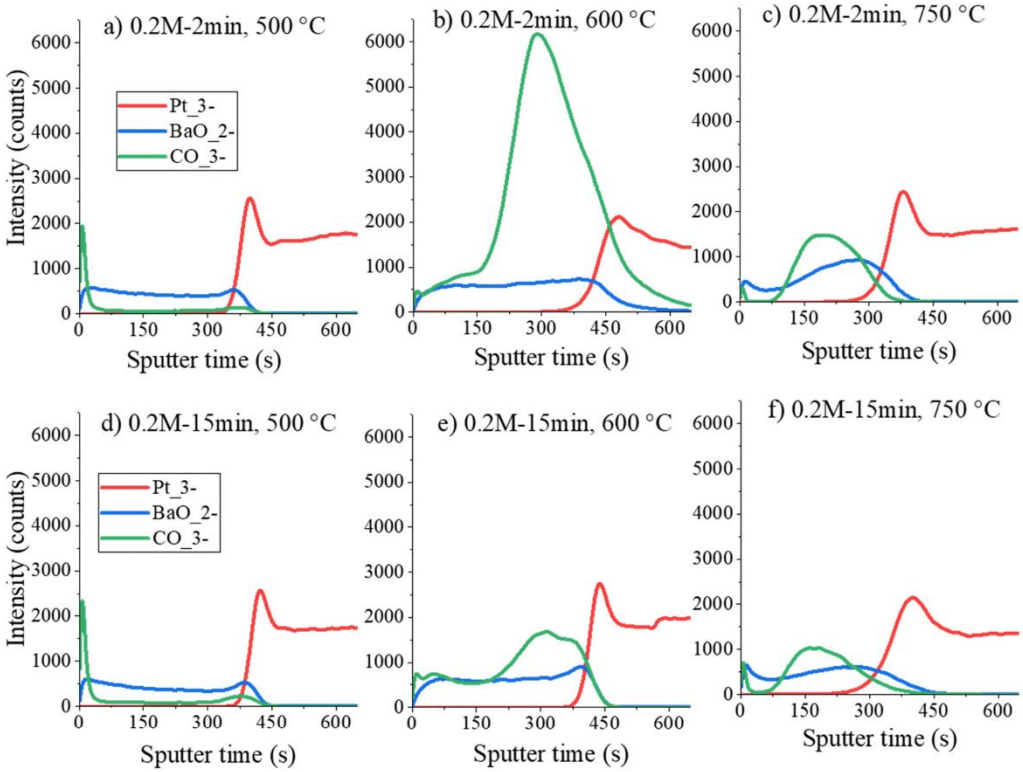

Fig. 5 ToF-SIMS depth profiles of (a)–(c) 0.2M-2min films and (d)–(f) 0.2M-15min films heated at 500 °C, 600 °C and 750 °C.

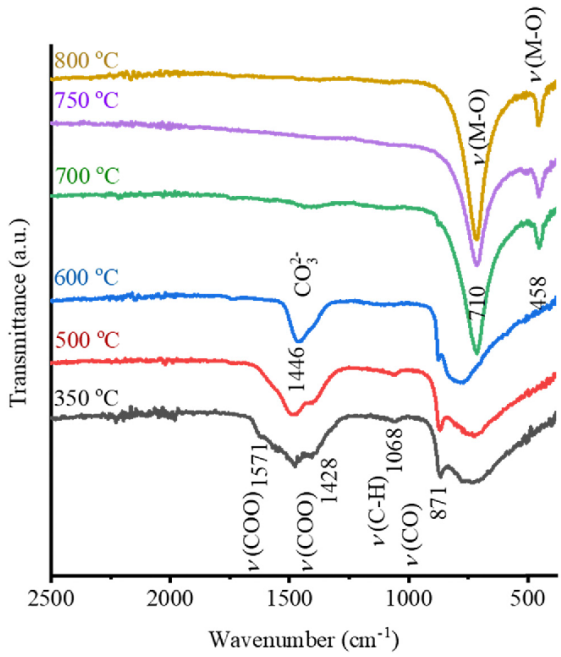

Fig. 6 FTIR spectra of 0.1M-15min film annealed at different temperatures for 6 seconds.

to oxidize the major carbon residues. In both cases, the ToF-SIMS analysis agrees with the FTIR and thermal analysis results that the carbonates are predominantly formed upon annealing at 600 °C. Upon annealing at 750 °C, up to the depth of approximately 5 nm (0 to 60 seconds of sputtering in Fig. 5(c) and (f)), some carbonate species are still present deeper in the film. This suggests that upon heating in an RTA furnace, the carbonates are decomposed starting from the top of the films, leading to the inference that the thinner the film is, the faster the carbonate groups will be decomposed. The broadening of the interfaces between the films and the Pt-layer (curves for BaO_2/Pt_3) in the SIMS depth profiles in Fig. 5 is due to an artifact related to the ion bombardment during SIMS depth profiling.

The concentration of the BZT–BCT coating solution was found to influence the films' microstructure. When processed at the same drying/pyrolysis/annealing conditions, the BZT–BCT films deposited from 0.2 M or 0.1 M solutions have granular or columnar microstructures, respectively.[28] We used FTIR to follow the thermal decomposition of the 0.1M-15min films to see if there was any difference in the thermal decomposition pathways of the films prepared from 0.1 M and 0.2 M solutions.

The FTIR spectra of the 0.1M-15min films are shown in Fig. 6. The band of the carbonate groups is present in the film annealed at 600 °C while it almost disappears in the film annealed at 700 °C. In this latter spectrum the M–O bands at 710 cm^{-1} and 458 cm^{-1} are recorded, indicating the oxide formation. Note that in the case of 0.2M-15min films, such a FTIR spectrum is observed only upon annealing at 750 °C, as shown in Fig. 4b. The influence of the concentration of the coating solution on the thin film crystallization is not surprising since it has been reported that by decreasing the coating solution concentration and thus reducing the individual layer thickness, columnar grains can be achieved in BT, $SrTiO_3$, and (Ba, Sr)TiO_3 films.[33–36]

By repeating the spin-coating 0.2 M or 0.1 M solutions, drying, pyrolysis and RTA steps 4 or 10 times, we prepared the films at the final temperatures of 600, 700, 800 and 850 °C. The phase composition of respective films is shown in Fig. 7.

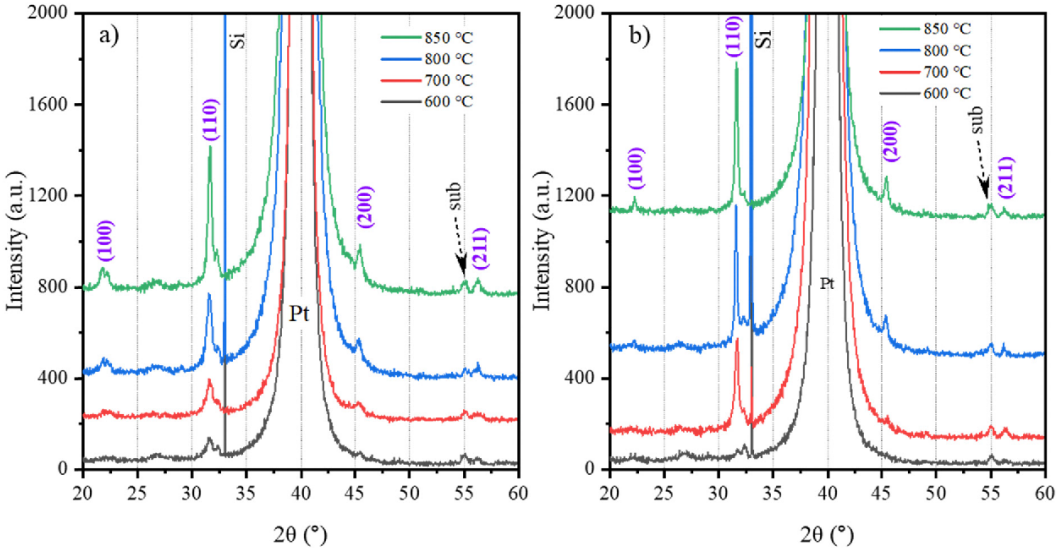

Fig. 7 XRD patterns of (a) 0.2M-600, 0.2M-700, 0.2M-800, and 0.1M-850 thin films and (b) 0.1M-600, 0.1M-700, 0.1M-800, and 0.1M-850 thin films.

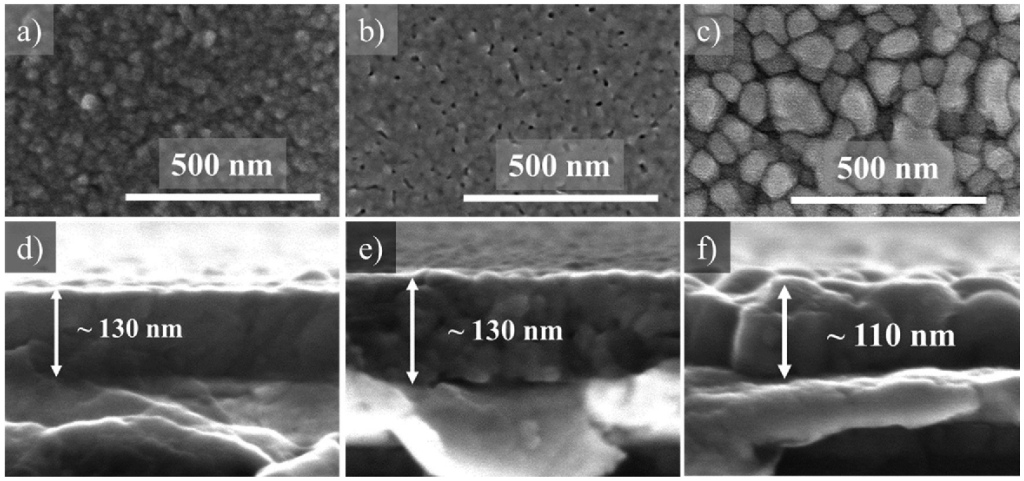

Fig. 8 SEM (a)–(c) plan view micrographs of 0.1M-700, 0.1M-800 and 0.1M-850 films and (d)–(f) their respective cross-sections.

In both 0.2M-600 and 0.1M-600 films, weak {110} and {211} peaks are observed, indicating the onset of crystallization. With increasing temperature, the intensity of the {110} peak increases, indicating that a higher crystallinity and also lower-intensity perovskite reflections emerge. Note that the perovskite {111} peak cannot be distinguished as it coincides with the Pt{111} peak. The intensity of the perovskite peaks in 0.1M-700, 0.1M-800, and 0.1M-850 films is stronger compared to the 0.2M-700, 0.2M-800, and 0.2M-850 films indicating higher crystallinity in the former group.

In our previous study, we prepared BZT–BCT films from the 0.2 M solution and annealed them at 800, 850, and 900 °C. All films had porous microstructures consisting of fine equiaxed grains.[30] We analyzed the microstructure of 0.1M-700, 0.1M-800, and 0.1M-850 thin films by using scanning electron microscopy, see Fig. 8. The surface microstructures of the films annealed at 700 °C and 800 °C are porous with fine grains of a few 10 nm. The film thickness is about 130 nm. The surface microstructure of the film annealed at 850 °C is dense, with grains ranging from 60 to 100 nm. The cross-section micrograph reveals columnar grains extending through the film thickness. The film thickness is about 110 nm, indicating densification at this temperature.

We selected 0.1M-850 films to investigate the distribution of the elements using XPS depth profiling across the area with a diameter of 400 μm. The spectrum shown in Fig. 9 reveals that

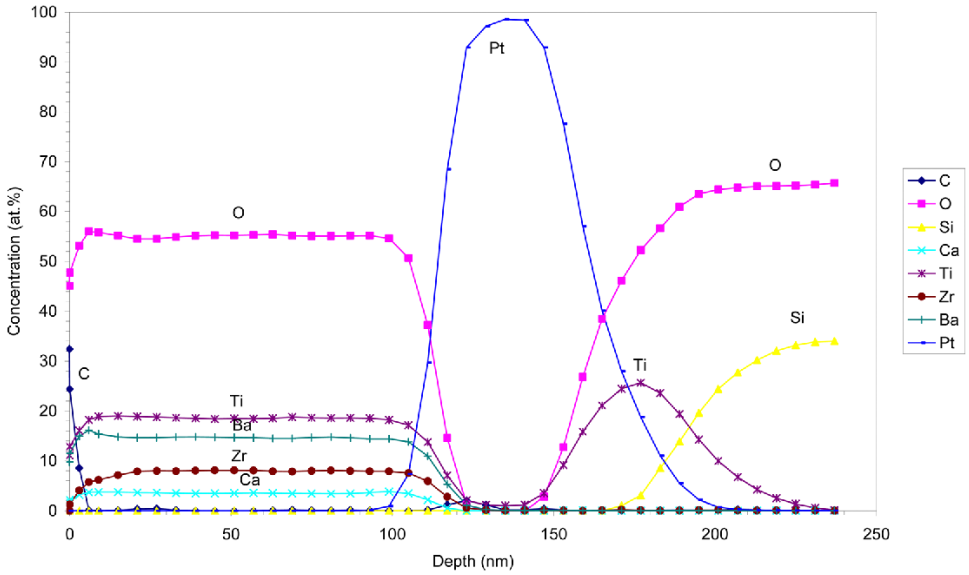

Fig. 9 XPS depth profile of the 0.1M-850 film.

View Article Online
Paper Journal of Materials Chemistry C

the film consists of Ba, Ca, Ti, Zr, and O with a thickness of about 110 nm. The film's surface is covered with a carbon-rich layer of 2 nm, probably due to contamination. The distribution of the elements throughout the film thickness is uniform. This indicates that the crystallization from the amorphous phase within each deposited BZT–BCT layer occurs without any change in chemical composition or segregation, as is the case in the crystallization of PZT thin films.[37] The interface with the $Pt/TiO_2/SiO_2$ substrate is sharp, indicating that there is no chemical interaction between the film and the substrate.

We note that in our previous study, the manganese-doped BZT–BCT film annealed at 850 °C with a columnar microstructure was analyzed by using scanning transmission electron microscopy (STEM) and energy dispersive X-ray spectroscopy (EDS). A homogeneous distribution of elements within one columnar grain across the film thickness was observed. Mn-dopant was added to BZT–BCT to reduce the leakage current, and its addition did not influence the crystallization and microstructure.[30] The results of STEM-EDS analysis are in a very good agreement with the XPS analysis, confirming that chemical homogeneity in the BZT–BCT films is achieved not only within individual grains but also across the area of about 0.1 mm^2.

Conclusions

The thermal processing of $0.5Ba(Ti_{0.8}Zr_{0.2})O_3$–$0.5(Ba_{0.7}Ca_{0.3})TiO_3$ (BZT–BCT) thin films from ethylene glycol-based precursor solution and the homogeneity of the crystalline films on a platinized silicon substrate were studied. Prolonging the drying and pyrolysis times from 2 minutes to 15 minutes of the one-layer films deposited from a 0.2 M solution contributes to the completion of the thermal decomposition of carbon residues at a lower temperature. By decreasing the concentration of the coating solution from 0.2 M to 0.1 M, or in other words, by reducing the deposited layer thickness to about 10 nm, the thermal decomposition of carbonate groups is significantly downshifted. Both approaches, extended drying and pyrolysis times and reducing the coating solution concentration, contribute to the perovskite crystallization at about 700 °C. Still, to obtain a dense columnar microstructure of BZT–BCT films, multi-step annealing at 850 °C was needed. Depth profiling revealed a homogeneous distribution of constituent elements across the thickness of the film. Our results show that processing optimization in the microstructure engineering of BZT–BCT thin films is key to optimizing their functional properties.

Author contributions

Conceptualization, S. W. K. and B. M.; methodology, B. M., S. W. K.: chemical solution deposition of thin films, FTIR analysis, XRD analysis, S. W. K.; thermal analysis, S. W. K., B. M.; SEM: K. Ž.; ToF-SIMS, XPS: J. E., J. K.; resources, B. M.; writing – original draft preparation, S. W. K. and B. M.; writing – review and editing, all authors; supervision, B. M.; funding acquisition, B. M., and J. K. All authors have read and agreed to the published version of the manuscript.

Data availability

No primary research results, software or code have been included and no new data were generated or analysed as part of this article.

Conflicts of interest

There are no conflicts to declare.

Acknowledgements

We thank Jana Cilenšek for performing the thermal analysis of xerogels. The authors acknowledge the financial support from the Slovenian Research and Innovation Agency (core funding P2-0105 and P2-0082, S. W. K., K. Ž., and J. E.: national postgraduate research funding).

References

1 W. Liu and X. Ren, Large piezoelectric effect in Pb-free ceramics, *Phys. Rev. Lett.*, 2009, **103**(25), 257602, DOI: 10.1103/PhysRevLett.103.257602.
2 M. Acosta, N. Novak, G. A. Rossetti and J. Rödel, Mechanisms of electromechanical response in $(1-x)$ $Ba(Zr_{0.2}Ti_{0.8})O_3$ $x(Ba_{0.7}Ca_{0.3})TiO_3$ ceramics, *Appl. Phys. Lett.*, 2015, **107**(14), 142906, DOI: 10.1063/1.4932654.
3 J. Gao, D. Xue, W. Liu, C. Zhou and X. Ren, Recent progress on $BaTiO_3$-based piezoelectric ceramics for actuator applications, *Actuators*, 2017, **6**(3), 24, DOI: 10.3390/act6030024.
4 J. Rödel, K. G. Webber, R. Dittmer, W. Jo, M. Kimura and D. Damjanovic, Transferring lead-free piezoelectric ceramics into application, *J. Eur. Ceram. Soc.*, 2015, **35**(6), 1659–1681, DOI: 10.1016/j.jeurceramsoc.2014.12.013.
5 D. S. Keeble, F. Benabdallah, P. A. Thomas, M. Maglione and J. Kreisel, Revised structural phase diagram of $(Ba_{0.7}Ca_{0.3}TiO_3)$–$(BaZr_{0.2}Ti_{0.8}O_3)$, *Appl. Phys. Lett.*, 2013, **102**(9), 092903, DOI: 10.1063/1.4793400.
6 J. Gao, X. Ke, M. Acosta, J. Glaum and X. Ren, High piezoelectricity by multiphase coexisting point: Barium titanate derivatives, *MRS Bull.*, 2018, **43**(8), 595–599, DOI: 10.1557/mrs.2018.155.
7 M. C. Ehmke, S. N. Ehrlich, J. E. Blendell and K. J. Bowman, Phase coexistence and ferroelastic texture in high strain $(1-x)$ Ba $(Zr_{0.2}Ti_{0.8})O_3$ $x(Ba_{0.7}Ca_{0.3})TiO_3$ piezoceramics, *J. Appl. Phys.*, 2012, **111**(12), 124110, DOI: 10.1063/1.4730342.
8 L. Zhang, M. Zhang, L. Wang, C. Zhou, Z. Zhang, Y. Yao and X. Ren, Phase transitions and the piezoelectricity around morphotropic phase boundary in $Ba(Zr_{0.2}Ti_{0.8})O_3$ $x(Ba_{0.7}Ca_{0.3})TiO_3$ lead-free solid solution, *Appl. Phys. Lett.*, 2014, **105**(16), 162908, DOI: 10.1063/1.4899125.
9 M. Maraj, W. Wei, B. Peng and W. Sun, Dielectric and energy storage properties of $Ba(1-x)Ca_xZr_yTi_{(1\ y)}O_3$ (BCZT): a review, *Materials*, 2019, **12**(21), 3641, DOI: 10.3390/ma12213641.

10 C.-B. Eom and S. Trolier-McKinstry, Thin-film piezoelectric MEMS, *MRS Bull.*, 2012, **37**(11), 1007–1017, DOI: **10.1557/mrs.2012.273**.

11 K. L. Ekinci and M. L. Roukes, Nanoelectromechanical systems, *Rev. Sci. Instrum.*, 2005, **76**(6), 061101, DOI: **10.1063/1.1927327**.

12 U. Hasenkox, S. Hoffmann and R. Waser, Influence of precursor chemistry on the formation of $MTiO_3$ (M= Ba, Sr) ceramic thin films, *J. Sol-Gel Sci. Technol.*, 1998, **12**, 67–79, DOI: **10.1023/A:1026480027046**.

13 H. S. Gopalakrishnamurthy, M. S. Rao and T. N. Kutty, Thermal decomposition of titanyl oxalates I: Barium titanyl oxalate, *J. Inorg. Nucl. Chem.*, 1975, **37**(4), 891–898, DOI: **10.1016/0022-1902(75)80668-3**.

14 O. A. Harizanov, Formation and crystallization of an acetate-acetylacetonate derived sol–gel $BaTiO_3$, *Mater. Lett.*, 1998, **34**(3–6), 345–350, DOI: **10.1016/S0167-577X(97)00199-7**.

15 S. M. Aygün, P. Daniels, W. J. Borland and J. P. Maria, In situ methods to explore microstructure evolution in chemically derived oxide thin films, *J. Mater. Res.*, 2010, **25**(3), 427–436.

16 T. Dechakupt, G. Yang, C. A. Randall, S. Trolier-McKinstry and I. M. Reaney, Chemical Solution-Deposited BaTiO3 Thin Films on Ni Foils: Microstructure and Interfaces, *J. Am. Ceram. Soc.*, 2008, **91**(6), 1845–1850, DOI: **10.1111/j.1551-2916.2008.02407.x**.

17 S. W. Konsago, K. Žiberna, B. Kmet, A. Benčan, H. Uršič and B. Malič, Chemical Solution Deposition of Barium Titanate Thin Films with Ethylene Glycol as Solvent for Barium Acetate, *Molecules*, 2022, **27**(12), 3753, DOI: **10.3390/molecules27123753**.

18 M. Bilton, A. P. Brown and S. J. Milne, Investigating the optimum conditions for the formation of calcium oxide, used for CO_2 sequestration, by thermal decomposition of calcium acetate, *J. Phys.: Conf. Ser.*, 2012, **371**(1), 012075, DOI: **10.1088/1742-6596/371/1/012075**.

19 K. S. Karunadasa, C. H. Manoratne, H. M. T. G. A. Pitawala and R. M. G. Rajapakse, Thermal decomposition of calcium carbonate (calcite polymorph) as examined by *in situ* high-temperature X-ray powder diffraction, *J. Phys. Chem. Solids*, 2019, **134**, 21–28, DOI: **10.1016/j.jpcs.2019.05.023**.

20 D. Van den Eynden, R. Pokratath and J. De Roo, Nonaqueous Chemistry of Group 4 Oxo Clusters and Colloidal Metal Oxide Nanocrystals, *Chem. Rev.*, 2022, **122**(11), 10538–10572, DOI: **10.1021/acs.chemrev.1c01008**.

21 C. J. Brinker and G. W. Scherer, *Sol-gel science: the physics and chemistry of sol-gel processing*, Academic Press, San Diego, 1990, pp. 52–59.

22 F. Babonneau, S. Doeuff, A. Leaustic, C. Sanchez, C. Cartier and M. Verdaguer, XANES and EXAFS study of titanium alkoxides, *Inorg. Chem.*, 1988, **27**(18), 3166–3172, DOI: **10.1021/ic00291a024**.

23 D. Peter, T. S. Ertel and H. Bertagnolli, EXAFS study of zirconium alkoxides as precursor in the sol-gel process: I. Structure investigation of the pure alkoxides, *J. Sol-Gel Sci. Technol.*, 1994, **3**, 91–99, DOI: **10.1007/BF00486715**.

24 H. Wang, J. Xu, C. Ma, F. Xu, L. Wang, L. Bian and A. Chang, Spectroscopic ellipsometry study of $0.5BaZr_{0.2}Ti_{0.8}O_3$ – $0.5Ba_{0.7}Ca_{0.3}TiO_3$ ferroelectric thin films, *J. Alloys Compd.*, 2014, **615**, 526–530, DOI: **10.1016/j.jallcom.2014.06.186**.

25 P. S. Barbato, V. Casuscelli, P. Aprea, R. Scaldaferri and D. Caputo, Optimization of the production process of BZT–BCT sol–gel thin films obtained from a highly stable and green precursor solution, *Mater. Manuf. Processes*, 2021, **36**(14), 1642–1649, DOI: **10.1080/10426914.2021.1926495**.

26 Z. Wang, Z. Cai, H. Wang, Z. Cheng, J. Chen, X. Guo and H. Kimura, Lead-free $0.5Ba(Ti_{0.8}Zr_{0.2})O_3$ – $0.5(Ba_{0.7}Ca_{0.3})TiO_3$ thin films with enhanced electric properties fabricated from optimized sol-gel systems, *Mater. Chem. Phys.*, 2017, **186**, 528–533, DOI: **10.1016/j.matchemphys.2016.11.030**.

27 G. Kang, K. Yao and J. Wang, $(1-x)$ $Ba(Zr_{0.2}Ti_{0.8})O_{3-x}$ $(Ba_{0.7}Ca_{0.3})TiO_3$ Ferroelectric Thin Films Prepared from Chemical Solutions, *J. Am. Ceram. Soc.*, 2012, **95**(3), 986–991, DOI: **10.1111/j.1551-2916.2011.04877.x**.

28 Z. L. Cai, Z. M. Wang, H. H. Wang, Z. X. Cheng, B. W. Li, X. L. Guo and A. Kasahara, An Investigation of the Nanomechanical Properties of 0.5 $Ba(Ti_{0.8}Zr_{0.2})O_{3-0.5}$ $(Ba_{0.7}Ca_{0.3})TiO_3$ Thin Films, *J. Am. Ceram. Soc.*, 2015, **98**(1), 114–118, DOI: **10.1111/jace.13228**.

29 J. Xu, Y. Zhou, Z. Li, C. Lin, X. Zheng, T. Lin and F. Wang, Microstructural, ferroelectric and photoluminescence properties of Er^{3+}-doped $Ba_{0.85}Ca_{0.15}Ti_{0.9}Zr_{0.1}O_3$ thin films, *Mater. Chem. Phys.*, 2021, **262**, 124320, DOI: **10.1016/j.matchemphys.2021.124320**.

30 S. W. Konsago, K. Žiberna, A. Matavž, B. Mandal, S. Glinšek, Y. Fleming, A. Benčan, L. G. Brennecka, H. Uršič and B. Malič, Engineering the Microstructure and Functional Properties of $0.5Ba(Zr_{0.2}Ti_{0.8})O_3$ – $0.5(Ba_{0.7}Ca_{0.3})TiO_3$ Thin Films, *ACS Appl. Electron. Mater.*, 2024, **6**(6), 4467–4477, DOI: **10.1021/acsaelm.4c00530**.

31 F. J. Moulder, W. F. Stickle, P. E. Sobol and K. D. Bomben, *X-ray photoelectron spectroscopy: A reference book of standard spectra for identification and interpretation of XPS data*, Physical Electronics Division, PerkinElmer Corporation, Eden Prairie, Minnesota, 1992.

32 P. S. Barbatoa, V. Casuscellib, P. Apreaa, R. Scaldaferrib, I. Pedacib and D. Caputoa, Green production of lead-free bzt-bct thin films for applications in mems devices, *Chem. Eng. Trans.*, 2021, **84**, 97–102, DOI: **10.3303/CET2184017**.

33 S. Hoffmann, U. Hasenkox, R. Waser, C. L. Jia and K. Urban, Chemical Solution Deposited $BaTiO_3$ and $SrTiO_3$ Thin Films with Columnar Microstructure, *MRS Online Proc. Libr.*, 1997, **474**, 9, DOI: **10.1557/PROC-474-9**.

34 S. Hoffmann and R. Waser, Control of the morphology of CSD-prepared $(Ba,Sr)TiO_3$ thin films, *J. Eur. Ceram. Soc.*, 1999, **19**(6–7), 1339–1343, DOI: **10.1016/S0955-2219(98)00430-0**.

35 C. Mansour, M. Benwadih and C. Revenant, Sol–gel derived barium strontium titanate thin films using a highly diluted precursor solution, *AIP Adv.*, 2021, **11**(8), 085302, DOI: **10.1063/5.0055584**.

36 J. F. Ihlefeld, A. M. Vodnick, S. P. Baker, W. J. Borland and J. P. Maria, Extrinsic scaling effects on the dielectric response of ferroelectric thin films, *J. Appl. Phys.*, 2008, **103**(7), 074112, DOI: **10.1063/1.2903211**.

37 F. Calame and P. Muralt, Growth and properties of gradient free sol-gel lead zirconate titanate thin films, *Appl. Phys. Lett.*, 2007, **90**(6), 062907, DOI: **10.1063/1.2472529**.

3.3. Engineering the Microstructure and Functional Properties of $0.5Ba(Zr_{0.2}Ti_{0.8})O_3$-$0.5(Ba_{0.7}Ca_{0.3})TiO_3$ Thin Films

Lead-free $0.5Ba(Zr_{0.2}Ti_{0.8})O_3$-$0.5(Ba_{0.7}Ca_{0.3})TiO_3$ (BZT–BCT) bulk ceramic exhibits piezoelectric properties comparable to those of $Pb(Zr,Ti)O_3$ (PZT) close to room temperature. However, frequently encountered microstructural features of BZT-BCT thin films prepared by chemical solution deposition (CSD), including porous and fine microstructures and intergranular cracks, contribute to poor functional properties of the films.

The article describes the design of the BZT-BCT thin film microstructure from granular, i.e., consisting of fine equiaxed grains, to columnar. Grazing-angle XRD and scanning transmission electron microscopy analyses confirm the preferential (111) orientation of the perovskite phase and orientational correspondence with the (111) Pt deposited on top of the silicon substrate, indicating that it serves as the nucleation layer. Such orientational correspondence has not been previously reported for $BaTiO_3$ or BZT-BCT films.

The dielectric permittivity of the BZT-BCT film with the columnar microstructure is about twice that of the film with the granular microstructure, which is in agreement with the dielectric grain-size effect. Manganese doping (1 mol %) increases the room-temperature permittivity and reduces the leakage current. Thin films exhibit high energy storage density and efficiency with an almost fatigue-free response after 2 million cycles at 800 kV/cm. The macroscopic piezoelectric response of BZT-BCT thin films is measured for the first time using double-beam laser interferometry.

Our results reveal that by designing the microstructure of BZT-BCT films and adequate doping, functional properties, such as low- and high-field dielectric properties and energy storage, are improved.

The results of this article confirm hypotheses 2, 3, 4, and 5; and address aims 2, 3, and 4.

Published in: S. W. Konsago, K. Žiberna, A. Matavž, B. Mandal, S. Glinšek, Y. Fleming, A. Benčan, G. L. Brennecka, H. Uršič, and B. Malič, "Engineering the Microstructure and Functional Properties of $0.5Ba(Zr_{0.2}Ti_{0.8})O_3$-$0.5(Ba_{0.7}Ca_{0.3})TiO_3$ Thin Films", *ACS Applied Electronic Materials*, Vol 6, Issue 6, pp. 4467 – 4477, 2024 (IF = 4.3, 2023)

My contribution: I synthesized the BZT-BCT coating solutions, and prepared the BZT-BCT films. I performed the XRD data analysis and conducted AFM and PFM analyses. I measured dielectric, ferroelectric, energy storage and leakage current measurements. I prepared the concept of the paper jointly with my supervisor and wrote the manuscript with all co-authors.

ACS APPLIED ELECTRONIC MATERIALS

pubs.acs.org/acsaelm

Article

Engineering the Microstructure and Functional Properties of $0.5Ba(Zr_{0.2}Ti_{0.8})O_3$-$0.5(Ba_{0.7}Ca_{0.3})TiO_3$ Thin Films

Sabi W. Konsago, Katarina Žiberna, Aleksander Matavž, Barnik Mandal, Sebastjan Glinšek, Yves Fleming, Andreja Benčan, Geoff L. Brennecka, Hana Uršič, and Barbara Malič*

Cite This: ACS Appl. Electron. Mater. 2024, 6, 4467−4477

Read Online

ACCESS | Metrics & More | Article Recommendations | Supporting Information

ABSTRACT: Lead-free piezoelectric $0.5Ba(Zr_{0.2}Ti_{0.8})O_3$-$0.5(Ba_{0.7}Ca_{0.3})TiO_3$ (BZT−BCT) thin films deposited by chemical solution deposition on platinized silicon substrates using ethylene glycol and ethanol solvents for alkaline-earth carboxylates and transition-metal alkoxides, respectively, are studied. Undoped and manganese-doped BZT-BCT films prepared by repeated deposition of a 0.1 M precursor solution and multistep annealing at 850 °C until reaching the thickness of about 120 nm exhibit a predominantly columnar microstructure with preferential (111) orientation of the perovskite phase. The Mn-doped films' room-temperature permittivity is about 670 at 1 kHz, which is ≈30% higher than the permittivity of their undoped counterparts at the same frequency and temperature while maintaining a similar tan $\delta \approx 0.02$. Mn-doping effectively reduces the leakage of BZT-BCT films, contributing to a saturated ferroelectric hysteresis loop with a remnant polarization of 5 μC cm^{-2} and a coercive field of 80 kV cm^{-1}. The maximum polarization and recoverable energy storage density are about 32 μC cm^{-2} and 10 J cm^{-3}, respectively, with 69% efficiency at 1160 kV cm^{-1}. The energy-storage properties remain almost unaffected after 2 million cycles at a field of 800 kV cm^{-1}. The piezoelectric d_{33} coefficient measured by double-beam laser interferometry is about 20 pm V^{-1}, while the corrected value of $d_{33} \approx 34$ pm V^{-1} taking into account the ratio of the electrode size to substrate thickness being equal to unity.

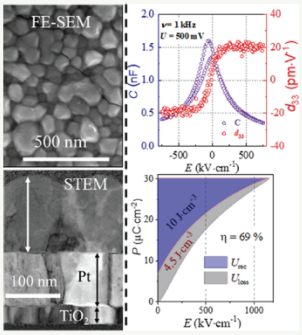

KEYWORDS: *$Ba(Zr_{0.2}Ti_{0.8})O_3$-$(Ba_{0.7}Ca_{0.3})TiO_3$ thin films, chemical solution deposition, crystallinity, dielectric permittivity, ferroelectric, piezoelectric response, energy storage*

1. INTRODUCTION

In the last two decades, legislation to restrict the use of certain hazardous substances, including lead (Pb), in electrical and electronic equipment by some countries, including the European Union, Japan, and the United States,[1−3] has triggered intensive research on lead-free piezoelectric ceramic materials that could be an alternative to lead zirconate titanate ($Pb(Zr_xTi_{1-x})O_3$, PZT), which is known for its excellent piezoelectric properties.[4] Barium zirconate titanate-barium calcium titanate ($0.5(Ba(Zr_{0.2}Ti_{0.8})O_3$-$0.5(Ba_{0.7}Ca_{0.3})TiO_3$, BZT-BCT) is among the promising lead-free ferroelectric materials with a piezoelectric response comparable to that of PZT ceramic.[5,6] Its large piezoelectric response was attributed to the morphotropic phase boundary (MPB) separating rhombohedral $Ba(Zr_{0.2}Ti_{0.8})O_3$ and tetragonal $(Ba_{0.7}Ca_{0.3})TiO_3$ by Liu and Ren in 2009.[5] Later, Keeble et al. reported the existence of a bridging orthorhombic phase between the rhombohedral and tetragonal phases.[7] Acosta et al. pointed out that the high-signal piezoelectric coefficients were related to the transition from tetragonal to orthorhombic phases.[8]

The large piezoelectric d_{33} coefficient in BZT−BCT bulk ceramic with the Curie temperature (T_c) of about 85 °C (the value depends on the grain size)[9] shows the potential of this material for versatile applications. A prototype intravascular ultrasound transducer was designed using BZT-BCT ceramics and tested by X. Yan et al. in 2013.[10] Biocompatibility and good piezoelectric properties make BZT-BCT attractive for biomedical applications.[11] BZT-BCT is becoming an interesting material for energy storage applications. The performance of energy storage capacitors is evaluated by energy storage density and energy storage efficiency, which are related to high saturated polarization, low remanent polarization, and low energy loss density.[12] A few articles reported good energy storage properties of bulk ceramic and thin films of Ca- and Zr-modified barium titanate (BT).[13−15]

BZT-BCT thin films are a viable option in terms of device miniaturization. In chemical solution deposition (CSD) of BZT-BCT thin films, the majority of studies followed the carboxylic acid-based route originally applied for BT,[16,17] with a carboxylic (acetic) acid and alcohol serving as solvents for alkaline-earth carboxylates and transition-metal alkoxides, respectively. How-

Received: March 26, 2024
Revised: May 7, 2024
Accepted: May 9, 2024
Published: May 17, 2024

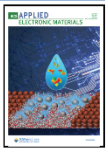

https://doi.org/10.1021/acsaelm.4c00530
ACS Appl. Electron. Mater. 2024, 6, 4467−4477

ever, BZT-BCT thin films by acetic-acid-based CSD often exhibited porosity, fine equiaxed grains, cracks, and, in some cases, chemical inhomogeneity.[18−21] BZT-BCT films prepared by single, double-, or multistep annealing at temperatures of 750−950 °C consisted of equiaxed grains.[20,22−26] Changes in the solution chemistry, such as introducing complexing agents, bi- or multifunctional solvents, or modifiers, were reported to increase the stability of the coating solutions.[19,21] On the other hand, increasing the organic content in the precursor may contribute to carbonaceous residues in the heterometallic framework requiring high decomposition temperatures, thus increasing the porosity in the films.[27]

A possible solution for obtaining a predominantly columnar microstructure in BZT-BCT films that presumably contributes to enhanced functional properties would be depositing a strongly diluted coating solution combined with multistep annealing as shown for BT thin films.[28] Following a similar procedure, a columnar microstructure was obtained in (Ba,Sr)-TiO_3 films.[29−31] In $Ba(Zr,Ti)O_3$ thin films, the grain size decreases with an increasing Zr content of 20% or more, with a concomitant decrease of dielectric permittivity. The films were prepared by a single annealing step at temperatures ranging from 900 to 1200 °C.[32−34] A similar trend of decreasing permittivity with increasing Ca-fraction was observed in $(Ba,Ca)TiO_3$ films.[35,36]

In our preliminary studies on CSD of BZT-BCT films using the acetic-acid-based route with alkaline-earth acetates and transition-metal butoxides diluted with 2-methoxyethanol, the precipitation of the coating solutions was observed after a few days. This was presumably due to the uncontrolled hydrolysis of the alkoxides by the in situ produced water in the esterification reaction of the two solvents. We investigated BT as a reference material for BZT-BCT thin films.[37] A bifunctional alcohol, ethylene glycol ($OHCH_2CH_2OH$, EG), was selected as the solvent for barium acetate, thereby eliminating the possibility of uncontrolled hydrolysis. The stability of the solution was extended from weeks to more than one year. Furthermore, introducing ethanol (EtOH) as the solvent for Ti-butoxide instead of 2-methoxyethanol downshifted the temperature range of organic residue decomposition for a few 100 °C. EG has previously been used in CSD of BZT-BCT films as a modifier[19] but not as the solvent for alkaline-earth reagents. Livage et al. used EG as the solvent for lead acetate in CSD of $Pb(Zr,Ti)O_3$ films.[38] (Note that both EG and EtOH quickly pick up water from the atmosphere if they are not kept dry.)

In this study, BZT-BCT thin films are deposited from the EG-EtOH-based coating solution. Upon multistep annealing at 850 °C, a predominantly columnar microstructure develops. With manganese doping, the leakage current is reduced. The dielectric, ferroelectric, energy-storage, and piezoelectric properties of the manganese-doped BZT-BCT films are reported.

2. EXPERIMENTAL METHODS

For the preparation of $0.5(Ba(Zr_{0.2}Ti_{0.8})O_3\text{-}0.5(Ba_{0.7}Ca_{0.3})TiO_3$, BZT−BCT thin films, alkaline-earth acetates barium acetate ($Ba(CH_3COO)_2$, $Ba(OAc)_2$) with a purity of 99.97%, Sigma-Aldrich, St. Louis, Missouri, USA, and calcium acetates ($Ca(CH_3COO)_2$, $Ca(OAc)_2$) 99.999%, Alfa Aesar, Karlsruhe, Germany, and transition-metal alkoxides: titanium butoxide ($Ti(OC_4H_9)_4$, $Ti(OnBu)_4$) 99.61% and zirconium butoxide ($Zr(OC_4H_9)_4$, $Zr(OnBu)_4$), 80% both purchased from Alfa Aesar, Karlsruhe, Germany, are used as reagents. The molar ratio of barium, calcium, zirconium, and titanium reagents is 0.85:0.15:0.1:0.9. Ethylene glycol ($OHCH_2CH_2OH$, EG, 99.8%) and absolute ethanol (CH_3CH_2OH, EtOH 99.9%) both from Sigma-Aldrich, St. Louis, Missouri, USA, were used to dissolve alkaline-earth acetates and to dilute transition-metal alkoxides, respectively. The volume ratio of EG/EtOH was kept at 3/2. The reagents and solvents were kept and manipulated in an inert atmosphere (N_2-filled glovebox). The solutions of alkaline-earth acetates and transition-metal alkoxides were mixed at room temperature, with the concentration adjusted to either 0.2 or 0.1 M as described in Figure 1. Manganese acetate

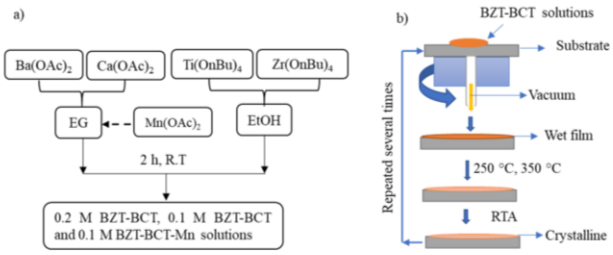

Figure 1. (a) Schematic preparation of BZT-BCT and BZT-BCT-Mn coating solutions. (b) BZT-BCT thin-film deposition. RTA: rapid thermal annealing.

($Mn(CH_3COO)_2$, $Mn(OAc)_2$) 98%, Alfa Aesar, Karlsruhe, Germany, in the amount of 1 mol % was included in the solution of alkaline-earth acetates before mixing with the solution of transition-metal alkoxides. The Mn dopant was added over stoichiometrically. The solution with a 0.1 M concentration, further denoted as 0.1 M BZT-BCT-Mn, was prepared following the same procedure as described above.

The 0.2 M BZT-BCT coating solution was deposited on a 625 μm thick $Pt(111)/TiO_2/SiO_2/(100)/Si$ substrate (Pt/Si, purchased from SINTEF, Oslo, Norway) by spin coating (WS-400B-6NPP/LITE, Laurell, North Wales, PA, USA) at 3000 rpm for 30 s, followed by drying, pyrolysis, and annealing steps. All steps were repeated four times. The drying and pyrolysis steps were at 250 °C for 15 min and 350 °C for 15 min, respectively, on the hot plate. The annealing temperatures were 800 °C, 850 °C, and 900 °C with a heating rate of 13.3 °C/second for all films, while the times were 15 min for the first and the last deposited layer and 5 min for the intermediate ones in a rapid thermal annealing furnace (Mila 5000, Ulvac-Riko, Yokohama, Japan).

The 0.1 M BZT-BCT and BZT-BCT-Mn-0.1 M solutions were deposited on Pt/Si following the same procedure as described above; only the number of the deposition-heat-treatment steps increased to 10 to reach similar film thicknesses as for the 0.2 M solutions.

In further text, the films prepared from the 0.2 M BZT-BCT, 0.1 M BZT-BCT, and 0.1 M BZT-BCT-Mn solutions are denoted BZT-BCT-0.2 M, BZT-BCT-0.1 M, and BZT-BCT-Mn-0.1 M. The list of the samples and their processing parameters are summarized in Table 1.

The phase composition of the films was characterized by XRD with Cu Kα radiation performed in the 2 theta ranges of 10−39 deg and 40−65 deg to avoid recording the Pt (111) peak on a high-resolution diffractometer (X'Pert PRO, PANalytical, Almelo, The Netherlands) with the following parameters: 128 channel detector X'Celerator with a capture angle of 2.122°, step = 0.034°, time per step = 100 s, soller slit = 0.02 rad, mask 10 mm, divergence and antiscatter slit: 10 mm. The phase analysis is performed using X'Pert High Score Plus software.

A Bruker D8 Discover instrument with Cu Kα radiation (λ = 0.154 nm) was used for grazing incidence X-ray diffraction (GIXRD). The experiment was conducted with an incident angle of 0.5°, scanning the 2θ-range from 20° to 60° with a step of 0.02, and a time per step set of 4 s. The same tool was used for the Ψ-scan ($\theta-2\theta$ scan with different tilt angles, Ψ) with a 1 mm collimator. The measurement was performed in a 2θ- and Ψ-range from 38.5° to 39.3° and from 0° to 10°, respectively. The 2θ-step was 0.02, and the time per step was 90 s.

The plan-view and cross-sectional microstructure of the films were imaged using a Verios 4G HP field emission scanning electron microscope (Thermo Fischer, Waltham, Massachusetts, USA) with an accelerating voltage of 10 kV. A 5 nm thick carbon was precoated using a Precise Etching and Coating System 628A (Gatan, Pleasanton,

https://doi.org/10.1021/acsaelm.4c00530
ACS Appl. Electron. Mater. 2024, 6, 4467−4477

3.3.Engineering the Microstructure and Functional Properties of $Ba(Ti_{0.8}Zr_{0.2})O_3$-$(Ba_{0.7}Ca_{0.3})TiO_3$ Thin Films

Table 1. List of the Samples and Their Processing Parameters

film	molar concentration	number of depositions	annealing temperature, °C
BZT-BCT-0.2M	0.2	4	800
BZT-BCT-0.2M	0.2	4	850
BZT-BCT-0.2M	0.2	4	900
BZT-BCT-0.1M	0.1	10	850
BZT-BCT-Mn-0.1M	0.1	10	850

California, USA). The average lateral grain size of the BZT-BCT-0.1 M and BZT-BCT-Mn-0.1 M films was determined on the obtained SEM images sing the linear intercept method. At least 300 grains were measured on each sample.

For scanning transmission electron microscopy (STEM) analysis, the BZT-BCT-Mn-0.1 M thin film was prepared into lamella form using a Ga^+-source focused ion beam (FIB) Helios Nanolab 650 HP (Thermo Fischer Scientific, Waltham, MA, USA). The structural STEM analysis was performed with a Cs-corrected ARM200CF (Jeol, Tokyo, Japan), operating at 200 kV. The 4D-STEM data set was acquired with the Merlin pixelated detector (Quantum Detectors, Oxford, U.K.).

The gold top electrodes with a diameter of 200 μm were deposited on the films through a shadow mask by magnetron sputtering (5 Pascal). The contact to the bottom platinum electrode was made by etching a part of the film with a mixture of HF 40%, Alfa Aeser, HCl 37–38%, J.T. Baker, and H_2O in a volume ratio (2:5:20).

The topography, roughness, and local ferroelectric/piezoelectric properties were investigated using tapping atomic force microscopy (AFM) mode and piezo-response force microscopy (PFM) mode on Jupiter XR AFM (AFM, Asylum Research, Santa Barbara, California, USA). The noncoated silicon tips (AC200TS, Oxford Instruments, USA) with a radius of 7 nm were used for scanning in tapping (AC Air Topography, Jupiter XR, Asylum Research, Santa Barbara, California, USA) mode. The root-mean-square roughnesses (rms) were determined in the 3 × 3 μm range. The PFM analyses were performed using a Pt-coated Si tip with a diameter of about 15 nm (OMCL-AC240TM, Olympus, Japan). For PFM scanning, an electrical voltage with an amplitude of 3 V and frequency of 300 kHz was applied between the bottom electrode of the sample and the conductive tip in dual alternating-current resonance tracking (DART) mode. The local hysteresis loops were also measured by PFM as described in[39] using DART switching spectroscopy mode at MFP-3D AFM (Asylum Research, Santa Barbara, California, USA). The sequence of increasing steps of the DC electric field was driven at 20 Hz, and a maximum amplitude of 18 V was applied. The frequency of the triangular envelope was 0.99 Hz. A superimposed sinusoidal AC signal with an amplitude of 3 V and a frequency of ~350 kHz was used. Three cycles were measured in off-electric field mode.

An impedance analyzer (HP 4284A, Keysight, Santa Rosa, USA) was used to measure the frequency dependence of the dielectric permittivity and losses at room temperature across a frequency range from 100 Hz to 1 MHz, and the dielectric permittivity and losses at temperatures range of 25 to 150 °C from 33 Hz to 100 kHz. The Aixacct TF Analyzer 2000 (Aixacct Systems GmbH, Aachen, Germany) was used to measure the ferroelectric polarization (P), current density (j), and strain (S) hysteresis loops with a sinusoidal test signal at room temperature. In addition, the energy storage properties, namely, energy storage density (U_{st}), recovered energy storage density (U_{rec}), energy loss (U_{loss}), and efficiency (η), were calculated from the unipolar electric field loop with a magnitude of 1160 kV cm^{-1} and a frequency of 1 kHz. Furthermore, the thin-film sample was cycled 2 million times at room temperature with an electric field amplitude of 800 kV cm^{-1}. The two consecutive unipolar hysteresis loops were measured at 1 kHz to monitor the energy storage properties. The data of the unipolar loop of the first E-cycle can be found in the main part of the paper, and the data of the second E-cycle can be found in the Supporting Information. The capacitance as a function of the DC field (C–E_{DC}) was measured at 1 kHz with a small-signal amplitude of 50 mV. The piezoelectric d_{33} coefficient was measured at 1 kHz with a small-signal amplitude of 500 mV with a double-beam laser interferometer (DBLI, Aixacct Systems GmbH, Aachen, Germany).

3. RESULTS AND DISCUSSION

3.1. Phase Composition and Microstructure of BZT-BCT-0.2 M Films. XRD patterns of the BZT-BCT-0.2 M films annealed at 800, 850, and 900 °C are shown in Figure 2. All films

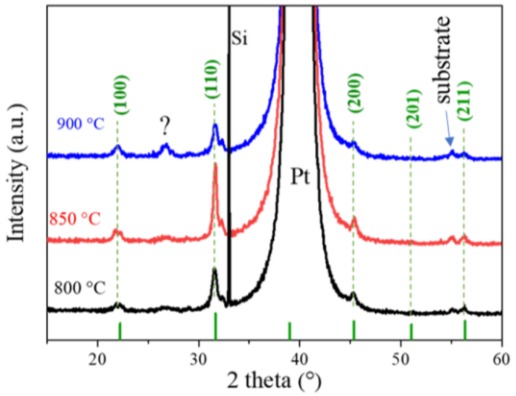

Figure 2. XRD patterns of BZT-BCT-0.2 M films on Pt/Si annealed at different temperatures. The peaks corresponding to the perovskite phase are indexed according to the cubic $BaTiO_3$ phase (PDF 01-074-4539). The question mark indicates an unidentified peak.

crystallized in the perovskite phase. The (110) peak has the highest intensity; however, the Pt (111) peak overlaps with BZT-BCT (111); consequently, the orientation cannot be inferred. We note a low-intensity peak at 2 theta 26.6° in the film annealed at 900 °C, which could indicate a possible reaction of the film with the substrate.

The field emission scanning electron microscopy (FE-SEM) cross-section, plan view, and AFM topography height images of the BZT-BCT-0.2 M thin films are presented in Figure 3. The thickness of the films annealed at 850 and 900 °C is about 120 nm, while the film annealed at 800 °C is about 10 nm thicker due to porosity. In contrast to BT thin films, which at similar deposition and annealing conditions crystallize in columnar microstructure,[37] the BZT-BCT-0.2 M films annealed at 800 and 850 °C have fine equiaxed grains. Studies of BT precursors revealed that the thermal decomposition was concluded at about 800 °C.[40] In comparison, carbonaceous residues were detected in a BZT-BCT precursor up to about 1000 °C.[41]

The surface microstructures reveal that the grain size of the films slightly increases with increasing annealing temperature, reaching about 50 nm at 900 °C, while the porosity decreases. AFM topography height images support FE-SEM analysis. The root-mean-square (rms) roughness of the films annealed at 800 and 850 °C is between 4 and 5 nm notwithstanding the annealing temperature.

https://doi.org/10.1021/acsaelm.4c00530
ACS Appl. Electron. Mater. 2024, 6, 4467–4477

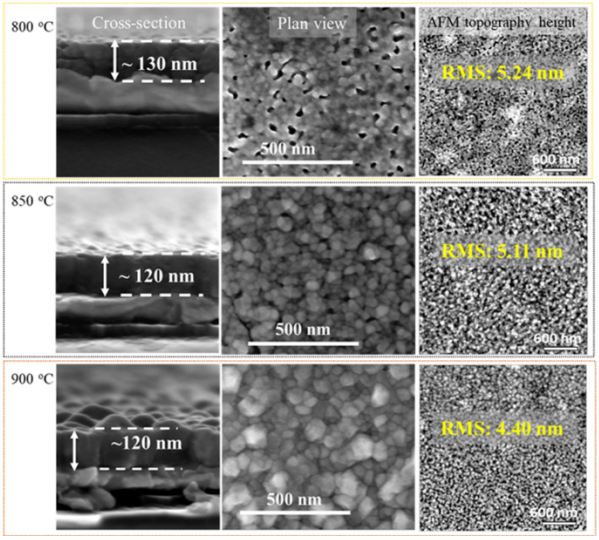

Figure 3. Cross-section (left) and plan-view (middle) FE-SEM micrographs and AFM topography images (right) of BZT-BCT-0.2 M films annealed at 800, 850, and 900 °C.

The dielectric permittivity and losses of the film annealed at 850 °C are about 350 and 0.02 at 1 kHz, respectively, while the films annealed at 800 and 900 °C exhibit lower permittivity of about 260 and 250, respectively, with similar losses at lower frequencies (Table 2). The lower relative permittivity of the film annealed at 800 °C compared to the film annealed at 850 °C could be explained by lower crystallinity and high porosity, while the lower relative permittivity of the film annealed at 900 °C is most likely due to interaction between the film and the substrate supported by a nonidentified low-intensity peak in the XRD pattern, cf. Figure 2. The dielectric data of the films as a function of the frequency are collected in Supporting Information S1. The polarization-electric field (*P-E*) loops show no saturation (see Supporting Information S2) in agreement with the literature on BZT-BCT films prepared following a similar procedure,[21] which could be related to fine grain size and/or leakage. We conclude that 850 °C is the optimal annealing temperature for BZT-BCT thin films with a dense, smooth microstructure without obvious impurities.

Table 2. Dielectric Permittivity and Losses Measured at Room Temperature and at 1 kHz of BZT-BCT-0.2M, BZT-BCT-0.1M, and BZT-BCT-Mn-01M Films Compared with Literature Data[a]

film	conc. of solution	annealing temperature	thickness	ε'	tan δ	ref
BZT-BCT	0.35 M	700 °C	300 nm	220	0.63	55
BZT-BCT	0.2 M	700 °C	400 nm	377	0.22	56
BZT-BCT	0.35 M	750 °C	200 nm	280	0.04	20
BZT-BCT	0.35 M	700 °C	450 nm	157	0.03	57
BZT-BCT-0.2M	0.2 M	800 °C	130 nm	260	0.02	this work
BZT-BCT-0.2M	0.2 M	850 °C	120 nm	350	0.02	this work
BZT-BCT-0.2M	0.2 M	900 °C	120 nm	250	0.02	this work
BZT-BCT-0.1M	0.1 M	850 °C	120 nm	~510	0.02	this work
BZT-BCT-Mn-0.1M	0.1 M	850 °C	120 nm	~670	0.02	this work

[a]All films were deposited on Pt/Si substrates.

3.2. Optimization of the Microstructure of the Films. Lowering the concentration of the coating solution and sequential crystallization of individual layers by multistep annealing enabled the formation of a predominantly columnar microstructure of BT and $SrTiO_3$ thin films.[42] Following such an approach, we diluted the coating solutions to a 0.1 M concentration. Also, we increased the number of deposited layers from 4 to 10 to reach thicknesses similar to those in the case of films deposited from the 0.2 M solution. Furthermore, we introduced Mn-dopant (1 mol %) to reduce the leakage current.[43] The BZT-BCT-0.1 M and BZT-BCT-Mn-0.1 M films on Pt/Si substrates annealed at 850 °C crystallize in the perovskite phase, with the (110) peak being the most intense in both cases (XRD patterns recorded in Bragg−Brentano geometry are collected in Supporting Information S3).

Further XRD analysis was performed to obtain deeper insight into the crystalline orientation of the perovskite phase. GIXRD was measured to enhance the signal coming from the film (Figure 4a). The (111) peak is now nicely revealed, as the Pt signal present in Figure 2 is strongly suppressed. However, GIXRD is not a very convenient method to quantify the orientation of the films, as the scattering vector changes during the 2θ scan and is not normal to the surface of the film.[44,45] Therefore, tilt-angle (Ψ)-dependent XRD patterns were measured around the (111) peak. This enables gradual probing of the peak, going from completely out-of-plane ($\Psi = 0^{\circ}$) to completely in-plane ($\Psi = 90^{\circ}$) conditions. The decrease of the peak intensity at $\Psi > 0^{\circ}$, observed in Figure 4b, therefore indicates a strong (111) out-of-plane orientation of the film. The orientation was further confirmed with a (110) pole figure measurement (see Supporting Information S4).

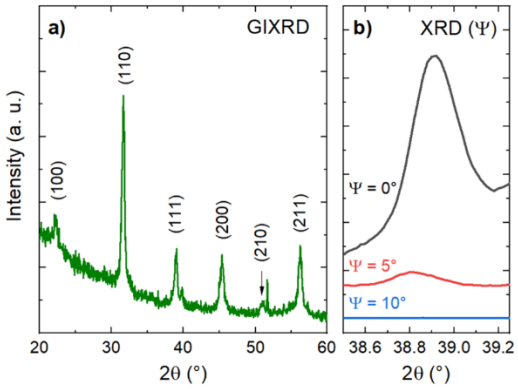

Figure 4. BZT-BCT-Mn-0.1 M film on Pt/Si annealed at 850 °C. (a) GIXRD pattern. Peaks that are not denoted with Miller indices correspond to the substrate. (b) XRD pattern around the (111) peak as a function of a tilt angle (Ψ).

Figure 5 shows plan-view and cross-sectional FE-SEM micrographs of BZT-BCT-0.1 M and BZT-BCT-Mn-0.1 M films. There is no obvious difference in their microstructural features. The surface microstructures are dense and uniform, with average lateral grain sizes of 72 and 74 nm for BZT-BCT-0.1 M and BZT-BCT-Mn-0.1 M, respectively. Their respective thicknesses are about 110 and 120 nm.

https://doi.org/10.1021/acsaelm.4c00530
ACS Appl. Electron. Mater. 2024, 6, 4467−4477

3.3.Engineering the Microstructure and Functional Properties of $Ba(Ti_{0.8}Zr_{0.2})O_3$-$(Ba_{0.7}Ca_{0.3})TiO_3$ Thin Films

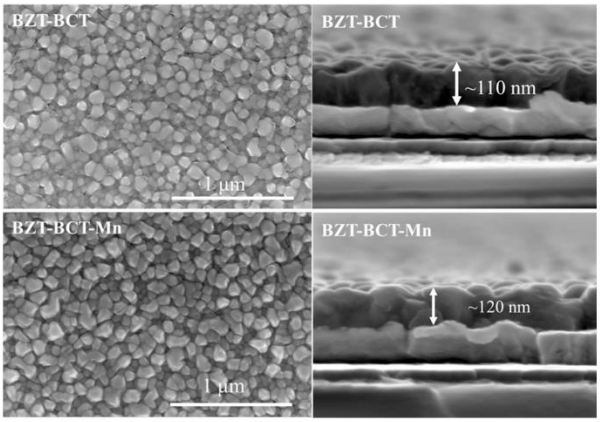

Figure 5. Plan-view (left) and cross-section (right) FE-SEM micrographs of BZT-BCT-0.1 M and BZT-BCT-Mn-0.1 M films on Pt/Si, annealed at 850 °C.

We noticed the appearance of cracks in thicker films, which we attributed to a large thermal expansion mismatch between the film and the silicon substrate. BZT-BCT ceramic and silicon thermal expansion coefficients are $\approx 12 \times 10^{-6}$/K between 100 and 600 °C[46] and $\approx 3 \times 10^{-6}$/K,[47] respectively.

Figure 6a shows the STEM micrographs of the cross-section of the BZT-BCT-Mn-0.1 M film at different magnification scales. The microstructure consists of predominantly columnar grains extending throughout the thickness of the film, as well as some fine equiaxed grains. The bright-field STEM images of a single columnar grain (center and far-right parts of panel a) reveal boundaries between about 10 nm thick individual layers that formed upon repeating the deposition/annealing steps. Each newly deposited layers crystallize on top of preceding layers, and such homoepitaxial growth within individual columnar grains was previously observed in CSD-derived barium and strontium titanate thin films.[48]

The selected area electron diffraction (SAED) pattern is shown in Figure 6b. We note that the grains in the film are preferentially [111] and to a minor degree [110] oriented, according to SAED, in agreement with GIXRD analysis; see Figure 4. The platinum substrate is [111] oriented and has a small lattice mismatch with the BZT-BCT film, so it may serve as a nucleation layer for [111] oriented BZT-BCT columnar grains. Jia and Urban found a [111] orientational relationship between the Pt substrate and columnar grains in the $SrTiO_3$ film. Interestingly, the microstructure of $BaTiO_3$ film on Pt substrate was columnar but without texture, which was attributed to a different mechanism of phase formation involving Ba-Ti-oxycarbonate.[48]

Figure 6c shows the center of mass (CoM) vector magnitude image.[49] Different contrast observed within individual grains infers the existence of domain walls, as indicated by the arrows in the CoM vector magnitude image. We may conclude that columnar grains are multidomain.

Figure 7 shows the chemical analysis of the BZT-BCT-Mn-0.1 M film obtained by energy-dispersive X-ray spectroscopy (EDS) mapping (STEM-EDS). The clear interface between the film and the substrate evidence that the film does not react with the substrate upon annealing at 850 °C. The EDS analysis reveals a homogeneous distribution of elements across the film thickness. This indicates that the crystallization from the amorphous phase occurs without segregation, i.e., the chemical homogeneity of the amorphous phase is retained during the crystallization of the perovskite phase. We note that manganese could not be detected due to its low concentration, which implies that it is not segregated but rather homogeneously distributed in the perovskite matrix.

3.3. Functional Properties of BZT-BCT-0.1 M and BZT-BCT-Mn-0.1 M Films. Figure 8 shows the dielectric permittivity and losses of BZT-BCT-0.1 M and BZT-BCT-

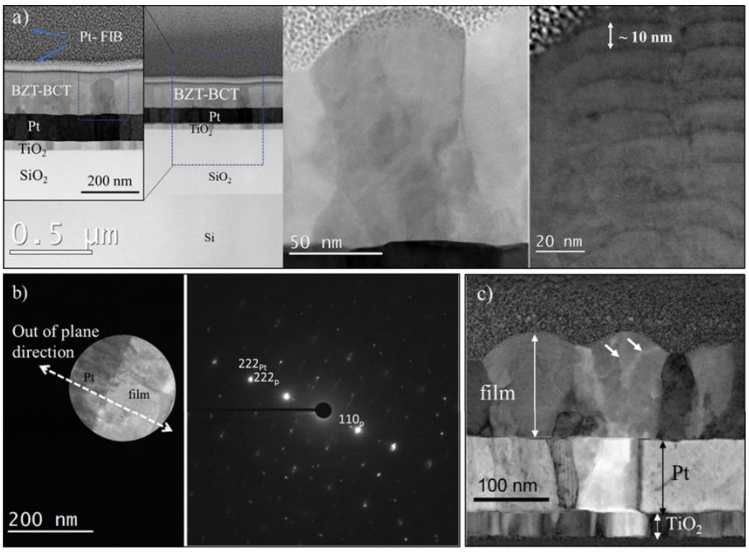

Figure 6. (a) Bright-field STEM images of a cross-section of BZT-BCT-Mn-0.1 M film on Pt/Si at different magnifications. (b) SAED pattern (right) of the selected region (left). Both the (110) and (111) planes of BZT-BCT-Mn, which are perpendicular to the film substrate, are parallel to the (111) Pt planes. The direction perpendicular to the film substrate is indicated by a double arrow on the image of the selected region, which was taken across ~4 perovskite (p) and ~5 Pt grains. (c) Magnitude map of the vector field calculated from the center of mass (CoM) image showing the existence of different domains in the grains.

https://doi.org/10.1021/acsaelm.4c00530
ACS Appl. Electron. Mater. 2024, 6, 4467−4477

ACS Applied Electronic Materials pubs.acs.org/acsaelm Article

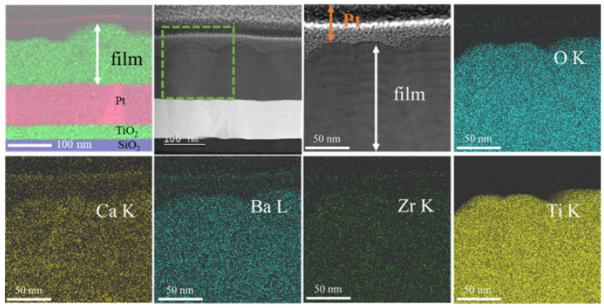

Figure 7. EDS-STEM compositional analysis of the BZT-BCT-Mn-0.1 M film on a Pt/Si substrate. For the EDS mapping, the spectral lines O K, Ca K, Ba L, Zr K, and Ti K were used. The upper layer of Pt is due to FIB preparation.

Mn-0.1 M films at different frequencies in the 25 to 200 °C temperature range. The room-temperature dielectric permittivity and tan δ losses of the BZT-BCT-0.1 M film at 1 kHz are about 510 and 0.02, respectively. It is difficult to determine the Curie temperature because the permittivity and losses also increase with increasing temperature, which we connect to the increased conductivity of the film. The hardly discernible permittivity peak is estimated to be around 70−90 °C. This temperature range is roughly comparable to the reported Curie temperature in BZT-BCT bulk ceramic.[9,50]

The BZT-BCT-Mn-0.1 M film exhibits dielectric permittivity of about 30% higher than its undoped counterpart while maintaining a similar tan $\delta \approx 0.02$ at room temperature. With increasing temperature, its lossy behavior is effectively reduced due to manganese doping.[51−53] The strongly broadened dielectric permittivity peak is at about 55−75 °C. Lowering the Curie temperature upon manganese doping observed in the studied films was also reported for other perovskite oxides.[52,54] Despite a broad peak due to presumed phase transition, the dielectric properties are almost temperature-independent ($\Delta\varepsilon <$ 5% between 25 °C − 125 °C), which is favorable for implication in many applications.

In Table 2, the room-temperature dielectric properties of our films are compared with literature data.[20,55−57] In our case, the coating solution concentration and the film thickness are lower and the annealing temperature is higher. Still, the dielectric permittivity is about two times higher, and losses are comparable or lower than the literature data. This increase in the permittivity is attributed to the dense columnar microstructure.

Local ferro- and piezoelectric properties of both films BZT-BCT-0.1 M and BZT-BCT-Mn-0.1 M are investigated by the piezo-response force module of AFM (Figure 9). The topography height and deflection AFM images reveal a dense, uniform microstructure consistent with the FE-SEM micrograph shown in Figure 5. The surface roughness is about 4.5 and 4 nm for BZT-BCT-0.1 M and BZT-BCT-Mn-0.1 M films, respectively. The PFM amplitude (c) and phase (d) images show different contrasts under the applied voltage, indicating the local piezoelectric/ferroelectric response in both films, which is also confirmed by the PFM amplitude (e) and phase (f) hysteresis loops.

Figure 10a shows the *P-E* loops of BZT-BCT-0.1 M and BZT-BCT-Mn-0.1 M films. The manganese-doped film has a saturated *P-E* hysteresis loop, with remanent polarization P_r of 5 μC cm^{-2}, coercive field E_c of 80 kV cm^{-1}, and maximum polarization P_s of 32 μC cm^{-2} at an electric field of 1160 kV cm^{-1}. A saturated hysteresis *P-E* loop could not be obtained in the undoped BZT-BCT-0.1 M film that only survived electric fields below 300 kV cm^{-1} without breakdown. To evaluate the

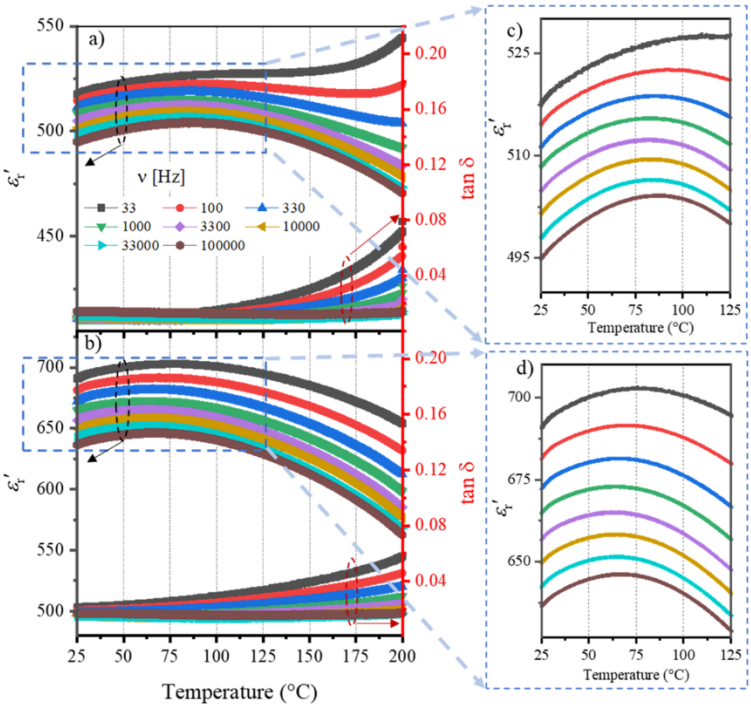

Figure 8. Dielectric permittivity (ε_r') and losses (tan δ) as a function of temperature at different frequencies (ν) of (a) BZT-BCT-0.1 M and (b) BZT-BCT-Mn-01 M films on Pt/Si annealed at 850 °C. (c, d) Magnified *y* scale of ε_r'.

https://doi.org/10.1021/acsaelm.4c00530
ACS Appl. Electron. Mater. 2024, 6, 4467−4477

3.3.Engineering the Microstructure and Functional Properties of $Ba(Ti_{0.8}Zr_{0.2})O_3$-$(Ba_{0.7}Ca_{0.3})TiO_3$ Thin Films

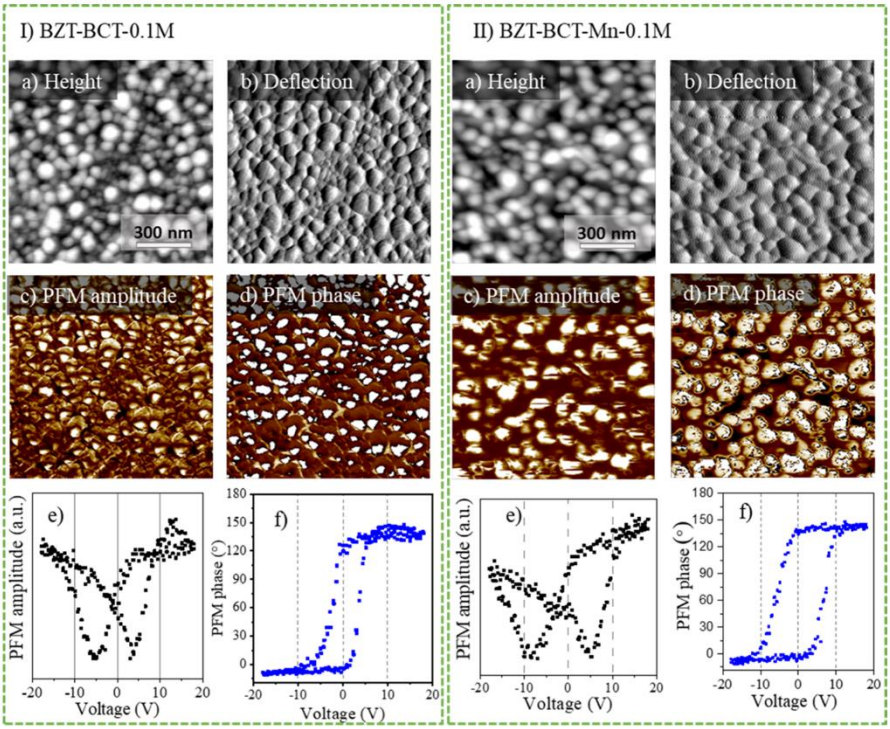

Figure 9. AFM topography (a) height and (b) deflection images, PFM (c) amplitude and (d) phase images, PFM (e) amplitude and (f) phase hysteresis loops of (I) BZT-BCT-0.1 M and (II) BZT-BCT-Mn-0.1 M films on Pt/Si annealed at 850 °C. The second and third cycles are shown in panels (e) and (f).

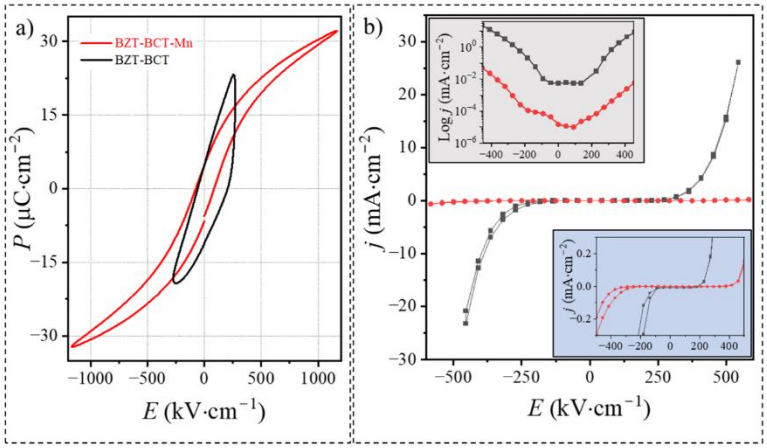

Figure 10. (a) *P-E* loops and (b) *j-E* dependence of BZT-BCT-0.1 M and BZT-BCT-Mn-0.1 M films on Pt/Si. Top inset in panel (b): logarithmic *y*-axis, bottom inset in panel (b): magnified linear *y*-axis. The *P-E* and *j-E* measurements were performed at 1 kHz.

effect of Mn doping on BZT-BCT film, the current density (j) under an applied electric field was measured in both films, see Figure 10b. The leakage current density in the BZT-BCT-0.1 M film is about 15 mA·cm^{-2} at the applied field of 500 kV cm^{-1}. Manganese doping significantly reduces the leakage to about 0.18 mA cm^{-2} in the same field. The effect of Mn-doping on the leakage current at low fields is clearly seen on the logarithmic scale; see the inset of Figure 10b.

Due to the slim *P -E* loop, high maximum polarization, high breakdown field, and low current density, cf. Figure 10, the BZT-BCT-Mn-0.1 M films could be considered for energy storage. Figure 11 shows the unipolar *P-E* loop measured at 1 kHz (first cycle). The calculated energy storage density (U_{st}), recovered energy storage density (U_{rec}), energy loss (U_{loss}), and efficiency (η) are 14.5, 10, 4.5 J cm^{-3}, and 69%, respectively, at 1160 kV cm^{-1}. These properties are comparable to the energy storage properties of the PZT thin film deposited on (001) $SrRuO_3$/$SrTiO_3$/Si by pulsed laser deposition (PLD).[58] The U_{rec} of $(Ba,Ca)(Zr,Ti)O_3$ films prepared by PLD and ion beam sputtering deposition were reported to be 39 J·cm^{-3} and 2.3 J·cm^{-3}, respectively, with the respective η of 33% and 28.5%.[15,59]

https://doi.org/10.1021/acsaelm.4c00530
ACS Appl. Electron. Mater. 2024, 6, 4467−4477

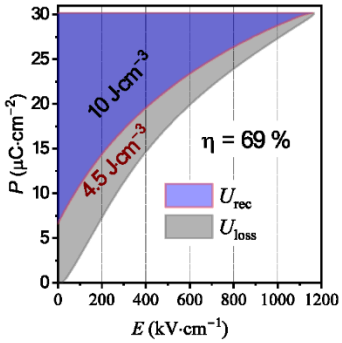

Figure 11. Energy storage properties obtained from the unipolar *P-E* loop (first cycle) of a BZT-BCT-Mn-0.1 M thin film on Pt/Si annealed at 850 °C.

In our case, η is about twice as high as compared to the film prepared by PLD, which has a higher U_{rec}.

Furthermore, the BZT-BCT-Mn-0.1 M film's endurance was measured by electric field cycling two consecutive unipolar *P-E* loops at 800 kV cm^{-1} with a frequency of 1 kHz, see Figure 12.

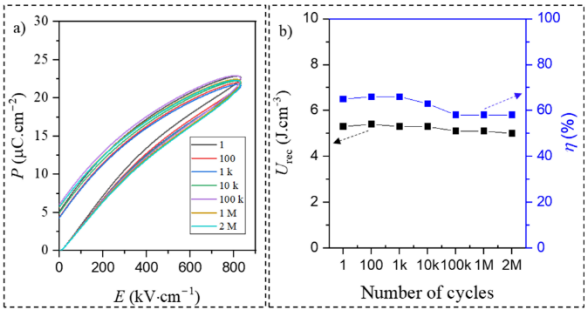

Figure 12. (a) Unipolar P-E loops and (b) U_{rec} and η of BZT-BCT-Mn-0.1 M film upon electric field cycling.

After 2 million cycles, there is no significant change in the *P-E* loops. The U_{rec} of 5.3 J cm^{-3} is linear upon cycling, while the efficiency of about 65% is slightly decreased down to 58% above 10^5 cycles. A similar value and linear behavior of U_{rec} are also observed from the data calculated using the second-cycle *P-E* loops (Supporting Information S5). Here, the energy storage efficiency (η) is slightly higher than the value from the first cycle. This can be explained by the fact that in the second cycle, the sample is already partially poled, reducing the charging energy and increasing the efficiency.

The field-induced strain (*S-E*), capacitance tunability (*C-E*), and the extracted piezoelectric d_{33} coefficient of BZT-BCT-Mn-0.1 M film were obtained by double-beam laser interferometry (DBLI), see Figure 13. The maximum field-induced strain is 0.18% at 1 MV·cm^{-1} measured at 1 kHz. A very similar value was obtained at 100 Hz. The capacitance response to the electric field indicates the switching behavior of domains, thus confirming the ferroelectricity of the film.[19] The calculated and plotted relative permittivity as a function of the electric field (see Figure 13b) matches the value of permittivity obtained by temperature-dependent dielectric measurements. The small-signal d_{33} coefficient of BZT-BCT-Mn-0.1 M measured on an electrode with a diameter of 200 μm is about 22 pm V^{-1}. The value of d_{33} is likely somewhat underestimated due to the small ratio between the electrode size and the substrate thickness (0.32). Ideally, the ratio should be around 1,[60] as also supported by our previous study.[61] The corrected value, considering the respective ratio of 1, is about 34 pm V^{-1}. To our knowledge, macroscopic measurement of the field-induced strain of BZT-BCT films has not been reported previously.

4. CONCLUSIONS AND OUTLOOK

In summary, we investigated the microstructure and functional properties of BZT-BCT thin films deposited on the platinized silicon substrates. The films were undoped or doped with manganese. By carefully designed processing, which included adapted solution chemistry that prevented uncontrolled hydrolysis of transition-metal reagents, diluting the coating solution to decrease the thickness of individual deposited layers, and multistep annealing at 850 °C, BZT-BCT films crystallized with a columnar microstructure. The perovskite phase was preferentially (111) oriented, as shown by GIXRD and supported by STEM analysis. The STEM-EDS analysis revealed a homogeneous distribution of elements across the film thickness, indicating that the homogeneity of the solid solution was retained upon crystallization.

The room-temperature dielectric permittivity of the films with a columnar microstructure was 510, almost twice as much as the value obtained in the film with a fine, granular microstructure, in agreement with the dielectric grain-size effect. Manganese

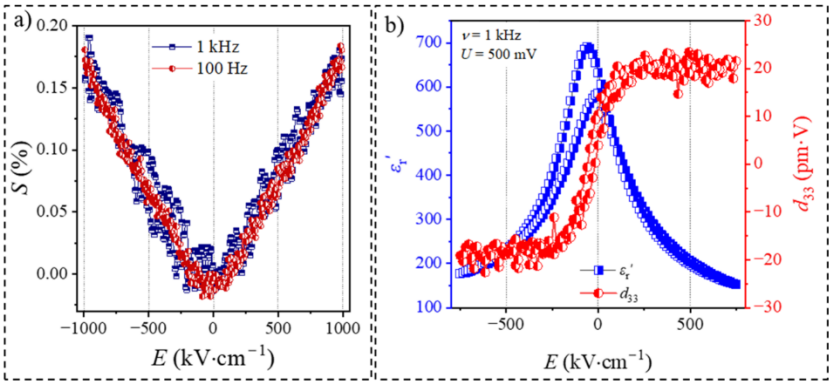

Figure 13. Electric field dependence of (a) strain and (b) dielectric permittivity (ε_r') and small-signal piezoelectric d_{33} coefficient of BZT-BCT-Mn film on Pt/Si prepared from 0.1 M coating solution and annealed at 850 °C measured by DBLI.

https://doi.org/10.1021/acsaelm.4c00530
ACS Appl. Electron. Mater. 2024, 6, 4467−4477

3.3.Engineering the Microstructure and Functional Properties of $Ba(Ti_{0.8}Zr_{0.2})O_3$-$(Ba_{0.7}Ca_{0.3})TiO_3$ Thin Films

doping contributed to a higher room-temperature dielectric permittivity (670), a downshift of a very broad permittivity peak, and a significant leakage reduction of BZT-BCT thin films. The manganese-doped BZT-BCT films exhibit ferroelectric properties. A slim polarization-electric field loop, high maximum polarization, high breakdown field, and almost fatigue-free response after 2 million cycles at 800 kV cm^{-1} make them good candidates for energy-storage applications. The piezoelectric response of BZT-BCT was confirmed by DBLI.

Future research could focus on the multifunctionality of BZT-BCT thin films following the proposed processing approach and possibly using other substrates, such as platinized sapphire or metal foils, for versatile energy conversion applications.

■ ASSOCIATED CONTENT

Supporting Information

The Supporting Information is available free of charge at https://pubs.acs.org/doi/10.1021/acsaelm.4c00530.

Frequency dependence of dielectric permittivity (ε_r') and losses (tan δ) at room temperature of BZT-BCT-0.2 M annealed at different temperatures; electric-field dependence of the electrical polarization of BZT-BCT-0.2 M films annealed at different temperatures; XRD patterns of BZT-BCT-0.1 M and BZT-BCT-Mn-0.1 M films on Pt/Si annealed at 850 °C recorded in Bragg−Brentano geometry; and unipolar *P-E* loops and recoverable energy density (U_{rec}) and efficiency (η) of BZT-BCT-Mn-0.1 M film upon electric field cycling (PDF)

■ AUTHOR INFORMATION

Corresponding Author

Barbara Malič − *Electronic Ceramics Department, Jožef Stefan Institute, 1000 Ljubljana, Slovenia; Jožef Stefan International Postgraduate School, 1000 Ljubljana, Slovenia;* Email: barbara.malic@ijs.si

Authors

Sabi W. Konsago − *Electronic Ceramics Department, Jožef Stefan Institute, 1000 Ljubljana, Slovenia; Jožef Stefan International Postgraduate School, 1000 Ljubljana, Slovenia;* orcid.org/0000-0002-2880-5543

Katarina Žiberna − *Electronic Ceramics Department, Jožef Stefan Institute, 1000 Ljubljana, Slovenia; Jožef Stefan International Postgraduate School, 1000 Ljubljana, Slovenia*

Aleksander Matavž − *Condensed Matter Physics Department, Jožef Stefan Institute, 1000 Ljubljana, Slovenia*

Barnik Mandal − *Materials Research and Technology Department (MRT), Luxembourg Institute of Science and Technology (LIST), L-4422 Belvaux, Luxembourg; University of Luxembourg, L-4422 Belvaux, Luxembourg*

Sebastjan Glinšek − *Materials Research and Technology Department (MRT), Luxembourg Institute of Science and Technology (LIST), L-4422 Belvaux, Luxembourg;* orcid.org/0000-0002-5614-0825

Yves Fleming − *Materials Research and Technology Department (MRT), Luxembourg Institute of Science and Technology (LIST), L-4422 Belvaux, Luxembourg*

Andreja Benčan − *Electronic Ceramics Department, Jožef Stefan Institute, 1000 Ljubljana, Slovenia; Jožef Stefan International Postgraduate School, 1000 Ljubljana, Slovenia*

Geoff L. Brennecka − *Department of Metallurgical and Materials Engineering, Colorado School of Mines, Golden, Colorado 80401, United States;* orcid.org/0000-0002-4476-7655

Hana Uršič − *Electronic Ceramics Department, Jožef Stefan Institute, 1000 Ljubljana, Slovenia; Jožef Stefan International Postgraduate School, 1000 Ljubljana, Slovenia;* orcid.org/0000-0003-4525-404X

Complete contact information is available at: https://pubs.acs.org/10.1021/acsaelm.4c00530

Notes

The authors declare no competing financial interest.

■ ACKNOWLEDGMENTS

Slovenian Research Agency (core funding P2-0105, J7-4637, P1-0125, S.W.K - young researcher programme and bilateral cooperation BI-US/22-24-039), NANOCENTER for access to FIB, MSCA-PF grant agreement n° 101110882. Ivana Goričan and Matej Šadl are acknowledged for help related to energy storage properties. The authors thank V. Fišinger for assistance in the AFM laboratory. Barnik Mandal and Sebastjan Glinsek acknowledge the Luxembourg National Research Fund (FNR) for financial support through the project INTER/NWO/20/15079143/TRICOLOR. Geoff Brennecka acknowledges financial support by the Fulbright US Scholar Program, which is sponsored by the US Department of State.

■ REFERENCES

(1) EU-Directive 2002/95/EC. Restriction of the Use of Certain Hazardous Substances in Electrical and Electronic Equipment (RoHS). *Official J. Eur. Union* **2003**, *46* (L37), 19. https://eur-lex.europa.eu/LexUriServ/LexUriServ.do?uri=OJ:L:2003:037:0019:0023:en:PDF

(2) JIS c 0950:2005 (E); *The marking for presence of the specific chemical substances for electrical and electronic equipment*; Japanese Standards Association, 2005, https://www.iaeg.com/binaries/content/assets/iaeg/wg9/rohs-regulatory-alert/japan_rohs-regulation_jis-c-0950_english.pdf (accessed 2024−03−11).

(3) Reczek, K.; Benson, L. M.; *A guide to United States electrical and electronic equipment compliance requirements*; NIST Interagency/Internal Report (NISTIR) 8118r2, 2021, DOI: .

(4) Rödel, J.; Webber, K. G.; Dittmer, R.; Jo, W.; Kimura, M.; Damjanovic, D. Transferring lead-free piezoelectric ceramics into application. *Journal of the European Ceramic Society* **2015**, *35* (6), 1659−1681.

(5) Liu, W.; Ren, X. Large piezoelectric effect in Pb-free ceramics. *Physical review letters* **2009**, *103* (25), No. 257602.

(6) Acosta, M.; Novak, N.; Rossetti, G. A., Jr; Rödel, J. Mechanisms of electromechanical response in $(1-x)Ba(Zr_{0.2}Ti_{0.8})O_3$-$x(Ba_{0.7}Ca_{0.3})TiO_3$ ceramics. *Appl. Phys. Lett.* **2015**, *107* (14), 142906.

(7) Keeble, D. S.; Benabdallah, F.; Thomas, P. A.; Maglione, M.; Kreisel, J. Revised structural phase diagram of $(Ba_{0.7}Ca_{0.3}TiO_3)$-$(BaZr_{0.2}Ti_{0.8}O_3)$. *Appl. Phys. Lett.* **2013**, *102* (9), No. 092903.

(8) Acosta, M.; Novak, N.; Jo, W.; Rödel, J. Relationship between electromechanical properties and phase diagram in the $Ba(Zr_{0.2}Ti_{0.8})$-$O_3-x(Ba_{0.7}Ca_{0.3})TiO_3$ lead-free piezoceramic. *Acta Mater.* **2014**, *80*, 48−55.

(9) Hao, J.; Bai, W.; Li, W.; Zhai, J. Correlation between the microstructure and electrical properties in high-performance $(Ba_{0.85}Ca_{0.15})(Zr_{0.1}Ti_{0.9})O_3$ lead-free piezoelectric ceramics. *J. Am. Ceram. Soc.* **2012**, *95* (6), 1998−2006.

(10) Yan, X.; Lam, K. H.; Li, X.; Chen, R.; Ren, W.; Ren, X.; Shung, K. K. Correspondence: Lead-free intravascular ultrasound transducer using BZT-50BCT ceramics. *IEEE Trans. Sonics Ultrason.* **2013**, *60* (6), 1272−1276.

(11) Scarisoreanu, N. D.; Craciun, F.; Ion, V.; Birjega, R.; Bercea, A.; Dinca, V.; Gruionu, G. Lead-free piezoelectric $(Ba,Ca)(Zr,Ti)O_3$ thin

films for biocompatible and flexible devices. *ACS Appl. Mater. Interfaces* **2017**, *9* (1), 266−278.
(12) Palneedi, H.; Peddigari, M.; Hwang, G. T.; Jeong, D. Y.; Ryu, J. High-performance dielectric ceramic films for energy storage capacitors: progress and outlook. *Adv. Funct. Mater.* **2018**, *28* (42), No. 1803665.
(13) Puli, V. S.; Pradhan, D. K.; Chrisey, D. B.; Tomozawa, M.; Sharma, G. L.; Scott, J. F.; Katiyar, R. S. Structure, dielectric, ferroelectric, and energy density properties of (1−x)BZT−x BCT ceramic capacitors for energy storage applications. *J. Mater. Sci.* **2013**, *48*, 2151−2157.
(14) Syal, R.; Goel, R.; De, A.; Singh, A. K.; Sharma, G.; Thakur, O. P.; Kumar, S. Flattening of free energy profile and enhancement of energy storage efficiency near morphotropic phase boundary in lead-free BZT-xBCT. *J. Alloys Compd.* **2021**, *873*, No. 159824.
(15) Puli, V. S.; Pradhan, D. K.; Adireddy, S.; Martínez, R.; Silwal, P.; Scott, J. F.; Katiyar, R. S. Nanoscale polarisation switching and leakage currents in $(Ba_{0.955}Ca_{0.045})(Zr_{0.17}Ti_{0.83})O_3$ epitaxial thin films. *J. Phys. D: Appl. Phys.* **2015**, *48* (35), No. 355502.
(16) Hasenkox, U.; Hoffmann, S.; Waser, R. Influence of precursor chemistry on the formation of $MTiO_3$ (M= Ba, Sr) ceramic thin films. *J. Sol-Gel Sci. Technol.* **1998**, *12*, 67−79.
(17) Krupanidhi, S. B.; Peng, C. J. Studies on structural and electrical properties of barium strontium titanate thin films developed by metallo-organic decomposition. *Thin Solid Films* **1997**, *305* (1−2), 144−156.
(18) Kang, G.; Yao, K.; Wang, J. $(1-x)Ba(Zr_{0.2}Ti_{0.8})O_3$ − $x(Ba_{0.7}Ca_{0.3})TiO_3$ Ferroelectric Thin Films Prepared from Chemical Solutions. *J. Am. Ceram. Soc.* **2012**, *95* (3), 986−991.
(19) Wang, Z.; Cai, Z.; Wang, H.; Cheng, Z.; Chen, J.; Guo, X.; Kimura, H. Lead-free 0.5 $Ba(Ti_{0.8}Zr_{0.2})O_3$ - $0.5(Ba_{0.7}Ca_{0.3})TiO_3$ thin films with enhanced electric properties fabricated from optimized sol-gel systems. *Mater. Chem. Phys.* **2017**, *186*, 528−533.
(20) Li, W. L.; Zhang, T. D.; Xu, D.; Hou, Y. F.; Cao, W. P.; Fei, W. D. $LaNiO_3$ seed layer induced enhancement of piezoelectric properties in (100)-oriented (1−x) BZT−xBCT thin films. *Journal of the European Ceramic Society* **2015**, *35* (7), 2041−2049.
(21) Barbato, P. S.; Casuscelli, V.; Aprea, P.; Scaldaferri, R.; Caputo, D. Optimization of the production process of BZT−BCT sol−gel thin films obtained from a highly stable and green precursor solution. *Materials and Manufacturing Processes* **2021**, *36* (14), 1642−1649.
(22) Xu, J.; Zhou, Y.; Li, Z.; Lin, C.; Zheng, X.; Lin, T.; Wang, F. Microstructural, ferroelectric and photoluminescence properties of Er^{3+}-doped $Ba_{0.85}Ca_{0.15}Ti_{0.9}Zr_{0.1}O_3$ thin films. *Mater. Chem. Phys.* **2021**, *262*, No. 124320.
(23) Liu, S.; Zhang, Z.; Shan, Y.; Hong, Y.; Farooqui, F.; Lam, F. S.; Yang, Z. A flexible and lead-free BCZT thin film nanogenerator for biocompatible energy harvesting. *Mater. Chem. Front.* **2021**, *5* (12), 4682−4689.
(24) Reddy, S. R.; Kumar, A.; James, A. R.; Prasad, V. B.; Roy, S. K. Ferroelectric and nano-mechanical properties of the chemical solution deposited lead-free BCZT films. *Materials Science and Engineering* **2021**, *265*, No. 115037. B
(25) Sharma, H.; Maurya, K. K.; Shah, J.; Kotnala, R. K.; Negi, N. S. Enhanced dielectric and ferroelectric properties of chemical solution processed lead-free $Ba_{1-x}Ca_xZr_{0.1}Ti_{0.9}O_3$ thin films. *Ferroelectrics* **2021**, *582* (1), 80−97.
(26) Wang, H.; Xu, J.; Ma, C.; Xu, F.; Wang, L.; Bian, L.; Chang, A. Spectroscopic ellipsometry study of $0.5BaZr_{0.2}Ti_{0.8}O_3$− $0.5Ba_{0.7}Ca_{0.3}TiO_3$ ferroelectric thin films. *Journal of alloys and compounds* **2014**, *615*, 526−530.
(27) Mandeljc, M.; Kosec, M.; Malič, B.; Samardzija, Z. Low temperature processing of lanthanum doped PZT thin films. *Integr. Ferroelectr.* **2000**, *30* (1−4), 149−156.
(28) Hoffmann, S.; Waser, R. Control of the morphology of CSD-prepared $(Ba,Sr)TiO_3$ thin films. *Journal of the European Ceramic Society* **1999**, *19* (6−7), 1339−1343.
(29) Mansour, C.; Benwadih, M.; Revenant, C. Sol−gel derived barium strontium titanate thin films using a highly diluted precursor solution. *AIP Advances* **2021**, *11* (8), No. 085302.
(30) Aygün, S. M.; Ihlefeld, J. F.; Borland, W. J.; Maria, J. P. Permittivity scaling in $Ba_{1-x}Sr_xTiO_3$ thin films and ceramics. *J. Appl. Phys.* **2011**, *109* (3), No. 034108.
(31) Pečnik, T.; Benčan, A.; Glinšek, S.; Malič, B. Tailoring the microstructure and dielectric properties of $Ba_{0.5}Sr_{0.5}TiO_3$ thin films by solution-based processing in the frame of the Microstructural Zone Model. *J. Alloys Compd.* **2018**, *743*, 812−818.
(32) Ihlefeld, J. F.; Maria, J. P.; Borland, W. Dielectric and microstructural properties of barium titanate zirconate thin films on copper substrates. *Journal of materials research* **2005**, *20* (10), 2838−2844.
(33) Teranishi, T.; Kajiyama, S.; Hayashi, H.; Kishimoto, A. Polarization behavior of sol-gel-derived relaxor $Ba(Zr,Ti)O_3$ films. *J. Am. Ceram. Soc.* **2017**, *100* (4), 1542−1550.
(34) Zhai, J.; Yao, X.; Shen, J.; Zhang, L.; Chen, H. Structural and dielectric properties of $Ba(Zr_xTi_{1-x})O_3$ thin films prepared by the sol−gel process. *J. Phys. D: Appl. Phys.* **2004**, *37* (5), 748.
(35) Singh, B.; Kumar, S.; Arya, G. S.; Negi, N. S. Room temperature structural and electrical properties of barium calcium titanate (BCT) thin films. *AIP Conf. Proc.* **2015**, *1661* (1), No. 060005, DOI: 10.1063/1.4915375.
(36) Jia, Q.; Shen, B.; Hao, X.; Song, S.; Zhai, J. Anomalous dielectric properties of $Ba_{1-x}Ca_xTiO_3$ thin films near the solubility limit. *Mater. Lett.* **2009**, *63* (3−4), 464−466.
(37) Konsago, S. W.; Žiberna, K.; Kmet, B.; Benčan, A.; Uršič, H.; Malič, B. Chemical Solution Deposition of Barium Titanate Thin Films with Ethylene Glycol as Solvent for Barium Acetate. *Molecules* **2022**, *27* (12), 3753.
(38) Livage, C.; Safari, A.; Klein, L. C. Glycol-based sol-gel process for the fabrication of ferroelectric PZT thin films: Code: EP28. *J. Sol-Gel Sci. Technol.* **1994**, *2*, 605−609.
(39) Uršič, H.; Prah, U. Investigations of ferroelectric polycrystalline bulks and thick films using piezoresponse force microscopy. *Proceedings of the Royal Society A* **2019**, *475* (2223), No. 20180782.
(40) Jung, W. S.; Min, B. K.; Park, J.; Yoon, D. H. Formation mechanism of barium titanate by thermal decomposition of barium titanyl oxalate. *Ceram. Int.* **2011**, *37* (2), 669−672.
(41) Barbatoa, P. S.; Casuscellib, V.; Apreaa, P.; Scaldaferrib, R.; Pedacib, I.; Caputoa, D. Green production of lead-free BZT-BCT thin films for applications in MEMS devices. *Chem. Eng. Trans.* **2021**, *84*, 97−102.
(42) Hoffmann, S.; Hasenkox, U.; Waser, R.; Jia, C. L.; Urban, K. Chemical Solution Deposited $BaTiO_3$ AND $SrTiO_3$ Thin Films with Columnar Microstructure. *MRS Online Proceedings Library (OPL)* **1997**, *474*, 9.
(43) Abazari, M.; Akdoğan, E. K.; Safari, A. Effect of manganese doping on remnant polarization and leakage current in $(K_{0.44},Na_{0.52},Li_{0.04})(Nb_{0.84},Ta_{0.10},Sb_{0.06})$ O_3 epitaxial thin films on $SrTiO_3$. *Appl. Phys. Lett.* **2008**, *92* (21), 212903.
(44) Birkholz, M.; *Thin film analysis by X-ray scattering*; John Wiley & Sons, 2006.
(45) Schenk, T.; Bencan, A.; Drazic, G.; Condurache, O.; Valle, N.; Adib, B. E.; Glinsek, S. Enhancement of ferroelectricity and orientation in solution-derived hafnia thin films through heterogeneous grain nucleation. *Appl. Phys. Lett.* **2021**, *118* (16), No. 162902.
(46) Konsago, S. W.; Debevec, A.; Cilenšek, J.; Kmet, B.; Malič, B. Linear Thermal Expansion of $0.5Ba(Zr_{0.2}Ti_{0.8})O_3$-$0.5(Ba_{0.7}Ca_{0.3})TiO_3$ Bulk Ceramic. *Inform. MIDEM* **2023**, *53* (4), 233−238.
(47) Okaji, M. Absolute thermal expansion measurements of single-crystal silicon in the range 300−1300 K with an interferometric dilatometer. *Int. J. Thermophys.* **1988**, *9*, 1101−1109.
(48) Jia, C. L.; Urban, K.; Hoffmann, S.; Waser, R. Microstructure of columnar-grained $SrTiO_3$ and $BaTiO_3$ thin films prepared by chemical solution deposition. *J. Mater. Res.* **1998**, *13* (8), 2206−2217.
(49) Ophus, C. Four-Dimensional Scanning Transmission Electron Microscopy (4D-STEM): From Scanning Nanodiffraction to Ptychography and Beyond. *Microsc. Microanal.* **2019**, *25*, 563−582.
(50) Amorín, H.; Venet, M.; García, J. E.; Ochoa, D. A.; Ramos, P.; López-Sánchez, J.; Algueró, M. Insights into the Early Size Effects of

https://doi.org/10.1021/acsaelm.4c00530
ACS Appl. Electron. Mater. 2024, 6, 4467−4477

Lead-Free Piezoelectric $Ba_{0.85}Ca_{0.15}Zr_{0.1}Ti_{0.9}O_3$. *Adv. Electronic Mater.* **2023**, *10*, No. 2300556.
(51) Noguchi, Y.; Miyayama, M. Effect of Mn doping on the leakage current and polarization properties in $K_{0.14}Na_{0.86}NbO_3$ ferroelectric single crystals. *Journal of the Ceramic Society of Japan* **2010**, *118* (1380), 711−716.
(52) Mgbemere, H. E.; Hinterstein, M.; Schneider, G. A. Structural phase transitions and electrical properties of $(K_xNa_{1-x})NbO_3$-based ceramics modified with Mn. *Journal of the European Ceramic Society* **2012**, *32* (16), 4341−4352.
(53) Borderon, C.; Nadaud, K.; Coulibaly, M.; Renoud, R.; Gundel, H. Mn-Doped $Ba_{0.8}Sr_{0.2}TiO_3$ Thin Films for Energy Storage Capacitors. *Int. J. Adv. Res. Phys. Sci.* **2019**, *6* (2), 2349−7882.
(54) Semenov, A.; Dedyk, A.; Mylnikov, I.; Pakhomov, O.; Eskov, A.; Anokhin, A.; Kholkin, A. Mn-doped $BaTiO_3$ ceramics: Thermal and electrical properties for multicaloric applications. *Materials* **2019**, *12* (21), 3592.
(55) Chi, Q. G.; Zhang, C. H.; Sun, J.; Yang, F. Y.; Wang, X.; Lei, Q. Q. Interface optimization and electrical properties of 0.5 $Ba(Zr_{0.2}Ti_{0.8})O_3$−0.5$(Ba_{0.7}Ca_{0.3})TiO_3$ thin films prepared by a sol−gel process. *J. Phys. Chem. C* **2014**, *118* (28), 15220−15225.
(56) Lin, Y.; Wu, G.; Qin, N.; Bao, D. Structure, dielectric, ferroelectric, and optical properties of (1−x)$Ba(Zr_{0.2}Ti_{0.8})O_3$−x-$(Ba_{0.7}Ca_{0.3})TiO_3$ thin films prepared by sol−gel method. *Thin Solid Films* **2012**, *520* (7), 2800−2804.
(57) Chi, Q. G.; Zhu, H. F.; Xu, J. C.; Wang, X.; Lin, J. Q.; Sun, Z.; Lei, Q. Q. Microstructures and electrical properties of 0.5$(Ba_{0.7}Ca_{0.3})$-TiO_3−0.5$Ba(Zr_{0.2}Ti_{0.8})O_3$ thin films prepared by a sol−gel route. *Ceram. Int.* **2013**, *39* (7), 8195−8198.
(58) Nguyen, M. D.; Rijnders, G. Comparative study of piezoelectric response and energy-storage performance in normal ferroelectric, antiferroelectric and relaxor-ferroelectric thin films. *Thin solid films* **2020**, *697*, No. 137843.
(59) Silva, J. P.; Silva, J. M.; Oliveira, M. J.; Weingärtner, T.; Sekhar, K. C.; Pereira, M.; Gomes, M. J. High-performance ferroelectric−dielectric multilayered thin films for energy storage capacitors. *Adv. Funct. Mater.* **2019**, *29* (6), No. 1807196.
(60) Sivaramakrishnan, S.; Mardilovich, P.; Schmitz-Kempen, T.; Tiedke, S. Concurrent wafer-level measurement of longitudinal and transverse effective piezoelectric coefficients ($d_{33,f}$ and $e_{31,f}$) by double beam laser interferometry. *J. Appl. Phys.* **2018**, *123* (1), No. 014103, DOI: 10.1063/1.5019568.
(61) Matavž, A.; Bradeško, A.; Rojac, T.; Malič, B.; Bobnar, V. Self-assembled porous ferroelectric thin films with a greatly enhanced piezoelectric response. *Applied Materials Today* **2019**, *16*, 83−89.

https://doi.org/10.1021/acsaelm.4c00530
ACS Appl. Electron. Mater. 2024, 6, 4467−4477

Supporting Information

Engineering the Microstructure and Functional Properties of $0.5Ba(Zr_{0.2}Ti_{0.8})O_3$-$0.5(Ba_{0.7}Ca_{0.3})TiO_3$ Thin Films

*[1,2]Sabi William Konsago, [1,2]Katarina Žiberna, [3]Aleksander Matavž, [4,5]Barnik Mandal, [5]Sebastjan Glinšek, [4]Yves Fleming, [1,2]Andreja Benčan, [6]Geoff L. Brennecka, [1,2]Hana Uršič, [1,2]Barbara Malič**

[1] Electronic Ceramics Department, Jožef Stefan Institute, Jamova Cesta 39, 1000 Ljubljana, Slovenia

[2]Jožef Stefan International Postgraduate School, Jamova Cesta 39, 1000 Ljubljana, Slovenia,

[3]Condensed Matter Physics Department, Jožef Stefan Institute, Jamova Cesta 39, 1000 Ljubljana, Slovenia

[4]Materials Research and Technology Department (MRT), Luxembourg Institute of Science and Technology (LIST), 41 rue du Brill, L-4422 Belvaux, Luxembourg,

[5]University of Luxembourg, 41 rue du Brill, L-4422, Belvaux, Luxembourg

[6]Department of Metallurgical and Materials Engineering, Colorado School of Mines, Golden, Colorado 80401, USA

*Corresponding author's email address: barbara.malic@ijs.si

3.3.Engineering the Microstructure and Functional Properties of $Ba(Ti_{0.8}Zr_{0.2})O_3$-$(Ba_{0.7}Ca_{0.3})TiO_3$ Thin Films

Supporting Information

Supplement Material S1. Dielectric data as a function of the frequency of the BZT-BCT-0.2M films

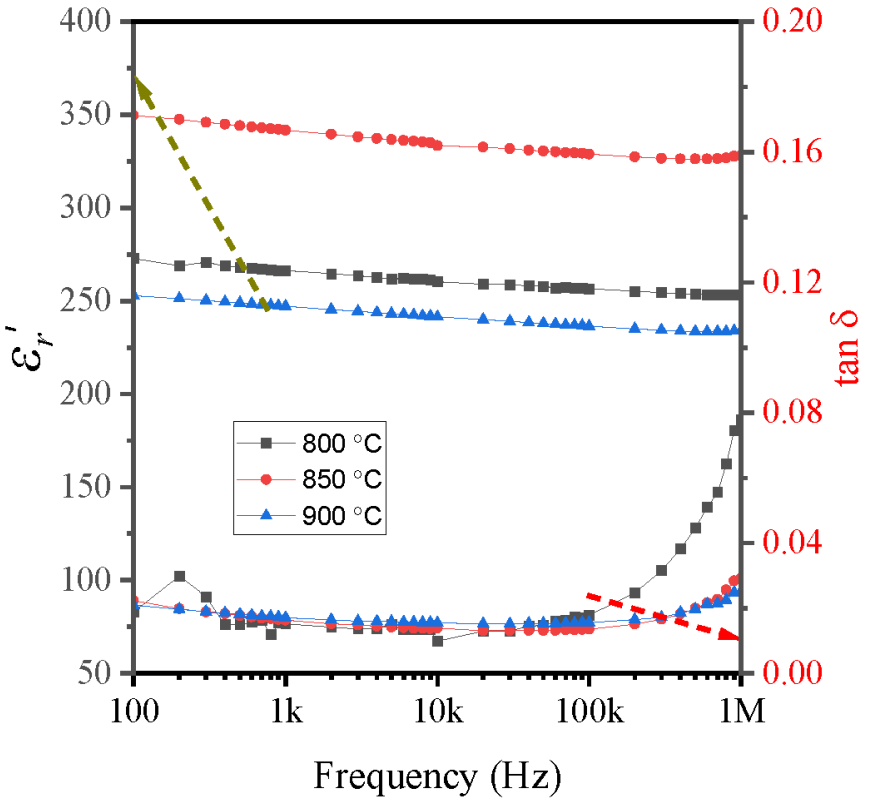

Figure S1. Frequency dependence of dielectric permittivity (ε_r') and losses (tan δ) at room temperature of BZT-BCT-0.2M annealed at different temperatures.

Supporting Information

Supplement Material S2. The polarization-electric field (*P*-*E*) loops of the BZT-BCT-0.2M films

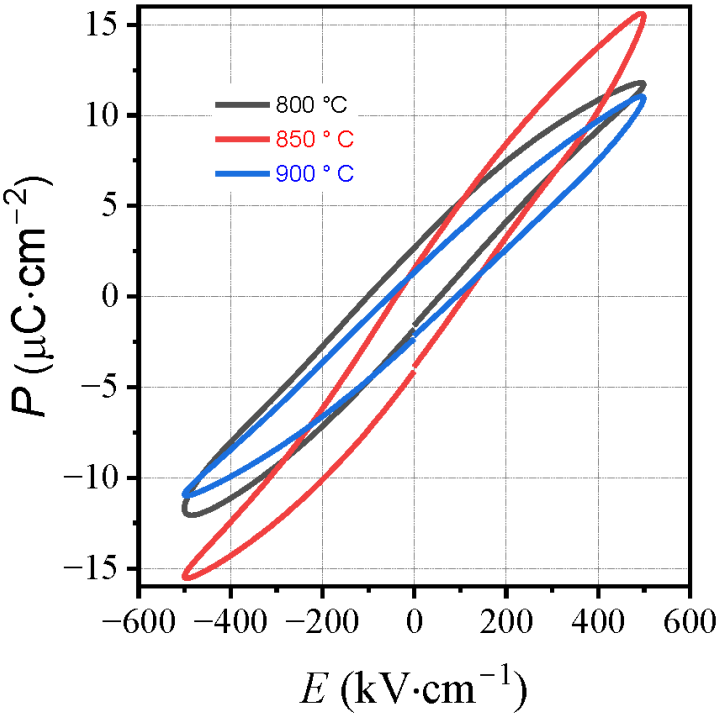

Figure S2. Electric-field dependence of the electrical polarization of BZT-BCT-0.2M films annealed at different temperatures.

Supporting Information

Supplement Material S3. XRD patterns recorded in Bragg-Brentano geometry of the BZT-BCT-0.1M and BZT-BCT-Mn-0.1M films

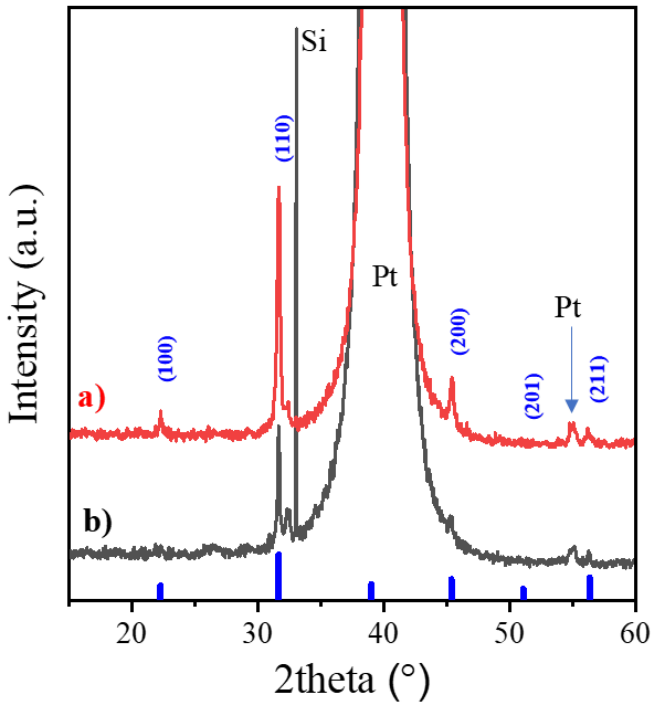

Figure S3. XRD patterns of a) BZT-BCT-0.1M and b) BZT-BCT-Mn-0.1M films on Pt/Si annealed at 850 °C recorded in Bragg-Brentano geometry.

Supporting Information

Supplement Material S4. (110) XRD pole figure of the BZT-BCT-Mn-0.1M film

A strong intensity ring is observed at a tilt angle Ψ = ~35 °. As the angle between [111] and [110] in (pseudo-)cubic systems is 35.3 °, this further confirms (111) out-of-plane orientation of the film. The fact that the intensity of the ring is constant at all rotational φ angles indicates random in-plane orientation of the film.

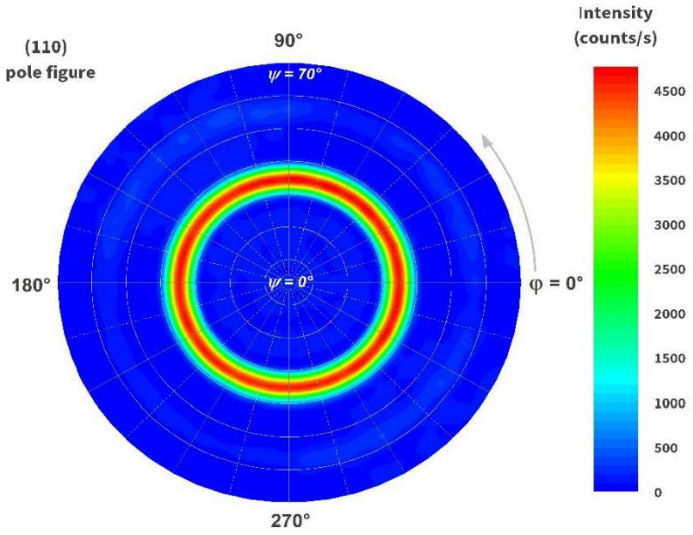

Figure S4. BZT-BCT-Mn-0.1M film on Pt/Si annealed at 850 °C. Pole figure of (110) peak. Measurement conditions: The measurements were performed with 2θ fixed at 31.5 °. Tilt angle Ψ was ranging from 0 to 72 ° (step = 3 °) and rotational angle φ was ranging from 0 to 355 ° (step = 5 °). Collection time for each data point was 18 s. The measurement was performed with a 1 mm collimator.

Supporting Information

Supplement Material S4. The second-cycle unipolar (*P-E*) loops and calculated energy storage properties of the BZT-BCT-Mn-0.1M film

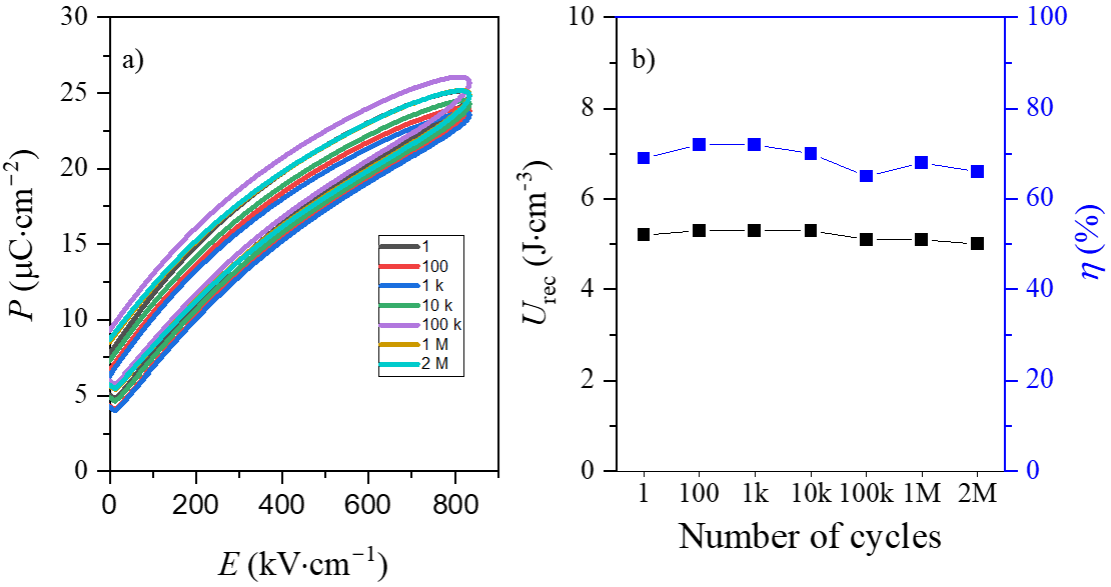

Figure S5. a) Unipolar *P-E* loops and b) recoverable energy density (U_{rec}) and efficiency (η) of BZT-BCT-Mn-0.1M film upon electric field cycling.

3.4. $0.5Ba(Zr_{0.2}Ti_{0.8})O_3$-$0.5(Ba_{0.7}Ca_{0.3})TiO_3$ Thin Films on Platinized Sapphire Substrates

3.4.1. High Energy Storage Density and Efficiency of $0.5Ba(Zr_{0.2}Ti_{0.8})O_3$-$0.5(Ba_{0.7}Ca_{0.3})TiO_3$ Thin Films on Platinized Sapphire Substrates

In our previous work, we prepared $0.5Ba(Zr_{0.2}Ti_{0.8})O_3$-$0.5(Ba_{0.7}Ca_{0.3})TiO_3$ (BZT–BCT) thin films doped with manganese by chemical solution deposition on platinized silicon (Pt/Si) substrates. The films showed promising energy storage properties. However, due to a large difference in thermal expansion coefficient (TEC) of BZT-BCT and silicon substrate, intergranular cracks evolved concurrent with decreased functional properties when the thickness of the films exceeded about 120 nm (see Chapter 3.3).

In this study, we used platinized sapphire substrates, characterized by a much larger TEC than Si, which allowed us to prepare crack-free BZT-BCT films with thicknesses up to 340 nm. The multistep annealing resulted in the films with columnar microstructure. The tilt-angle (Ψ)-dependent XRD analysis revealed that the tensile stresses in the 100 nm and 340 nm thick films are 649 MPa and 781 MPa, respectively.

The dielectric permittivity of the 340 nm thick film is about 820, ≈60 % higher than that of the 100 nm thick film measured at 1 kHz and room temperature. The thinner film exhibits a larger coercive field and remnant polarization of about 110 $kV \cdot cm^{-1}$ and 6 $\mu C \cdot cm^{-2}$ at 1 $MV \cdot cm^{-1}$ compared to 45 $kV \cdot cm^{-1}$ and 4 $\mu C \cdot cm^{-2}$ for the thicker film. The improved properties of the 340 nm thick films are attributed to the dielectric grain size and film-thickness effects. Interestingly, the 340 nm thick films conserve the ferroelectric properties from -75 °C to 150 °C, well beyond the broad permittivity peak between 40 °C and 50 °C, indicating a relaxor-like behaviour. The recoverable energy storage density of the films is about 46 $J \cdot cm^{-3}$, and the energy storage efficiency is 89%. The obtained values are above or comparable to those of lead-based and lead-free perovskite relaxor or antiferroelectric thin films reported in the literature.

Our results reveal that by selecting the appropriate substrate and designing the microstructure of the BZT-BCT films, high energy storage density and energy storage efficiency are achieved in a wide temperature range. Such films show potential for energy storage applications in different environments.

The results of this article confirm the hypotheses 5 and 6; and address the aims 3 and 4.

Published in: S. W. Konsago, K. Žiberna, A. Matavž, B. Mandal, S. Glinšek, Y. Fleming, A. Benčan, G. L. Brennecka, H. Uršič, and B. Malič, "High Energy Storage Density and Efficiency of $0.5Ba(Zr_{0.2}Ti_{0.8})O_3$-$0.5(Ba_{0.7}Ca_{0.3})TiO_3$ Thin Films on Platinized Sapphire Substrates", *RSC Journal of Materials Chemistry A*, Vol 13, Issue 4, pp. 2911 – 2919, 2025 (IF = 10.7)

My contribution: I synthesized the BZT-BCT coating solution and prepared the BZT-BCT films. I performed the XRD data analysis. I measured dielectric, ferroelectric, and energy storage properties. I prepared the concept of the paper jointly with my supervisor and wrote the manuscript with all co-authors.

Journal of Materials Chemistry A

ROYAL SOCIETY OF CHEMISTRY

PAPER

View Article Online
View Journal | View Issue

Check for updates

Cite this: J. Mater. Chem. A, 2025, 13, 2911

High energy storage density and efficiency of $0.5Ba(Zr_{0.2}Ti_{0.8})O_3$–$0.5(Ba_{0.7}Ca_{0.3})TiO_3$ thin films on platinized sapphire substrates

Sabi William Konsago, *[ab] Katarina Žiberna,[ab] Aleksander Matavž,[a] Barnik Mandal,[cd] Sebastjan Glinšek,[d] Geoff L. Brennecka,[e] Hana Uršič[ab] and Barbara Malič *[ab]

Received 13th August 2024
Accepted 4th December 2024

DOI: 10.1039/d4ta05675b

rsc.li/materials-a

Manganese-doped $0.5Ba(Zr_{0.2}Ti_{0.8})O_3$–$0.5(Ba_{0.7}Ca_{0.3})TiO_3$ (BZT–BCT) ferroelectric thin films deposited on platinized sapphire substrates by chemical solution deposition and multistep-annealed at 850 °C, are investigated. The 100 nm and 340 nm thick films are crack-free and have columnar microstructures with average lateral grain sizes of 58 nm and 92 nm, respectively. The 340 nm thick films exhibit a relative permittivity of about 820 at 1 kHz and room temperature, about 60% higher than the thinner films, which is attributed to the dielectric grain size effect. The thinner films exhibit a larger coercive field and remanent polarization of about 110 kV cm^{-1} and 6 μC cm^{-2} respectively, at 1 MV cm^{-1} compared to 45 kV cm^{-1} and 4 μC cm^{-2} for the thicker films. The 340 nm thick films exhibit a maximum polarization of about 47 μC cm^{-2} at 3.5 MV cm^{-1} and slim polarization loops, resulting in high energy storage properties with 46 J cm^{-3} of recoverable energy storage density and 89% energy storage efficiency.

1. Introduction

Rapid development and massive use of electronics have increased the demand for energy storage. Many efforts have been made to improve existing energy storage technologies, especially batteries and capacitors. In contrast to batteries, capacitors are charged and can release the charged energy within milliseconds or even nanoseconds with relatively high efficiency.[1,2] Due to the fast charging and release of electrical energy or voltage, capacitors are increasingly required in many medical devices such as pacemakers, defibrillators, and military equipment such as ballistic missiles, radars, *etc.*[3–5] In the group of ferroics, ferroelectrics are not the optimum choice due to the high remanent polarization and coercive field, thus low energy storage efficiency, while antiferroelectrics and relaxor ferroelectrics are among the most efficient materials for energy storage.[6,7] The thin film form of these materials with a higher electric breakdown field than bulk and high polarization enable high energy storage density and efficiency.[6–9]

Lead-free materials, including $0.5Ba(Zr_{0.2}Ti_{0.8})O_3$–$0.5(Ba_{0.7}Ca_{0.3})TiO_3$ (BZT–BCT), which has been reported to be a relaxor-like ferroelectric in its bulk form,[10] are investigated for energy storage applications.[8,9] However, the microstructure and ferroelectric/piezoelectric and energy storage properties of BZT–BCT thin films prepared by chemical solution deposition (CSD), are difficult to control.[11,12] An alternative ethylene glycol-based CSD of barium titanate (BT) films instead of the conventional carboxylic acid-based synthesis enables the decomposition of organic residues at a relatively low temperature. It thus contributes to decreasing the crystallization temperature and controlling the microstructure of $BaTiO_3$ (BT) films.[13]

In our earlier study, we used a similar solution chemistry, and by optimizing the processing conditions, we prepared BZT–BCT films with a columnar microstructure upon multistep annealing at 850 °C. However, crack-free BZT–BCT films could only be obtained if the film thickness did not exceed about 100 nm. In contrast, in thicker films, the evolution of intergranular cracks was attributed to the biaxial stress stemming from the thermal expansion mismatch between the ceramic film and platinized silicon substrate. Note that BZT–BCT thin films were doped with manganese (1 mol%) to reduce the leakage current critical for electric field-dependent properties.[14]

In the present study, we report the energy storage properties of BZT–BCT thin films. Using platinized sapphire substrates with about three times the thermal expansion coefficient of silicon allowed us to reduce the thermal stress and obtain crack-free BZT–BCT films with a thickness of about 300 nm exhibiting energy storage properties comparable to state-of-the-art lead-

[a]Jožef Stefan Institute, Jamova cesta 39, 1000 Ljubljana, Slovenia. E-mail: sabi.william.konsago@ijs.si; barbara.malic@ijs.si

[b]Jožef Stefan International Postgraduate School, Jamova cesta 39, 1000 Ljubljana, Slovenia

[c]University of Luxembourg, 41 rue du Brill, L-4422, Belvaux, Luxembourg

[d]Luxembourg Institute of Science and Technology (LIST), 41, rue du Brill, L-4422 Belvaux, Luxembourg

[e]Colorado School of Mines, Golden, Colorado 80401, USA

View Article Online
Journal of Materials Chemistry A Paper

based relaxor and anti-ferroelectric films, with stable performance across a wide temperature range.

2. Experimental part

The $0.5Ba(Zr_{0.2}Ti_{0.8})O_3$–$0.5(Ba_{0.7}Ca_{0.3})TiO_3$, (BZT–BCT) precursor is prepared from alkaline earth acetates (barium acetate ($Ba(CH_3COO)_2$, $Ba(OAc)_2$), 99.97%), calcium acetate (($Ca(CH_3COO)_2$, $Ca(OAc)_2$), 99.999%), purchased from Sigma-Aldrich, St. Louis, Missouri, USA and Alfa Aesar, Karlsruhe, Germany and transition metal alkoxides (zirconium butoxide ($Zr(OC_4H_9)_4$ or $Zr(OnBu)_4$), 80%) and titanium butoxide (($Ti(OC_4H_9)_4$ or $Ti(OnBu)_4$), 99.61%) both purchased from Alfa Aesar, Karlsruhe, Germany. The alkaline earth acetates are dissolved in ethylene glycol ($OHCH_2CH_2OH$, EG, 99.8%, Sigma-Aldrich, St. Louis, Missouri, USA) at room temperature separately from the transition metal alkoxides, which are diluted in ethanol (CH_3CH_2OH, EtOH 99.9%, Sigma-Aldrich, St. Louis, Missouri, USA). Manganese acetate (($Mn(CH_3COO)_2$, $Mn(OAc)_2$), 98%, Alfa Aesar, Karlsruhe, Germany) is added to the solution of alkaline-earth acetates overstoichiometrically in the amount of 1 mol% as a doping agent. After the complete dissolution of acetates in EG, both solutions are mixed. The concentration of BZT–BCT coating solution is adjusted to 0.1 M, keeping the volume ratio of EG/EtOH at 3/2. The reagents are manipulated in a nitrogen-filled glove box.

C-Sapphire (500 μm-thick, Siegert Wafer, Aachen, Germany) was used as a substrate. 23 nm of HfO_2 was deposited on top using atomic layer deposition (TFS-200, Beneq, Espoo, Finland), followed by sputtering of Pt (100 nm, MED-020, Baltec Leica, Wetzlar, Germany). The 0.1 M BZT–BCT coating solution was deposited on platinized *C*-Sapphire substrates by spin coating (WS-400B-6NPP/LITE, Laurell, North Wales, Pennsylvania, USA) at 3000 rpm for 30 seconds, followed by drying at 250 °C for 15 minutes, pyrolysis at 350 °C for 15 minutes and annealing at 850 °C. The films were annealed with a heating rate of 13.3 °C s^{-1} after each deposition, and the times were 15 min for the first and the last deposited layers and 5 min for the intermediate layers. All steps were repeated 10 and 30 times to reach the BZT–BCT-Mn films with thicknesses of about 100 nm and 340 nm, respectively, denoted BZT–BCT-100 and BZT–BCT-340.

The phase composition of the films was characterized by XRD with Cu Kα radiation performed in the 2θ ranges of 10–39° and 40–65° to avoid recording the Pt (111) peak on a high-resolution diffractometer (X'Pert PRO, PANalytical, Almelo, The Netherlands, step = 0.034°, time per step = 100 s, soller slit

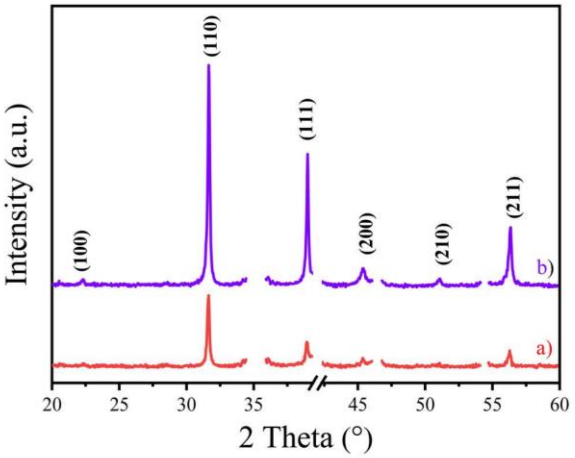

Fig. 2 XRD patterns of (a) BZT–BCT-100, (b) BZT–BCT-340 films. The diffraction peaks of the substrate were removed to have a better view of the perovskite pattern.

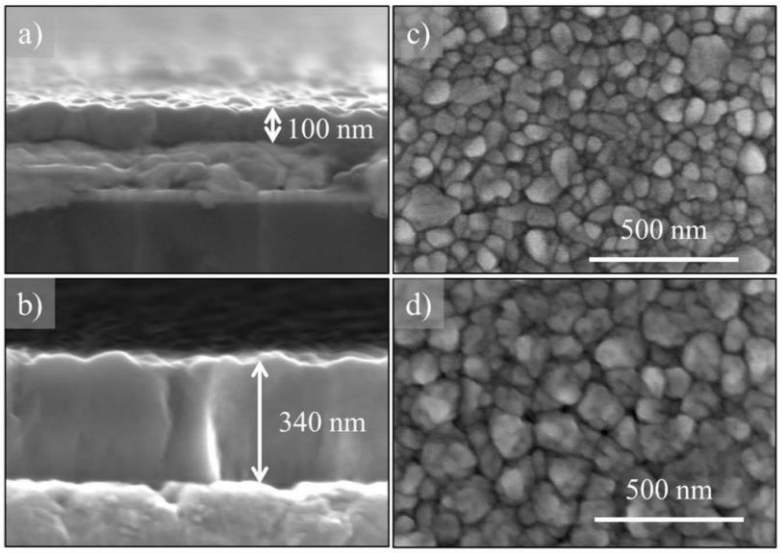

Fig. 1 SEM cross-section micrographs of (a) BZT–BCT-100, (b) BZT–BCT-340, and (c and d) their respective plan view micrographs.

View Article Online
Paper Journal of Materials Chemistry A

= 0.02 rad, mask10). The phase analysis was performed using X'Pert High Score Plus software.

A Bruker D8 Discover with Cu Kα radiation was used for grazing incidence X-ray diffraction (GIXRD). The experiment was conducted with an incident angle of 0.5°, scanning the 2θ-range from 20° to 60° with the step of 0.02°, and time per step set of 4 s. The same tool was used for the Ψ-scan (θ–2θ scan with different tilt angles, Ψ) with a 1 mm collimator. The measurement was performed in a 2θ- and Ψ-range from 30.5° to 32.5° and from 0° to 50°, respectively. The 2θ-step was 0.02° and the time per step was 90 s.

The microstructure was characterized using a Verios 4G HP field emission scanning electron microscope (Thermo Fischer, Waltham, Massachusetts, USA) with an accelerating voltage of 5 kV. Before SEM imaging, a 5 nm-thick carbon layer was coated on the film using a Precise Etching and Coating System 628A (Gatan, Pleasanton, California, USA). The average grain size was determined using the linear intercept method on the obtained SEM images, measuring at least 400 grains on each sample.

For the electrical measurements, top gold electrodes with a diameter of 400 μm were deposited on the films through a shadow mask by magnetron sputtering (5 pascal, Trezzano sul Naviglio, Milan, Italy). The films were etched at the edge using a mixture of HF 40% (Alfa Aeser, Karlsruhe, Germany) HCl 37–38% (J.T. Baker, Phillipsburg, New Jersey USA) and deionized H_2O in the volume ratio (2 : 5 : 20) to reach the bottom electrode.

The dielectric properties as functions of frequency and temperature were measured using an impedance analyzer (HP 4284A, Keysight, Santa Rosa, USA) from 1 kHz to 1 MHz at room temperature and from −50 to 150 °C across a frequency range from 33 Hz to 100 kHz.

The capacitance (C) and the polarization (P) as functions of the electric field (E) were measured using the Aixacct TF Analyzer 2000 (Aixacct Systems GmbH, Aachen, Germany) at 1 kHz with a small-signal amplitude of 50 mV for C–E measurement and with a sinusoidal signal for P–E measurement, respectively. The BZT–BCT-340 film was selected to investigate the ferroelectric properties at temperatures from −75 to 150 °C.

3. Results and discussion

The SEM plan view and cross-section micrographs of BZT–BCT-100, and BZT–BCT-340 films are shown in Fig. 1. The thicknesses of the films are about 100 nm and 340 nm, respectively, as evident from the cross-sections shown in Fig. 1a and b. The columnar microstructure results from the multistep annealing strategy.[14] Both films are crack-free and with very few pores. The average lateral grain sizes are 58 nm and 92 nm for BZT–BCT-100 and BZT–BCT-340 films, respectively. The increase of the grain size with increasing thickness is in agreement with earlier studies.[15–17] Crack-free BZT–BCT films with thicknesses of up to 340 nm are achieved by using Pt/sapphire (Pt/Sa) as a substrate, whose thermal expansion coefficient (TEC) is closer to that of BZT–BCT. Previous works reported the evolution of cracks in BZT–BCT films on Pt/Si substrates[11,14,18,19] with thicknesses of about 100–200 nm. Generation of cracks is attributed to the significant difference in TEC between BZT–BCT with a TEC $\sim 12 \times 10^{-6}$ K^{-1} (ref. 20) and the silicon with a TEC $\sim 3 \times 10^{-6}$ K^{-1} (ref. 21 and 22) in the same temperature range 100–600 °C. The sapphire substrate with a TEC $\sim 8 \times 10^{-6}$ K^{-1} (ref. 21) contributes to substantially lower tensile stress in the film upon cooling.

Table 1 Summary of strain and stress calculations. Fitted slope (see Fig. 3c), calculated strain $\varepsilon_{11/22}$, stress $\sigma_{11/22}$, and adjusted R^2 of the fit

Films	Slope (pm)	Strain, $\varepsilon_{11/22}$ (%)	Stress, $\sigma_{11/22}$ (MPa)	Adjusted R^2
BZT–BCT-100	1.843	0.34	649	0.994
BZT–BCT-340	2.221	0.42	781	0.997

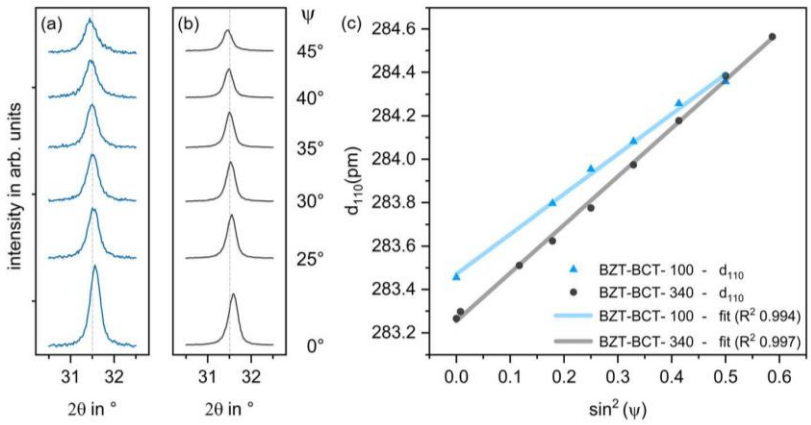

Fig. 3 Tilt-angle Ψ-dependent XRD patterns of (a) BZT–BCT-100 and (b) BZT–BCT-340 films. (c) Interplanar spacing d_{110} as a function of $\sin^2(\Psi)$. Different (yet both positive) slopes observed in (c) indicate different absolute values of residual biaxial strain in both films.

View Article Online
Journal of Materials Chemistry A Paper

The BZT–BCT films crystallize in the perovskite phase with no preferential orientation indexed according to $BaTiO_3$ PDF 01-074-4539, see Fig. 2.

To evaluate residual stresses in the films, the tilt-angle Ψ-dependent XRD patterns were measured around the (110) peak (Fig. 3a and b). In both films, the (110) peak shifts towards lower 2θ values with increasing ψ, suggesting the presence of tensile stress. The interplanar d_{110} plot shown in Fig. 3c reveals a linear dependence on $\sin^2\Psi$ for both films, with a smaller slope (see also Table 1) in the case of the thinner film.

To calculate biaxial strain $\varepsilon_{11/22}$ and stress $\sigma_{11/22}$ we used the method described in detail by Schenk *et al.*[23] We assumed negligible shear strain and rotationally symmetric in-plane stress. For the latter, see our previous publication, where the (110) pole figure of the BZT–BCT film on platinized silicon reveals constant intensity at all φ angles. Young's modulus and Poisson ratio were estimated at 130 GPa and 0.3, respectively.[24] Results are collected in Table 1. The calculated strain (stress) value for the BZT–BCT-100 is 0.34 (649 MPa), and it increases for the BZT–BCT-340 film to 0.42 (781 MPa). Note that in both cases, the adjusted R^2 is above 0.99. Residual tensile strain can be ascribed to the difference in thermal expansion coefficients between the film and the substrate (see the discussion above).

The dielectric properties of BZT–BCT-100 and BZT–BCT-340 films as functions of frequency, electric field, and temperature are shown in Fig. 4. The relative permittivity of BZT–BCT-100 is about 500 in the 100 Hz–1 MHz frequency range at room temperature, while the permittivity of the thicker film, BZT–BCT-340, is about 820, which is ~64% higher (Fig. 4a). The smaller permittivity in the former film is attributed to the lower film thickness and smaller grain size, *i.e.*, the dielectric grain size effect.[25,26] The losses ($\tan\delta$) from 1 kHz to about 100 kHz are slightly higher in the thinner film and begin to increase at frequencies lower than a few kHz, which indicates higher

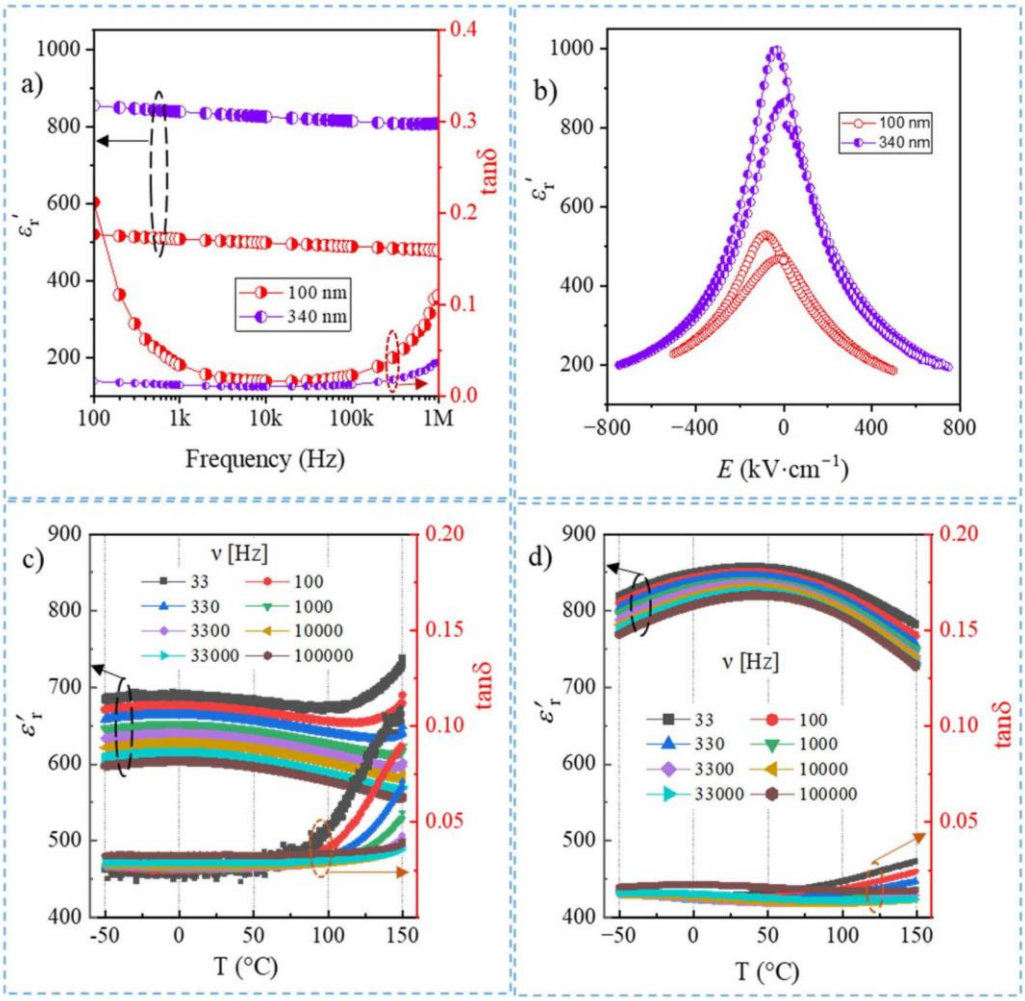

Fig. 4 Room-temperature dielectric properties as a function of (a) frequency, and (b) electric field of BZT–BCT-100 and BZT–BCT-340 films. The relative dielectric permittivity and losses of (c) BZT–BCT-100 and (d) BZT–BCT-340 films as functions of temperature at different frequencies (ν).

View Article Online
Paper Journal of Materials Chemistry A

conductivity of the thinner film. The increasing losses observed at high frequencies are due to the parasitic LCR effect of the measurement setup.

The double peak of the electric field-dependent relative permittivity of the films indicates their ferroelectric behavior (Fig. 4b).[14,27] The imprint nature of ε_r' peaks can be due to the different work functions of platinum bottom electrode and gold top electrode.[28] In addition, rf-sputtering which was used to deposit electrodes can introduce charged defects that result in asymmetry in the electric field-dependent capacitance measurements.[29,30]

The frequency-dependent dielectric permittivity curves of the two films as a function of temperature are shown in Fig. 4c and d. In the case of the BZT–BCT-100 film, there is no evident permittivity peak, which we ascribe to its fine grain size and low film thickness.[25,26,31] The losses increase with increasing temperature, which is attributed to the increase in the film's conductivity. However, in the BZT–BCT-340 film, a broad permittivity peak is observed between 40 °C and 50 °C, which we attribute to a diffuse phase transition.

In our previous study, about 110 nm thick films with the same composition (1 mole% Mn dopant) but deposited on Pt/Si substrates exhibited a broad dielectric permittivity peak with transition temperature in the range from 55 to 75 °C.[14] Compared to the phase transition temperatures of the films on Pt/Si substrates, a further downshift of the permittivity peak of the BZT–BCT-340 on the sapphire substrate is presumably related to the tensile stress developed in the film due to thermal expansion mismatch.[15] A weak frequency dispersion could indicate a relaxor-like behaviour of the BZT–BCT-340 film.[10] The $\tan\delta$ of BZT–BCT-340 remains below 0.03 in the whole temperature range, up to 150 °C, while in the thinner film, it noticeably increases above 100 °C.

The polarization as a function of the electric field (P–E) is measured for both films at 1 kHz and is shown in Fig. 5. Ferroelectric properties: remanent polarization (P_r), coercive field (E_c), and maximum polarization (P_{max}) of both films are collected in Table 2. The thinner film has a lower P_{max}, and rounded tips of the loop indicate leakage contribution. The thicker film has a higher P_{max} and sharp tips. The higher coercive field and remanent polarization in the thinner films could be related to the existence of the so-called "dead layers" in addition to the grain size effect and leakage contribution. The dead or nonswitching layers are the interfacial discontinuity at the electrode–ferroelectric material interface, affecting the polarization and coercive field.[32–34]

The BZT–BCT-340 exhibits better dielectric and ferroelectric properties with higher relative dielectric permittivity, lower losses, and significantly higher maximum polarization than the BZT–BCT-100. Due to its slim P–E loop, low remanent polarization, small coercive field, and high saturated polarization, the thicker BZT–BCT film can be considered a viable candidate for energy storage applications.

Table 2 Ferroelectric properties BZT–BCT-100 and BZT–BCT-340 measured at 1 kHz

Film	E_{max} (MV cm^{-1})	E_c (kV cm^{-1})	P_r (μC cm^{-2})	P_{max} (μC cm^{-2})
BZT–BCT-100	1	110	6	28
BZT–BCT-340	1	45	4	36

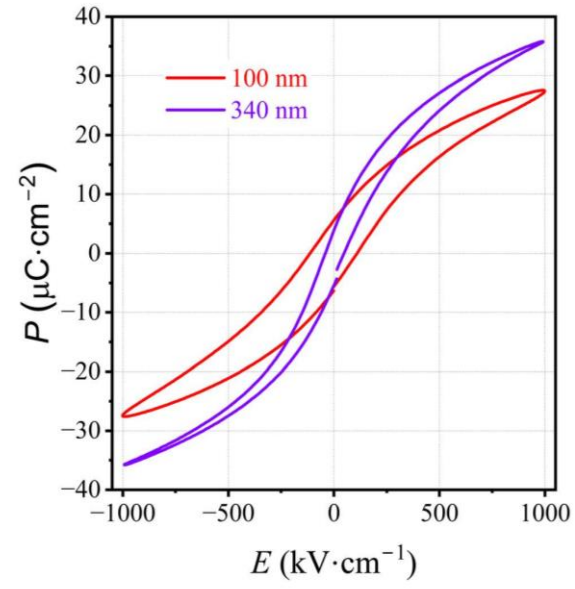

Fig. 5 P–E loops of BZT–BCT-100 and BZT–BCT-340 measured at 1 kHz and at room temperature.

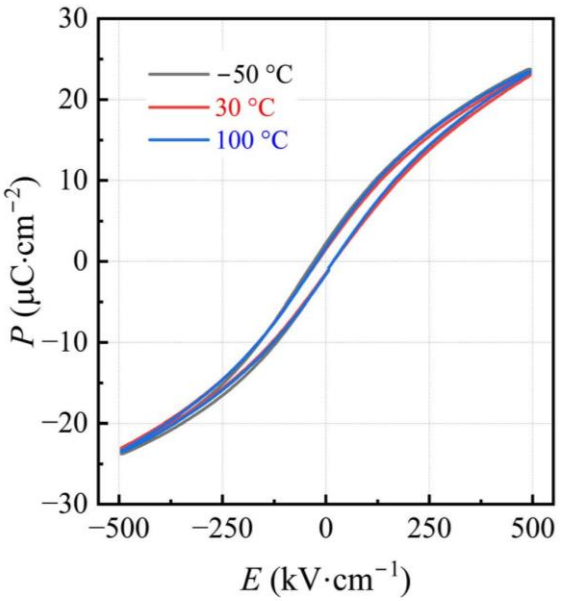

Fig. 6 P–E loops of BZT–BCT-340 at different temperatures at 1 kHz.

View Article Online
Journal of Materials Chemistry A Paper

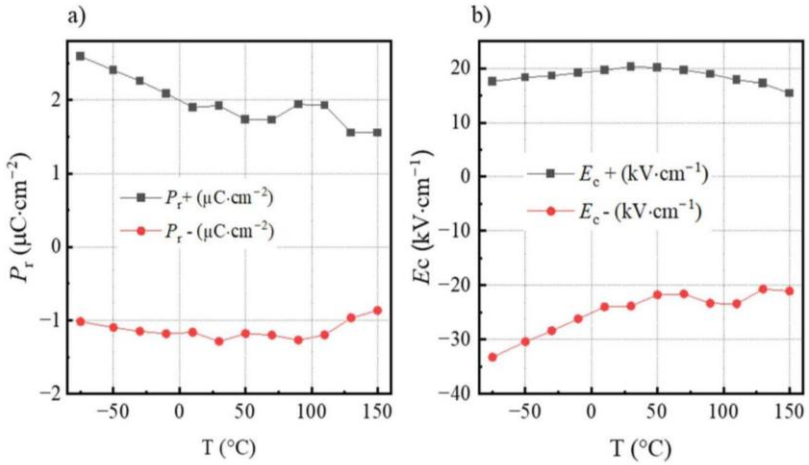

Fig. 7 (a) Remanent polarization (P_r), and (b) coercive field (E_c) of BZT–BCT-340 measured at different temperatures at the applied electric field of 500 kV cm^{-1}.

We measured the *P*–*E* loops of the BZT–BCT-340 film at different temperatures from −50 °C to 100 °C, as shown in Fig. 6. The *P*–*E* loops do not show any significant change in the shape in the whole temperature range. The temperature-independent *P*–*E* loops of the film could suggest that the polarization as a function of the electric field is rather governed by the existence of nano-domains, *i.e.*, polar nano regions in Mn-doped BZT–BCT films, indicating a relaxor-like behavior as reported in $NaNbO_3$ films or $BaTi_{0.75}Zr_{0.25}O_3$ ceramic,[35,36] than the ferroelectric polar phase which should disappear above the T_c. The P_r and E_c measurements from −75 °C to 150 °C show the imprint behavior of P_r and E_c, *i.e.*, asymmetry of positive and negative P_r and E_c, presumably due to the different top and bottom electrodes, as shown in the electric field-dependent dielectric permittivity, see Fig. 4b. A progressive decrease of P_r and E_c with the increase in temperature is observed in Fig. 7a and b, yet, these values are not close to zero. It should be noted that at such high temperatures, the conductivity in the films may increase, contributing to the persistence of apparent E_c and P_r. Still, the existence of the polar nano regions in BZT–BCT thin films cannot be excluded.

Unipolar *P*–*E* loops of BZT–BCT-340 films were measured at different electric fields to evaluate the energy storage (ES) properties. Fig. 8 shows the unipolar *P*–*E* loops measured at progressively higher electric fields up to 3.5 MV cm^{-1} at 1 kHz and a *P*–*E* loop at an *E*-field of 3.5 MV cm^{-1} with calculated recoverable energy and losses. The maximum polarization is about 47 μC cm^{-2}. The calculated recoverable energy (U_{rec}) and energy losses (U_{loss}) are 46.0 J cm^{-3} and 5.5 J cm^{-3}, respectively. The charging or stored energy (U_{st}) is 51.5 J cm^{-3}, and energy storage efficiency (η) is 89.2%. The high energy storage performance is due to the high maximum polarization and a high electric field that the film survives without breakdown.

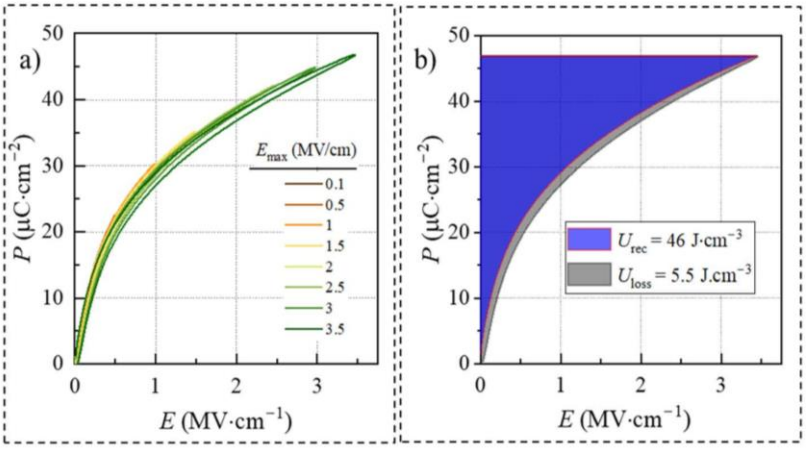

Fig. 8 (a) Unipolar *P*–*E* loops (b) *P*–*E* and ES properties at E_{max} of BZT–BCT-340. The measurements were performed at 1 kHz.

View Article Online
Paper Journal of Materials Chemistry A

Table 3 Recoverable energy density and efficiency of BZT–BCT-340 (this work) and barium-, lead- and bismuth-based perovskite oxide thin films obtained by different methods reported in the literature

Film	Dopant	Substrate	Thickness (nm)	Method	E_{max} (MV cm^{-1})	U_{rec} (J cm^{-3})	η (%)	Ref.
BZT–BCT	—	Pt/Si	150	IBSD	0.15	2.3	28.5	37
BCZT[a]	—	MgO	360	PLD	2.08	39	33	38
BCZT[b]	La	Pt/Si	280	CSD	3.335	15	93	39
BZT–BCT	Mn	Pt/Si	120	CSD	1.16	10	69	14
BZT	Sm	STO	1000	PLD	7	133	89	40
BFO–STO	—	STO	500	PLD	3.85	70	70	41
PCZ	—	Pt/Si	300	CSD	2.8	50	83	42
PLZT	La	Ti-foil	1200	PLD	3	41	80	43
PHO	—	ITO/glass	330	CSD	3	25	73	44
BZT–BCT	Mn	Pt/Sa	340	CSD	3.5	46	89	This work

BCZT[a]: $(Ba_{0.955}Ca_{0.045})(Zr_{0.17}Ti_{0.83})O_3$. BCZT[b]: $(Ba_{0.904}Ca_{0.096})_{0.9775} + 0.0075La_{0.015}(Zr_{0.136}Ti_{0.864})O_3$, BZT: $Ba(Zr_{0.35}Ti_{0.65})O_3$. BFO–STO: $0.4(BiFeO_3)$–$0.6(SrTiO_3)$, PCZ: $Pb_{0.88}Ca_{0.12}ZrO_3$, PLZT: $Pb_{0.9}La_{0.1}(Zr_{0.52}Ti_{0.48})O_3$, PHO: $PbHfO_3$, ITO/glass: indium tin oxide deposited on glass substrate.

Compared to the energy storage properties of BZT–BCT thin films with different cation molar ratios, or dopants, deposited on different substrates or prepared with different deposition techniques, including Pulsed Laser Deposition (PLD), Ion Beam Sputtering (IBSD),[37,38] our BZT–BCT-340 film shows promising performance. The comparison of the reported values with BZT–BCT-340 is summarized in Table 3. For example, the lanthanum-doped $(Ba_{0.904}Ca_{0.096})_{0.9775} + xLa_{0.015}(Zr_{0.136}Ti_{0.864})O_3$ (BCZT) film reported by He *et al.* has a very high efficiency of about 93%, which is attributed to almost no remanent polarization and a maximum applied field of about 3.33 MV cm^{-1},[39] which is about 5% lower than the field applied to our BZT–BCT-340.

The energy storage efficiency of our BZT–BCT-340 is above or comparable to the values obtained by antiferroelectric and relaxor barium-, lead- and bismuth-based perovskite thin films which are considered to be the ideal candidates for energy storage, for details, please refer to Table 3.

4. Conclusion

We prepared Mn-doped BZT–BCT thin films by chemical solution deposition on platinized sapphire substrates in a multistep deposition and annealing process at 850 °C. The about 100 nm and 340 nm thick crack-free films with columnar microstructure were achieved. The platinized sapphire substrate with a thermal expansion coefficient closer to that of BZT–BCT is a better choice for preparing crack-free BZT–BCT thin films with a thickness of a few 100 nm compared to the commonly used platinized silicon substrate with much lower thermal expansion coefficient resulting in the crack-generation often observed in BT-based thin films with thicknesses above 100 nm. The 100 nm thick BZT–BCT film exhibits a dielectric permittivity of about 500 at 1 kHz, which is 64% lower than the permittivity of the 340 nm thick film. The latter film is characterized by a slim polarization–electric field loop which persists well above the dielectric permittivity peak between 40 °C and 50 °C, suggesting its relaxor-like behavior. The recoverable energy of 46 J cm^3 with an energy storage efficiency of about 89% was achieved at 3.5 MV cm^{-1}. The properties of the BZT–BCT thin films reveal their promising potential for energy storage applications in a wide temperature range from −75 °C up to about 150 °C.

Data availability

The authors declare that the data supporting the findings of this study are available within the paper.

Conflicts of interest

There are no conflicts of interest to declare.

Acknowledgements

Slovenian Research and Innovation Agency (core funding P2-0105, J7-4637, P1-0125, S. W. K. – young researcher programme and bilateral cooperations BI-US/22-24-039 and BI-US/24-26-094), MSCA-PF grant agreement no. 101110882. Vid Bobnar is acknowledged for providing access to the impedance analyzer and Aixacct TF Analyzer 2000. Barnik Mandal and Sebastjan Glinšek acknowledge Luxembourg National Research Fund (FNR) for financial support through the project INTER/NWO/20/15079143/TRICOLOR. Geoff Brennecka acknowledges financial support by the Fulbright US Scholar Program, which is sponsored by the US Department of State. Dean Birmančević is acknowledged for his help related to the film deposition.

References

1 F. MacDougall, T. Jow, J. Ennis, X. Yang, S. Yen, R. Cooper and J. Bates, Pulsed power and power conditioning capacitors, *Acta Phys. Pol. A*, 2009, **115**(6), 989–991, DOI: 10.12693/APhysPolA.115.989.

2 X. Li, X. Chen, J. Sun, M. Zhou and H. Zhou, Novel lead-free ceramic capacitors with high energy density and fast discharge performance, *Ceram. Int.*, 2020, **46**(3), 3426–3432, DOI: 10.1016/j.ceramint.2019.10.055.

3 M. Peddigari, J. H. Park, J. H. Han, C. K. Jeong, J. Jang, Y. Min and G. T. Hwang, Flexible self-charging, ultrafast, high-power-density ceramic capacitor system, *ACS Energy Lett.*, 2021, **6**(4), 1383–1391, DOI: **10.1021/acsenergylett.1c00170**.

4 H. Palneedi, M. Peddigari, G. T. Hwang, D. Y. Jeong and J. Ryu, High-performance dielectric ceramic films for energy storage capacitors: progress and outlook, *Adv. Funct. Mater.*, 2018, **28**(42), 1803665, DOI: **10.1002/adfm.201803665**.

5 A. Ben Amar, A. B. Kouki and H. Cao, Power approaches for implantable medical devices, *Sensors*, 2015, **15**(11), 28889–28914, DOI: **10.3390/s151128889**.

6 J. P. Silva, K. C. Sekhar, H. Pan, J. L. MacManus-Driscoll and M. Pereira, Advances in dielectric thin films for energy storage applications, revealing the promise of group IV binary oxides, *ACS Energy Lett.*, 2021, **6**(6), 2208–2217, DOI: **10.1021/acsenergylett.1c00313**.

7 V. Veerapandiyan, F. Benes, T. Gindel and M. Deluca, Strategies to improve the energy storage properties of perovskite lead-free relaxor ferroelectrics: a review, *Materials*, 2020, **13**(24), 5742, DOI: **10.3390/ma13245742**.

8 V. S. Puli, D. K. Pradhan, D. B. Chrisey, M. Tomozawa, G. L. Sharma, J. F. Scott and R. S. Katiyar, Structure, dielectric, ferroelectric, and energy density properties of (1− x) BZT–x BCT ceramic capacitors for energy storage applications, *J. Mater. Sci.*, 2013, **48**, 2151–2157, DOI: **10.1007/s10853-012-6990-1**.

9 R. Syal, R. Goel, A. De, A. K. Singh, G. Sharma, O. P. Thakur and S. Kumar, Flattening of free energy profile and enhancement of energy storage efficiency near morphotropic phase boundary in lead-free BZT-xBCT, *J. Alloys Compd.*, 2021, **873**, 159824, DOI: **10.1016/j.jallcom.2021.159824**.

10 S. Lu, G. Chen, Y. Zhang, Z. Zhao, F. Li, Z. Lv and S. Li, Electrocaloric effect in lead-free $0.5Ba(Zr_{0.2}Ti_{0.8})O_3$-$0.5(Ba_{0.7}Ca_{0.3})TiO_3$ ceramic measured by direct and indirect methods, *Ceram. Int.*, 2018, **44**(17), 21950–21955, DOI: **10.1016/j.ceramint.2018.08.308**.

11 W. L. Li, T. D. Zhang, D. Xu, Y. F. Hou, W. P. Cao and W. D. Fei, $LaNiO_3$ seed layer induced enhancement of piezoelectric properties in (100)-oriented (1−x) BZT–xBCT thin films, *J. Eur. Ceram. Soc.*, 2015, **35**(7), 2041–2049, DOI: **10.1016/j.jeurceramsoc.2015.01.018**.

12 J. Xu, Y. Zhou, Z. Li, C. Lin, X. Zheng, T. Lin and F. Wang, Microstructural, ferroelectric and photoluminescence properties of Er^{3+}-doped $Ba_{0.85}Ca_{0.15}Ti_{0.9}Zr_{0.1}O_3$ thin films, *Mater. Chem. Phys.*, 2021, **262**, 124320, DOI: **10.1016/j.matchemphys.2021.124320**.

13 S. W. Konsago, K. Žiberna, B. Kmet, A. Benčan, H. Uršič and B. Malič, Chemical Solution Deposition of Barium Titanate Thin Films with Ethylene Glycol as Solvent for Barium Acetate, *Molecules*, 2022, **27**(12), 3753, DOI: **10.3390/molecules27123753**.

14 S. W. Konsago, K. Žiberna, A. Matavž, B. Mandal, S. Glinšek, Y. Fleming, A. Benčan, L. G. Brennecka, H. Uršič and B. Malič, Engineering the Microstructure and Functional Properties of $0.5Ba(Zr_{0.2}Ti_{0.8})O_3$-$0.5(Ba_{0.7}Ca_{0.3})TiO_3$ Thin Films, *ACS Appl. Electron. Mater.*, 2024, **6**(6), 4467–4477, DOI: **10.1021/acsaelm.4c00530**.

15 T. Pečnik, S. Glinšek, B. Kmet and B. Malič, Combined effects of thickness, grain size and residual stress on the dielectric properties of $Ba_{0.5}Sr_{0.5}TiO_3$ thin films, *J. Alloys Compd.*, 2015, **646**, 766–772, DOI: **10.1016/j.jallcom.2015.06.192**.

16 L. J. Sinnamon, M. M. Saad, R. M. Bowman and J. M. Gregg, Exploring grain size as a cause for "dead-layer" effects in thin film capacitors, *Appl. Phys. Lett.*, 2002, **81**(4), 703–705, DOI: **10.1063/1.1494837**.

17 W. J. Lee, H. G. Kim and S. G. Yoon, Microstructure dependence of electrical properties of $(Ba_{0.5}Sr_{0.5})TiO_3$ thin films deposited on $Pt/SiO_2/Si$, *J. Appl. Phys.*, 1996, **80**(10), 5891–5894, DOI: **10.1063/1.363583**.

18 G. Kang, K. Yao and J. Wang, (1−x) $Ba(Zr_{0.2}Ti_{0.8})O_3$–x $(Ba_{0.7}Ca_{0.3})TiO_3$ Ferroelectric Thin Films Prepared from Chemical Solutions, *J. Am. Ceram. Soc.*, 2012, **95**(3), 986–991, DOI: **10.1111/j.1551-2916.2011.04877.x**.

19 P. S. Barbato, V. Casuscelli, P. Aprea, R. Scaldaferri and D. Caputo, Optimization of the production process of BZT–BCT sol–gel thin films obtained from a highly stable and green precursor solution, *Mater. Manuf. Processes*, 2021, **36**(14), 1642–1649, DOI: **10.1080/10426914.2021.1926495**.

20 S. W. Konsago, A. Debevec, J. Cilenšek, B. Kmet and B. Malič, Linear Thermal Expansion of 0.5 $Ba(Zr_{0.2}Ti_{0.8})O_3$-$0.5(Ba_{0.7}Ca_{0.3})TiO_3$ Bulk Ceramic, *Inf. MIDEM*, 2023, **53**(4), 233–238, DOI: **10.33180/InfMIDEM2023.403**.

21 W. M. Yim and R. J. Paff, Thermal expansion of AlN, sapphire, and silicon, *J. Appl. Phys.*, 1974, **45**(3), 1456–1457, DOI: **10.1063/1.1663432**.

22 M. Okaji, Absolute thermal expansion measurements of single-crystal silicon in the range 300–1300 K with an interferometric dilatometer, *Int. J. Thermophys.*, 1988, **9**, 1101–1109, DOI: **10.1007/BF01133277**.

23 T. Schenk, C. M. Fancher, M. H. Park, C. Richter, C. Künneth, A. Kersch, L. Jacob, J. L. Jones, T. Mikolajick and U. Schroeder, On the origin of the large remanent polarization in La: HfO_2, *Adv. Electron. Mater.*, 2019, **5**(12), 1900303, DOI: **10.1002/aelm.201900303**.

24 K. Maruyama, Y. Kawakami and F. Narita, Young's modulus and ferroelectric property of $BaTiO_3$ films formed by aerosol deposition in consideration of residual stress and film thickness, *Jpn. J. Appl. Phys.*, 2022, **61**(SN), SN1011, DOI: **10.35848/1347-4065/ac7d96**.

25 U. Böttger, Dielectric Properties of Polar Oxides, in *Polar Oxides*, ed. R. Waser, U. Böttger and S. Tiedke, Wiley, 2004, pp. 11–38, DOI: **10.1002/3527604650.ch1**.

26 J. F. Ihlefeld, J. P. Maria and W. Borland, Dielectric and microstructural properties of barium titanate zirconate thin films on copper substrates, *J. Mater. Res.*, 2005, **20**(10), 2838–2844, DOI: **10.1557/JMR.2005.0342**.

27 R. Placeres-Jiménez, J. P. Rino and J. A. Eiras, Modeling ferroelectric permittivity dependence on electric field and estimation of the intrinsic and extrinsic contributions, *J. Phys. D: Appl. Phys.*, 2015, **48**(3), 035304, DOI: **10.1088/0022-3727/48/3/035304**.

28 L. Pintilie, I. Vrejoiu, D. Hesse and M. Alexe, The influence of the top-contact metal on the ferroelectric properties of epitaxial ferroelectric Pb $(Zr_{0.2}Ti_{0.8})O_3$ thin films, *J. Appl. Phys.*, 2008, **104**(11), 114101, DOI: 10.1063/1.3021293.

29 A. Matavž, J. Kovač, M. Čekada, B. Malič and V. Bobnar, Enhanced electrical response in ferroelectric thin film capacitors with inkjet-printed $LaNiO_3$ electrodes, *Appl. Phys. Lett.*, 2018, **113**(1), 012904, DOI: 10.1063/1.5037027.

30 Y. Ahn and J. Y. Son, Imprint phenomenon of ferroelectric switching characteristics in $BaTiO_3$/$PbTiO_3$ multilayer thin films, *J. Alloys Compd.*, 2022, **891**, 162088, DOI: 10.1016/j.jallcom.2021.162088.

31 V. Buscaglia, M. T. Buscaglia, M. Viviani, L. Mitoseriu, P. Nanni, V. Trefiletti and J. Petzelt, Grain size and grain boundary-related effects on the properties of nanocrystalline barium titanate ceramics, *J. Eur. Ceram. Soc.*, 2006, **26**(14), 2889–2898.

32 S. K. Streiffer, C. Basceri, C. B. Parker, S. E. Lash and A. I. Kingon, Ferroelectricity in thin films: The dielectric response of fiber-textured $(Ba_xSr_{1-x})Ti_{1+y}O_{3+z}$ thin films grown by chemical vapor deposition, *J. Appl. Phys.*, 1999, **86**(8), 4565–4575, DOI: 10.1063/1.371404.

33 L. J. Sinnamon, M. M. Saad, R. M. Bowman and J. M. Gregg, Exploring grain size as a cause for "dead-layer" effects in thin film capacitors, *Appl. Phys. Lett.*, 2002, **81**(4), 703–705, DOI: 10.1063/1.1494837.

34 J. Pérez De La Cruz, E. Joanni, P. M. Vilarinho and A. L. Kholkin, Thickness effect on the dielectric, ferroelectric, and piezoelectric properties of ferroelectric lead zirconate titanate thin films, *J. Appl. Phys.*, 2010, **108**(11), 114106, DOI: 10.1063/1.3514170.

35 B. Cai, J. Schwarzkopf, E. Hollmann, D. Braun, M. Schmidbauer, T. Grellmann and R. Wördenweber, Electronic characterization of polar nanoregions in relaxor-type ferroelectric $NaNbO_3$ films, *Phys. Rev. B*, 2016, **93**(22), 224107, DOI: 10.1103/PhysRevB.93.224107.

36 T. Badapanda, S. K. Rout, S. Panigrahi and T. P. Sinha, Phase formation and dielectric study of Bi doped $BaTi_{0.75}Zr_{0.25}O_3$ ceramic, *Curr. Appl Phys.*, 2009, **9**(4), 727–731, DOI: 10.1016/j.cap.2008.06.014.

37 J. P. Silva, J. M. Silva, M. J. Oliveira, T. Weingärtner, K. C. Sekhar, M. Pereira and M. J. Gomes, High-performance ferroelectric–dielectric multilayered thin films for energy storage capacitors, *Adv. Funct. Mater.*, 2019, **29**(6), 1807196, DOI: 10.1002/adfm.201807196.

38 V. S. Puli, D. K. Pradhan, S. Adireddy, R. Martínez, P. Silwal, J. F. Scott and R. S. Katiyar, Nanoscale polarisation switching and leakage currents in $(Ba_{0.955}Ca_{0.045})(Zr_{0.17}Ti_{0.83})O_3$ epitaxial thin films, *J. Phys. D: Appl. Phys.*, 2015, **48**(35), 355502, DOI: 10.1088/0022-3727/48/35/355502.

39 S. He, B. Peng, G. J. Leighton, C. Shaw, N. Wang, W. Sun and Q. Zhang, High-performance La-doped BCZT thin film capacitors on $LaNiO_3$/Pt composite bottom electrodes with ultra-high efficiency and high thermal stability, *Ceram. Int.*, 2019, **45**(9), 11749–11755, DOI: 10.1016/j.ceramint.2019.03.051.

40 H. T. Vu, H. N. Vu, G. Rijnders and M. D. Nguyen, Sm-doping driven state-phase transition and energy storage capability in lead-free Ba $(Zr_{0.35}Ti_{0.65})O_3$ films, *J. Alloys Compd.*, 2023, **968**, 171837, DOI: 10.1016/j.jallcom.2023.171837.

41 H. Pan, J. Ma, J. Ma, Q. Zhang, X. Liu, B. Guan and C. W. Nan, Giant energy density and high efficiency achieved in bismuth ferrite-based film capacitors via domain engineering, *Nat. Commun.*, 2018, **9**(1), 1813, DOI: 10.1038/s41467-018-04189-6.

42 Y. Z. Li, Z. J. Wang, Y. Bai and Z. D. Zhang, High energy storage performance in Ca-doped $PbZrO_3$ antiferroelectric films, *J. Eur. Ceram. Soc.*, 2020, **40**(4), 1285–1292, DOI: 10.1016/j.jeurceramsoc.2019.11.063.

43 C. T. Nguyen, H. N. Vu and M. D. Nguyen, High-performance energy storage and breakdown strength of low-temperature laser-deposited relaxor PLZT thin films on flexible Ti-foils, *J. Alloys Compd.*, 2019, **802**, 422–429, DOI: 10.1016/j.jallcom.2019.06.205.

44 X. X. Huang, T. F. Zhang, W. Wang, P. Z. Ge and X. G. Tang, Tailoring energy-storage performance in antiferroelectric $PbHfO_3$ thin films, *Mater. Des.*, 2021, **204**, 109666, DOI: 10.1016/j.matdes.2021.109666.

3.4.2. Electromechanical Properties and Tunability of 340-nm Thick $0.5Ba(Zr_{0.2}Ti_{0.8})O_3$-$0.5(Ba_{0.7}Ca_{0.3})TiO_3$ Films on Platinized Sapphire Substrates

This Chapter continues Chapter 3.4.1. It reports the electromechanical properties and capacitance tunability of the 340 nm thick Mn-doped BZT-BCT films on platinized sapphire substrates.

Materials and methods

The reagents, solution preparation procedure, and thin film processing are identical to those described in Chapter 3.4.1. The unipolar strain (*S*) was measured using the Aixacct TF Analyzer 2000 (Aixacct Systems GmbH, Aachen, Germany) as described in Chapter 3.3. Also, the piezoelectric d_{33} coefficient and the capacitance as a function of the DC field (*C*-*E*) were measured at the same conditions as described in Chapter 3.3.

Results and discussion

Electromechanical properties and tunability of the 340 nm thick BZT-BCT films doped with 1 mole % of manganese deposited on platinized sapphire substrate (BZT-BCT-340) are summarized in Figure 21. Panels a) and b) show the strain measured at different electric fields (*S*-*E*), capacitance (*C*-*E*), and piezoelectric d_{33} coefficient measured at room temperature, while panel c) shows the large signal piezoelectric coefficient (d^{LS}_{33}) as function of temperature.

The maximum strain is about 0.77% at 3.5 MV·cm^{-1}. Such a large strain could be obtained in PZT thin films with columnar microstructure and with thicknesses of about 2 μm or above [112]. The obtained d_{33} is about 40 pm·V^{-1}. It is worth noting that there is no significant change in d_{33} over a temperature range from -50 °C up to 150 °C which is well beyond the T_c of BZT-BCT (as evident from the measurement of the dielectric permittivity versus temperature; see Chapter 3.4.1, Figure 4). This implies a relaxor-like behaviour of BZT-BCT-340 as previously discussed in Chapter 3.4.1. An extended temperature range of piezoelectric activity would be an advantage for various MEMS applications, including bio-medical applications such as blood pressure sensors; and piezoelectric haptic actuators in which PZT is still the most considered material [113], [114], [115].

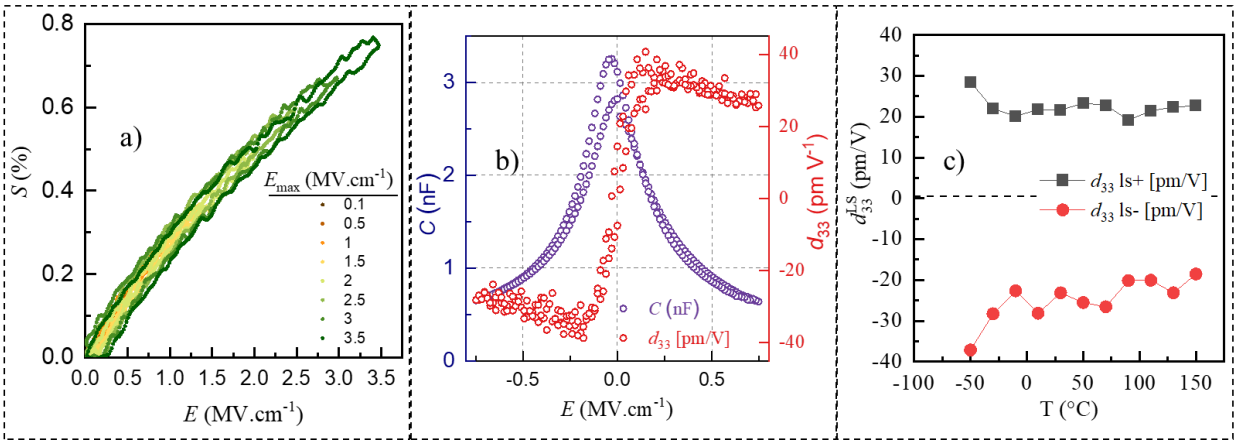

Figure 21: The unipolar electric field dependence of strain (a), capacitance and small-signal piezoelectric d_{33} coefficient (b) and temperature dependence of large signal d_{33} coefficient (c) of BZT-BCT-340 films on Pt/sapphire measured by DBLI at 1 kHz.

3.4.3. Microstructure and Functional Properties of 680-nm Thick $0.5Ba(Zr_{0.2}Ti_{0.8})O_3$-$0.5(Ba_{0.7}Ca_{0.3})TiO_3$ Films on Platinized Sapphire Substrates

This Chapter reports the results of 680 nm thick BZT-BCT films doped with 1 mole % of manganese deposited on platinized sapphire substrates and multistep annealed at 850 °C.

Materials and methods

The materials and solution preparation procedure are identical to the description included in Chapter 3.4.1. The film is prepared under the same conditions as in the previous chapter, with the exception of the number of depositions, which was increased to 60. The XRD and field-emission scanning electron microscopy (FE-SEM) analyses and the measurements of the functional properties were performed under the conditions described in parts 3.4.1 and 3.4.2.

Microstructure and properties of 680 nm thick films

The plan-view and cross-section SEM micrographs of the 680 nm thick BZT-BCT film show crack-free and dense, predominantly columnar microstructure as shown in Figure 22. The average lateral grain size of the film is 132 nm, obtained from the plan-view image using the linear intercept method. The absence of intergranular cracks on the film's surface suggests that the thermal expansion coefficient (TEC) mismatch between the film and sapphire substrate (TEC ~12.4 x 10^{-6} K^{-1} for BZT-BCT and ~8.1 x 10^{-6} K^{-1} for sapphire in the temperature ranges of 100 °C – 600 °C and 20 °C – 800 °C respectively) is low enough to suppress the evolution of cracks [103], [116]. Contrarily, in the case of BZT-BCT films on Pt/Si, the thermal stress contributed to intergranular crack generation even at much lower film thicknesses of about 120 nm (Chapter 3.3, Figure 5) due to the much lower TEC of silicon which is about 4 times lower than that of BZT-BCT in the same temperature range [116], [117].

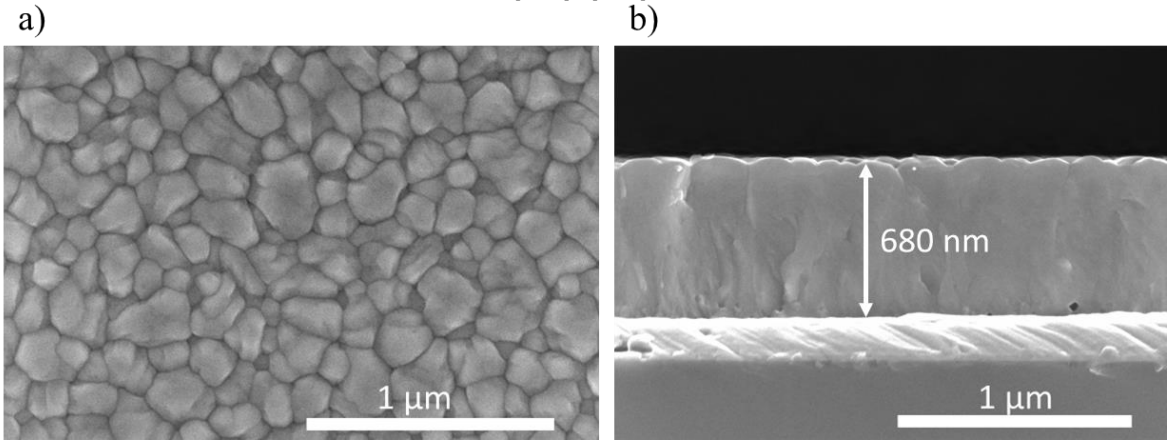

Figure 22: FE-SEM a) plan view b) cross-section of the 680 nm thick BZT-BCT film deposited on the platinized sapphire substrate and multistep annealed at 850 °C.

The relative permittivity and losses of 680 nm thick BZT-BCT films measured at 1 kHz and at room temperature are 840 and 0.02, respectively, as shown in Figure 23 a). The permittivity slightly decreases with the increase of frequency while the losses are constant up to 100 kHz and then increase up to 0.07. The increase of losses at higher frequencies is due to the parasitic LCR effect of the measurement setup. The dielectric permittivity of our film was 3 or even 5 times higher than the reported values obtained in BZT-BCT thin films with thicknesses of a few 100 nm prepared from 0.35 M coating solutions and annealed at 700 °C and 750 °C [91], [94], [96].

The relative permittivity measured as a function of temperature reaches peak values in the temperatures range between 60 to 90 °C. There is no significant difference in the peak values of dielectric permittivity of 680 nm and 340 nm thick films (see Chapter 3.4.2), but the broad permittivity peak of the 680 nm thick film is upshifted for about 30 °C compared to that of the 340 nm thick BZT-BCT film. The T_c of the 680 nm thick film is in the same temperature range as bulk ceramic 90 °C [24].

The maximum polarization and strain of the 680 nm thick BZT-BCT film are 32 μC·cm^{-2} and 0.35%, respectively, measured at 100 Hz under an applied field of 1.2 MV/cm as shown in Figure 23 c). The coercive field of about 40 kV/cm which is quite low compared to some other ferroelectric perovskite thin films [118], [119], [120], indicating that BZT-BCT is a soft ferroelectric material [12]. The sharp and saturated *P-E* loop indicates the film is not lossy, in agreement with the low-field permittivity measurements as function of frequency. The permittivity response to the applied electric field shows a good tunability and the permittivity peaks around 30 kV·cm^{-1} confirm a low coercive field. The d_{33} of the film measured on gold electrodes with a diameter of 400 μm by DBLI is about 40 pm·V^{-1}. This value could be underestimated due to the small size of the electrode as explained in Chapter 3.3., i.e the ratio of the electrode diameter and the substrate thickness should be around 1, but in our case, it is 0.64 [121], [122]. The thickness of platinized sapphire is 623 μm.

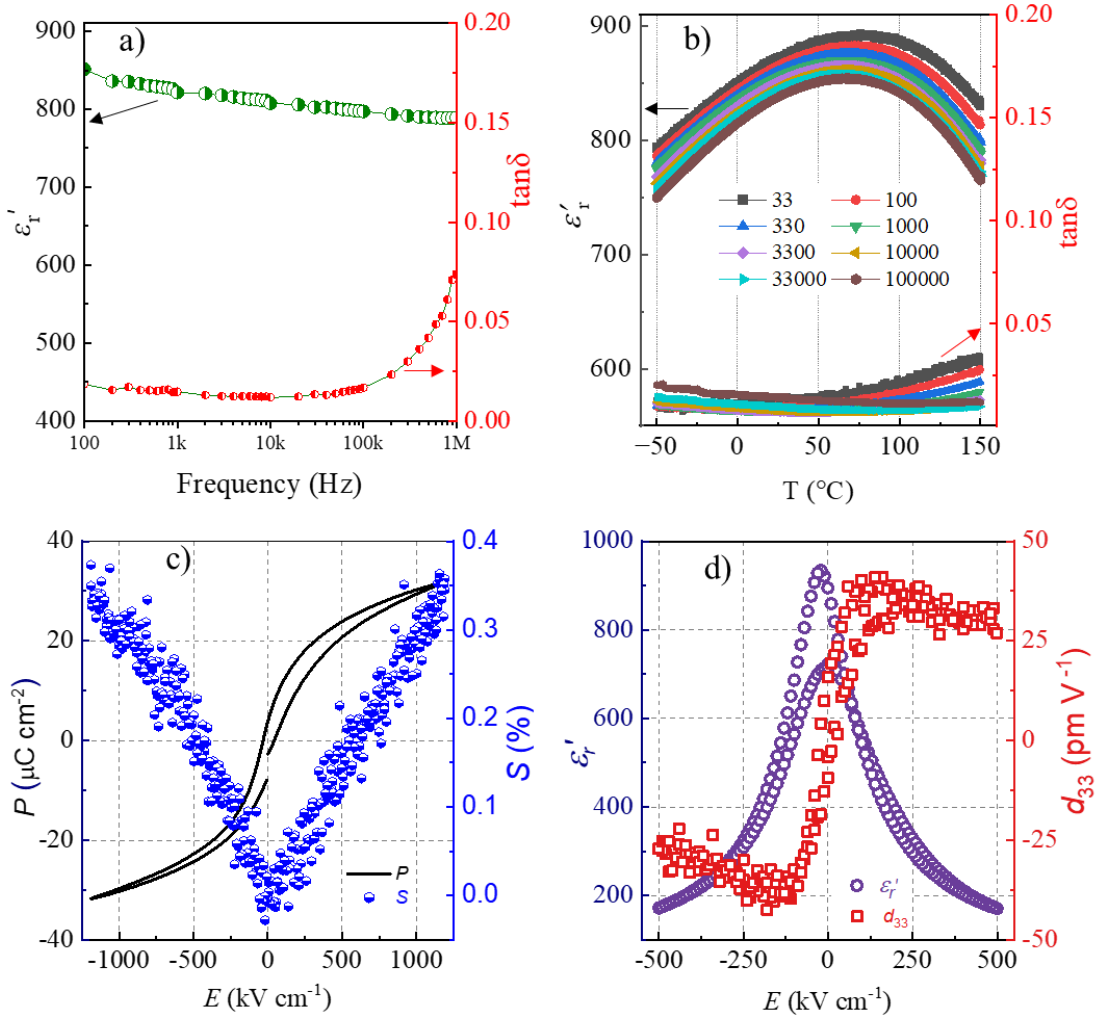

Figure 23: Dielectric properties of the 680 nm thick BZT-BCT film on the platinized sapphire substrate measured as a function of a) frequency at room temperature, b) temperature at different frequencies. The electric field dependent properties: c) *P-E* loops, *S-E* and b) the permittivity tunability and piezoelectric d_{33} coefficient.

Chapter 4

Summary, Conclusion and Outlook

In the thesis, we establish the processing - microstructure - properties relationship of $0.5Ba(Zr_{0.2}Ti_{0.8})O_3$-$0.5(Ba_{0.7}Ca_{0.3})TiO_3$ (BZT–BCT) thin films prepared by chemical solution deposition (CSD). To achieve this goal, we investigated $BaTiO_3$ (BT) thin films as a reference for BZT-BCT films. An alternative synthesis approach of BT-based coating solution, the optimization of the CSD process, microstructure design using the multistep annealing, and functional properties characterization of BT and BZT–BCT thin films are reported and discussed.

In CSD of BT thin films, the conventional coating solution synthesis involves barium carboxylate and titanium alkoxide as reagents and carboxylic acid, mainly acetic acid (AcOH) and alcohol, mainly 2-methoxyethanol (MOE) as solvents. BT coating solution with AcOH and MOE solvents was used as a reference to compare with the solution in which ethylene glycol (EG) was selected as a solvent for barium acetate. While EG is often used in CSD as a modifying agent, it has not been previously reported to dissolve poorly soluble alkaline earth acetates. The influence of the choice of the alcohol solvent for transition metal alkoxide on the stability of the coating solutions, thermal decomposition of BT precursor (xerogel), and the microstructure of BT films was studied.

We relate the instability of BT coating solution using AcOH-MOE solvents to progressive esterification reaction between the solvents, resulting in water formation and eventual hydrolysis of titanium alkoxide, leading to its precipitation. The stability of the coating solution increased from weeks to more than a year using EG instead of AcOH-MOE. The combination of EG and ethanol (EtOH) solvents for barium acetate and titanium butoxide led to the thermal decomposition of carbon residues at 719 °C compared to 1076 °C for the xerogel in which EG was used as a single solvent and 1127 °C for the xerogel derived from the combination of EG and MOE solvents. The films were spin-coated on platinized silicon substrates (Pt/Si), dried at 250 °C, pyrolyzed at 350 °C for 15 minutes, and multistep annealed at 800 °C. The ≈100 nm thick films have a dense columnar microstructure and good functional properties, with room-temperature dielectric permittivity of about 600 at 1kHz, and withstand electric fields of up to 2.4 $MV{\cdot}cm^{-1}$ without breakdown.

The selected EG-EtOH solvent combination was used to synthesize the BZT-BCT coating solution. Like BT, the BZT-BCT solution was stable for at least one year. The thermal analysis of BZT-BCT xerogel revealed that the decomposition of carbon residues is completed at 775 °C. Fourier transform infrared spectroscopy (FTIR) and Time of Flight Secondary Ion Mass Spectrometry (ToF-SIMS) of BZT-BCT thin films deposited on Pt/Si reveal that increasing the times of drying and pyrolysis at 250 °C and 350 °C from 2 minutes to 15 minutes and lowering the coating solution concentration from 0.2 M to 0.1 M contribute to a more complete thermal oxidation of trace organic residues. The ≈120 nm thick BZT-BCT films deposited on Pt/Si from a 0.1 M coating solution and multistep annealed at 850 °C crystallize in a perovskite phase with a columnar microstructure. In comparison, the films deposited from a 0.2 M solution consist of fine equiaxed grains. X-ray Photoelectron Spectroscopy (XPS) and Scanning Transmission

Electron Microscopy (STEM) analyses confirmed the chemical homogeneity of the films. Grazing-angle XRD and STEM analyses revealed the preferential (111) orientation of the perovskite phase and orientational correspondence with the (111) Pt, indicating that it serves as a nucleation layer, which has not been previously observed.

The room-temperature dielectric permittivity of the BZT-BCT film with the columnar microstructure is 510 at 1 kHz which is 46 % higher than that of the film with equiaxed grains, in agreement with the dielectric grain-size effect. Doping with manganese (1 mol %) increases the room-temperature permittivity and reduces the leakage current in columnar films. The recoverable energy storage density and efficiency are 10 $J \cdot cm^{-3}$ and 69 % at 1.16 $MV \cdot cm^{-1}$, respectively. The films show an almost fatigue-free response after 2 million cycles at 0.8 $MV \cdot cm^{-1}$. The macroscopic piezoelectric response of BZT-BCT thin films measured on the top electrodes with a diameter 200 μm using double-beam laser interferometry is about 22 $pm \cdot V^{-1}$. The corrected value, considering the ratio of the electrode size to the substrate's thickness [121], [122], which is 0.32 (ideally should 1), is 34 $pm \cdot V^{-1}$.

Intergranular cracks in BZT-BCT films on Pt/Si with thicknesses exceeding ≈120 nm were attributed to the stress that develops in the film due to the thermal expansion mismatch between the film and Si substrate. To increase the film thickness, we used platinized sapphire substrates (Pt/Sapp), characterized by an almost 3 times larger thermal expansion coefficient (TEC) than Si. Using a sapphire substrate enabled us to prepare crack-free Mn-doped BZT-BCT films with columnar microstructure with up to 680 nm thicknesses. The tilt-angle (Ψ)-dependent XRD analysis revealed that the tensile stress in the 100 nm and 340 nm thick films is 649 MPa and 781 MPa, respectively. The stress in the 680 nm thick film was not evaluated. The dielectric permittivity of the 340 nm and 680 nm thick films is ≈800, about 60 % higher than that of the 100 nm thick film measured at 1 kHz and room temperature. The increase in dielectric permittivity is related to increased film thickness and concomitant lateral grain growth, i.e., the film-thickness and dielectric grain-size effects. The film-thickness effect on functional properties of BZT-BCT films is not linear, which agrees with the literature on PZT films [101]. The permittivity of the 100 nm thick film is almost independent of temperature, while broad transition peaks between 30 °C and 60 °C and between 60 °C and 90 °C can be observed for the 340 nm and 680 nm thick films, respectively.

The 100 nm thick films exhibit a coercive field and remnant polarization of about 110 $kV \cdot cm^{-1}$ and 6 $\mu C \cdot cm^{-2}$ at 1 $MV \cdot cm^{-1}$ compared to 40-45 $kV \cdot cm^{-1}$ and 4 $\mu C \cdot cm^{-2}$ for thicker films. Unexpectedly, 340 nm thick films conserve the ferroelectric properties up to 150 °C, well beyond the broad permittivity peak between 30 °C and 60 °C, indicating a relaxor-like behaviour as previously observed in some BZT-BCT bulk ceramics [123]. The recoverable energy storage density and the energy storage efficiency of the 340 nm thick films are ≈46 $J \cdot cm^{-3}$and 89%. The obtained values are comparable to those of lead-based and lead-free perovskite relaxor or antiferroelectric thin films reported in the literature.

The piezoelectric d_{33} coefficient of the 100 nm thick film is about 20 $pm \cdot V^{-1}$ (the corrected value is 33 $pm \cdot V^{-1}$), which is significantly lower than 40 $pm \cdot V^{-1}$ (54 $pm \cdot V^{-1}$) of the 340 nm and 680 nm thick films. The piezoelectric d_{33} coefficient of CSD-derived BZT-BCT films has not been previously reported. Our results reveal that BZT-BCT thin films could be used as active components in micro-electro-mechanical systems operating even at temperatures well beyond the Tc.

Functional properties of BZT-BCT films studied in the thesis are collected in Table 2. The choice of the concentration of the coating solution and, thus, the type of the microstructure; doping to reduce the leakage; heat treatment conditions influencing the removal of trace organic residues; and the substrate that determines the stress state influence the film properties. Dielectric permittivity, ferroelectric and energy storage properties and piezoelectric d33 coefficient are enhanced in about 300 nm thick Mn-doped BZT-BCT films deposited on Pt/Sapp substrates with a columnar microstructure.

Table 2: Functional properties of BZT-BCT thin films on Pt/Si and Pt/Sapp substrates dried at 250 °C for 15 minutes, pyrolyzed at 350 °C for 15 minutes and multistep annealed at 850 °C.

	BZT-BCT films					
Conc. (mol/l)	0.2	0.1	0.1	0.1	0.1	0.1
Doping	-	-	Mn	Mn	Mn	Mn
Substrate	Pt/Si	Pt/Si	Pt/Si	Pt/Sapp	Pt/Sapp	Pt/Sapp
Thickness, nm	120	120	120	100	340	680
Microstructure	Equiaxed	Columnar	Columnar	Columnar	Columnar	Columnar
ε' at 1 kHz at R.T.	350	510	670	500	820	820
tanδ at 1 kHz at R.T.	0.02	0.02	0.02	0.03	0.02	0.02
E_{max} (kV·cm^{-1})	-	-	1160	1000	3500	1400
E_c (kV·cm^{-1})	-	-	80	110	45	40
P_r (μC·cm^{-2})	-	-	5	6	4	4
P_{max} (μC·cm^{-2})	-	-	32	28	47	32
U_{rec} (J·cm^{-3})	-	-	10	-	47	-
η (%)	-	-	69	-	89	-
d_{33} (pm.V^{-1})	-	-	22 (34)	20 (33)	40 (54)	40 (54)

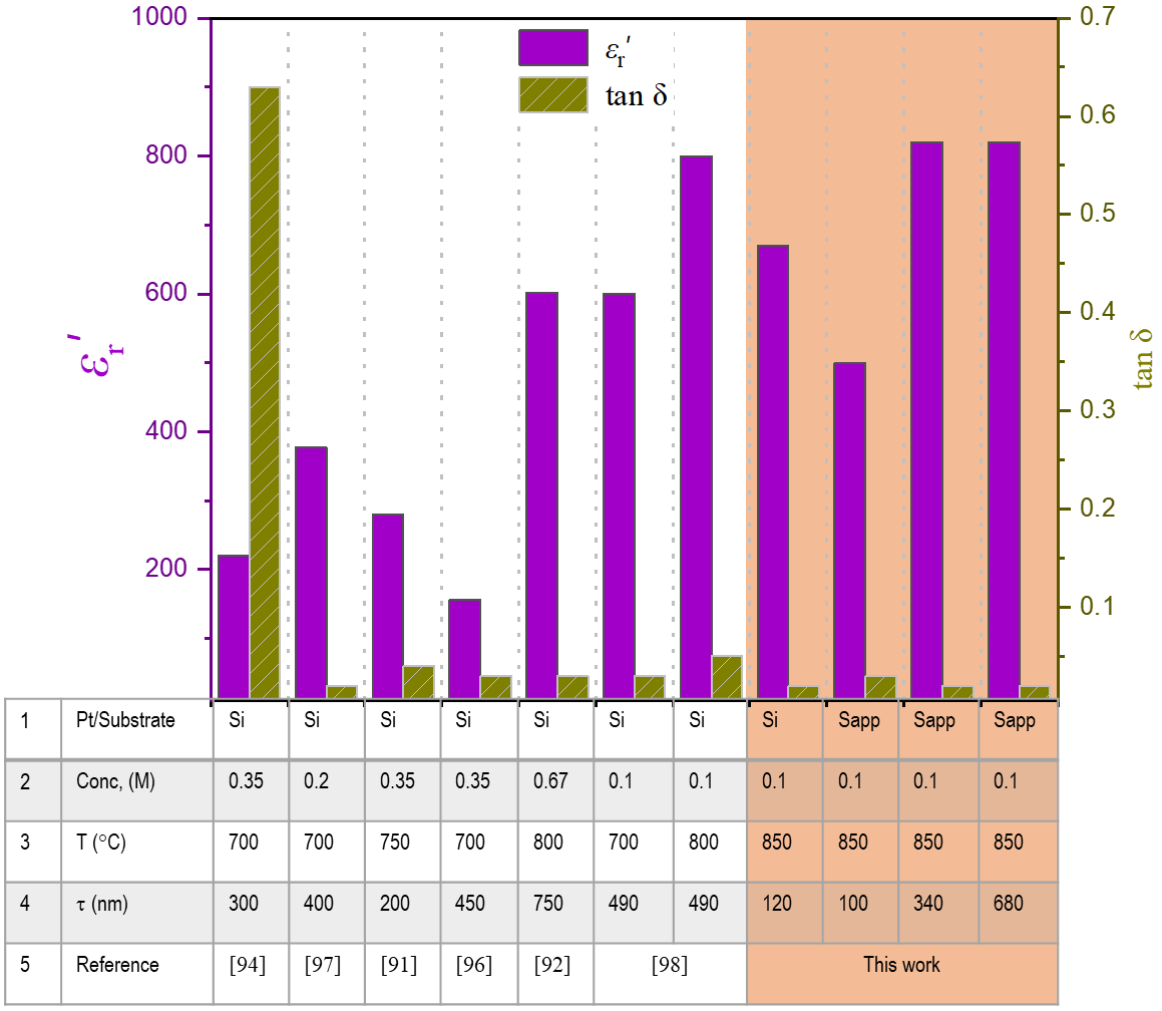

1	Pt/Substrate	Si	Si	Si	Si	Si	Si	Si	Si	Sapp	Sapp	Sapp
2	Conc, (M)	0.35	0.2	0.35	0.35	0.67	0.1	0.1	0.1	0.1	0.1	0.1
3	T (°C)	700	700	750	700	800	700	800	850	850	850	850
4	τ (nm)	300	400	200	450	750	490	490	120	100	340	680
5	Reference	[94]	[97]	[91]	[96]	[92]	[98]		This work			

Figure 24: Comparison of dielectric properties of Mn-doped BZT-BCT from this thesis with data from the literature on the films with the same composition prepared by CSD (1: Platinized substrate, 2: concentration of coating solution, 3: annealing temperature, 4: the film thickness, and 5: reference).

Figure 24 compares the dielectric properties of BZT-BCT thin films studies in the thesis with data from the literature. We selected BZT-BCT films deposited on Pt/Si substrates with different thicknesses prepared by conventional carboxylic acid-acid-based CSD annealed at different temperatures. Our results are comparable to or higher than the reported values for BZT-BCT films; however, the comparison is not straightforward as the films' characteristics are very different. We can conclude that a high annealing temperature and increasing film thickness contribute to higher dielectric permittivity and low losses.

A comparison of energy storage properties of BZT-BCT films studied in the thesis with the candidates for energy storage applications, lead-based antiferroelectric [124], [125], relaxor [126], ferroelectric [127], and promising lead-free thin films [95], [106], [128], [129] reported in the literature, with the energy storage properties of BZT-BCT films (BZT-BCT-1 and BZT-BCT-2) measured in this thesis is shown in Figure 25. Table 3 summarizes the film deposition methods, substrates, dopants, and electric fields at which the films were measured.

Our BZT-BCT thin films show comparable or even higher energy storage efficiency than lead-based antiferroelectric films. They possess suitable properties for energy storage applications and are a viable alternative to lead-based materials.

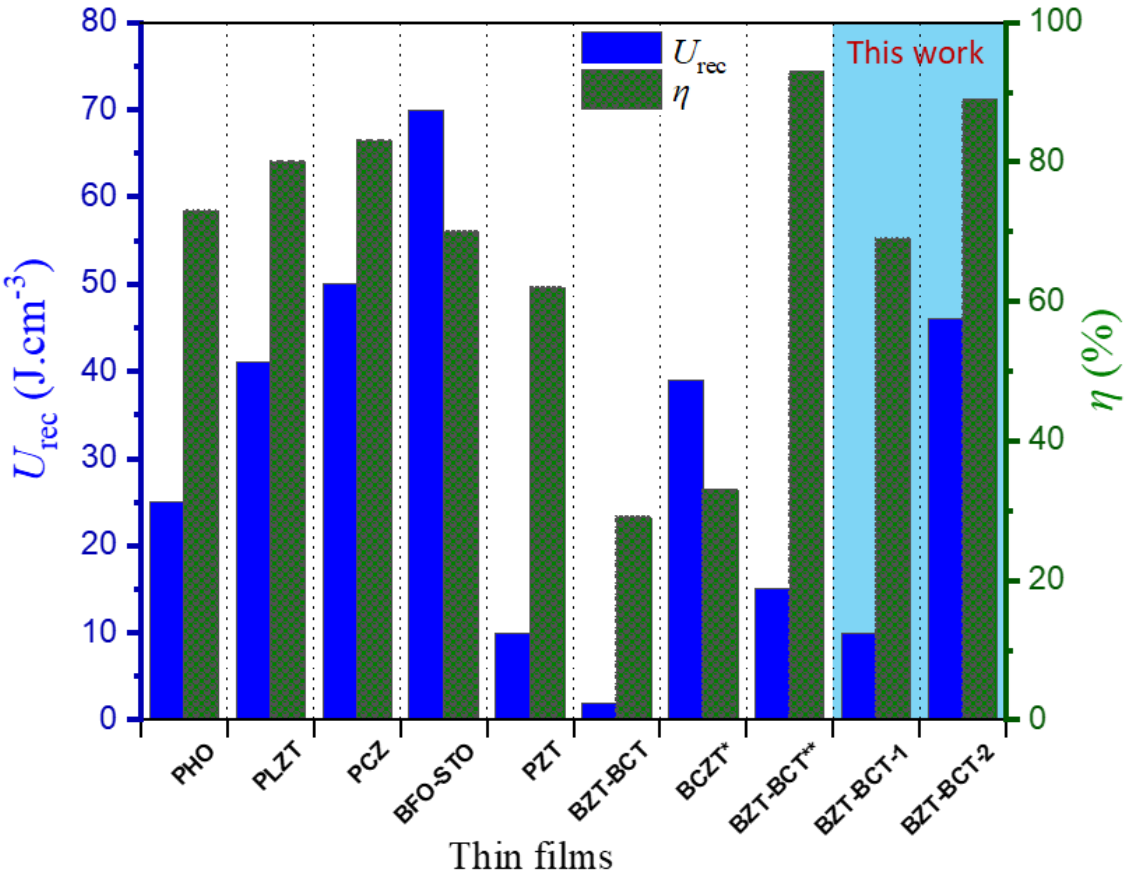

Figure 25: Recoverable energy density (U_{rec}) and efficiency (η) of BZT-BCT thin films from the thesis and the films from the literature. For details, please refer to Table 3.

Table 3: Characteristics of BZT-BCT films (this work) and barium-, lead- and bismuth-based perovskite oxide thin films obtained by different methods reported in the literature.

Film	**Dopant**	**Substrate**	**Thickness (nm)**	**Method**	$E_{max,}$ **(MV·cm^{-1})**	**Ref**
PHO	-	ITO/glass	330	CSD	3	[124]
PLZT	La	Ti-foil	1200	PLD	3	[126]
PCZ	-	Pt/Si	300	CSD	2.8	[125]
PZT	-	SRO/STO	1000	PLD	1	[127]
BZT-BCT	-	Pt/Si	150	IBSD	0.15	[129]
BCZT*	-	MgO	360	PLD	2.08	[106]
BZT-BCT**	La	Pt/Si	280	CSD	3.335	[95]
BFO-STO	-	STO	500	PLD	3.85	[128]
BZT-BCT-1	Mn	Pt/Si	120	CSD	1.16	This work
BZT-BCT-2	Mn	Pt/Sap.	340	CSD	3.5	

PHO: $PbHfO_3$, PLZT: $Pb_{0.9}La_{0.1}(Zr_{0.52}Ti_{0.48})O_3$, PCZ: $Pb_{0.88}Ca_{0.12}ZrO_3$, BFO-STO: $0.4(BiFeO_3)–0.6(SrTiO_3)$, BCZT*: $(Ba_{0.955}Ca_{0.045})(Zr_{0.17}Ti_{0.83})O_3$, BZT-BCT**: $(Ba_{0.904}Ca_{0.096})_{0.9775}+0.0075La_{0.015}(Zr_{0.136}Ti_{0.864})O_3$, ITO: In-Sn-oxide, SRO: $SrRuO_3$, STO: $SrTiO_3$, PLD: pulsed layer deposition, IBSD: ion beam sputtering deposition.

Future work on BZT-BCT thin films could be focused on individual applications to optimize the performance of the intended device. Here are some ideas:

- Doping with lanthanum could be introduced to reduce the remanant polarization and coercive field, thus increasing the energy storage efficiency.
- Deposition of BZT-BCT thin films on flexible substrates, suitable for energy storage and MEMS applications in wearable devices.

Appendix A

Dielectric, Piezoelectric, and Ferroelectric Materials

Dielectrics refer to insulating materials or very poor conductors of electric current. They can be polarized by an external electric field. Dielectric materials are characterized by several physical properties:

Dielectric polarization (P) is the separation of positive and negative charges induced by an applied electric field (E) and is expressed by the following relationship:

$$P = \varepsilon_o(\varepsilon_r'\text{-}1)\, E = \varepsilon_o\, \chi_e\, E \tag{5}$$

Where P is the polarization, ε_o the dielectric permittivity of the vacuum, ε_r' is the relative dielectric permittivity, χ_e is the dielectric susceptibility, and E is the applied electric field.

The stored charge in a dielectric material under applied alternating voltage is the combination of in-phase and out-of-phase components known as the real (ε') and imaginary (ε'') parts of permittivity. Therefore, the relative permittivity can be expressed as follows:

$$\varepsilon_r' = \varepsilon' - i\varepsilon'' \tag{6}$$

The dielectric losses or tan δ in a dielectric material is expressed as follows:

$$\tan\delta = \frac{\varepsilon''}{\varepsilon'} \tag{7}$$

Another physical property of a dielectric material is dielectric displacement (D), which refers to the total surface charge density induced in the material under an applied electric field.

$$D = \varepsilon_o + P = \varepsilon_o\varepsilon_r'E \tag{8}$$

Piezoelectrics are a subgroup of dielectric materials that react to an applied mechanical stimulus by generating electric charge (direct effect) or conversely, by applying an external electric field, mechanical deformation is obtained (conversed effect). Piezoelectrics are characterized by crystal structure with no center of symmetry (20 out of 32 crystal classes). Direct and converse piezoelectric effects can be described by the following equations:

$$D = d\cdot\sigma \tag{9}$$

$$S = d \cdot E \tag{10}$$

Where σ is the applied stress, S is the induced strain, d is the piezoelectric coefficient and E is the electric field.

Half (10 classes) of the piezoelectric crystal groups are pyroelectrics with spontaneous polarization (P_s), which changes with temperature in a given temperature range. A subgroup of pyroelectric materials possesses a spontaneous polarization, the direction of which can be switched by an external electric field. Those are ferroelectric materials. The hysteretic *P-E* dependences of a perfect single-domain crystal and a polycrystalline material are shown in Figure 26. The differences are due to individual grains and domains, i.e., crystal regions with uniformly oriented spontaneous polarization, in the latter material [1], [8]. In polycrystalline ferroelectric materials, the dipoles with unfavourable directions of polarization progressively switch in the direction of the applied electric field as the electric field is increased. When the dipoles are orientated to the highest extent, the *P-E* curve saturates. When the electric field decreases and finally reaches zero, the polarization remains nonzero and is called remanent polarization (P_r). The electric field in the opposite direction called the coercive field (E_c), must be applied to bring the polarisation back to zero. As we further decrease the electric field, we induce a new alignment of dipoles in the opposite direction and eventually reach saturation. In an ideal *P-E* hysteresis, the positive and negative coercive field and the positive and negative remanent polarization are equal in size.

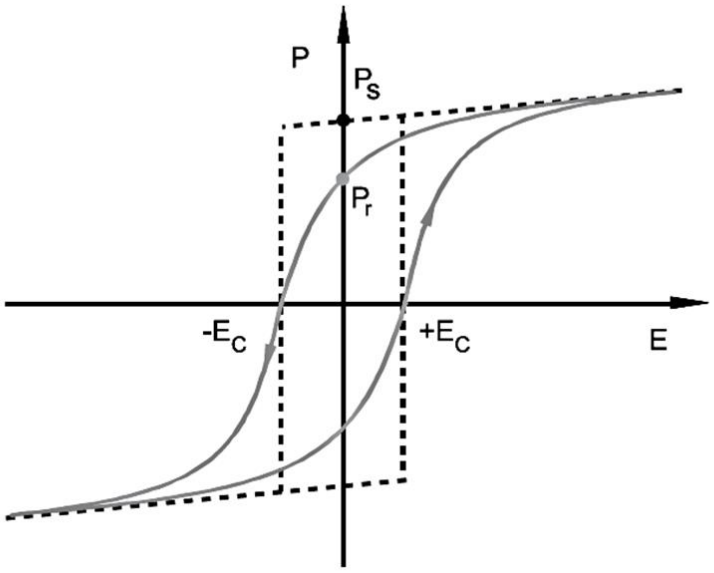

Figure 26: *P-E* loops of a single domain single ferroelectric crystal (dashed line) and a polycrystalline ferroelectric (full line) (from [8]).

Another characteristic of ferroelectric materials is the tunability of the capacitance or permittivity in response to an applied electric field. The equation (1) where $\chi = \varepsilon' - 1$ is valid only for small fields. If a large AC field is applied to a material in the paraelectric phase, the permittivity response is non-linear [8]. In contrast, the material in the ferroelectric phase shows the so-called sub-loops of hysteresis loops of permittivity or capacitance in response to the applied large AC electric field, as shown in Figure 27, characteristic butterfly-shaped loops [8], [130], [131], [132].

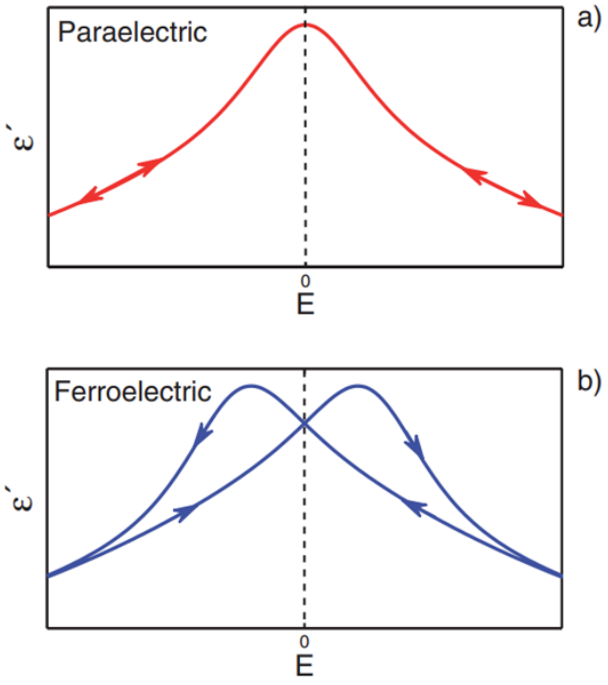

Figure 27: Electric field dependence of permittivity of a ferroelectric material in the paraelectric phase a) and ferroelectric phase b) (from [133]).

For energy storage applications, high maximum polarization and breakdown field are desirable for higher energy-storage density (U_{st}). Low remanant polarization and coercive field contribute to higher energy storage efficiency (η) [134], [135]. The U_{st} and recoverable energy (U_{rec}) in non-linear dielectrics are calculated by integrating the area between the charge and discharge curves respectively, and the polarization-electric field loop axis[136], [137], [138]. The energy dissipation or loss (U_{loss}) is the integral area between the charge and discharge curves as shown in Figure 28.

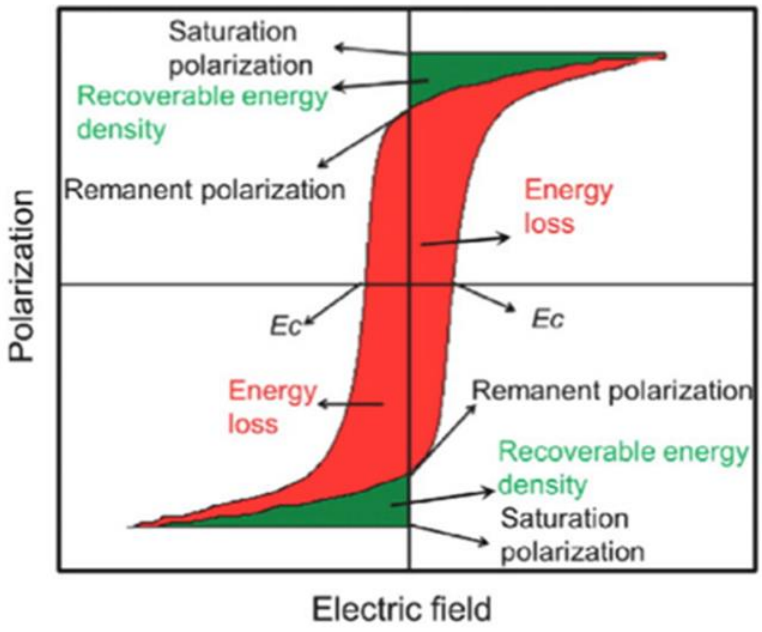

Figure 28. Diagram of the energy storage for ferroelectric materials (from [138]).

Appendix B

Linear Thermal Expansion of $0.5Ba(Zr_{0.2}Ti_{0.8})O_3$-$0.5(Ba_{0.7}Ca_{0.3})TiO_3$ Bulk Ceramic

Barium zirconate titanate barium calcium titanate solid solution $0.5Ba(Zr_{0.2}Ti_{0.8})O_3$-$0.5(Ba_{0.7}Ca_{0.3})TiO_3$ (BZT-BCT) is one the most promising lead-free ferroelectric with piezoelectric properties comparable to those of $(Pb(Zr,Ti)O_3$ or PZT). In numerous miniature devices, such as micro-electro-mechanical systems (MEMS) or energy harvesters, the space constraints favour the use of piezoelectric ceramic elements in the form of thin or thick films. One of the key parameters for designing such devices mentioned above includes the linear thermal expansion coefficients of the constituent materials. To our knowledge, there has been no reported study on the linear thermal expansion coefficient of BZT-BCT ceramic. Such data would contribute to efficiently designing the processing of dense and crack-free BZT-BCT thin films on various substrates (silicon, perovskite single crystals, sapphire) or thick films where the powder slurry is screen-printed on a platinized alumina substrate. Such films could find applications in energy harvesting or energy storage.

Published in: S. W. Konsago, A. Debevec, J. Cilenšek, B. Kmet, and B. Malič, "Linear Thermal Expansion of $0.5Ba(Zr_{0.2}Ti_{0.8})O_3$-$0.5(Ba_{0.7}Ca_{0.3})TiO_3$ Bulk Ceramic", *Informacije MIDEM*, vol.53, no.4, pp. 233-238, 2023 (IF = 1.2, 2022).

My contribution: Participation in the synthesis of the BZT-BCT powders, sintering of the ceramics, polishing, and density measurements. I have performed the XRD data analysis and the dielectric and ferroelectric data treatment. I have prepared the concept of the paper jointly with my supervisor and wrote the manuscript with co-authors.

Original scientific paper
https://doi.org/10.33180/InfMIDEM2023.403

Informacije MIDEM
Journal of Microelectronics, Electronic Components and Materials
Vol. 53, No. 4(2023), 233 – 238

Linear Thermal Expansion of $0.5Ba(Zr_{0.2}Ti_{0.8})O_3$-$0.5(Ba_{0.7}Ca_{0.3})TiO_3$ Bulk Ceramic

Sabi William Konsago[1,2], Andrej Debevec[1], Jena Cilenšek[1], Brigita Kmet[1,2], Barbara Malič[1,2]

[1]Electronic Ceramics Department, Jožef Stefan Institute, Ljubljana, Slovenia
[1]Jožef Stefan International Postgraduate School, Ljubljana, Slovenia

Abstract: We report the linear thermal expansion coefficient of lead-free ferroelectric ceramic barium zirconate titanate - barium calcium titanate $0.5Ba(Zr_{0.2}Ti_{0.8})O_3$-$0.5(Ba_{0.7}Ca_{0.3})TiO_3$ (BZT-BCT). The material was prepared by solid-state synthesis and consolidated by sintering at 1450°C. BZT-BCT crystallizes in the perovskite phase. The microstructure of the ceramic with about 95 % relative density consists of about 10 μm-sized grains. The contact dilatometry of the ceramic specimen reveals the change of slope of the linear thermal expansion curve at 84°C. This is in good agreement with the peak of the dielectric permittivity versus temperature at about 85°C indicating the transition from the low-temperature polar ferroelectric phase to a high-temperature nonpolar phase or Curie temperature. The thermal expansion coefficients of the polar tetragonal and nonpolar cubic phases of BZT-BCT are 7.69×10^{-6} K^{-1} (40°C – 80°C) and 12.39×10^{-6} K^{-1} (100°C – 600°C), respectively. The thermal expansion data are among the material data needed in the design of thin- and thick-film structures for energy-harvesting and energy-storage applications.

Keywords: $0.5Ba(Zr_{0.2}Ti_{0.8})O_3$-$0.5(Ba_{0.7}Ca_{0.3})TiO_3$ (BZT-BCT), lead-free, ferroelectric ceramic, linear thermal expansion

Linearni temperaturni raztezek volumenske keramike $0.5Ba(Zr_{0.2}Ti_{0.8})O_3$-$0.5(Ba_{0.7}Ca_{0.3})TiO_3$

Izvleček: V delu poročamo o linearnem temperaturnem raztezku volumenske keramike barijevega cirkonata titanata - barijevega kalcijevega titanata $0.5Ba(Zr_{0.2}Ti_{0.8})O_3$-$0.5(Ba_{0.7}Ca_{0.3})TiO_3$ (BZT-BCT). Material smo pripravili s sintezo v trdnem stanju in sintranjem pri 1450°C. BZT-BCT kristalizira v perovskitni fazi. Mikrostrukturo keramike s ≈95% relativno gostoto sestavljajo zrna velikosti okrog 10 μm. Linearni temperaturni raztezek keramike smo izmerili s kontaktno dilatometrijo od sobne temperature do 600°C. Pri temperaturi 84°C opazimo spremembo naklona krivulje raztezka. Ta podatek se ujema s temperaturo maksimuma dielektričnosti v odvisnosti od temperature, ki označuje prehod nizkotemperaturne polarne feroelektrične faze v visokotemperaturno nepolarno fazo oziroma Curiejevo temperaturo. Vrednosti linearnega temperaturnega raztezka polarne in nepolarne faze BZT-BCT sta 7.69×10^{-6} K^{-1} (40°C – 80°C) in 12.39×10^{-6} K^{-1} (100°C – 600°C). Podatke o temperaturnem raztezku keramike potrebujemo pri načrtovanju tanko- in debeloplastnih struktur, namenjenih zbiranju in shranjevanju energije.

Ključne besede: $0.5Ba(Zr_{0.2}Ti_{0.8})O_3$-$0.5(Ba_{0.7}Ca_{0.3})TiO_3$ (BZT-BCT), brez svinca, feroelektrična keramika, linearni temperaturni raztezek

* *Corresponding Author's e-mail: barbara.malic@ijs.si*

1 Introduction

The discovery of the high piezoelectric properties of the barium zirconate titanate - barium calcium titanate solid solution $0.5Ba(Zr_{0.2}Ti_{0.8})O_3$-$0.5(Ba_{0.7}Ca_{0.3})TiO_3$ (BZT-BCT) bulk ceramic has revealed its great potential for many piezoelectric applications including actuators, transducers, and energy harvesting devices [1] - [3]. As an example, an intravascular ultrasound transducer made of BZT-BCT has been prototyped [4]. It is also being studied as a promising biocompatible material for bone regeneration [5], [6]. BZT-BCT has gained the attention of the ferroelectric/piezoelectric communities as one of the most promising environment-friendly alternatives to commercially widely spread lead-based piezoelectric ceramic materials such as $Pb(Zr,Ti)O_3$ (PZT) due to the Restriction of Hazardous Substances

How to cite:
S. W. Konsago et al., "Linear Thermal Expansion of $0.5Ba(Zr_{0.2}Ti_{0.8})O_3$-$0.5(Ba_{0.7}Ca_{0.3})TiO_3$ Bulk Ceramic", Inf. Midem-J. Microelectron. Electron. Compon. Mater., Vol. 53, No. 3(2023), pp. 233–238

(RoHS) regulations [7] - [9]. Recently it has been reported that it possesses promising energy storage properties [10], [11].

BZT-BCT exhibits a Curie temperature of about 85-90 °C. In the proximity of room temperature, the coexistence of rhombohedral, orthorhombic, and tetragonal phases of solid solutions of $Ba(Zr_{0.2}Ti_{0.8})O_3$ and $(Ba_{0.7}Ca_{0.3})TiO_3$ with the molar ratios close to unity contributes to enhanced piezoelectric properties [12], [13]. It was shown that the grain size strongly influences the piezoelectric properties and the phase transitional behaviour of BZT-BCT bulk ceramic; the enhanced piezoelectric response was characteristic for grain sizes exceeding 10 μm [14].

In numerous miniature devices, such as microelectromechanical systems (MEMS) or energy harvesters, the space constraints favour the use of piezoelectric ceramic elements in the form of thin or thick films [15], [16]. One of the key parameters for designing such devices includes the thermal expansion coefficients of the constituent materials. In case of a large difference in thermal expansion coefficients of the film and the substrate, the induced stresses may contribute to lowering the piezoelectric response [17] - [19]. Clamping the screen-printed thick film by the substrate results in poor densification during sintering [20]. Tensile stresses in the film that arise due to the thermal expansion coefficient mismatch may lead to the evolution of cracks [19]. Various effects of stresses generated by the thermal expansion mismatch also affect other functional properties, such as breakdown strength [21], [22], which is important in energy storage applications.

There are some publications on the thermal expansion coefficient of Ca- and Zr-modified barium titanate ceramics [23] - [26] but to our knowledge, there is no reported study on the linear thermal expansion coefficient of BZT-BCT ceramic. Such data would contribute to efficiently designing the processing of dense and crack-free BZT-BCT thick films where the powder slurry is screen-printed on a platinized alumina substrate. Such films could find applications in energy harvesting.

Our study aims to prepare perovskite BZT-BCT ceramic with a high relative density, uniform microstructure, and adequate low- and high-field dielectric properties. The linear thermal expansion coefficient from room temperature to 600 °C is measured.

2 Materials and methods

BZT-BCT powder was prepared using alkaline earth carbonates (($BaCO_3$, 99.8% and $CaCO_3$, 99,95% both from Alfa Aesar, Karlsruhe, Germany) and transition metal oxides (TiO_2, 99.8% also from Alfa Aesar, Karlsruhe, Germany and ZrO_2, 99.8% from Tosoh, Japan). The metal content was checked gravimetrically. The 25 g batches of stoichiometric fractions of the reagents were homogenized using isopropanol in a planetary mill (PM 400, Retsch) with yttria-stabilized zirconia milling bodies (3 mm, Tosoh, Japan) for 2 h at 200 rpm. The median particle size of the milled powder was 0.45 μm as determined by laser granulometry (Microtrac S3500 Particle Size Analyzer) using isopropanol as a dispersion liquid. The calcination of the loosely pressed reagent mixture (P = 50 MPa) took place at 1300 °C for 4 hours in the air with heating and cooling rates of 5 K/min. The powder was again milled for 2h at 200 rpm in a planetary mill, dried at 120 °C and sieved. The powder was shaped into pellets (diameter: 8 mm) or bars (40 mm x ≈7 mm x ≈5 mm) by uniaxial (P = 50 MPa) and isostatic pressing (P = 300 MPa). The powder compacts were sintered at 1450 °C for 4 hours in the air with heating and cooling rates of 5 K/min.

The phase composition of the calcined powders and crushed sintered specimens was analyzed by X-ray diffraction (XRD, X'Pert PRO MPD, PANanalytical, CuKa1 radiation, time/step: 100 s, interval between data points: 0.0016°). The density of the sintered samples was determined pycnometrically (Micromeritics, AccuPyc III 1340 Pycnometer).

The ceramic samples were ground and polished using standard ceramographic techniques. Thermal etching of the polished sections at 1350 °C for a few minutes revealed the grain boundaries. A field-emission scanning electron microscope (FE-SEM JEOL JSM-7600) with an energy-dispersive X-ray spectrometer (EDXS, INCA Oxford 350 EDS SDD) was used for the analysis of the microstructure. The grain size was determined using the Image Tool software.

For low- and high-field dielectric measurements, the disks were cut to the thickness of 0.5 mm and polished. An annealing step to 600 °C for 1 h followed by a slow cooling (1 K/min) was used to release the stresses of mechanical operations. The Au electrodes with a diameter of 3 mm were RF-magnetron sputtered on the faces of the disks (5 Pascal). The dielectric permittivity (ε) and losses (tan δ) were measured between +150 °C and -40°C with a cooling rate of 1 K/min (Agilent E4980A Precision LCR meter, 1V). The polarization-electric field hysteresis loops were measured at room temperature with a sine voltage at the frequency of 50 Hz (Aixacct TF analyzer 2000).

For the measurement of the thermal expansion, the ceramic bars were cut to the dimensions of 25 mm x 5 mm x 4 mm. The faces of the bars were plan-parallel

S. W. Konsago et al.; Informacije Midem, Vol. 53, No. 4(2023), 233 – 238

polished. Thermal stresses were released as described above. The dimensional changes of the specimen upon heating and cooling were measured with a contact dilatometer with a corundum measuring system (Netzsch DIL 402 PC) between room temperature and 600 °C with the heating and cooling rates of 5 K/min in air.

3 Results and discussion

Figure 1 contains the XRD patterns of BZT-BCT powder after the calcination at 1300 °C (a) and the ceramic sintered at 1450 °C (b). The XRD patterns of both samples reveal a perovskite phase without any noticeable secondary phases. The unit cell distortion could not be determined using a standard X-ray diffractometer, synchrotron radiation would be needed to obtain a deeper insight into the phase composition of the material, c.f. [13], [27] - [29]. According to the phase diagram [13], the coexistence of the orthorhombic phase cannot be excluded at room temperature besides rhombohedral and tetragonal phases in the morphotropic phase boundary region.

The relative density of BZT-BCT ceramic is 95.4 %. The microstructure shown in Figure 2 a) is uniform, with a unimodal grain size distribution and a mean grain size of 9.66 ± 4.84 µm (Figure 2 b)). EDXS analysis confirmed a uniform distribution of elements within and between individual grains (EDXS spectra are not shown). Trace amounts of a secondary phase were observed at some grain junctions (see the inset of Figure 2 a)) but due to their small size, their chemical composition could not be reliably determined on the level of FE-SEM.

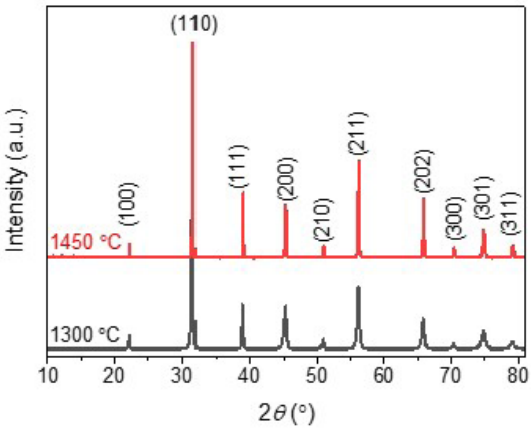

Figure 1: XRD patterns of BZT-BCT powder calcined at 1300 °C and ceramic sintered at 1450 °C. The peaks are indexed according to the $BaTiO_3$ cubic phase (PDF 01-074-4539).

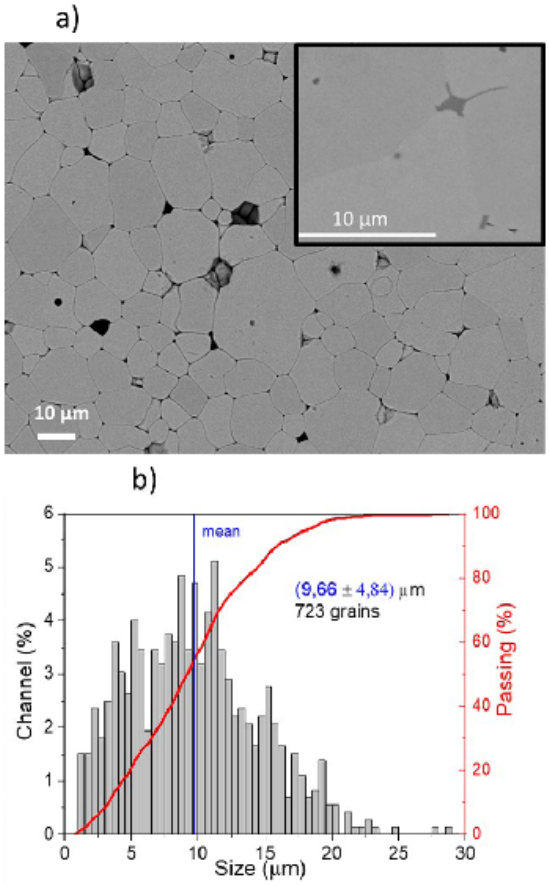

Figure 2: a) SEM micrograph of the microstructure of BZT-BCT ceramic and b) grain size distribution. Inset in panel a) reveals an intergranular phase located at a grain junction.

Figure 3 shows the temperature dependence of the dielectric permittivity and losses as a function of temperature in the frequency range from 100 Hz to 100 kHz. Dielectric permittivity and losses at room temperature and 1 kHz are 3165 and 0.029 in agreement with reported values for ceramics with similar grain sizes [14]. There is no significant change in the dielectric permittivity in the frequency range from 100 Hz to 100 kHz in the measured temperature range. The change of slope at about 40 °C is attributed to the rhombohedral–tetragonal phase transition, and the dielectric permittivity peak at about 85 °C to transition to the cubic phase or Curie temperature. The grain size influences both phase transition temperatures; for the ceramic with about 10 µm-sized grains, the respective values were 87 °C and 35 °C [14]. Broadening of the permittivity peak, characteristic of polycrystalline ferroelectrics, is related to the micron size of the crystallites and the presence of two cations on each cation sublattice

site. We do not observe any noticeable frequency peak shifting in the measured frequency range supporting the ferroelectric nature of the BZT-BCT ceramic. It has been shown that processing conditions and grain size strongly influence the ferroelectric or relaxor nature of BZT-BCT [14], [27].

Figure 4 shows the room temperature polarization–electric field (*P–E*) hysteresis loops measured at 50 Hz. The sample survived the maximum applied field of 70 kV/cm, indicating its good dielectric breakdown resistance. The remnant polarization P_r and coercive field E_c are about 13 μC/cm^2 and 5.9 kV/cm, respectively, indicating a good ferroelectric response of BZT-BCT. Hao et al obtained similar P_r and E_c values for the ceramic with 10 μm-sized grains [14].

Figure 5 shows the dilatometric curves of BZT-BCT ceramic, revealing linear thermal expansion or contraction upon heating or cooling. There is not much difference between the heating and cooling curves. Two main slopes are discerned in both cases with the inflexion point at 84.0 °C. The thermal hysteresis between the heating and cooling runs is quite small. We note that the inflexion temperature corresponds well to the dielectric permittivity peak temperature, cf. Figure 3. The thermal expansion coefficient (TEC = $(\Delta L/L_0)/\Delta T$), determined from the cooling curve in the temperature range from 40 °C to 80 °C, is 7.69×10^{-6} K^{-1}. In this temperature range the tetragonal phase prevails [13], but the coexistence of a rhombohedral phase cannot be excluded judging from the evident change of slope at about 40 °C in the dielectric permittivity curve (cf. Figure 3). As the temperature increases, the TEC progressively increases as well. From 100 °C to the final temperature of 600 °C, in the temperature range of the cubic phase, the TEC is 12.39×10^{-6} K^{-1}.

As explained earlier we could not find the thermal expansion data for BZT-BCT. The TEC of the base formulation of BZT-BCT solid solution, the prototype ferroelectric $BaTiO_3$, is 6.5×10^{-6} K^{-1} in the tetragonal phase and 9.8×10^{-6} K^{-1} in the cubic phase (125 °C – 200 °C) measured by contact dilatometry [30]. It is noted that the change in the slope of the thermal expansion of $BaTiO_3$ at the phase transition temperature is sharp and accompanied by a noticeable shrinkage which is a fingerprint of a first-order phase transition and is not the case with BZT-BCT. Here, we observe only the change in the slope of the thermal expansion. Tian et al. studied $(Ba,Ca)TiO_3$-$Ba(Zr,Ti)O_3$ with slightly different molar ratios of cations compared to BZT-BCT formulation, and they incorporated various rare-earth dopants. They measured a TEC of about 5×10^{-6} K^{-1} at lower temperatures and a TEC of about 11×10^{-6} K^{-1} at higher temperatures, the final temperature being 400 °C. The exact value of TEC and the TEC-inflexion point's temperature depended on the studied materials' chemical composition[31], [32]. Our results are in good agreement with these latter dilatometric studies of the $(Ba,Ca)TiO_3$-$Ba(Zr,Ti)O_3$ solid solutions.

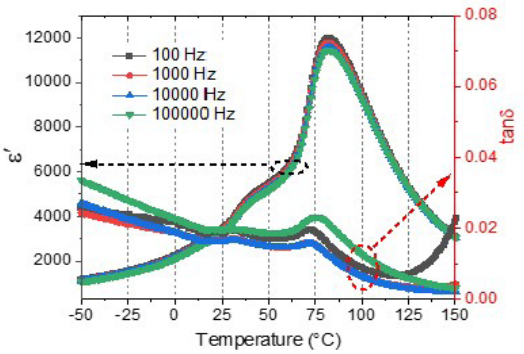

Figure 3: The dielectric permittivity and losses as a function of the temperature of BZT-BCT ceramic.

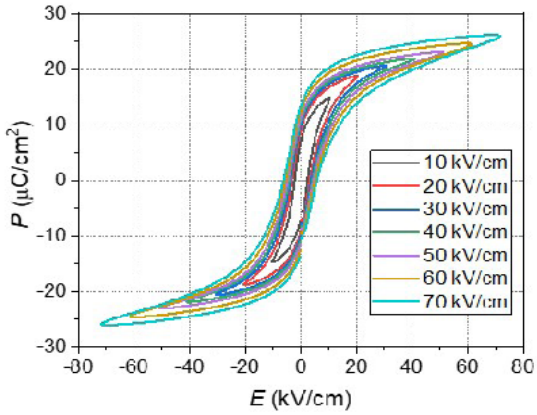

Figure 4: Polarization - electric field - loops of BZT-BCT ceramic measured at 50 Hz and room temperature.

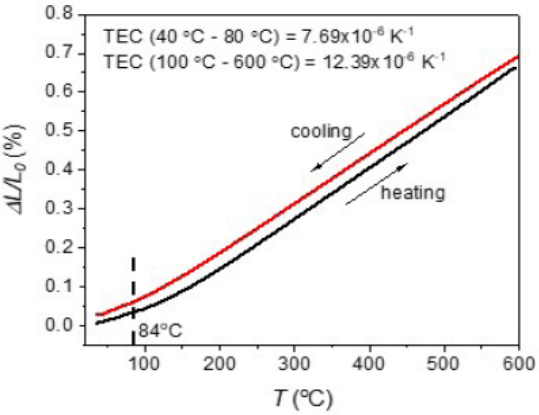

Figure 5: The linear thermal expansion of BZT-BCT ceramic measured between room temperature and 600 °C. The inflexion point and TEC were determined from the cooling curve.

4 Conclusions

In conclusion, this study focused on determining the thermal expansion behavior of 0.5Ba($Zr_{0.2}Ti_{0.8}$)O_3-05($Ba_{0.7}Ca_{0.3}$)TiO_3 (BZT-BCT) bulk ceramic. The powder, prepared by solid-state synthesis, was compacted and sintered to a high relative density at 1450 °C for 4 hours. The ceramic crystallized in the perovskite phase. The microstructure consisted of about 10 μm sized grains. The measurement of the dielectric permittivity versus temperature revealed two anomalies which could be related to the phase transitions of the predominantly rhombohedral to tetragonal phase at about 40 °C and to cubic phase at about 90 °C. The hysteretic dependence of the polarization versus the electric field confirmed the ferroelectric nature of the ceramic. The dilatometric measurements revealed the thermal expansion coefficients of the polar and cubic phases of 7.69×10^{-6} K^{-1} (40 °C – 80 °C) and 12.39×10^{-6} K^{-1} (100 °C – 600 °C). The study results contribute to the design of thick and thin-film structures based on BZT-BCT in various energy-harvesting and/or energy-storage applications.

5 Acknowledgments

The authors acknowledge the advice and technical support of Silvo Drnovšek, Electronic Ceramics Department, Jožef Stefan Institute.

6 Conflict of interest

The authors declare no conflict of interest.

The authors acknowledge the financial support of the Slovenian Research Agency (core funding P2-0105).

7 References

1. W. Liu and X. Ren, "Large piezoelectric effect in Pb-free ceramics," *Phys Rev Lett*, vol. 103, no. 25, 257602, Dec. 2009, https://doi.org/10.1103/PhysRevLett.103.257602.
2. M. Acosta, N. Novak, W. Jo, and J. Rödel, "Relationship between electromechanical properties and phase diagram in the Ba($Zr_{0.2}Ti_{0.8}$)O_3-x ($Ba_{0.7}Ca_{0.3}$)TiO_3 lead-free piezoceramic," *Acta Mater*, vol. 80, pp. 48–55, 2014, https://doi.org/10.1016/j.actamat.2014.07.058.
3. J. Rödel, K. G. Webber, R. Dittmer, W. Jo, M. Kimura, and D. Damjanovic, "Transferring lead-free piezoelectric ceramics into application," *J Eur Ceram Soc*, vol. 35, no. 6, pp. 1659–1681, Jun. 2015, https://doi.org/10.1016/j.jeurceramsoc.2014.12.013.
4. X. Yan *et al.*, "Correspondence: Lead-free intravascular ultrasound transducer using BZT-50BCT ceramics," *IEEE Trans Ultrason Ferroelectr Freq Control*, vol. 60, no. 6, pp. 1272–1276, 2013, https://doi.org/10.1109/TUFFC.2013.2692.
5. K. K. Poon, M. C. Wurm, D. M. Evans, M. Einarsrud, R. Lutz, and J. Glaum, "Biocompatibility of (Ba,Ca)(Zr,Ti)O_3 piezoelectric ceramics for bone replacement materials," *J Biomed Mater Res B Appl Biomater*, vol. 108, no. 4, pp. 1295–1303, May 2020, https://doi.org/10.1002/jbm.b.34477.
6. C. S. Manohar *et al.*, "Novel Lead-free biocompatible piezoelectric Hydroxyapatite (HA) – BCZT ($Ba_{0.85}Ca_{0.15}Zr_{0.1}Ti_{0.9}O_3$) nanocrystal composites for bone regeneration," *Nanotechnol Rev*, vol. 8, no. 1, pp. 61–78, May 2019, https://doi.org/10.1515/ntrev-2019-0006.
7. "DIRECTIVE 2002/95/EC OF THE EUROPEAN PARLIAMENT AND OF THE COUNCIL of 27 January 2003 on the restriction of the use of certain hazardous substances in electrical and electronic equipment."
8. "JIS-C-0950: 2005 (E), 'The marking for presence of the specific chemical substances for electrical and electronic equipment', Japanese Standards Association, 2005".
9. L. M. Benson and K. K. Reczek, "A guide to United States electrical and electronic equipment compliance requirements," Jun. 2021. https://doi.org/10.6028/NIST.IR.8118r2.
10. V. S. Puli *et al.*, "Structure, dielectric, ferroelectric, and energy density properties of (1 – x)BZT–xBCT ceramic capacitors for energy storage applications," *J Mater Sci*, vol. 48, no. 5, pp. 2151–2157, Mar. 2013, https://doi.org/10.1007/s10853-012-6990-1.
11. Neha, R. Pandey, M. Bhatnagar, P. Kumar, R. K. Malik, and C. Prakash, "Improved dielectric and energy storage properties in (1-x)$BaTi_{0.80}Zr_{0.20}O_3$-x$Ba_{0.70}Ca_{0.30}Ti_{0.99}Fe_{0.01}O_3$ ceramics near morphotropic phase boundary," *Mater Lett*, vol. 318, 132126, Jul. 2022, https://doi.org/10.1016/j.matlet.2022.132126.
12. M. Acosta, N. Novak, G. A. Rossetti, and J. Rödel, "Mechanisms of electromechanical response in (1 - X)Ba($Zr_{0.2}Ti_{0.8}$)O_3-x($Ba_{0.7}Ca_{0.3}$)TiO_3 ceramics," *Appl Phys Lett*, vol. 107, no. 14, 142906, Oct. 2015, https://doi.org/10.1063/1.4932654.
13. D. S. Keeble, F. Benabdallah, P. A. Thomas, M. Maglione, and J. Kreisel, "Revised structural phase diagram of ($Ba_{0.7}Ca_{0.3}TiO_3$)-($BaZr_{0.2}Ti_{0.8}O_3$)," *Appl Phys Lett*, vol. 102, no. 9, 092903, Mar. 2013, https://doi.org/10.1063/1.4793400.

14. J. Hao, W. Bai, W. Li, and J. Zhai, "Correlation between the microstructure and electrical properties in high-performance $(Ba_{0.85}Ca_{0.15})(Zr_{0.1}Ti_{0.9})O_3$ lead-free piezoelectric ceramics," *Journal of the American Ceramic Society*, vol. 95, no. 6, pp. 1998–2006, Jun. 2012, https://doi.org/10.1111/j.1551-2916.2012.05146.x.
15. L. Song, S. Glinsek, S. Drnovsek, V. Kovacova, B. Malic, and E. Defay, "Piezoelectric thick film for power-efficient haptic actuator," *Appl Phys Lett*, vol. 121, no. 21, 212901, Nov. 2022, https://doi.org/10.1063/5.0106174.
16. P. Muralt, "Polar oxide thin films for MEMS applications," T. Schneller, R. Waser, M. Kosec and D. Payne (Eds.), *Chemical Solution Deposition of Functional Oxide Thin Films, Wien, Austria, Springer-Verlag, 2013, Ch. 24, pp. 593-620*. https://doi.org/10.1007/978-3-211-99311-8_24.
17. T. A. Berfield, R. J. Ong, D. A. Payne, and N. R. Sottos, "Residual stress effects on piezoelectric response of sol-gel derived lead zirconate titanate thin films," *J Appl Phys*, vol. 101, no. 2, 024102, Jan. 2007, https://doi.org/10.1063/1.2422778.
18. L. Lian and N. R. Sottos, "Effects of thickness on the piezoelectric and dielectric properties of lead zirconate titanate thin films," *J Appl Phys*, vol. 87, no. 8, pp. 3941–3949, Apr. 2000, https://doi.org/10.1063/1.372439.
19. K. Coleman, J. Walker, T. Beechem, and S. Trolier-McKinstry, "Effect of stresses on the dielectric and piezoelectric properties of $Pb(Zr_{0.52}Ti_{0.48})O_3$ thin films," *J Appl Phys*, vol. 126, no. 3, 034101, Jul. 2019, https://doi.org/10.1063/1.5095765.
20. R. K. BORDIA and R. RAJ, "Sintering Behavior of Ceramic Films Constrained by a Rigid Substrate," *Journal of the American Ceramic Society*, vol. 68, no. 6, pp. 287–292, Jun. 1985, https://doi.org/10.1111/j.1151-2916.1985.tb15227.x.
21. A. M. Pashaev, A. Kh. Dzhanakhmedov, and A. A. Aliyev, "Effect of Tensile Stresses on the Breakdown Voltage of Thin Films," *Technical Physics*, vol. 65, no. 1, pp. 54–56, Jan. 2020, https://doi.org/10.1134/S1063784220010211.
22. Y.-N. Bie *et al.*, "Effect of Source Field Plate Cracks on the Electrical Performance of AlGaN/GaN HEMT Devices," *Crystals (Basel)*, vol. 12, no. 9, 1195, Aug. 2022, https://doi.org/10.3390/cryst12091195.
23. Y. Tian *et al.*, "Diversiform electrical and thermal expansion properties of $(1-x)Ba_{0.95}Ca_{0.05}Ti_{0.94}Zr_{0.06}O_3$–(x)Dy lead-free piezoelectric ceramics influenced by defect complexes," *J Mater Sci*, vol. 53, no. 16, pp. 11228–11241, Aug. 2018, https://doi.org/10.1007/s10853-018-2428-8.
24. Y. Tian *et al.*, "Electrical Properties and Thermal Expansion Characteristics of $(1-x)Ba_{0.948}Ca_{0.05}Er_{0.002}Ti_{0.94}Zr_{0.06}O_3$–(x)Pr Lead-Free Piezoelectric Ceramics Sintered at a Low-Temperature," *physica status solidi (a)*, vol. 216, no. 2, 1800622, Jan. 2019, https://doi.org/10.1002/pssa.201800622.
25. Y. Tian *et al.*, "Temperature-dependent ferroelectric and piezoelectric response of Yb^{3+} and Tm3+ co-doped $Ba_{0.95}Ca_{0.05}Ti_{0.90}Zr_{0.10}O_3$ lead-free ceramic," *Journal of Ceramic Processing Research*, vol. 23, no. 4, pp. 430–435, Aug. 2022, https://doi.org/10.36410/jcpr.2022.23.4.430.
26. Y. Tian *et al.*, "Piezoelectricity and Thermophysical Properties of $Ba_{0.90}Ca_{0.10}Ti_{0.96}Zr_{0.04}O_3$ Ceramics Modified with Amphoteric Nd3+ and Y3+ Dopants," *Materials*, vol. 16, no. 6, 2369, Mar. 2023, https://doi.org/10.3390/ma16062369.
27. F. Benabdallah *et al.*, "Structure–microstructure–property relationships in lead-free BCTZ piezoceramics processed by conventional sintering and spark plasma sintering," *J Eur Ceram Soc*, vol. 35, no. 15, pp. 4153–4161, Dec. 2015, https://doi.org/10.1016/j.jeurceramsoc.2015.06.030.
28. H. Amorín *et al.*, "Insights into the Early Size Effects of Lead-Free Piezoelectric $Ba_{0.85}Ca_{0.15}Zr_{0.1}Ti_{0.9}O_3$," *Adv Electron Mater*, https://doi.org/10.1002/aelm.202300556.
29. S. López-Blanco, D. A. Ochoa, H. Amorín, A. Castro, M. Algueró, and J. E. García, "Fine-grained high-performance $Ba_{0.85}Ca_{0.15}Zr_{0.1}Ti_{0.9}O_3$ piezoceramics obtained by current-controlled flash sintering of nanopowders," *J Eur Ceram Soc*, vol. 43, no. 16, pp. 7440–7445, Dec. 2023, https://doi.org/10.1016/j.jeurceramsoc.2023.08.012.
30. G. Shirane and A. Takeda, "Volume Change at Three Transitions in $BaTiO_3$ Ceramics," *J Physical Soc Japan*, vol. 6, no. 2, pp. 128–129, Mar. 1951, https://doi.org/10.1143/JPSJ.6.128.
31. Y. Tian *et al.*, "Diversiform electrical and thermal expansion properties of $(1-x)Ba_{0.95}Ca_{0.05}Ti_{0.94}Zr_{0.06}O_3$–(x)Dy lead-free piezoelectric ceramics influenced by defect complexes," *J Mater Sci*, vol. 53, no. 16, pp. 11228–11241, Aug. 2018, https://doi.org/10.1007/s10853-018-2428-8.
32. Y. Tian *et al.*, "Temperature-dependent ferroelectric and piezoelectric response of Yb^{3+} and Tm^{3+} co-doped $Ba_{0.95}Ca_{0.05}Ti_{0.90}Zr_{0.10}O_3$ lead-free ceramic," *Journal of Ceramic Processing Research*, vol. 23, no. 4, pp. 430–435, Aug. 2022, https://doi.org/10.36410/jcpr.2022.23.4.430.

Arrived: 09. 01. 2024
Accepted: 13. 02. 2024

References

[1] D. Damjanovic, "Ferroelectric, dielectric and piezoelectric properties of ferroelectric thin films and ceramics," *Reports on Progress in Physics*, vol. 61, no. 9, pp. 1267–1324, Sep. 1998, doi: 10.1088/0034-4885/61/9/002.

[2] S. K. Sharma, V. S. Chauhan, and C. S. Yadav, "A theoretical model for the electromagnetic radiation emission from ferroelectric ceramics," *Materials Today Communications*, vol. 14, pp. 180–187, Mar. 2018, doi: 10.1016/j.mtcomm.2018.01.002.

[3] K. K. Deb, M. D. Hill, and J. F. Kelly, "Pyroelectric characteristics of modified barium titanate ceramics," *Journal of Materials Research*, vol. 7, no. 12, pp. 3296–3305, Dec. 1992, doi: 10.1557/JMR.1992.3296.

[4] G. Arlt, D. Hennings, and G. de With, "Dielectric properties of fine-grained barium titanate ceramics," *Journal of Applied Physics*, vol. 58, no. 4, pp. 1619–1625, Aug. 1985, doi: 10.1063/1.336051.

[5] V. Buscaglia *et al.*, "Grain size and grain boundary-related effects on the properties of nanocrystalline barium titanate ceramics," *Journal of the European Ceramic Society*, vol. 26, no. 14, pp. 2889–2898, 2006, doi: 10.1016/j.jeurceramsoc.2006.02.005.

[6] R. Thomas, V. K. Varadan, S. Komarneni, and D. C. Dube, "Diffuse phase transitions, electrical conduction, and low temperature dielectric properties of sol–gel derived ferroelectric barium titanate thin films," *Journal of Applied Physics*, vol. 90, no. 3, pp. 1480–1488, Aug. 2001, doi: 10.1063/1.1367318.

[7] S. Chattopadhyay, A. R. Teren, J.-H. Hwang, T. O. Mason, and B. W. Wessels, "Diffuse Phase Transition in Epitaxial BaTiO3 Thin Films," *Journal of Materials Research*, vol. 17, no. 3, pp. 669–674, Mar. 2002, doi: 10.1557/JMR.2002.0095.

[8] U. Böttger, "Dielectric Properties of Polar Oxides," in *Polar Oxides*, R. Waser, U. Böttger, and S. Tiedke, Eds., Wiley, 2004, pp. 11–38. doi: 10.1002/3527604650.ch1.

[9] B. Tiwari, T. Babu, and R. N. P. Choudhary, "Piezoelectric lead zirconate titanate as an energy material: A review study," *Materials Today: Proceedings*, vol. 43, pp. 407–412, 2021, doi: 10.1016/j.matpr.2020.11.692.

[10] G. Tan *et al.*, "Crystallographic contributions to piezoelectric properties in PZT thin films," *Scientific Reports*, vol. 9, no. 1, p. 7309, May 2019, doi: 10.1038/s41598-019-43869-1.

[11] D. L. Polla *et al.*, "Applications of PZT and Related Thin Films in Piezoelectric Microsensors," *Materials Research Society Proceedings*, vol. 243, p. 55, Feb. 1991, doi: 10.1557/PROC-243-55.

[12] D. Damjanovic, "Lead-Based Piezoelectric Materials," in *Piezoelectric and Acoustic Materials for Transducer Applications*, Boston, MA: Springer US, 2008, pp. 59–79. doi: 10.1007/978-0-387-76540-2_4.

[13] "DIRECTIVE 2002/96/EC OF THE EUROPEAN PARLIAMENT AND OF THE COUNCIL of 27 January 2003 on waste electrical and electronic equipment (WEEE)."

[14] M. Acosta *et al.*, "$BaTiO_3$-based piezoelectrics: Fundamentals, current status, and perspectives," Dec. 01, 2017, *American Institute of Physics Inc.* doi: 10.1063/1.4990046.

[15] W. Liu and X. Ren, "Large piezoelectric effect in Pb-free ceramics," *Physical Review Letters*, vol. 103, no. 25, Dec. 2009, doi: 10.1103/PhysRevLett.103.257602.

[16] V. S. Puli *et al.*, "Structure, dielectric, ferroelectric, and energy density properties of $(1 - x)$BZT–xBCT ceramic capacitors for energy storage applications," *Journal of Materials Science*, vol. 48, no. 5, pp. 2151–2157, Mar. 2013, doi: 10.1007/s10853-012-6990-1.

[17] R. Syal *et al.*, "Flattening of free energy profile and enhancement of energy storage efficiency near morphotropic phase boundary in lead-free BZT-xBCT," *Journal of Alloys and Compounds*, vol. 873, Aug. 2021, doi: 10.1016/j.jallcom.2021.159824.

[18] M. Acosta *et al.*, "Cytotoxicity, chemical stability, and surface properties of ferroelectric ceramics for biomaterials," *Journal of the American Ceramic Society*, vol. 101, no. 1, pp. 440–449, Jan. 2018, doi: 10.1111/jace.15193.

[19] H. JAFFE, "Piezoelectric Ceramics," *Journal of the American Ceramic Society*, vol. 41, no. 11, pp. 494–498, Nov. 1958, doi: 10.1111/j.1151-2916.1958.tb12903.x.

[20] B. Noheda, D. E. Cox, G. Shirane, J. A. Gonzalo, L. E. Cross, and S.-E. Park, "A monoclinic ferroelectric phase in the $Pb(Zr_{1-x}Ti_x)O_3$ solid solution," *Applied Physics Letters*, vol. 74, no. 14, pp. 2059–2061, Apr. 1999, doi: 10.1063/1.123756.

[21] E. Aksel and J. L. Jones, "Advances in Lead-Free Piezoelectric Materials for Sensors and Actuators," *Sensors*, vol. 10, no. 3, pp. 1935–1954, Mar. 2010, doi: 10.3390/s100301935.

[22] M. Acosta, N. Novak, W. Jo, and J. Rödel, "Relationship between electromechanical properties and phase diagram in the $Ba(Zr_{0.2}Ti_{0.8})O_3$-x$(Ba_{0.7}Ca_{0.3})TiO_3$ lead-free piezoceramic," *Acta Materialia*, vol. 80, pp. 48–55, 2014, doi: 10.1016/j.actamat.2014.07.058.

[23] D. S. Keeble, F. Benabdallah, P. A. Thomas, M. Maglione, and J. Kreisel, "Revised structural phase diagram of $(Ba_{0.7}Ca_{0.3}TiO_3)$-$(BaZr_{0.2}Ti_{0.8}O_3)$," *Applied Physics Letters*, vol. 102, no. 9, Mar. 2013, doi: 10.1063/1.4793400.

[24] J. Hao, W. Bai, W. Li, and J. Zhai, "Correlation between the microstructure and electrical properties in high-performance $(Ba_{0.85}Ca_{0.15})(Zr_{0.1}Ti_{0.9})O_3$ lead-free piezoelectric ceramics," *Journal of the American Ceramic Society*, vol. 95, no. 6, pp. 1998–2006, Jun. 2012, doi: 10.1111/j.1551-2916.2012.05146.x.

[25] P. Muralt, "Polar oxide thin films for MEMS applications," in *Chemical Solution Deposition of Functional Oxide Thin Films*, vol. 9783211993118, 2013. doi: 10.1007/978-3-211-99311-8_24.

[26] R. W. Schwartz *et al.*, "Control of Microstructure and Orientation in Solution-Deposited $BaTiO_3$ and $SrTiO_3$ Thin Films", *Journal of the American Ceramic Society*, Vol. 82, no. 9, pp. 2359–2367, sep. 1999, doi: 10.1111/J.1151-2916.1999.TB02091.X

[27] T. Pečnik, S. Glinšek, B. Kmet, and B. Malič, "Combined effects of thickness, grain size and residual stress on the dielectric properties of $Ba_{0.5}Sr_{0.5}TiO_3$ thin films," *Journal of Alloys Compounds*, vol. 646, pp. 766–772, Oct. 2015, doi: 10.1016/j.jallcom.2015.06.192.

[28] U. Hasenkox, S. Hoffmann, and R. Waser, "Influence of Precursor Chemistry on the Formation of $MTiO_3$ (M = Ba, Sr) Ceramic Thin Films," *Journal of Sol-Gel Science and Technology*, vol. 12, no. 2, pp. 67–79, 1998, doi: 10.1023/A:1026480027046.

[29] B. Malič, S. Glinšek, T. Schneller, and M. Kosec, "Mixed Metallo-organic Precursor Systems," in *Chemical Solution Deposition of Functional Oxide Thin Films*, Vienna: Springer Vienna, 2013, pp. 51–69. doi: 10.1007/978-3-211-99311-8_3.

[30] T. Schneller and D. Griesche, "Carboxylate Based Precursor Systems," in *Chemical Solution Deposition of Functional Oxide Thin Films*, Vienna: Springer Vienna, 2013, pp. 29–49. doi: 10.1007/978-3-211-99311-8_2.

[31] J. M. Phillips, "Substrate Selection for Thin-Film Growth," *Materials Research Society Bulletin*, vol. 20, no. 4, pp. 35–39, Apr. 1995, doi: 10.1557/S0883769400044651.

[32] U. Schubert, "Chemical modification of titanium alkoxides for sol–gel processing," *Journal of Materials Chemistry*, vol. 15, no. 35–36, p. 3701, 2005, doi: 10.1039/b504269k.

[33] T. Schneller, "Simple Alkoxide Based Precursor Systems," in *Chemical Solution Deposition of Functional Oxide Thin Films*, Vienna: Springer Vienna, 2013, pp. 3–28. doi: 10.1007/978-3-211-99311-8_1.

[34] R. W. Schwartz, T. Schneller, and R. Waser, "Chemical solution deposition of electronic oxide films," *Comptes Rendus. Chimie*, vol. 7, no. 5, pp. 433–461, May 2004, doi: 10.1016/j.crci.2004.01.007.

[35] V. G. Kessler, "Single Source Precursor Approach," in *Chemical Solution Deposition of Functional Oxide Thin Films*, Vienna: Springer Vienna, 2013, pp. 71–92. doi: 10.1007/978-3-211-99311-8_4.

[36] D. Van den Eynden, R. Pokratath, and J. De Roo, "Nonaqueous Chemistry of Group 4 Oxo Clusters and Colloidal Metal Oxide Nanocrystals," *Chemical Reviews*, vol. 122, no. 11, pp. 10538–10572, Jun. 2022, doi: 10.1021/acs.chemrev.1c01008.

[37] Y. Takahashi, Y. Matsuoka, K. Yamaguchi, M. Matsuki, and K. Kobayashi, "Dip coating of PT, PZ and PZT films using an alkoxide-diethanolamine method," *Journal of Materials Science*, vol. 25, no. 9, pp. 3960–3964, Sep. 1990, doi: 10.1007/BF00582467.

[38] Q. Jia, B. Shen, X. Hao, S. Song, and J. Zhai, "Anomalous dielectric properties of $Ba_{1-x}Ca_xTiO_3$ thin films near the solubility limit," *Materials Letters*, vol. 63, no. 3–4, pp. 464–466, Feb. 2009, doi: 10.1016/j.matlet.2008.11.026.

[39] J. F. Ihlefeld, J.-P. Maria, and W. Borland, "Dielectric and microstructural properties of barium titanate zirconate thin films on copper substrates," *Journal of Materials Research*, vol. 20, no. 10, pp. 2838–2844, Oct. 2005, doi: 10.1557/JMR.2005.0342.

[40] A. M. Kobald, H. Kobald, and M. Deluca, "Phase stability and energy storage properties of polycrystalline antiferroelectric BaTiO3-substituted $NaNbO_3$ thin films," *Journal of the European Ceramic Society*, vol. 44, no. 5, pp. 2831–2841, May 2024, doi: 10.1016/j.jeurceramsoc.2023.11.071.

[41] T. Dechakupt, S. W. Ko, S.-G. Lu, C. A. Randall, and S. Trolier-McKinstry, "Processing of chemical solution-deposited $BaTiO_3$-based thin films on Ni foils," *Journal of Materials Science*, vol. 46, no. 1, pp. 136–144, Jan. 2011, doi: 10.1007/s10853-010-4873-x.

[42] C. Livage, A. Safari, and L. C. Klein, "Glycol-based sol-gel process for the fabrication of ferroelectric PZT thin films," *Journal of Sol-gel Science and Technology*, vol. 2, no. 1–3, pp. 605–609, 1994, doi: 10.1007/BF00486318.

[43] M. L. Calzada and R. Sirera, "Chemically derived ferroelectric calcium modified lead titanate thin films deposited from aquo-diol-solvent solutions," *Journal of Materials Science: Materials in Electronics*, vol. 7, no. 1, Feb. 1996, doi: 10.1007/BF00194091.

[44] R. Fernández, S. Holgado, Z. Huang, M. L. Calzada, and J. Ricote, "Use of the solvent chemistry for the control of the critical thickness of $PbTiO_3$ ultrathin films," *Journal of Materials Research*, vol. 25, no. 5, pp. 890–898, May 2010, doi: 10.1557/JMR.2010.0127.

[45] M. L. Calzada, R. Sirera, F. Carmona, and B. Jiménez, "Investigations of a Diol-based Sol-Gel Process for the Preparation of Lead Titanate Materials," *Journal of the American Ceramic Society*, vol. 78, no. 7, pp. 1802–1808, Jul. 1995, doi: 10.1111/j.1151-2916.1995.tb08892.x.

[46] Z. Wang *et al.*, "Lead-free $0.5Ba(Ti_{0.8}Zr_{0.2})O_3$-$0.5(Ba_{0.7}Ca_{0.3})TiO_3$ thin films with enhanced electric properties fabricated from optimized sol-gel systems," *Materials Chemistry Physics*, vol. 186, pp. 528–533, Jan. 2017, doi: 10.1016/j.matchemphys.2016.11.030.

[47] P. S. Barbato, V. Casuscelli, P. Aprea, R. Scaldaferri, and D. Caputo, "Optimization of the production process of BZT–BCT sol-gel thin films obtained from a highly stable and green precursor solution," *Materials and Manufacturing Processes*, vol. 36, no. 14, pp. 1642–1649, Oct. 2021, doi: 10.1080/10426914.2021.1926495.

[48] D. P. Birnie, "Spin Coating: Art and Science," in *Chemical Solution Deposition of Functional Oxide Thin Films*, Vienna: Springer Vienna, 2013, pp. 263–274. doi: 10.1007/978-3-211-99311-8_11.

[49] Y. Yin, "Advances and perspectives of spin coating techniques," *Applied and Computational Engineering*, vol. 7, no. 1, pp. 291–301, Jul. 2023, doi: 10.54254/2755-2721/7/20230495.

[50] B. K. Daniels, C. R. Szmanda, M. K. Templeton, and P. Trefonas III, "Surface Tension Effects In Microlithography - Striations," C. G. Willson, Ed., Jul. 1986, p. 192. doi: 10.1117/12.963641.

[51] X. Du Min, X. Orignac, and R. M. Almeida, "Striation-Free, Spin-Coated Sol-Gel Optical Films," *Journal of the American Ceramic Society*, vol. 78, no. 8, pp. 2254–2256, Aug. 1995, doi: 10.1111/j.1151-2916.1995.tb08650.x.

[52] D. P. Birnie, "Rational solvent selection strategies to combat striation formation during spin coating of thin films," *Journal of Materials Research*, vol. 16, no. 4, pp. 1145–1154, Apr. 2001, doi: 10.1557/JMR.2001.0158.

[53] F. Remondiere, B. Malič, M. Kosec, and J.-P. Mercurio, "Study of the crystallization pathway of $Na_{0.5}Bi_{0.5}TiO_3$ thin films obtained by chemical solution deposition," *Journal of Sol-gel Science and Technology*, vol. 46, no. 2, pp. 117–125, May 2008, doi: 10.1007/s10971-008-1717-0.

[54] B. Malič, A. Kupec, and M. Kosec†, "Thermal Analysis," in *Chemical Solution Deposition of Functional Oxide Thin Films*, Vienna: Springer Vienna, 2013, pp. 163–179. doi: 10.1007/978-3-211-99311-8_7.

[55] H. S. Gopalakrishnamurthy, M. Subba Rao, and T. R. Narayanan Kutty, "Thermal decomposition of titanyl oxalates—I," *Journal of Inorganic and Nuclear Chemistry*, vol. 37, no. 4, pp. 891–898, Apr. 1975, doi: 10.1016/0022-1902(75)80668-3.

[56] A. Kareiva, S. Tautkus, R. Rapalaviciute, J.-E. Jørgensen, and B. Lundtoft, "Sol-gel synthesis and characterization of barium titanate powders," *Journal of Materials Science*, vol. 34, no. 19, pp. 4853–4857, 1999, doi: 10.1023/A:1004615912473.

[57] S. M. Aygün, P. Daniels, W. J. Borland, and J.-P. Maria, "In situ methods to explore microstructure evolution in chemically derived oxide thin films," *Journal Materials Research*, vol. 25, no. 3, pp. 427–436, Mar. 2010, doi: 10.1557/JMR.2010.0066.

[58] R. W. Schwartz, "Chemical Solution Deposition of Perovskite Thin Films," *Chemistry of Materials*, vol. 9, no. 11, pp. 2325–2340, Nov. 1997, doi: 10.1021/cm970286f.

[59] Robert Schwartz, Theodor Schneller, Rainer Waser, and Harold Dobberstein, "Chemical Solution Deposition of Ferroelectric Thin Films," in *Chemical Processing of Ceramics*, 2nd ed., Burtrand Lee and Sridhar Komarneni, Eds., Boca Raton, Florida: Taylor & Francis Group, 2005, pp. 713–742.

[60] Robert W. Schwartz, "Chemical solution deposition - basic principles," in *Solution Processing of Inorganic Materials*, D. M. Mitzi, Ed., New Jersey, USA: John Wiley & Sons, Inc., 2009, pp. 33–76.

[61] P. Tanja, "MICROSTRUCTURE AND DIELECTRIC PROPERTIES OF SOLUTION-DERIVED (Ba,Sr)TiO_3 THIN FILMS," Jožef Stefan International Postgraduate School, Ljubljana, Slovenia, 2016.

[62] S. Hoffmann-Eifert and T. Schneller, "Orientation and Microstructure Design," in *Chemical Solution Deposition of Functional Oxide Thin Films*, S. Theodor, W. Rainer, K. Marija, and P. David, Eds., Vienna: Springer Vienna, 2013, pp. 407–429. doi: 10.1007/978-3-211-99311-8_17.

[63] S. Hoffmann and R. Waser, "Control of the morphology of CSD-prepared (Ba,Sr)TiO_3 thin films," *Journal of the European Ceramic Society*, vol. 19, no. 6–7, pp. 1339–1343, Jun. 1999, doi: 10.1016/S0955-2219(98)00430-0.

[64] C. Mansour, M. Benwadih, and C. Revenant, "Sol-gel derived barium strontium titanate thin films using a highly diluted precursor solution," *American Institute of Physics: Advances*, vol. 11, no. 8, Aug. 2021, doi: 10.1063/5.0055584.

[65] E. Wainer, "High Titania Dielectrics," *Transactions of The Electrochemical Society*, vol. 89, no. 1, p. 331, 1946, doi: 10.1149/1.3071718.

[66] H. Han, J. Wang, Z. Wang, C. Liu, and B. Xiang, "Integrated barium titanate electro-optic modulators operating at CMOS-compatible voltage," *Applied Optics*, vol. 62, no. 22, p. 6053, Aug. 2023, doi: 10.1364/AO.499065.

[67] A. Karvounis, F. Timpu, V. V. Vogler-Neuling, R. Savo, and R. Grange, "Barium Titanate Nanostructures and Thin Films for Photonics," *Advanced Optical Materials*, vol. 8, no. 24, Dec. 2020, doi: 10.1002/adom.202001249.

[68] J. Y. Hsu, J. Y. M. Lee, J. J. Wang, L. Y. Yeh, J. T. Lai, and J. Gong, "Electrical properties of barium titanate ferroelectric thin films fabricated by rf magnetron sputtering for memory devices application," in *International Electron Devices and Materials Symposium*, IEEE, 1994, pp. 11-32-128-11-32–131. doi: 10.1109/EDMS.1994.863878.

[69] K. J. Choi *et al.*, "Enhancement of Ferroelectricity in Strained $BaTiO_3$ Thin Films," *Science (1979)*, vol. 306, no. 5698, pp. 1005–1009, Nov. 2004, doi: 10.1126/science.1103218.

[70] P. Firek, A. Werbowy, and J. Szmidt, "MIS field effect transistor with barium titanate thin film as a gate insulator," *Materials Science and Engineering: B*, vol. 165, no. 1–2, pp. 126–128, Nov. 2009, doi: 10.1016/j.mseb.2009.02.018.

[71] C.-Y. Wei *et al.*, "High-Performance Pentacene-Based Thin-Film Transistors and Inverters With Solution-Processed Barium Titanate Insulators," *IEEE Transactions on Electron Devices*, vol. 59, no. 2, pp. 477–484, Feb. 2012, doi: 10.1109/TED.2011.2174459.

[72] K. Sakayori *et al.*, "Curie Temperature of $BaTiO_3$," *Japanese Journal of Applied Physics*, vol. 34, no. 9S, p. 5443, Sep. 1995, doi: 10.1143/JJAP.34.5443.

[73] V. Petrovsky, T. Petrovsky, S. Kamlapurkar, and F. Dogan, "Dielectric Constant of Barium Titanate Powders Near Curie Temperature," *Journal of the American Ceramic Society*, vol. 91, no. 11, pp. 3590–3592, Nov. 2008, doi: 10.1111/j.1551-2916.2008.02693.x.

[74] H. Gong, X. Wang, S. Zhang, H. Wen, and L. Li, "Grain size effect on electrical and reliability characteristics of modified fine-grained BaTiO3 ceramics for MLCCs," *Journal of the European Ceramic Society*, vol. 34, no. 7, pp. 1733–1739, Jul. 2014, doi: 10.1016/j.jeurceramsoc.2013.12.028.

[75] P. Zheng, J. L. Zhang, Y. Q. Tan, and C. L. Wang, "Grain-size effects on dielectric and piezoelectric properties of poled $BaTiO_3$ ceramics," *Acta Materialia*, vol. 60, no. 13–14, pp. 5022–5030, Aug. 2012, doi: 10.1016/j.actamat.2012.06.015.

[76] Y. Huan, X. Wang, J. Fang, and L. Li, "Grain size effect on piezoelectric and ferroelectric properties of $BaTiO_3$ ceramics," *Journal of the European Ceramic Society,* vol. 34, no. 5, pp. 1445–1448, May 2014, doi: 10.1016/j.jeurceramsoc.2013.11.030.

[77] Q. Zhang and Y. Su, "Thickness and grain-size dependence of ferroelectric properties in columnar-grained $BaTiO_3$ thin films," *Journal of Applied Physics*, vol. 124, no. 14, Oct. 2018, doi: 10.1063/1.5041893.

[78] J. Zhai, X. Yao, J. Shen, L. Zhang, and H. Chen, "Structural and dielectric properties of $Ba(Zr_xTi_{1-x})O_3$ thin films prepared by the sol–gel process," *Journal of Physics D: Applied Physics*, vol. 37, no. 5, pp. 748–752, Mar. 2004, doi: 10.1088/0022-3727/37/5/016.

[79] J. F. Ihlefeld, J.-P. Maria, and W. Borland, "Dielectric and microstructural properties of barium titanate zirconate thin films on copper substrates," *Journal of Materials Research*, vol. 20, no. 10, pp. 2838–2844, Oct. 2005, doi: 10.1557/JMR.2005.0342.

[80] T. Ohno *et al.*, "Preparation and Characterization of Alkoxide-Derived Lead-Free Piezoelectric Barium Zirconate Titanate Thin Films with Different Compositions," *Japanese Journal of Applied Physics*, vol. 49, no. 9S, p. 09MA11, Sep. 2010, doi: 10.1143/JJAP.49.09MA11.

[81] R. Farhi, M. El Marssi, A. Simon, and J. Ravez, "A Raman and dielectric study of ferroelectric ceramics," *European Physical Journal B*, vol. 9, no. 4, pp. 599–604, Jul. 1999, doi: 10.1007/s100510050803.

[82] H. Tsukasaki, Y. Inoue, and Y. Koyama, "Crystallographic Features of the Relaxor State in the Mixed Ferroelectric System $Ba(Ti_{1-x}Zr_x)O_3$," *Materials Science Forum*, vol. 783–786, pp. 2400–2405, May 2014, doi: 10.4028/www.scientific.net/MSF.783-786.2400.

[83] L. Liu, S. Ren, J. Zhang, B. Peng, L. Fang, and D. Wang, "Revisiting the temperature-dependent dielectric permittivity of $Ba(Ti_{1-x}Zr_x)O_3$," *Journal of the American Ceramic Society*, vol. 101, no. 6, pp. 2408–2416, Jun. 2018, doi: 10.1111/jace.15410.

[84] T. Tohma, H. Masumoto, and T. Goto, "Dielectric Properties of $Ba(Ti_{0.85}Zr_{0.15})O_3$ Film Prepared by Metalorganic Chemical Vapor Deposition," *Japanese Journal of Applied Physics*, vol. 42, no. Part 1, No. 11, pp. 6969–6972, Nov. 2003, doi: 10.1143/JJAP.42.6969.

[85] T. Teranishi, S. Kajiyama, H. Hayashi, and A. Kishimoto, "Polarization behavior of sol-gel-derived relaxor $Ba(Zr,Ti)O_3$ films," *Journal of the American Ceramic Society*, vol. 100, no. 4, pp. 1542–1550, Apr. 2017, doi: 10.1111/jace.14768.

[86] J. F. Ihlefeld, J. P. Maria, and W. Borland, "Dielectric and microstructural properties of barium titanate zirconate thin films on copper substrates," *Journal of Materials Research*, vol. 20, no. 10, pp. 2838–2844, Oct. 2005, doi: 10.1557/JMR.2005.0342.

[87] A. Dixit, S. B. Majumder, A. Savvinov, R. S. Katiyar, R. Guo, and A. S. Bhalla, "Investigations on the sol–gel-derived barium zirconium titanate thin films," *Materials Letters*, vol. 56, no. 6, pp. 933–940, Nov. 2002, doi: 10.1016/S0167-577X(02)00640-7.

[88] Q. Jia, B. Shen, X. Hao, S. Song, and J. Zhai, "Anomalous dielectric properties of $Ba_{1-x}Ca_xTiO_3$ thin films near the solubility limit," *Materials Letters*, vol. 63, no. 3–4, pp. 464–466, Feb. 2009, doi: 10.1016/j.matlet.2008.11.026.

[89] B. Singh, S. Kumar, G. S. Arya, and N. S. Negi, "Room temperature structural and electrical properties of barium calcium titanate (BCT) thin films," *American Institute of Physics Conference Proceedings*, 2015, pp. 060005-. doi: 10.1063/1.4915375.

[90] M. Shi *et al.*, "Effect of annealing processes on the structural and electrical properties of the lead-free thin films of $(Ba_{0.9}Ca_{0.1})(Ti_{0.9}Zr_{0.1})O_3$," *Journal of Alloys Compounds*, vol. 562, pp. 116–122, Jun. 2013, doi: 10.1016/j.jallcom.2013.02.054.

[91] W. L. Li, T. D. Zhang, D. Xu, Y. F. Hou, W. P. Cao, and W. D. Fei, "$LaNiO_3$ seed layer induced enhancement of piezoelectric properties in (100)-oriented (1-x)BZT-xBCT thin films," *Journal of the European Ceramic Society*, vol. 35, no. 7, pp. 2041–2049, 2015, doi: 10.1016/j.jeurceramsoc.2015.01.018.

[92] S. R. Reddy, A. Kumar, A. R. James, V. V. B. Prasad, and S. K. Roy, "Ferroelectric and nano-mechanical properties of the chemical solution deposited lead-free BCZT films," *Materials Science and Engineering: B*, vol. 265, Mar. 2021, doi: 10.1016/j.mseb.2020.115037.

[93] G. Kang, K. Yao, and J. Wang, "(1-X)$Ba(Zr_{0.2}Ti_{0.8})O_3$-x$(Ba_{0.7}Ca_{0.3})TiO_3$ ferroelectric thin films prepared from chemical solutions," *Journal of the American Ceramic Society*, vol. 95, no. 3, pp. 986–991, Mar. 2012, doi: 10.1111/j.1551-2916.2011.04877.x.

[94] Q. G. Chi, C. H. Zhang, J. Sun, F. Y. Yang, X. Wang, and Q. Q. Lei, "Interface optimization and electrical properties of 0.5$Ba(Zr_{0.2}Ti_{0.8})O_3$-0.5$(Ba_{0.7}Ca_{0.3})TiO_3$ thin films prepared by a sol-gel process," *Journal of Physical Chemistry C*, vol. 118, no. 28, pp. 15220–15225, Jul. 2014, doi: 10.1021/jp5036103.

[95] S. He *et al.*, "High-performance La-doped BCZT thin film capacitors on $LaNiO_3$/Pt composite bottom electrodes with ultra-high efficiency and high thermal stability," *Ceramics International*, vol. 45, no. 9, pp. 11749–11755, Jun. 2019, doi: 10.1016/j.ceramint.2019.03.051.

[96] Q. G. Chi *et al.*, "Microstructures and electrical properties of 0.5$(Ba_{0.7}Ca_{0.3})TiO_3$-0.5$Ba(Zr_{0.2}Ti_{0.8})O_3$ thin films prepared by a sol-gel route," *Ceramics International*, vol. 39, no. 7, pp. 8195–8198, Sep. 2013, doi: 10.1016/j.ceramint.2013.04.001.

[97] Y. Lin, G. Wu, N. Qin, and D. Bao, "Structure, dielectric, ferroelectric, and optical properties of (1 - X)$Ba(Zr_{0.2}Ti_{0.8})O_3$ - X$(Ba_{0.7}Ca_{0.3})TiO_3$ thin films prepared by sol-gel method," *Thin Solid Films*, vol. 520, no. 7, pp. 2800–2804, Jan. 2012, doi: 10.1016/j.tsf.2011.12.030.

[98] N. Mamana, N. Pellegri, and M. G. Stachiotti, "Synthesis of lead-free $Ba_{0.85}Ca_{0.15}Zr_{0.1}Ti_{0.9}O_3$ thin films by the chelate route," *Journal of Sol-Gel Science and Technology*, vol. 102, no. 1, pp. 229–235, Apr. 2022, doi: 10.1007/s10971-021-05706-8.

[99] S. K. Streiffer, C. Basceri, C. B. Parker, S. E. Lash, and A. I. Kingon, "Ferroelectricity in thin films: The dielectric response of fiber-textured $(Ba_xSr_{1-x})Ti_{1+y}O_{3+z}$ thin films grown by chemical vapor deposition," *Journal of Applied Physics*, vol. 86, no. 8, pp. 4565–4575, Oct. 1999, doi: 10.1063/1.371404.

[100] L. J. Sinnamon, M. M. Saad, R. M. Bowman, and J. M. Gregg, "Exploring grain size as a cause for 'dead-layer' effects in thin film capacitors," *Applied Physics Letters*, vol. 81, no. 4, pp. 703–705, Jul. 2002, doi: 10.1063/1.1494837.

[101] J. Pérez de la Cruz, E. Joanni, P. M. Vilarinho, and A. L. Kholkin, "Thickness effect on the dielectric, ferroelectric, and piezoelectric properties of ferroelectric lead zirconate titanate thin films," *Journal of Applied Physics*, vol. 108, no. 11, Dec. 2010, doi: 10.1063/1.3514170.

[102] H. Wang *et al.*, "Spectroscopic ellipsometry study of $0.5BaZr_{0.2}Ti_{0.8}O_3$-$0.5Ba_{0.7}Ca_{0.3}TiO_3$ ferroelectric thin films," *Journal of Alloys and Compounds*, vol. 615, pp. 526–530, Dec. 2014, doi: 10.1016/j.jallcom.2014.06.186.

[103] S. W. Konsago, A. Debevec, J. Cilenšek, B. Kmet, and B. Malič, "Linear Thermal Expansion of $0.5Ba(Zr_{0.2}Ti_{0.8})O_3$-$0.5(Ba_{0.7}Ca_{0.3})TiO_3$ Bulk Ceramic," *Informacije MIDEM - Journal of Microelectronics, Electronic Components and Materials*, vol. 51, no. 3, Feb. 2024, doi: 10.33180/InfMIDEM2023.403.

[104] Z. M. Wang *et al.*, "Crystallization, phase evolution and ferroelectric properties of sol-gel-synthesized $Ba(Ti_{0.8}Zr_{0.2})O_3$-$x(Ba_{0.7}Ca_{0.3})TiO_3$ thin films," *Journal of Materials Chemistry C*, vol. 1, no. 3, pp. 522–530, Jan. 2013, doi: 10.1039/c2tc00020b.

[105] J. Xu *et al.*, "Microstructural, ferroelectric and photoluminescence properties of Er^{3+}-doped $Ba_{0.85}Ca_{0.15}Ti_{0.9}Zr_{0.1}O_3$ thin films," *Materials Chemistry and Physics*, vol. 262, Apr. 2021, doi: 10.1016/j.matchemphys.2021.124320.

[106] V. S. Puli *et al.*, "Nanoscale polarisation switching and leakage currents in $(Ba_{0.955}Ca_{0.045})(Zr_{0.17}Ti_{0.83})O_3$ epitaxial thin films," *Journal of Physics D: Applied Physics*, vol. 48, no. 35, Sep. 2015, doi: 10.1088/0022-3727/48/35/355502.

[107] J. Rödel, K. G. Webber, R. Dittmer, W. Jo, M. Kimura, and D. Damjanovic, "Transferring lead-free piezoelectric ceramics into application," *Journal of the European Ceramic Society*, vol. 35, no. 6, pp. 1659–1681, Jun. 2015, doi: 10.1016/j.jeurceramsoc.2014.12.013.

[108] C. Dagdeviren *et al.*, "Recent progress in flexible and stretchable piezoelectric devices for mechanical energy harvesting, sensing and actuation," *Extreme Mechanics Letters*, vol. 9, pp. 269–281, Dec. 2016, doi: 10.1016/j.eml.2016.05.015.

[109] Z. L. Cai *et al.*, "An investigation of the nanomechanical properties of $0.5Ba(Ti_{0.8}Zr_{0.2})O_3$-$0.5(Ba_{0.7}Ca_{0.3})TiO_3$ thin films," *Journal of the American Ceramic Society*, vol. 98, no. 1, pp. 114–118, 2015, doi: 10.1111/jace.13228.

[110] L. Huang, Y. Dai, Y. Wu, X. Pei, and W. Chen, "Enhanced ferroelectric and piezoelectric properties of $(1\text{-}x)BaZr_{0.2}Ti_{0.8}O_3$ –$xBa_{0.7}Ca_{0.3}TiO_3$ thin films by sol–gel process," *Applied Surface Science*, vol. 388, pp. 35–39, Dec. 2016, doi: 10.1016/j.apsusc.2016.05.030.

[111] S. R. Reddy, V. V. Bhanu Prasad, S. Bysakh, V. Shanker, J. Joardar, and S. K. Roy, "Ferroelectric and piezoelectric properties of $Ba_{0.85}Ca_{0.15}Ti_{0.90}Zr_{0.10}O_3$ films in 200 nm thickness range," *Journal of the American Ceramic Society*, vol. 102, no. 3, pp. 1277–1286, Mar. 2019, doi: 10.1111/jace.15983.

[112] M. D. Nguyen, E. P. Houwman, and G. Rijnders, "Large piezoelectric strain with ultra-low strain hysteresis in highly c-axis oriented $Pb(Zr_{0.52}Ti_{0.48})O_3$ films with columnar growth

on amorphous glass substrates," *Scientific Reports*, vol. 7, no. 1, p. 12915, Oct. 2017, doi: 10.1038/s41598-017-13425-w.

[113] S. Min *et al.*, "Clinical Validation of a Wearable Piezoelectric Blood-Pressure Sensor for Continuous Health Monitoring," *Advanced Materials*, vol. 35, no. 26, Jun. 2023, doi: 10.1002/adma.202301627.

[114] L. Song, S. Glinsek, S. Drnovsek, V. Kovacova, B. Malic, and E. Defay, "Piezoelectric thick film for power-efficient haptic actuator," *Applied Physics Letters*, vol. 121, no. 21, Nov. 2022, doi: 10.1063/5.0106174.

[115] S. Glinsek *et al.*, "Fully Transparent Friction-Modulation Haptic Device Based on Piezoelectric Thin Film," *Advanced Functional Materials*, vol. 30, no. 36, Sep. 2020, doi: 10.1002/adfm.202003539.

[116] W. M. Yim and R. J. Paff, "Thermal expansion of AlN, sapphire, and silicon," *Journal of Applied Physics*, vol. 45, no. 3, pp. 1456–1457, Mar. 1974, doi: 10.1063/1.1663432.

[117] S. W. Konsago *et al.*, "Engineering the Microstructure and Functional Properties of $0.5Ba(Zr_{0.2}Ti_{0.8})O_3$ -$0.5(Ba_{0.7}Ca_{0.3})TiO_3$ Thin Films," *American Chemical Society: Applied Electronic Materials*, May 2024, doi: 10.1021/acsaelm.4c00530.

[118] M. Kosec, B. Malic, and M. Mandeljc, "Chemical solution deposition of PZT thin films for microelectronics," *Materials Science in Semiconductor Processing*, vol. 5, no. 2–3, pp. 97–103, Apr. 2002, doi: 10.1016/S1369-8001(02)00089-6.

[119] L. Hao, H. Cheng, J. Ouyang, Y. Huan, and J. Yan, "Integration of Ferroelectric $K_{0.5}Na_{0.5}NbO_3$ films on Si at 400 ℃," *Materials Today Communications*, vol. 32, p. 104133, Aug. 2022, doi: 10.1016/j.mtcomm.2022.104133.

[120] S. W. Konsago, K. Žiberna, B. Kmet, A. Benčan, H. Uršič, and B. Malič, "Chemical Solution Deposition of Barium Titanate Thin Films with Ethylene Glycol as Solvent for Barium Acetate," *Molecules*, vol. 27, no. 12, p. 3753, Jun. 2022, doi: 10.3390/molecules27123753.

[121] S. Sivaramakrishnan, P. Mardilovich, T. Schmitz-Kempen, and S. Tiedke, "Concurrent wafer-level measurement of longitudinal and transverse effective piezoelectric coefficients (d_{33},f and e_{31},f) by double beam laser interferometry," *Journal of Applied Physics*, vol. 123, no. 1, Jan. 2018, doi: 10.1063/1.5019568.

[122] A. Matavž, A. Bradeško, T. Rojac, B. Malič, and V. Bobnar, "Self-assembled porous ferroelectric thin films with a greatly enhanced piezoelectric response," *Applied Materials Today*, vol. 16, pp. 83–89, Sep. 2019, doi: 10.1016/j.apmt.2019.04.008.

[123] V. L. Ene *et al.*, "Influence of Grain Size on Dielectric Behavior in Lead-Free 0.5 $Ba(Zr_{0.2}Ti_{0.8})O_3$–$0.5(Ba_{0.7}Ca_{0.3})TiO_3$ Ceramics," *Nanomaterials*, vol. 13, no. 22, p. 2934, Nov. 2023, doi: 10.3390/nano13222934.

[124] X.-X. Huang, T.-F. Zhang, W. Wang, P.-Z. Ge, and X.-G. Tang, "Tailoring energy-storage performance in antiferroelectric $PbHfO_3$ thin films," *Materials & Design*, vol. 204, p. 109666, Jun. 2021, doi: 10.1016/j.matdes.2021.109666.

[125] Y. Z. Li, Z. J. Wang, Y. Bai, and Z. D. Zhang, "High energy storage performance in Ca-doped $PbZrO_3$ antiferroelectric films," *Journal of the European Ceramic Society*, vol. 40, no. 4, pp. 1285–1292, Apr. 2020, doi: 10.1016/j.jeurceramsoc.2019.11.063.

[126] C. T. Q. Nguyen, H. N. Vu, and M. D. Nguyen, "High-performance energy storage and breakdown strength of low-temperature laser-deposited relaxor PLZT thin films on flexible

Ti-foils," *Journal of Alloys and Compounds*, vol. 802, pp. 422–429, Sep. 2019, doi: 10.1016/j.jallcom.2019.06.205.

[127] M. D. Nguyen and G. Rijnders, "Comparative study of piezoelectric response and energy-storage performance in normal ferroelectric, antiferroelectric and relaxor-ferroelectric thin films," *Thin Solid Films*, vol. 697, p. 137843, Mar. 2020, doi: 10.1016/j.tsf.2020.137843.

[128] H. Pan *et al.*, "Giant energy density and high efficiency achieved in bismuth ferrite-based film capacitors via domain engineering," *Nature Communications*, vol. 9, no. 1, p. 1813, May 2018, doi: 10.1038/s41467-018-04189-6.

[129] J. P. B. Silva *et al.*, "High-Performance Ferroelectric–Dielectric Multilayered Thin Films for Energy Storage Capacitors," *Advanced Functional Materials*, vol. 29, no. 6, Feb. 2019, doi: 10.1002/adfm.201807196.

[130] G. A. Boni, C. Chirila, L. D. Filip, I. Pintilie, and L. Pintilie, "Negative capacitance in epitaxial ferroelectric capacitors evidenced by dynamic dielectric characterization," *Materials Today Communications*, vol. 26, p. 102076, Mar. 2021, doi: 10.1016/j.mtcomm.2021.102076.

[131] Y. Hiranaga, T. Mimura, T. Shimizu, H. Funakubo, and Y. Cho, "Local C-V Characterization for Ferroelectric Films," in *2021 IEEE International Symposium on Applications of Ferroelectrics (ISAF)*, IEEE, May 2021, pp. 1–3. doi: 10.1109/ISAF51943.2021.9477316.

[132] N. Tayebi *et al.*, "Tuning the Built-in Electric Field in Ferroelectric $Pb(Zr_{0.2}Ti_{0.8})O_3$ Films for Long-Term Stability of Single-Digit Nanometer Inverted Domains," *Nano Letters*, vol. 12, no. 11, pp. 5455–5463, Nov. 2012, doi: 10.1021/nl302911k.

[133] R. Placeres-Jiménez, J. P. Rino, and J. A. Eiras, "Modeling ferroelectric permittivity dependence on electric field and estimation of the intrinsic and extrinsic contributions," *Journal of Physics D: Applied Physics*, vol. 48, no. 3, p. 035304, Jan. 2015, doi: 10.1088/0022-3727/48/3/035304.

[134] V. Veerapandiyan, F. Benes, T. Gindel, and M. Deluca, "Strategies to Improve the Energy Storage Properties of Perovskite Lead-Free Relaxor Ferroelectrics: A Review," *Materials*, vol. 13, no. 24, p. 5742, Dec. 2020, doi: 10.3390/ma13245742.

[135] M. Maraj, W. Wei, B. Peng, and W. Sun, "Dielectric and Energy Storage Properties of $Ba_{(1-x)}Ca_xZr_yTi_{(1-y)}O_3$ (BCZT): A Review," *Materials*, vol. 12, no. 21, p. 3641, Nov. 2019, doi: 10.3390/ma12213641.

[136] H. Palneedi, M. Peddigari, G. Hwang, D. Jeong, and J. Ryu, "High-Performance Dielectric Ceramic Films for Energy Storage Capacitors: Progress and Outlook," *Advanced Functional Materials*, vol. 28, no. 42, 2018, doi: 10.1002/adfm.201803665.

[137] M. Sadl *et al.*, "Energy-storage-efficient $0.9Pb(Mg_{1/3}Nb_{2/3})O_3$–$0.1PbTiO_3$ thick films integrated directly onto stainless steel," *Acta Materialia*, vol. 221, p. 117403, 2021, doi: 10.1016/j.actamat.2021.117403.

[138] H. Ghayour and M. Abdellahi, "A brief review of the effect of grain size variation on the electrical properties of $BaTiO_3$-based ceramics," *Powder Technology*, vol. 292, pp. 84–93, 2016, doi: 10.1016/j.powtec.2016.01.030.

Bibliography

Scientific Articles Related to the Thesis

[1]. Konsago, S. W., Žiberna, K., Kmet, B., Benčan, A., Uršič, H., & Malič, B., Chemical solution deposition of barium titanate thin films with ethylene glycol as solvent for barium acetate. *Molecules*, 2022, 27(12), 3753. DOI: 10.3390/molecules27123753.

[2]. Konsago, S. W., Žiberna, K., Matavž, A., Mandal, B., Glinšek, S., Fleming, Y., Benčan, A., Brennecka, G. L., Uršič, H., Malič, B., Engineering the Microstructure and Functional Properties of $0.5Ba(Zr_{0.2}Ti_{0.8})O_3$-$0.5(Ba_{0.7}Ca_{0.3})TiO_3$ Thin Films. *ACS Applied Electronic Materials*, 2024, 6(6), 4467–4477. DOI: 10.1021/acsaelm.4c00530.

[3]. Konsago, S. W., Žiberna, K., Ekar, J., Kovac, J., & Malic, B., Designing the thermal processing of $Ba(Ti_{0.8}Zr_{0.2})O_3$-$(Ba_{0.7}Ca_{0.3})TiO_3$ thin films from ethylene glycol-derived precursor, *Journal of Materials Chemistry C.*, 12(36), 14658-14666, 2024. DOI: 10.1039/D4TC02495H.

[4]. Konsago, S. W., Debevec, A., Cilenšek, J., Kmet, B., & Malič, B., Linear Thermal Expansion of $0.5Ba(Zr_{0.2}Ti_{0.8})O_3$-0.5 $(Ba_{0.7}Ca_{0.3})TiO_3$ Bulk Ceramic. *Informacije MIDEM*, 2023, 53(4), 233-238. DOI: 10.33180/InfMIDEM2023.403.

[5]. Konsago, S.W., Žiberna, K., Matavž, A., Mandal, B., Glinšek, S., Brennecka, G. L., Hana Uršič, H., and Malič, B., "High Energy Storage Density and Efficiency of $0.5Ba(Zr_{0.2}Ti_{0.8})O_3$-$0.5(Ba_{0.7}Ca_{0.3})TiO_3$ Thin Films on Platinized Sapphire Substrates", *Journal of Materials Chemistry A*, Vol 13, Issue 4, pp. 2911 – 2919, 2025.

Published Scientific Conference Contributions – Abstracts

[1]. Konsago, S.W., Žiberna, K., Ekar, J., Matavž, A., Kovač, J., Benčan, A., Uršič, H., Malič, B., Energy storage properties of $0.5Ba(Zr_{0.2}Ti_{0.8})O_3$-$0.5(Ba_{0.7}Ca_{0.3})TiO_3$ thin films by ethylene glycol-based chemical solution deposition, 59^{th} International Conference on Microelectronics, Devices and Materials & Workshop on Electromagnetic Compatibility: From Theory to Practice; conference proceedings: October 2-October 4,2024, Rimske Toplice, Slovenia. [COBISS.SI-ID - 211771907].

[2]. Konsago, S.W., Žiberna, K., Ekar, J., Matavž, A., Kovač, J., Benčan, A., Uršič, H., Malič, B., Homogeneity and multifunctionality of $0.5Ba(Zr_{0.2}Ti_{0.8})O_3$-$0.5(Ba_{0.7}Ca_{0.3})TiO_3$ ceramic thin films by chemical solution deposition Electroceramics XIX Conference 2024: proceedings: August 19 -August 22, Vilnius, Lithuania. [COBISS.SI-ID - 205620483].

[3]. Konsago, S.W., Žiberna, K., Matavž, A., Mandal, B., Benčan, A., Glinšek, S., Malič, B., Microstructure design for optimized functional properties of $Ba(Zr_{0.2}Ti_{0.8})O_3$-$(Ba_{0.7}Ca_{0.3})TiO_3$ thin films by chemical solution deposition, ECAPD 2024: European

Conference on Applications of Polar Dielectrics: proceedings: June 16 – June 19, Trondheim, Norway, [COBISS.SI-ID - 201796099].

[4]. Malič, B., Konsago, S.W., Kmet, B., Benčan, A., Barium zirconate titanate barium calcium titanate thin films from the viewpoint of processing-microstructure-properties-relationship, ECAPD 2024: European Conference on Applications of Polar Dielectrics: proceedings: June 16 – June 19, Trondheim, Norway, [COBISS.SI-ID - 203723779].

[5]. Konsago, S.W., Žiberna, K., Benčan, A., Uršič, H., Malič, B., Ethylene-glycol based chemical solution deposition of $0.5Ba(Zr_{0.2}Ti_{0.8})O_3$—$0.5(Ba_{0.8}Ca_{0.3})TiO_3$ thin films, 58th International Conference on Microelectronics, Devices and Materials & The Workshop on Chemical sensors: Materials and Applications: conference 2023: proceedings: September 27- September 29, Lipica, Slovenia (Str. 97-98), [COBISS.SI-ID - 167128067].

[6]. Konsago, S. W., Žiberna, K., Matavž, A., Mandal, B., Glinšek, S., Benčan, A., Uršič, H., Brennecka, L. G., Malič, B., Enhanced dielectric, electromechanical and energy storage properties of $0.5Ba(Zr_{0.2}Ti_{0.8})O_3$—$0.5(Ba_{0.8}Ca_{0.3})TiO_3$ thin films by the ethylene glycol based chemical solution deposition, 7th International School of Oxide Electronics: Cargèse, August 29 -September 8, 2023 (Str. [57]), https://isoe.cnrs.fr/wp-content/uploads/2023/08/Booklet_ISOE2023.pdf, [COBISS.SI-ID - 164286979].

[7]. Konsago, S. W., Žiberna, K., Kmet, B., Benčan, A., Uršič, H., Brennecka, L. G., Malič, B., Microstructure and properties of $0.5Ba(Zr_{0.2}Ti_{0.8})O_3$-$0.5(Ba_{0.7}Ca_{0.3})TiO_3$ thin films by ethylene-glycol based solution route, Conference & Exhibition of the European Ceramic Society: Lyon-France, 2/6 July 2023, conference contribution, https://www.ecers2023.org/en/program/full-conference-program/34?paramSearch34-0=%C5%BEiberna [COBISS.SI-ID 158593027].

[8]. Konsago, S. W., Žiberna, K., Kmet, B., Benčan, A., Uršič, H., Malič, B., Influence of the choice of the solvents on microstructure and properties of solution-derived barium titanate-based thin films, 57th International Conference on Microelectronics, Devices and Materials & The Workshop on Energy Harvesting: Materials and Applications: conference 2022: proceedings: September 14 - September 16 2022, Maribor, Slovenia. Ljubljana: MIDEM - Society for Microelectronics, Electronic Components and Materials, 2022. Str. 107-108. ISBN 978-961-95495-1-3. [COBISS.SI-ID 121794307].

[9]. Konsago, S. W., Žiberna, K., Kmet, B., Benčan, A., Uršič, H., Malič, B., Influence of solution formulation on microstructural features of solution-derived barium titanate-based thin films. V: NOVAK, Rok (ur.), et al. 14. študentska konferenca Mednarodne podiplomske šole Jožefa Stefana = 14th Jožef Stefan International Postgraduate School Students' Conference: knjiga povzetkov = book of abstracts: 1. - 3. junij 2022, Kamnik, Slovenia = 1st - 3rd June, 2022, Kamnik, Slovenia. Slovenia. Ljubljana: Jožef Stefan Institute: Jožef Stefan International Postgraduate School, 2022. Str. 92. http://ipssc.mps.si/Book_of_Abstracts.pdf. [COBISS.SI-ID 113713411].

[10]. Konsago, S. W., Žiberna, K., Kmet, B., Benčan, A., Uršič, H., Malič, B., $Ba(Zr,Ti)O_3$—$(Ba,Ca)TiO_3$ ferroelectric thin films from ethylene glycol-based solutions. V: ISAF 2022: ISAF-PFM-ECAPD [joint conference]: June 27-July 1, 2022, Tours, France. Piscataway: IEEE = Institute of Electrical and Electronics Engineers. 2022, str. 56. https://isaf-virtual.org/presentation/lecture/bazrtio3bacatio3-ferroelectric-thin-films-ethylene-glycolbased-solutions. [COBISS.SI-ID 114805507].

[11]. Konsago, S. W., Žiberna, K., Kmet, B., Uršič, H., Malič, B., Preparation of solid solution of barium titanate-based thin films by chemical solution deposition, Throughout knowledge towards a green new world: 13. Študentska konferenca Mednarodne podiplomske šole Jožefa Stefana in 15. dan mladih raziskovalcev (Konferenca KMBO), 27-28 maj 2021, Ljubljana, Slovenija: knjiga povzetkov = 13th Jožef Stefan International Postgraduate School Students' Conference and 15th Young Researchers' Day of Chemistry, material science, biochemistry and environment, (CMBE day), 27th-28th May 2021, online: book of abstracts. Jožef Stefan International Postgraduate School: Inštitut Jožef Stefan, 2021, Str. 83. http://ipssc.mps.si/bookOfAbstracts/Book_of_abstracts_v04.pdf. [COBISS.SI-ID 66792707].

[12]. Žiberna, K., Konsago, S. W., Condurache, O., Kmet, B., Malič, B., Benčan, A., Microstructural characterisation of ferroelectric BaTiO3-based thin films, Throughout knowledge towards a green new world: 13. Študentska konferenca Mednarodne podiplomske šole Jožefa Stefana in 15. dan mladih raziskovalcev (Konferenca KMBO), 27-28 maj 2021, Ljubljana, Slovenija: knjiga povzetkov = 13th Jožef Stefan International Postgraduate School Students' Conference and 15th Young Researchers' Day of Chemistry, material science, biochemistry and environment, (CMBE day), 27th-28th May 2021, online: book of abstracts. Ljubljana: Mednarodna podiplomska šola Jožefa Stefana: = Jožef Stefan International Postgraduate School: Inštitut Jožef Stefan: = Jožef Stefan Institute, 2021. Str. 81-82. http://ipssc.mps.si/bookOfAbstracts/Book_of_abstrašcts_v04.pdf. [COBISS.SI-ID 65624323].

[13]. Žiberna, K., Konsago, S. W., Malič, B., Kmet, B., Condurache, O., Benčan, A., Electron microscopy study of BaTiO3-based thin films prepared by chemical solution deposition. Book of abstracts: Slovenski kemijski dnevi 2021 = 27th Annual Meeting of the Slovenian Chemical Society: 22.-24. September 2021, Portorož, Portorose, Slovenija. Ljubljana: Slovensko kemijsko društvo, 2021. Str. 206. ISBN 978-961-93849-9-2. [COBISS.SI-ID 79246851].

[14]. Konsago, S. W., Žiberna, K., Kmet, B., Uršič, H., Malič, B., Chemical solution deposition of $BaTiO_3$-based thin films on $LaNiO_3$ seed layers. 56th International Conference on Microelectronics, Devices and Materials & the Workshop on Personal Sensor for Remote Health Care Monitoring: conference 2021: proceedings: September 22 - September 24, 2021, Ljubljana, Slovenia. Ljubljana: MIDEM - Society for Microelectronics, Electronic Components and Materials, 2021. Str. 45-46, ilustr. ISBN 978-961-95495-0-6. [COBISS.SI-ID 84529667].

[15]. Konsago, S. W., Kmet, B., Uršič, H., Dragomir, M., Malič, B., Chemical solution deposition of $0.5Ba(Ti_{0.9}Zr_{0.1})O_3{-}0.5(Ba_{0.8}Ca_{0.2})TiO_3$ thin films using ethylene-glycol as a co-solvent. V: Piezo 2021: Piezoelectrics for End Users XI, 24-24 February, fe. 21-24, 2021, Sassari: online winter school. [S. l.: s. n.], 2021. https://www.piezo2021.org. [COBISS.SI-ID 53017091].

[16]. Konsago, S. W., Kmet, B., Dragomir, M., Uršič, H., Malič, B., Barium titanate based ferroelectric thin films prepared by aqueous chemical solution deposition, Electroceramics XVII, International Conference: virtual Darmstadt: book of abstracts. 2020. Str. 250.

https://www.electroceramics.org/electroceramics17-book-of-abstracts.pdf. [COBISS.SI-ID 30671619].

Unpublished Scientific Conference Contributions

[1]. Konsago, S. W., Žiberna, K., Kmet, B., Uršič, H., Malič, B., Chemical solution deposition of barium titanate based thin films using different combinations of solvents: 7th Japan-Slovenia web workshop on piezoelectric thin films, April 4th, 2022, [COBISS.SI-ID – 154345987]

[2]. Konsago, S. W., Žiberna, K., Matavž, A., Brennecka, L. G., Uršič, H., Malič, B., $0.5Ba(Zr_{0.2}Ti_{0.8})O_3$–$0.5(Ba_{0.8}Ca_{0.3})TiO_3$ thin films by the ethylene glycol based chemical solution deposition, 8th Japan-Slovenia web workshop on piezoelectric thin films, June, 2nd, 2023, [COBISS.SI-ID – 154347267].

Biography

I was born on the 1st of January 1993 in Dassari, Benin. After finishing high school at Natitingou General Education College, Benin in 2011, I have enrolled in the programme of chemistry at Kalmyk State University, Russia in 2012. Graduated in July 2016 with a bachelor in chemistry. The diploma thesis entitled "identification of the features of the chemical composition of vegetable oils by the chromatographic method". The Bachelor thesis was supervised by Assoc. Prof Oleg Ermolaevich Romanov and carried out at Kalmyk State University.

In September 2016, I was enrolled in a fundamental and applied chemistry programme, specializing in organic chemistry, at the Faculty of Science, Peoples' Friendship University of Russia, Moscow, Russia. In June 2018, I graduated with a Master's degree in fundamental and applied chemistry. The thesis was entitled "Synthesis of 1-R-1-(R2-ethynyl) substituted tetrahydroisoquinolines and study of their transformations involving activated alkynes in protic and aprotic solvents". The work on my Master's thesis was carried out at the Peoples' Friendship University of Russia, under the supervision of Assoc. Prof Alexander Anatolievich Titov.

In November 2019, I started working as a young researcher at the "Electronic Ceramics Department K5, Jožef Stefan Institute" and enrolled in doctoral studies under the supervision of Prof. Dr. Barbara Malič, in the Sensor Technologies programme at the Jožef Stefan International Postgraduate School, Ljubljana, Slovenia. My current work at JSI is focused on the chemical solution deposition of Ca, Zr modified barium titanate thin films, the chemistry of coating solutions, the decomposition process of gels, the characterization of the microstructure, and the dielectric, ferroelectric/piezoelectric properties of the films and also the energy storage properties of BZT-BCT thin films.

During my PhD study, I had the chance to visit two foreign laboratories: the Materials Center in Leoben, Austria, and the Instituto de Ciencia de Materiales de Madrid, CSIC, Spain.

Attendance at workshops and schools:

- ECerS Summer Schools: Characterization and Modeling of Electroceramics, August 24 – 27, 2020, in Darmstadt, Germany, online.
- Winter School Piezo2021: Piezoelectrics for End Users XI edition. 21-24 February 2021, Sassari, Italy.
- The 1st Japan-Slovenia web workshop on piezoelectric thin films, online via Zoom October 8th 2021,
- Workshop on the personal sensor for remote health care monitoring, Slovenia, September 24th 2021.
- The 2nd Japan-Slovenia web workshop on piezoelectric thin films, online via Zoom December 3rd 2021
- The 3rd Japan-Slovenia web workshop on piezoelectric thin films, online via Zoom February 4th, 2022
- The 4th Japan-Slovenia web workshop on piezoelectric thin films, online via Zoom April 1st 2022
- The 5th Japan-Slovenia web workshop on piezoelectric thin films, online via Zoom June 10th 2022

- ❖ Workshop Energy Harvesting: Materials and Applications, Maribor, Slovenia, September 15th 2022.
- ❖ ECerS Summer School: Advanced Characterization Techniques. June 29th – 30th , 2023, Lyon, France
- ❖ The 7th International School of Oxide Electronics: August 29th -September 8th, 2023, Cargèse, France.
- ❖ Workshop Energy Harvesting: Materials and Applications, Lipica, Slovenia, September 28th, 2023.
- ❖ Workshop Versatile usefulness of ferroic materials, November 21st -22nd, 2023, Ankaran, Slovenia.
- ❖ The 8th Japan-Slovenia web workshop on piezoelectric thin films, online via Zoom December, 1st, 2023.
- ❖ Electroceramics Summer School on "Advanced characterisation on Electroceramics" August 17- 18th,2024, Vilnius, Lithuania.
- ❖ Workshop Electromagnetic Compatibility: From Theory to Practice, October 2nd - 4th, 2024, Rimske Toplice, Slovenia.
- ❖ FerroSchool 2024: November 18th - 21st, 2024, at Jožef Stefan Institute, Ljubljana, Slovenia.